Fall 12-22-2010

Mapping Trabecular Bone Fabric Tensor by in Vivo Magnetic Resonance Imaging

Michael J. Wald
University of Pennsylvania, Philadelphia, mikewald@gmail.com

Mapping Trabecular Bone Fabric Tensor by in Vivo Magnetic Resonance Imaging

Abstract
The mechanical competence of bone depends upon its quantity, structural arrangement, and chemical composition. Assessment of these factors is important for the evaluation of bone integrity, particularly as the skeleton remodels according to external (e.g. mechanical loading) and internal (e.g. hormonal changes) stimuli. Micro magnetic resonance imaging (μMRI) has emerged as a non-invasive and non-ionizing method well-suited for the repeated measurements necessary for monitoring changes in bone integrity. However, in vivo image-based directional dependence of trabecular bone (TB) has not been linked to mechanical competence or fracture risk despite the existence of convincing ex vivo evidence. The objective of this dissertation research was to develop a means of capturing the directional dependence of TB by assessing a fabric tensor on the basis of in vivo μMRI. To accomplish this objective, a novel approach for calculating the TB fabric tensor based on the spatial autocorrelation function was developed and evaluated in the presence of common limitations to in vivo μMRI. Comparisons were made to the standard technique of mean-intercept-length (MIL). Relative to MIL, ACF was identified as computationally faster by over an order of magnitude and more robust within the range of the resolutions and SNRs achievable in vivo. The potential for improved sensitivity afforded by isotropic resolution was also investigated in an improved μMR imaging protocol at 3T. Measures of reproducibility and reliability indicate the potential of images with isotropic resolution to provide enhanced sensitivity to orientation-dependent measures of TB, however overall reproducibility suffered from the sacrifice in SNR. Finally, the image-derived TB fabric tensor was validated through its relationship with TB mechanical competence in specimen and in vivo μMR images. The inclusion of trabecular bone fabric measures significantly improved the bone volume fraction-based prediction of elastic constants calculated by micro-finite element analysis. This research established a method for detecting TB fabric tensor in vivo and identified the directional dependence of TB as an important determinant of TB mechanical competence.

Degree Type
Dissertation

Degree Name
Doctor of Philosophy (PhD)

Graduate Group
Bioengineering

First Advisor
Felix W. Wehrli

Keywords
osteoporosis, bone, morphology, biomechanics, magnetic resonance imaging

Subject Categories
Bioimaging and Biomedical Optics | Mechanics of Materials | Musculoskeletal System | Radiology

MAPPING TRABECULAR BONE FABRIC TENSOR BY IN VIVO MAGNETIC RESONANCE IMAGING

Michael J. Wald

A Dissertation in Bioengineering

Presented to the Faculties of the University of Pennsylvania in Partial Fulfillment of the Requirements for the Degree of Doctor of Philosophy

2010

Doctor Felix W. Wehrli:
Supervisor of Dissertation

Doctor Susan Margulies:
Graduate Group Chairperson

Dissertation committee:

Doctor Dawn M. Elliott, Department of Bioengineering

Doctor Charles L. Epstein, Department of Mathematics

Doctor Hee Kwon Song, Department of Radiology

DEDICATION

In recognition of my wife's "PhD" in patience and my family's continual support and love

ACKNOWLEDGEMENTS

For guidance, support, and exemplary science:

Dr. Felix W. Wehrli

Dr. Jeremy F. Magland

Current and former LSNI colleagues:

Dr. Sailaja Anumula, Dr. Yusuf Bhagat, Tom Connick, Holly Flachs, Dr. Benny Lam, Dr. Michael Langham, Henry Ong, Dr. Chamith Rajapakse, Dr. Punam K. Saha, Dr. Aranee Techawiboonwong, Dr. Branimir Vasilic, Dr. Alexander Wright

ABSTRACT

MAPPING TRABECULAR BONE FABRIC TENSOR BY *IN VIVO* MAGNETIC RESONANCE IMAGING

MICHAEL J. WALD

FELIX W. WEHRLI

The mechanical competence of bone depends upon its quantity, structural arrangement, and chemical composition. Assessment of these factors is important for the evaluation of bone integrity, particularly as the skeleton remodels according to external (e.g. mechanical loading) and internal (e.g. hormonal changes) stimuli. Micro magnetic resonance imaging (μMRI) has emerged as a non-invasive and non-ionizing method well-suited for the repeated measurements necessary for monitoring changes in bone integrity. However, *in vivo* image-based directional dependence of trabecular bone (TB) has not been linked to mechanical competence or fracture risk despite the existence of convincing *ex vivo* evidence. The objective of this dissertation research was to develop a means of capturing the directional dependence of TB by assessing a fabric tensor on the basis of *in vivo* μMRI. To accomplish this objective, a novel approach for calculating the TB fabric tensor based on the spatial autocorrelation function was developed and evaluated in the presence of common limitations to *in vivo* μMRI. Comparisons were made to the standard technique of mean-intercept-length (MIL). Relative to MIL, ACF was identified as computationally faster by over an order of magnitude and more robust within the range of the resolutions and SNRs achievable *in vivo*. The potential for improved sensitivity afforded by isotropic resolution was also

investigated in an improved μMR imaging protocol at 3T. Measures of reproducibility and reliability indicate the potential of images with isotropic resolution to provide enhanced sensitivity to orientation-dependent measures of TB, however overall reproducibility suffered from the sacrifice in SNR. Finally, the image-derived TB fabric tensor was validated through its relationship with TB mechanical competence in specimen and *in vivo* μMR images. The inclusion of trabecular bone fabric measures significantly improved the bone volume fraction-based prediction of elastic constants calculated by micro-finite element analysis. This research established a method for detecting TB fabric tensor *in vivo* and identified the directional dependence of TB as an important determinant of TB mechanical competence.

TABLE OF CONTENTS

LIST OF TABLES

LIST OF FIGURES

1 Chapter 1 Introduction

1.1 Motivation

Morphological and mechanical properties of human trabecular bone (TB) have been studied by anatomists and engineers for more than a century. In 1892, the German anatomist/surgeon Julius Wolff first hypothesized that bone continually adapts to its mechanical environment, a mechanism that has since been readily observed in the varying trabecular architectures of the calcaneus, femur, vertebrae, tibia and radius. Wolff's theory was eventually followed by the conjecture that the elastic properties of fully adapted bone match the forces experienced in the native mechanical environment [Cowin, 1986], i.e. bone optimizes its quantity, architecture, and composition according to its mechanical burden.

Currently, clinical evaluation of fracture risk focuses on measures of bone mineral density (BMD). While a useful tool for diagnosis of osteoporosis, BMD provides information on the quantity of mineral in bone, only one of the components involved in bone strength. New imaging modalities assessing bone strength, independent of BMD, have recently emerged demonstrating enhanced abilities to assess the risk of fracture and the subsequent response to treatment. Sufficient *ex vivo* evidence portends the orientation or structural anisotropy of TB is an important determinant of bone strength [Hodgskinson and Currey, 1990]. The structural anisotropy of TB greatly enhances bone's load-carrying capacity without increasing mass, thus improving its structural efficiency. Changes in the directional dependence of TB in response to disease, usage, and treatment are reflective of the skeleton's functional integrity. To capture the structural anisotropy of TB, a fabric tensor representation (second-rank symmetric

tensor) has been adopted. However, its assessment is largely restricted to high-resolution *ex vivo* images where binarization of the TB structure is straightforward. A fabric tensor representation of bone has not been used to predict mechanical properties of bone on the basis of *in vivo* images. The focus of this thesis is on detecting TB orientation by way of mapping a fabric tensor on the basis of *in vivo* magnetic resonance imaging.

The following introductory chapter presents a background for the thesis, beginning with the fundamentals of bone biology, bone remodeling, and disease, followed by a description of the current diagnostic technologies used to assess bone quality. A brief overview of biomechanical analysis of TB is also provided. The final section outlines the objectives addressed in this thesis throughout the subsequent chapters.

1.2 Bone biology

Skeletal function and composition can be considered separately for the axial (head, neck, and torso) and appendicular (limbs) zones of the body (see Table 1.1). Bones of the axial skeleton function as a structural support for the body and as housing for blood cell formation. In the appendicular zone, bone's primary function relates to locomotion and weight bearing. Consequently, it is no surprise that the composition of bone differs between the axial and appendicular skeleton. Here, bone anatomy will be considered at the macroscopic, microscopic, and chemical levels.

Feature	Axial	Appendicular
Main tissue type	Cancellous	Cortical
Adjacent soft tissue	Viscera	Muscle
Cortices	Thin	Thick
Marrow type	Hematopoietic	Fatty
Turnover	High	Low
Cortical	Mechanical	Mechanical
Cancellous	Metabolic	Mechanical

Table 1.1 Summary of composition and functional differences between bones of the axial and appendicular skeletons.

1.2.1 Macroscopic level

Bone is essential to the proper functioning of vital organs as it provides the scaffold to which organs are anchored. Bone is classified into two types: 1) cortical bone and 2) trabecular or cancellous bone. All long bones of the appendicular skeleton have a general structure similar to that shown in Figure 1.1: a diaphysis or shaft composed of thick cortical bone (CB) surrounding a marrow-filled medullary cavity and two metaphyses or ends each containing an interior network of TB enclosed by a thinner cortical bone shell. The axial skeleton's structure mimics that seen in the metaphyses of long bones: thin cortices surrounding TB. The primary difference between the TB in the two skeletal regions is the presence of red (hematopoietic) marrow in the axial region versus yellow (fatty) marrow in the appendicular region.

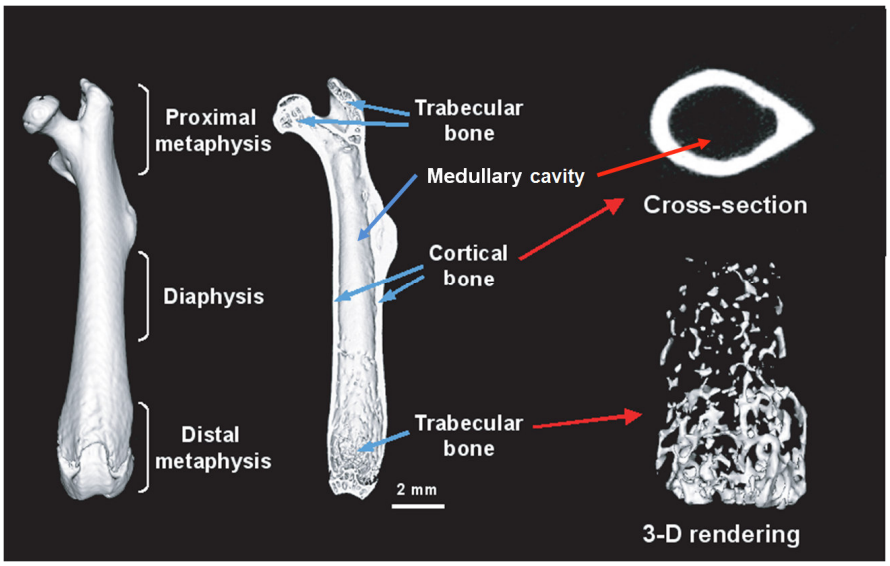

Figure 1.1 Macroscopic view of bone anatomy showing cortical and trabecular compartments within a mouse femur (adapted from [Jepsen, 2009]).

Structurally, the two types of bone are quite different as CB is hard and dense while TB is porous. More specifically, TB is a lattice of interconnected plate- and rod-like bone structures interspersed with bone marrow. Cortical bone has a porosity of 5-10% versus 50-90% for trabecular bone [Michigan, 2010]. Cortical bone contains eighty percent of the body's bone volume while trabecular bone possesses roughly twice the surface area of cortical bone [Jee, 1983]. Consequently, trabecular bone is considered more metabolically active than its counterpart as bone remodeling typically occurs on the bone surface.

Mechanically, TB tissue is 20 to 30% less stiff than cortical bone tissue [Kuhn, Goldstein et al., 1989; Choi and Goldstein, 1992]. This disparity was not explained by differences in mineralization [Choi, Kuhn et al., 1990], suggesting that it originates from variances in microscopic arrangement. The importance of TB in preventing fracture seems to vary according to fracture site and the nature of the mechanical impetus. TB provides a majority of the mechanical strength of vertebral bodies [Hulme, Boyd et al., 2007]. In the mid-femoral neck, a common site of fracture, the amount of TB exceeds

that of CB [Bagi, Wilkie et al., 1997]. In a study of cadaveric left and right femur pairs, removal of the TB component caused a mean 39.5% reduction in mechanical strength while BMC reduced by mean 23.5% [Werner, Iversen et al., 1988]. Further, the correlation between lost BMC and lost fracture strength was poor [Werner, Iversen et al., 1988], suggesting the TB compartment is more than simply additional bone mineral. The load-carrying contribution of TB in the femoral neck during a fall has been estimated at 50% [Lotz, Cheal et al., 1995], further illustrating its importance in preventing femoral-neck fracture.

1.2.2 Microscopic level

On the microscopic level, CB is comprised of osteons or Haversian systems packed closely together. An osteon (Figure 1.2a) is a neurovascular Haversian canal surrounded by concentric sheets of bone tissue called lamellae. Osteocytes, cells embedded in the bone tissue, inhabit the spaces between lamellae called lacunae. The narrow channels through which osteocyte processes extend from the lacunae to the Haversian canal are called canaliculi. The network of canaliculi serves as a passage through which osteocytes transmit signals to one another and to bone lining cells.

Trabecular bone's basic unit is a trabecula or strut of bone surrounded by marrow (see Figure 1.2b). The typical thickness of trabeculae is in the range of 60-200 μm with a marrow separation of approximately 400-2000 μm. In the mature skeleton, marrow space is typically filled with adipocytes whereas in the developing skeleton, there are regions of hematopoietic marrow. Trabeculae do not have a central canal with a blood vessel, but still possess lamellae, lacunae, and canaliculi, as shown in Figure

1.2c. The bone tissue within each lamella of trabecular and cortical bone is identical [Baron, 1999].

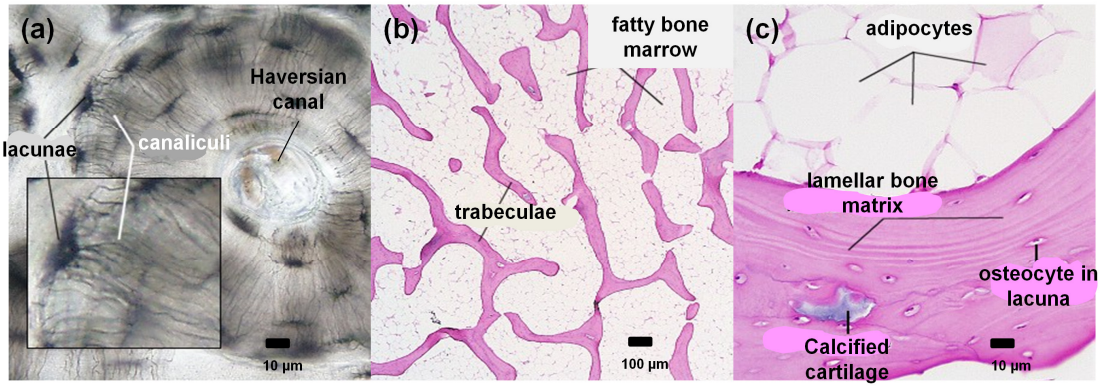

Figure 1.2 Histomorphometry images showing micro-structure of cortical (a) and trabecular bone (b and c). Osteocytes are present in both cortical and trabecular bone. (Adapted from [Cork, 2010].)

1.2.3 Chemical level

The durability and strength of bone is a consequence of the proper combination of its organic and inorganic components. The organic component includes osteoclasts, osteoblasts, and the osteoid. Osteoclasts are large multi-nucleated cells that excrete enzymes to resorb bone matrix. Smaller cells called osteoblasts deposit the bone matrix in the form of thin lamellar sheets. The osteoid is comprised of type I collagen (~94%) and noncollagenous proteins. Bone's hardness and rigidity are due to the presence of mineral salt in the osteoid matrix, which is a crystalline complex of calcium and phosphate (hydroxyapatite) - $Ca_{10}(PO_4)_6(OH)_2$. By percentage weight, calcified bone contains approximately 25% organic matrix (2-5% of which are cells), 5% water and 70% inorganic mineral (hydroxyapatite). In total, bone stores 99% of the body's calcium and 85% of its phosphorus [Lian, Gorski et al., 2004].

1.3 Bone remodeling and disease

Bone is constantly renewed over our lifetime through the process of bone remodeling. This process is believed to renew up to 25% of the trabecular bone volume annually [Huiskes, Ruimerman et al., 2000]. Remodeling can be summarized in five steps as shown by Figure 1.3: 1) activation: cytokine- and growth factor- induced differentiation of preosteoclasts into mature osteoclasts; 2) resorption: digestion of old bone by osteoclasts; 3) reversal: completion of resorption; 4) formation: synthesis of new bone by osteoblasts; and 5) quiescence: deactivation of osteoblasts into bone-lining cells which serve as system monitors for future remodeling cycles. The remodeling process occurs within the Haversian system of CB and on the surface of trabeculae. The balance between bone resorption and formation, i.e. bone metabolism, is governed by four major factors: biomechanical loading, nutrition, hormones, and genetics. A remodeling imbalance can be caused by deviations of any of these factors, leading to increased osteoclastic resorption depth and loss of connectivity, increased turnover rate limiting new mineralization, decreased turnover rate increasing brittleness, and reduced osteoblastic assignment [Favus, 1999]. A prolonged imbalance may lead to situations of low bone mineral density (i.e. osteomalacia) or severe bone loss (i.e. osteoporosis).

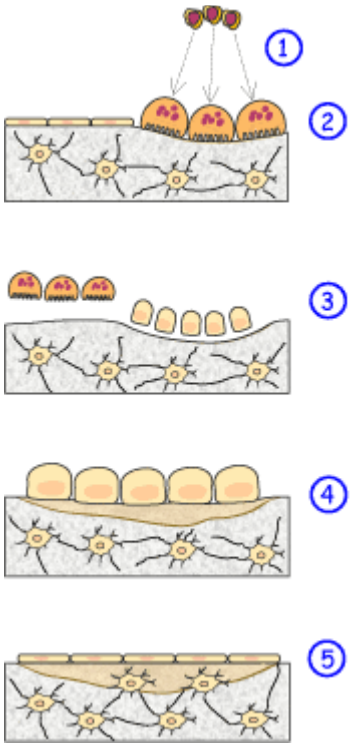

Figure 1.3 Steps of bone remodeling: 1) activation of osteoclasts; 2) resorption of bone matrix; 3) reversal; 4) formation of bone by osteoblasts; and 5) quiescence. From [Foundation, 2009].

Mechanical stimuli are directly associated with the physical mass and architecture of the bone [Frost, 1987]. This type of control is believed to act locally [Currey, 2003; Dempster, 2003], whereas nutrition, hormones, and genetics are thought to govern systemic skeletal remodeling. The roles of nutrition and hormones are briefly discussed in Section 1.4. Genetic influences on an individual's quantity and quality of bone and the bone's response to environmental cues or underlying physiological conditions is expectedly enormous [Jepsen, 2009]. Adequate coverage of genetics research in relation to bone is outside the scope of this thesis.

Although it is agreed upon that growth and bone adaptation is directly tied to mechanical impetus, the mechanism underlying bone remodeling remains in dispute. Roux hypothesized the concept of local mechanical control where resorption and deposition are stochastic processes dependent on mechanical stimulus [Roux, 1881]. This idea was later reported by Julius Wolff in *The Law of Bone Transformation* in 1892 [Wolff, 1892]. The concept of bone's continuous and probabilistic adaptation to stress became known as Wolff's Law. Wolff's Law established the idea of a bone remodeling unit composed of osteoblasts, osteoclasts, and local biological factors (hormones, etc). Alternatively, Frost posed the idea of a 'mechanostat' in which upper and lower strain thresholds had to be breached to induce mass accumulation or bone resorption, respectively. Otherwise, bone was in a 'lazy zone' of bone mass maintenance [Frost, 1987]. Regardless of the control mechanism, it is generally accepted that mechanical signals are transmitted through bone matrix and interpreted by a network of osteocytes entrapped within the matrix [Kreider and Goldstein, 2009]. Burger and Klein-Nulend hypothesized that increased strain in the local mineralized matrix signals the osteocyte to transmit stimuli to the surface cells, which in turn, produce bone until the strains

become normalized [Burger and Klein-Nulend, 1999]. Improper functioning of this system may result in a reduction of bone mass and a loss of architectural integrity.

1.4 Osteoporosis and its causes

The World Health Organization (WHO) defines osteoporosis as "...a systemic skeletal disease characterized by low bone mass and micro-architectural deterioration of bone tissue, with a consequent increase in bone fragility and susceptibility to fracture" [World Health Organization, 1994]. Unfortunately, osteoporosis remains frequently undiagnosed until a fracture occurs [Osteoporosis and related bone diseases national resource center, 2009]. Vertebral fractures (Figure 1.4a) are the most common type of fracture, representing nearly half of all osteoporotic fractures [Ray, Chan et al., 1997]. In some cases, the vertebrae become so fragile that normal activities and even actions such as sneezing may result in vertebral deformities. Many patients remain undiagnosed even though direct consequences of vertebral fracture include chronic pain, deformity (kyphosis), loss of height, crowding of internal organs, and inactivity-induced physical deconditioning [Ensrud, Thompson et al., 2000]. The presence of a vertebral fracture in individuals is associated with a nine-fold greater risk of death than in their healthy counterparts [Trone, Kritz-Silverstein et al., 2007]. Hip fractures (Figure 1.4b), which represent 15-20% of all osteoporotic fractures, are the most severe – incurring costs ranging from $36,000 to over $47,000 in the first year [Burge, Dawson-Hughes et al., 2007]. An average of 24% of hip fracture patients aged 50 or older die in the year following a fracture [Assessment, 1994].

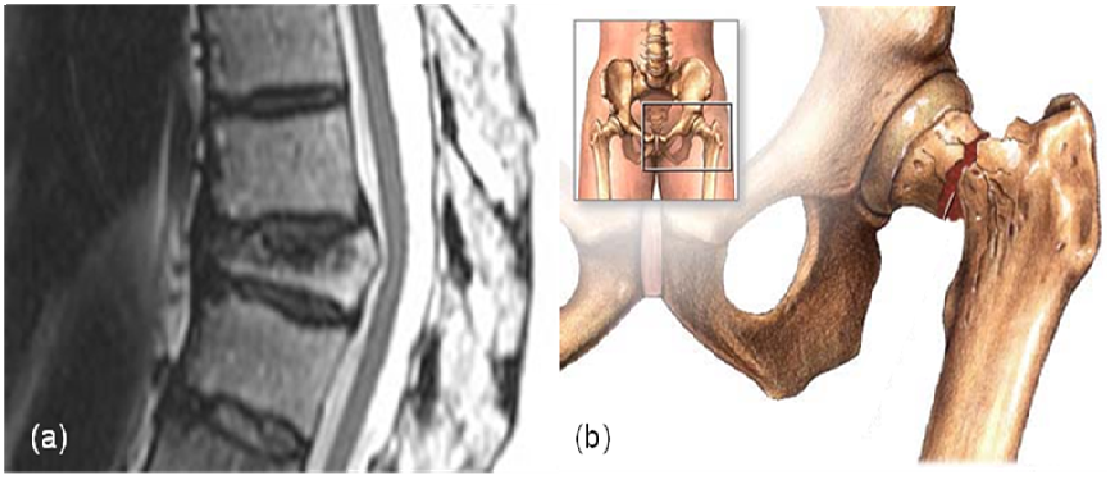

Figure 1.4 The most common and severe types of osteoporotic fractures: a) sagittal T1-weighted image of spine depicting crush fracture of T7 vertebra [Giles, 2009] and b) drawing of compound femoral neck (hip) fracture [Encyclopedia, 2008].

The largest group of individuals who suffer from osteoporosis is post-menopausal women. Women reach peak bone mass around 30 years of age which is conserved until menopause, at which time a phase of rapid bone loss occurs, eventually slowing but continuing throughout the remainder of their lifetime. Post-menopausal bone loss is associated with a deficiency in estrogen, a steroid known to hinder bone resorption [Riggs, Khosla et al., 1998].

Other than estrogen, there are many systemic hormones that either stimulate (+) or hinder (-) bone-forming or bone-resorbing processes, many of which are noted in Table 1.2. Vitamin D, vital for efficient intestinal absorption of calcium, increases bone formation (+F). Alternatively, osteoporosis can be induced by prolonged use of glucocorticoid steroids (e.g. prednisone and hydrocortisone), which are often used as immunosuppressives in transplant patients and those suffering from auto-immune diseases.

Hormone	Type	Action	Mode
Parathyroid hormone (PTH)	Polypeptide	+R	I
Intermittent PTH	Polypeptide	+F	I
Calcitonin	Polypeptide	-F	I
Insulin	Polypeptide	+F	D
Growth hormone	Polypeptide	+F	I
Vitamin D	Steroid	+F	I
Glucocorticoid	Steroid	+R	D
Estrogen	Steroid	-R	I
Testosterone	Steroid	-R	I
Thyroid hormones	Steroid	+R	D

Table 1.2 Hormones involved in regulating bone remodeling: F-Formation, R-Resorption, D-Direct, and I-Indirect. Plus sign (+) indicates stimulation while minus sign (-) indicates inhibition.

Secondary causes of osteoporosis include, but are not limited to, dietary disorders (e.g. anorexia), alcoholism, sedentary lifestyle, and prolonged exposure to micro-gravity. These secondary causes of osteoporosis are often overlooked by healthcare professionals in younger women and in men due to the association of the disease with elderly women. Since the level of peak bone mass attained is more contributory to the development of osteoporosis than the rate at which bone is lost, the risk of developing osteoporosis could be anticipated and potentially managed well in advance of its onset [Steiniche, 1995].

Current prevention strategies focus on maintaining adequate calcium and vitamin D levels through diet and supplementation [Jackson, LaCroix et al., 2006] and on

performing regular weight-bearing exercise [Bonaiuti, Shea et al., 2002]. With patients in whom osteoporotic fractures have already occurred, exercise and supplementation are not sufficient, and pharmacological intervention is often the best strategy. Bisphosphonates (e.g. alendronate and risedronate) have been shown to significantly reduce the incidence of new vertebral fractures by almost 50 percent [Watts, 2000]. Raloxifene, a selective estrogen receptor modulator, reduced new vertebral fractures by approximately 30 percent [Ettinger, Black et al., 1999]. Calcitonin has recently been shown to lower new vertebral fracture risk by roughly one-third in women with prevalent vertebral fractures [Chesnut, Azria et al., 2008]. In 2010, Denosumab was approved to treat postmenopausal women at risk of osteoporosis after showing a 35% risk reduction in vertebral fractures relative to placebo. Denosumab is designed to target the RANKL ligand, a protein that behaves as the primary signal promoter of pre-osteoclast activity. Most drugs approved to treat osteoporosis are evaluated relative to fracture incidence. Non-invasive imaging techniques can offer higher sensitivity to treatment-induced changes for the evaluation of current and future therapies. These imaging tools may eventually serve as earlier predictors of drug efficacy.

1.5 Tools and techniques for assessing fracture risk

The following section discusses various tools and techniques currently used to assess bone health. These techniques focus on measurable properties of bone, such as quantity and structural organization, which are essential to bone strength. However, fracture risk is a more complex issue. In addition to bone strength, it is also influenced by muscle tone, balance and coordination, impaired vision, and neurological health.

Evaluation of these risk factors should also be considered when assessing fracture susceptibility.

Various diagnostic tools and techniques exist for assessing bone quality – encompassing trabecular and cortical micro-architecture, mass, and the mechanical and compositional properties of tissue. The following section provides brief overviews of common tools and their associated techniques, beginning with techniques determining bone mineral density and continuing into micro-structural assessment. This section concludes with a brief discussion on biomechanical testing and mechanical simulation as a more direct approach of inferring mechanical integrity of bone.

1.5.1 Dual energy X-ray absorptiometry

Dual energy X-ray absorptiometry (DXA) is the most common clinical technique for assessing fracture risk. DXA utilizes high energy X-rays that travel through bone tissue and attenuate through absorption and scattering according to the existing tissue density. The attenuated x-rays produce a projection image of the region of interest. A DXA image of the hip is shown in Figure 1.5.

The Beer-Lambert law describes the attenuation of a single wavelength photon beam with initial intensity I_0 passing through a material of thickness L: $I = I_0 \exp(-\mu L)$. The linear attenuation coefficient μ (m^{-1}) is the product of the mass attenuation coefficient α ($m^2 kg^{-1}$) and the tissue mass density ρ (kg m^{-3}). The mass density ρ can be determined by: knowing α for the particular material, the distance L between emitter and detector, and I_0 of the incident X-ray beam; and measuring the resulting intensity I using a planar film or detector. In practice, where both bone and soft tissue exist, μ is

the sum of the products of each tissue's mass attenuation coefficient and their unknown mass densities: $\mu = \alpha_b \rho_b + \alpha_{st} \rho_{st}$. To eliminate the contribution from the soft tissue, two different (dual) energies of X-rays are necessary. From the projection images, two measures are calculated and used to determine bone mass: areal bone mineral density (aBMD) (g/cm^2) and bone mineral content (BMC) (g).

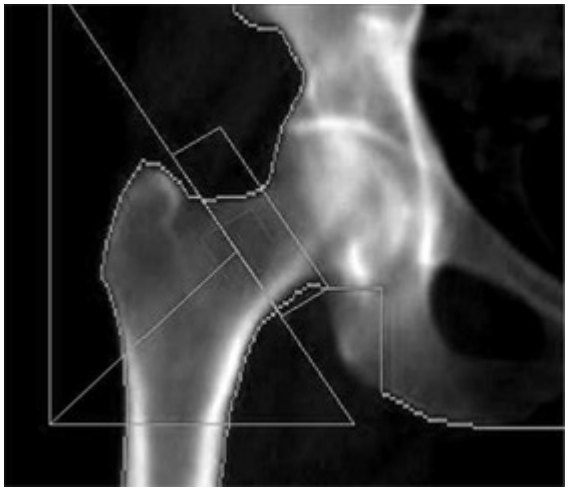

Figure 1.5 DXA image of femur from [Kentucky, 2009].

Advantages of DXA include low radiation dose (measured in Sievert for biological tissues**)**, low cost, ease of use, and speed of measurement. DXA can measure aBMD at virtually any skeletal site, although clinical use has been directed towards fracture sites - spine, proximal femur, and forearm. A patient's bone mineral density is commonly related to a reference value for young normal adults of the same sex by using T-scores. One's T-score is the number of standard deviations aBMD is above (+) or below (-) the reference aBMD for a healthy thirty-year-old adult (femur aBMD ≈1.0g/cm^2). The World Health Organization established a T-score cutoff value for osteoporosis of -2.5 in 1994 [World Health Organization, 1994]. There is sufficient evidence of a relationship between aBMD and increasing fracture risk [Ross, Davis et al., 1990], an example of which is shown in Figure 1.6. The DXA measure of aBMD is the "gold standard" for T-

score assessment and the standard against which other bone imaging measures are evaluated.

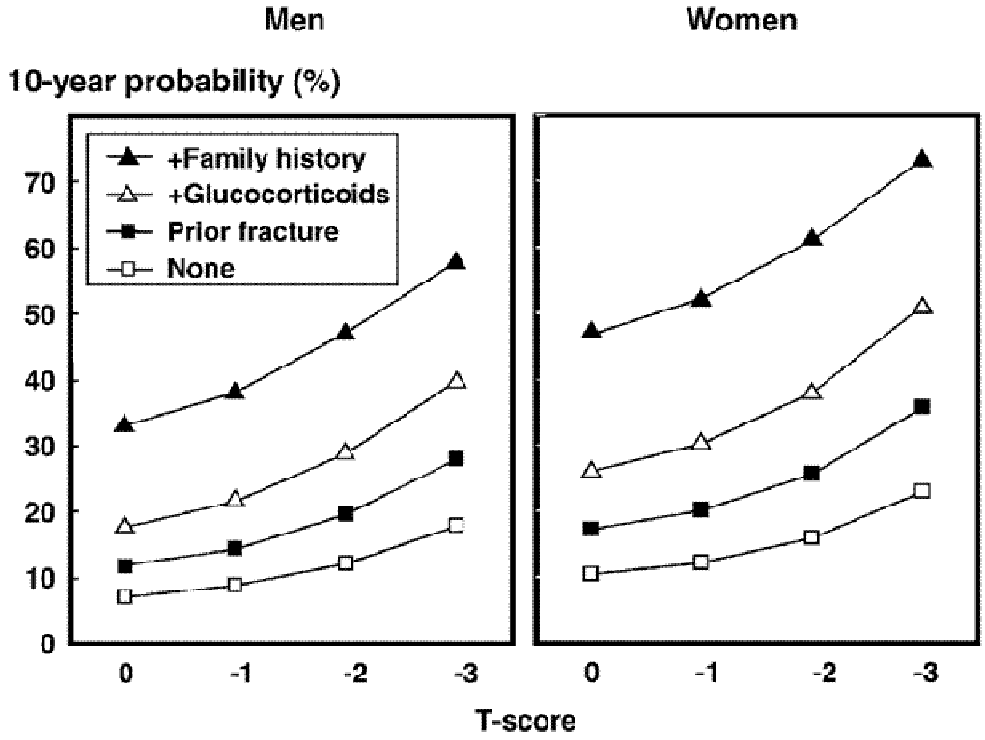

Figure 1.6 Role of T-score and other risk factors on 10-year probability of fracture in 65 year-old men and women (from [Kanis, Oden et al., 2009]).

There is strong evidence that bone mineral density is associated with mechanical usage. Bone mineral content was found to be higher in the dominant arms of tennis players relative to their sedentary age-matched peers [Pirnay, Bodeux et al., 1987]. Bone loss in the lower extremities and lumbar spine is an established consequence of long-duration human space flight. Astronauts typically lose as much bone mass in the proximal femur in one month as postmenopausal women lose in one year [Cavanagh, Licata et al., 2005].

The most significant drawback of aBMD is the significant overlap between ranges of bone mass in populations with and without fracture, as evident in Figure 1.7 [Recker, 1989; Heaney, 1990]. This weakness can be attributed to limitations inherent to DXA measurements. Since DXA is a projection-based technique, bone mineral density lacks true volumetric information, meaning it cannot distinguish changes in bone geometry (e.g., increases in the third dimension) from those purely due to increased bone density (within a fixed volume of bone). Skeletal size differences cause observed aBMD measures in men to be higher than those of women [Faulkner and Pocock, 2001]. Similarly, aBMD is not sensitive to differential changes in the cortical or trabecular bone compartments. Inaccuracies may also result from variable soft tissue density and aortic calcification which falsely elevates spinal aBMD in posteroanterior DXA [Brunader and Shelton, 2002].

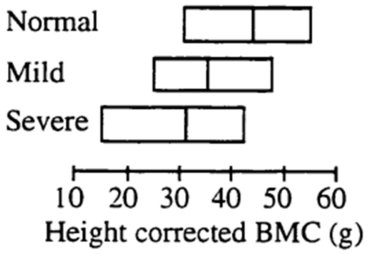

Figure 1.7 Significant overlap in bone mineral content exists for subjects with spinal deformity indices of normal (N=0), mild (N<3), and severe (N≥3) (from [Heaney, 1990]).

1.5.2 Quantitative ultrasound

Bone mineral density can also be measured using quantitative ultrasound (QUS). Clinical QUS measures the transmission of high frequency sound through bone using transmitting and receiving piezoelectric transducers. As ultrasound energy, with a standard frequency bandwidth centered at 1MHz, travels through bone, it attenuates according to the density of bone tissue. Two measures are produced in QUS: normalized Broadband Ultrasound Attenuation (nBUA) in dB/cm*MHz [Laugier, Droin et al., 1997] and Speed of Sound (SOS) in m/s [Haiat, Padilla et al., 2006]. Both

parameters are computed by comparing the signals transmitted through bone to those transmitted through water. There is a strong correlation between SOS and BMD (R^2=88-93%) [Hans, Wu et al., 1999]. The most common location for these measurements is the calcaneus. Ultrasonic parameters at the calcaneus have shown similar accuracy in predicting hip fractures in elderly women as does femoral bone mineral density (BMD) obtained by DXA [Hans, Fuerst et al., 1996].

The QUS device is portable and relatively inexpensive. Measurements can be performed with relative ease at skeletal sites, such as the calcaneus, radius, tibia, patella and phalanges, with minimal and consistent soft tissue covering. Newer systems now incorporate imaging QUS scanning in an effort to aid in positioning and increase precision [Falgarone, Porcher et al., 2004]. QUS is inappropriate for long term monitoring of osteoporosis and treatment efficacy due to its limited use in specific anatomical sites and low sensitivity [Moyad, 2003].

1.5.3 Histomorphometry

Information about biological structure can be obtained in a number of ways. Histomorphometry, or light microscopy, is considered the "gold standard." Bone histomorphometry involves removing a tissue sample or taking a biopsy from an accessible location (e.g. the iliac crest), sectioning the sample onto slides, and recording images from which structural parameters such as trabecular bone volume (BV/TV), trabecular bone separation (Tb.Sp), trabecular number (Tb.N), osteoid thickness, and texture (woven versus lamellar) of the bone matrix can be assessed [Steiniche, 1995]. Histomorphometric images of cortical and trabecular bone are shown in Figure 1.2.

Bone histomorphometry has been useful for the evaluation of treatment effects. Trabecular realignment was observed in TB from the proximal tibia of adult sheep subjected to prolonged walking on a concrete floor [Radin, Orr et al., 1982]. Another study showed treadmill running for 12 weeks improved bone strength in the rat tibia through changes in bone geometry [Bennell, Khan et al., 2002]. In addition, the ability to capture cellular activity, through the use of florescent staining, makes histomorphometry extremely valuable for studying bone remodeling dynamics. Guldberg et al. [Guldberg, Caldwell et al., 1997] used procollagen monoclonal antibody staining to detect large increases in the number of osteoblasts expressing type I procollagen (precursor to collagen formation) in trabecular bone tissue mechanically stimulated using an implantable hydraulic chamber. The large number of osteoblasts recruited to the trabecular bone surface due to mechanical stimulation is evident in Figure 1.8.

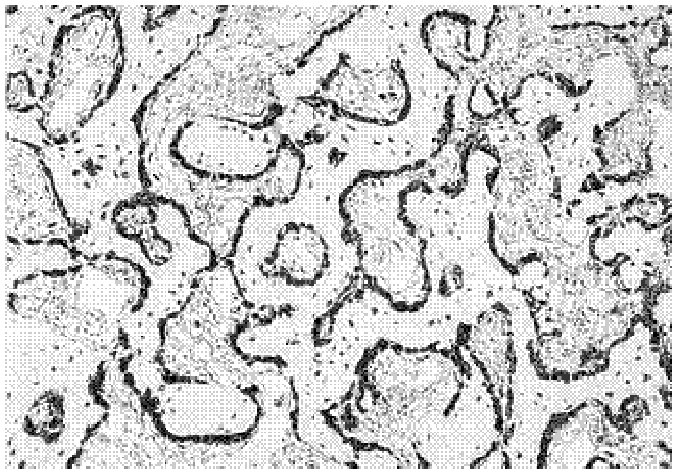

Figure 1.8 Type I procollagen expression in osteoblasts lining the surfaces of trabecular bone tissue removed from canine tibia after two days of mechanical stimulation using implantable device (from [Guldberg, Caldwell et al., 1997]).

The usefulness of histomorphometry in clinical applications is offset by the need for invasive biopsy. Consequently, histomorphometry is not suitable for longitudinal tracking of fracture risk and is practiced less frequently with the advent of high-resolution *in vivo* imaging modalities.

1.5.4 Micro computed tomography

Micro CT is considered the gold standard of reference with respect to three-dimensional imaging modalities as it is capable of resolutions up to 6 μm isotropic, or higher using a synchrotron source. The technique is based on the same principal of x-ray imaging, however projection measurements are made for a series of rotations (of either the sample or the source-detector ensemble) and the resulting three-dimensional images are reconstructed using the Radon transform [Deans, 1983].

Structural parameters from μCT correlate well with those from traditional histology. Through the use of mineralized phantoms and beam hardening corrections, tissue mineralization data can be obtained to study the effects of aging, disease, and medication on tissue composition at high spatial resolutions. A characteristic μCT image of the human distal tibia is shown in Figure 1.9.

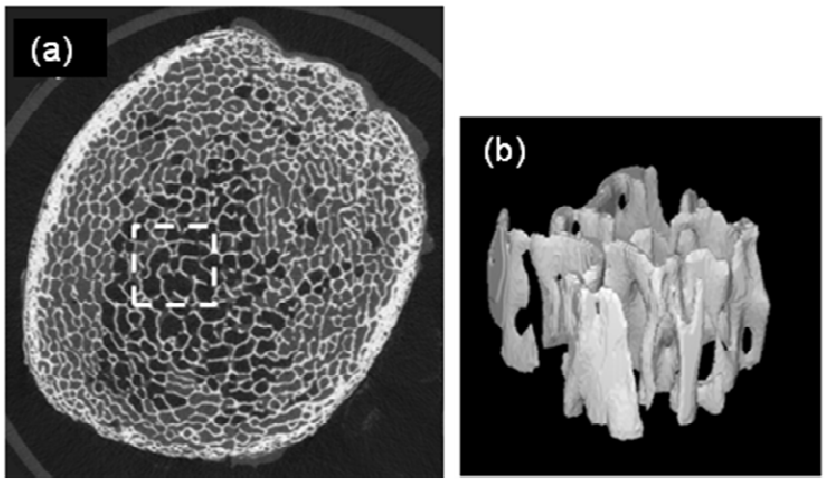

Figure 1.9 a) Axial μCT image of human distal tibia specimen at 25 μm isotropic resolution. Bone appears bright relative to bone marrow (light gray) and air (darkest). b) Rendering of TB subvolume indicated by box in (a).

Micro-CT has provided insights into the mechanisms of bone loss as well as evidence of mechanically-induced remodeling. An in-vivo μCT study of aging and postmenopausal bone loss (modeled by ovariectomization) in rats showed similarities in TB resorption

due to aging and estrogen depletion: bone resorption resulted in fewer trabeculae of increased thickness with orientations matching the primary loading direction. It was also concluded that estrogen depletion resulted in the acceleration of the adaptation process seen in normal bone (Figure 1.10) [Waarsing, Day et al., 2006]. Campbell et al. found similar results and a coincident reduction in mechanical strength in the OVX group using the same model [Campbell, Buie et al., 2008]. A similar aging effect was observed in TB from cadaveric human vertebrae. Morphological analysis of μCT images showed decreases in Tb.N and increases in trabecular thickness (Tb.Th) with age [Stauber and Muller, 2006]. Unfortunately, such findings are limited due to the high dosage of radiation and a bore size too small for human *in vivo* imaging. Nonetheless, μCT has demonstrated changes in bone structure that serve as a reference for modalities capable of human *in vivo* imaging.

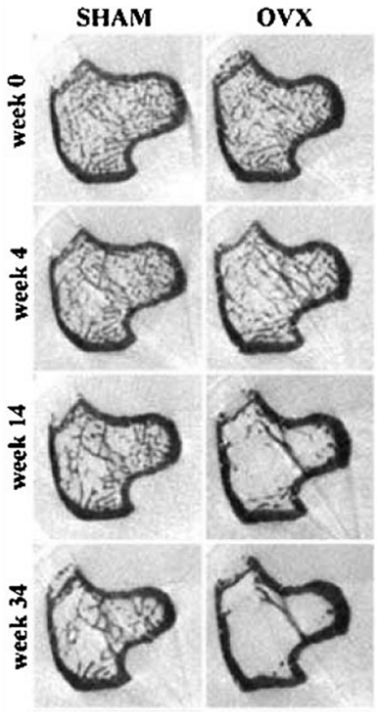

Figure 1.10 *In vivo* axial μCT images of tibia metaphysis of a normally aging (SHAM) and a ovariectomized (OVX) rat over course of 34 weeks. As early as week 4 in the OVX rat, trabeculae were resorped and the remaining trabeculae were increasing in thickness. Similar bone loss was seen in the SHAM rat, but at a slower rate.

1.5.5 Radiographs

An alternative to measuring BMD, 2D x-ray projections can be acquired in the form of radiographs. Structural analysis of bone in radiographs is performed using texture and fractal analyses [Geraets, Van der Stelt et al., 1998]. Studies have shown that texture parameters from radiographs of the lumbar spine can detect differences between age-matched groups with and without spine fractures [Caligiuri, Giger et al., 1994].

Radiographs are readily available and easy to use. However, sensitivity is limited and severe bone loss must occur before an abnormality is noticed [Moyad, 2003]. This effect is greatest in central sites like the vertebrae. An example of a vertebral radiograph is shown in Figure 1.11.

Figure 1.11 Radiograph of lumbar spine. Longitudinally oriented trabeculae are barely visible making their detection difficult unless done through texture based analyses [Geraets, Van der Stelt et al., 1998]. Image is from Lenchik et al. [Lenchik, Rogers et al., 2004].

1.5.6 Quantitative computed tomography

True volumetric bone density (g/cm^3) can be examined using quantitative computed tomography (QCT). In QCT, a radiation source-detector pair rotates about the imaged object, and the attenuated X-rays are obtained as a set of projections. Reconstruction algorithms produce a three dimensional data set of the spatial variation in X-ray attenuation. Calibration phantoms are used to convert attenuation to mineral density, yielding volumetric BMD or vBMD (g/cm^3).

The important advantage of QCT over DXA or QUS is the three-dimensional spatial resolution, which provides the ability to assess both vBMD and macro-architecture. Unlike projection-based techniques, QCT has the ability to differentiate cortical and trabecular bone, an important facet when assessing pharmaceutical treatments with differential effects on these two types of bone.

High-resolution QCT using a multi-detector arrays of up to 320 rows (MDCT), has also been explored as a means for assessing trabecular bone microstructure as shown in Figure 1.12. However, MDCT's achievable resolution of 234µm in-plane is not sufficient to accurately segment the TB structure, thus making image analyses contend with partial volume effects. Consequently, texture and fractal analyses are used to characterize the trabecular organization [Ito, Ikeda et al., 2005]. In cadaveric calcanei, significant correlations between MDCT- and µCT-derived measures of BV/TV, Tb.Th, and Tb.Sp were found (R^2=0.19-0.65, $p<0.01$ or 0.05) [Diederichs, Link et al., 2009]. MDCT-derived parameters were also fairly predictive (25-60%) of the variation in bone strength ($p<0.01$) [Diederichs, Link et al., 2009].

However, QCT has not conclusively outperformed DXA in predicting spinal fracture [Yamada, Ito et al., 1994], although the inclusion of geometric measures such as cross-sectional area, have improved QCT-based strength prediction [Lotz and Hayes, 1990]. Texture parameters of TB from QCT images perform similarly to volumetric BMD in predicting fractures [Ito, Ohki et al., 1995]. Combining vBMD and texture achieves better correlations with bone strength than either measure alone [Waldt, Meier et al., 1999].

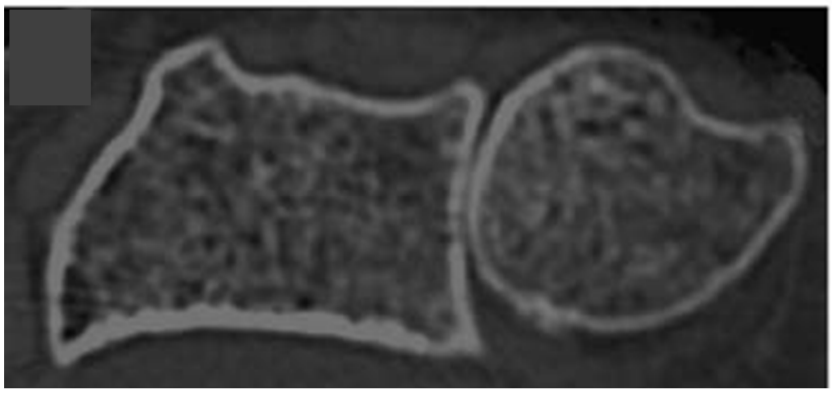

Figure 1.12 *In vivo* axial image of a radius and ulna acquired using a 64 slice multi-detector computed tomography system. Voxel size is 234x234x500 μm^3. Figure adapted from Issever et al. [Issever, Link et al., 2010].

The advantages of QCT over DXA come at the costs of a higher radiation dose and larger, more expensive equipment. Radiation dose is of a concern as the X-rays are capable of ionizing molecules vital for cellular activity. A rough idea of the relationship between dose D, spatial resolution x, image noise η, and size of the object, is given by: $\eta^2 \Delta x^4 D \cong e^{\int_0^L \mu \cdot dx}$, where $\int_0^L \mu \cdot dx$ is the attenuation over the length of the object L. A two-fold increase in resolution results in 16-fold increase in dose with all other parameters

held constant. If the object size is small, then $\int_0^L \mu \cdot dx$ is small and so is D, thereby allowing higher resolutions without exceeding the allowable dose.

1.5.7 Peripheral quantitative computed tomography

Peripheral QCT was developed to improve the resolution capabilities of QCT in appendicular sites like the distal radius and tibia. These scanners can achieve nominal spatial resolutions of up to 82 µm isotropic voxels, sufficient for depicting individual trabeculae. Even at voxel sizes of 82 µm, some partial volume effects will occur as trabecular thickness can be as low as 50 µm [Cowin, 2001]. Structural parameters synonymous with those of histomorphometry, such as Tb.Th, Tb.Sp and Tb.N can be calculated using algorithms considerate of the partial volume and noise artifacts [Laib and Ruegsegger, 1999].

Peripheral scanners are less expensive, easier to use, and more accessible than traditional CT scanners. Additionally, pQCT offers a lower radiation dose to the central body. However, despite being confined to peripheral sites, the ability to visualize trabecular bone is the greatest advantage. One high-resolution pQCT study showed trabecular density at the distal radius is significantly different in osteopenic women with facture than in those without fracture while DXA of both the spine and hip were not significantly fracture sensitive [Boutroy, Bouxsein et al., 2005]. The importance of detecting TB structure by HR-pQCT is evident in Figure 1.13 where subjects with similar aBMD have very different TB architecture.

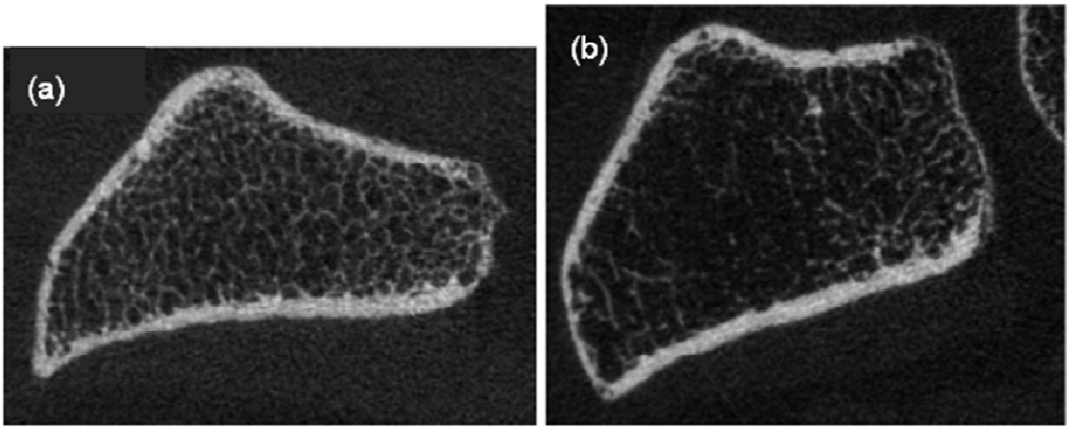

Figure 1.13 Axial pQCT images of radii from two subjects, a) and b), with similar ultradistal radius aBMD showing obvious TB structural differences. Images were yielded at a 82x82x82 μm^3 voxel size in 3 minutes with an effective dose of <3 µSV. Adapted from Kazakia et al. [Kazakia, Hyun et al., 2008].

1.5.8 Magnetic resonance imaging

Magnetic resonance imaging (MRI) is a fundamentally different from CT-based instruments for the assessment of bone quality. Unlike X-ray based technologies, MRI is free of ionizing radiation. Instead, it relies on high magnetic fields to polarize the spin energy of specific chemical species, radiofrequency pulses and directionally dependent gradient fields to manipulate and record the magnetization or signal. By varying the timing, power, and frequency characteristics of the radiofrequency pulses and gradients, image contrast can be significantly modified.

The most frequently studied component in biological tissue is hydrogen, which is present in large quantities in tissue water and lipid fatty-acid chains. Bone tissue has extremely low water content. The water present in the small pores of bone tissue relaxes very quickly (i.e. short T2 relaxation time) after radio-frequency excitation. As a result, standard pulse sequences produce images where bone has no signal and is dark

(see Figure 1.14). As the bone's medullary cavity contains bone marrow, the TB network is indirectly revealed against the bright bone marrow signal.

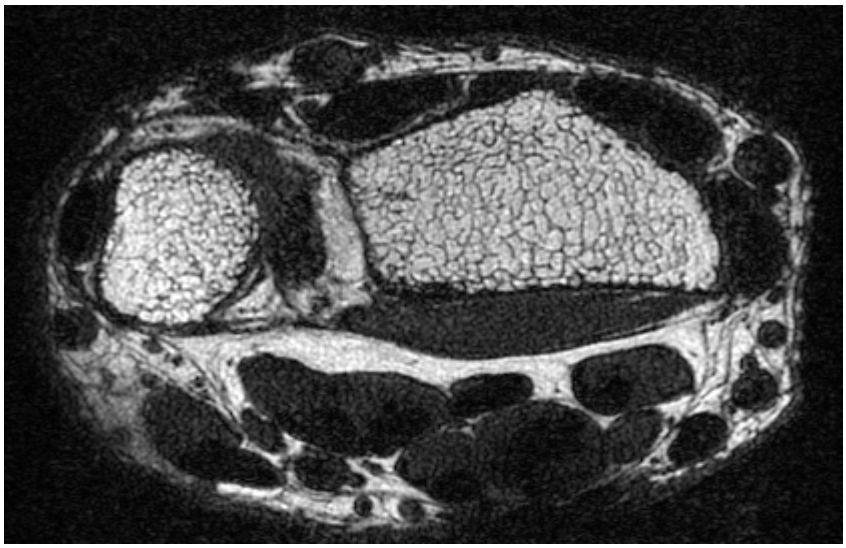

Figure 1.14 Axial image of a right wrist acquired using μMRI with 137x137x410μm^3 voxel size. Bone appears dark against the bright signal of fatty bone marrow.

High-resolution MRI (μMRI) is most easily performed at peripheral sites such as the knee, ankle, heel, and wrist where the bone tissue depth is low and the receiver hardware can be placed in close proximity. The achievable resolutions *in vivo* are on the order of the trabecular thickness ~100μm. For 3D imaging, anisotropic voxels sizes (such as 137x137x410μm^3, the voxel size of Figure 1.14) are typically used to achieve sufficient SNR within a reasonable scan time [Wehrli, Saha et al., 2002]. Structural quantification techniques must consider partial volume effects and contend against limited SNR. Nonetheless, TB structural parameters in the distal radius predicted vertebral fractures better than wrist aBMD [Ladinsky, Vasilic et al., 2008] and showed improvement in eugonadal men treated with testosterone gel [Benito, Vasilic et al., 2005]. MR-derived morphological parameters have also shown good correlations with experimentally derived biomechanical measures [Majumdar, Newitt et al., 1996; Beuf, Newitt et al., 2001].

Advantages of MR imaging of bone include its lack of ionizing radiation and the widespread availability of MR scanners. The flexible nature of MRI is also valuable as multiple acquisitions directed towards different anatomical regions and/or information can be performed in the same visit (e.g. spine imaging for the detection of vertebral fracture can be performed following a high-resolution wrist scan). While x-ray based techniques are also flexible, concern over total radiation dose limits the number of consecutive acquisitions.

The biggest challenge in MR imaging of bone is the long acquisition times required for 3D imaging sequences. Long scan times increase the propensity for motion corruption caused by patient discomfort. Additionally, due to the complexity of image contrast mechanisms, morphological parameters are highly influenced by pulse sequence parameters, thereby necessitating standardization at the expense of flexibility. Finally, patients with claustrophobia, metal implants, or pacemakers are generally barred from MR imaging. Further detail pertaining to TB imaging with MRI is provided in Chapter 2.

1.5.9 Bone turnover markers

Besides BMD and imaging techniques, bone turnover markers are useful in detecting changes in bone metabolism associated with disease or treatment. Women with high bone resorption rates, identified by sex hormone-binding globulin, were at higher risk of hip fracture, independent of other predictors [Chapurlat, Garnero et al., 2000]. Studies have indicated that a significant reduction in bone resorption markers occurs within four to six weeks after initiation of antiresorptive therapy, followed by a decrease in bone formation markers in two to three months [Garnero, Shih et al., 1994;

Pereda, Hannon et al., 2002]. Resorption markers can also indicate the possibility of a patient not adhering to medication in the prescribed manner or that a dosage or type of therapy needs changing. Thus, the temporal sensitivity of bone turnover markers is much higher than a follow-up BMD test two years after initiation of therapy. However, there is no consensus that bone turnover markers can accurately determine if an individual would respond to therapy as confirmed by subsequent BMD measurements [Haderslev, Jeppesen et al., 2002]. More work is necessary to determine the clinical usefulness of following markers in patients being treated for osteoporosis.

1.5.10 Inter-modality comparisons

The various techniques described above offer tremendous potential for improving osteoporosis diagnosis, fracture prevention, and therapeutic intervention. Peripheral QCT and μMRI hold the greatest promise for *in vivo* assessment of trabecular bone micro-architecture. Differences in acquisition and image analysis complicate direct comparison between measures derived from both imaging modalities. Structural parameters obtained from pQCT and μMRI differ in absolute terms, yet correlate reasonably well with micro-CT as a standard of reference [Kazakia, Hyun et al., 2008]. Currently, it's unclear which imaging modality will be best for identifying osteoporotic fractures and monitoring treatment-related changes in bone structure. It's possible both will play important roles in the determination of bone health and treatment efficacy.

1.5.11 Bone biomechanics and micro-finite element analysis

Fracture risk, or conversely bone strength, can also be assessed by biomechanical experiments on bone biopsies. Bone strength is commonly described by

several biomechanical parameters reflective of the relationship between the load applied to bone and the displacement resulting from the applied load. Engineering terms of stress (T) and strain (ε) are used to describe load and displacement, respectively. Stress, in units of force per unit area (N/cm^2), is applied either normal to or tangential to the plane in which the surface area is defined. Strain is a unitless measure of geometric change. In an object of length L, strain is defined by the change in length ΔL divided by the original length L: $\varepsilon = \frac{\Delta L}{L}$.

A typical loading experiment is depicted in Figure 1.15. Under compressive loading in a rectilinear parallelepiped sample of TB, the stress versus strain plot, shown in Figure 1.15, has a linear elastic regime and a non-linear plastic regime which are defined to the left and right, respectively, of the yield point. Although indicated as a point, the yield point represents a gradual transition, above which stresses begin to cause permanent damage to the bone structure. Consequently, the elastic regime is the range of strains and stresses that can be reproduced as the specimen fully recovers to its normal configuration after the load is removed. The slope of the elastic region of the stress-strain curve is the elastic modulus or Young's modulus (E) which implies the material's rigidity and is often referred to as stiffness. Ultimate stress T_{max}, ultimate strain ε_{max}, and toughness U are also parameters derived from the curve. Each of these measures reflects a different mechanical property of the bone specimen: T_{max} indicates the general integrity of the bone structure, ε_{max} is inversely related to the brittleness of the bone, and U is the amount of energy or work necessary to fracture the bone [Cowin, 2001]. All of these measures are reflective of the mechanical integrity of the bone under compression. For example, osteoporotic bone is marked by lower E and lower T_{max} than

normal bone whereas in osteopetrosis, bone is stiffer (higher E) and more brittle (lower ε_{max}) than normal bone. Both osteoporotic and osteopetrotic bone have lower toughness than normal bone, i.e. less work is required to break them.

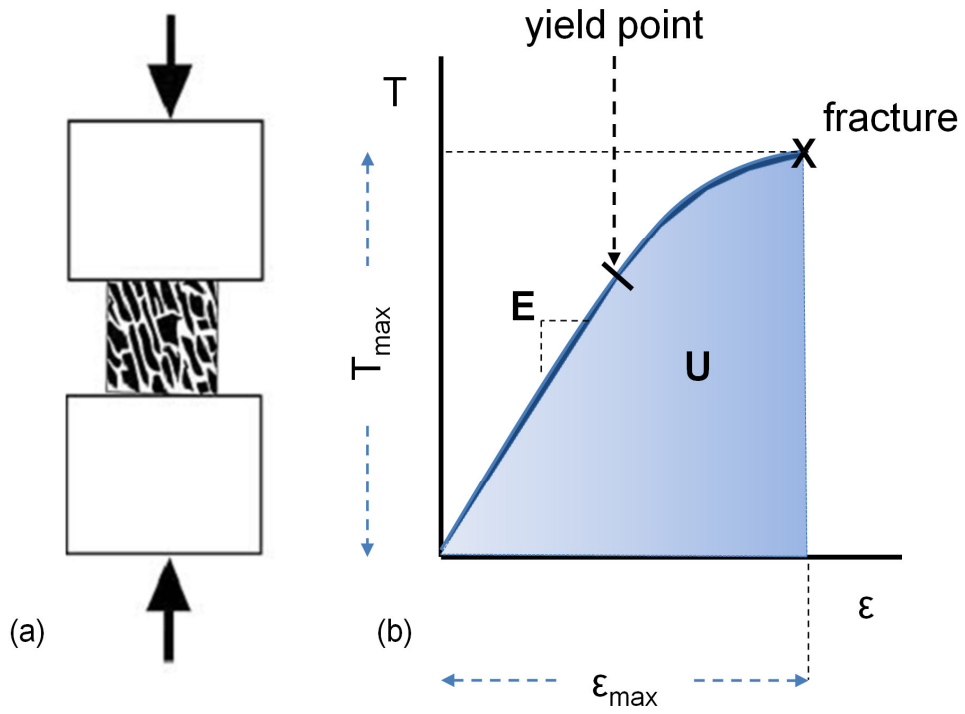

Figure 1.15 (a) Illustration of a rectilinear parallelepiped specimen of TB being compressed between two platens (Illustration from [Cowin, 2001]). (b) The resulting stress-strain (T-ε) curve is characterized by four biomechanical parameters: E-stiffness, U-toughness, T_{max}-ultimate stress, and ε_{max}-ultimate strain. The yield point indicates the stress beyond which damage is incurred.

While the four parameters illustrated in Figure 1.15 describe the strength of bone during compression, bone is also prone to fracture under situations of tension [Carter, Schwab et al., 1980] and shear [McKee, Jupiter et al., 1996]. Testing bone under tension and shear use similar set-ups and produce similar stress-strain curves as shown in Figure 1.15. Briefly, tensile tests are performed by fixing the bone sample to the platens using adhesives. Tensile tests are considered the most accurate, although specimens must be relatively large and carefully machined to assure that the strain

occurs in the central portion of the specimen. To prepare a TB specimen for tensile testing, Keaveny et al. begins with a 40-mm cylinder of TB [Keaveny, Guo et al., 1994]. This size requirement limits the usefulness for tensile testing of TB [Harrigan, Jasty et al., 1988]. Compression testing permits the use of smaller specimens, but end-effects related to misaligned surfaces, damage due to cutting, and strain concentrations reduce the accuracy of compression tests [Keaveny and Hayes, 1993]. Shearing also involves bonding the specimen to the platens, however in shearing, forces are applied tangential to the surface of the bone sample. Shear strains are the change in angle between the orthogonal faces of the rectilinear parallelepiped sample. Testing under shear is challenged by inaccuracies in the detection of small shear strains which typically involve the usage of multiple strain gauges [Cowin, 2001]. In addition to the challenges of each type of testing, TB is mechanically anisotropic, necessitating independent testing relative to the three orthogonal sample boundaries. Consequently, tests are typically restricted to the linear elastic regime by using small strains (<1%) and strain rates.

The invasiveness of obtaining bone biopsies limits the feasibility of mechanical testing as a meaningful assessment of bone integrity beyond a single time point. Further biopsies are typically obtained from non-loading skeletal sites such as the iliac crest. Up until the last two decades, mechanical properties of bone were solely interrogated using experimental tests on bone biopsies. With the emergence of high-resolution imaging, bone biopsies and mechanical tests have become less practiced.

On the basis of images acquired from one of the aforementioned imaging techniques, micro finite element analysis (μFEA) offers a powerful means of assessing bone's mechanical properties. Micro-FEA involves the conversion of an image into a

collection of discrete sub-domains, or elements, governed by a set of partial differential equations. This process is known as homogenization [Hollister, Fyhrie et al., 1991]. An image based finite element conversion is shown in Figure 1.16 where an image voxel is transformed directly into a hexahedral (brick) finite element with dimensions corresponding to image voxel size. Once the TB structure is homogenized, the system is virtually compressed (or sheared) using predefined boundary conditions (e.g. closed, opened, mirrored, etc.). Through numerical integration techniques (e.g. Euler's method, Runge-Kutta, or conjugate gradient descent), measures of stiffness or strength predictive of experimental values are computed (R^2>0.73) [Hollister, Brennan et al., 1994]. The mechanical anisotropy is probed by repeating the simulation relative to the other directions, i.e. forces are applied to the orthogonal boundaries of the sample.

Besides obviating the invasiveness of bone biopsy, other advantages of μFEA include higher reproducibility [Mueller, Stauber et al., 2009] and fewer sources of error [Keaveny, Borchers et al., 1993] than mechanical experiments. The primary disadvantage is the inability to capture absolute measures [van Rietbergen, Huiskes et al., 1995]. In order to achieve absolute measures, additional experiments must be performed to determine the heterogeneity of the tissue modulus [Hengsberger, Enstroem et al., 2003]. For simplicity, the tissue modulus is often considered homogeneous and thus, only relative measures are computed.

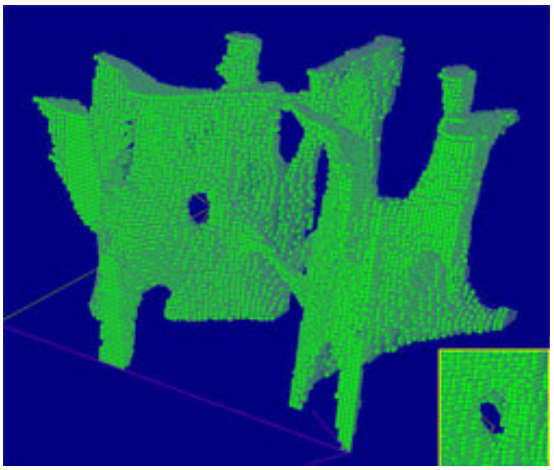

Figure 1.16 Voxel-based µFE model of TB imaged using µCT. Illustration from [Bone Bioengineering Laboratory, 2010].

Micro-FE simulations on the basis of high-resolution *ex vivo* images have been widely practiced to assess bone mechanics. Young's moduli from µFEA have been shown to predict experimentally determined stiffness rather well, $R^2 \geq 0.95$ [Goulet, Goldstein et al., 1994] and $R^2 \geq 0.87$ [Hou, Lang et al., 1998]. Failure loads calculated using µFE models derived from pQCT scans of distal radii have been found to predict experimental failure loads of whole radii better ($R^2=0.66$) than either vBMD ($R^2=0.48$) or structural parameters ($R^2=0.47$) [Pistoia, van Rietbergen et al., 2004]. Computational advancements and the maturation of non-linear µFEA will permit the study of bone failure mechanisms in whole bone sections.

Despite the lower resolution of presently available *in vivo* imaging techniques (i.e. pQCT and MRI), µFEA can provide meaningful elastic properties of trabecular bone *in vivo*. µFE models derived from MR images have successfully detected longitudinal differences associated with idoxifene treatment [van Rietbergen, Majumdar et al., 2002]. *In vivo* MR images of the distal radius showed greater difference in the direction of weaker modulus between normal and osteopenic subjects [Newitt, Majumdar et al., 2002], supporting the notion that thinner trabeculae are lost first with aging and

osteoporosis [Mosekilde, 1989]. Recently, the reproducibility error of HR-pQCT derived mechanical parameters was shown to be sufficiently low (~3%) as to differentiate normal and osteoporotic subjects [Mueller, Stauber et al., 2009]. As image resolutions improve, μFEA of *in vivo* data is expected to provide important insights into bone mechanics and disease.

1.6 Bone adaptation

Bone's adaptation to the mechanical environment is evident from changes in aBMD measurements in response to usage and in alterations of TB architecture during bone loss. Many studies have shown the anabolic effects of exercise on aBMD. Snow et al. observed increases in aBMD in collegiate gymnasts during the eight month competitive seasons followed by decreases in aBMD during the four month off-seasons [Snow, Williams et al., 2001]. In a cross-sectional study of post-menopausal women, aerobics, weight bearing, and resistance exercises were all shown to be effective in increasing aBMD at various skeletal locations [Bonaiuti, Shea et al., 2002]. Finally, a comparison study in prepubescent children between jumping from 61cm boxes versus stretching determined that the jumpers experienced a relative 2% increase in aBMD of the lumbar spine [Fuchs, Bauer et al., 2001].

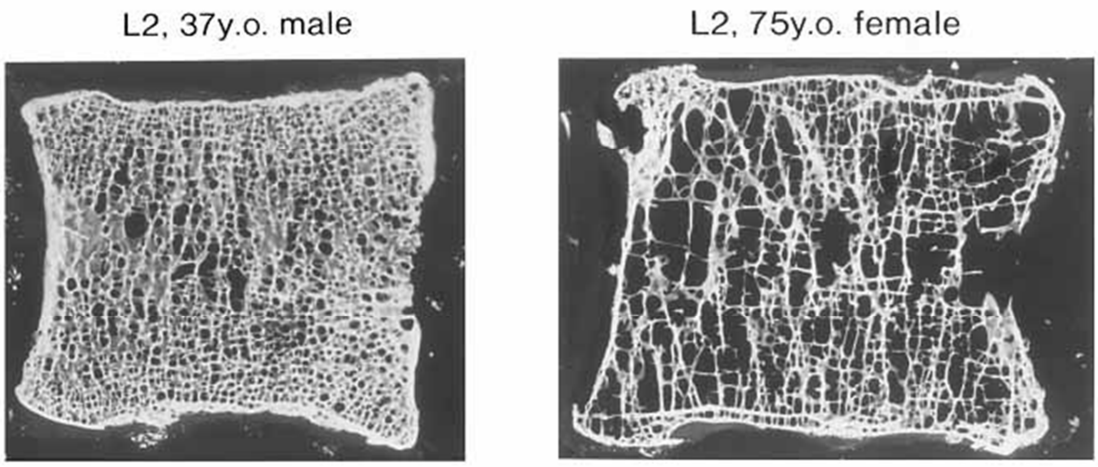

Figure 1.17 Serial sections of lumbar vertebrae from healthy and elderly subjects showing the loss of transversely oriented trabeculae with aging. From [Turner, 2010].

As mechanical stimulus impacts bone metabolism, it also impacts how bone is lost. Instead of losing bone uniformly, significant evidence suggests bone is removed preferentially based on the local mechanical environment. As bone mass is lost, the loss occurs more rapidly in the transverse direction while longitudinal elements are retained in support of habitual loading [Mosekilde, 1989; Mosekilde, Bentzen et al., 1989]. The effect of preferential loss of horizontal trabeculae with aging in the vertebra can be appreciated in Figure 1.17. During bone loss in the spine, this mechanism ensures adequate stiffness for normal daily loading, but increases the likelihood of fracture due to off-axis "error" loads [Homminga, Van-Rietbergen et al., 2004]. This mechanism of strength conservation, which is also evident in TB trajectories of the femoral neck, is precarious as the TB in the hip becomes ill-suited for abnormal loading conditions [Homminga, McCreadie et al., 2002], such as those experienced during a fall (see Figure 1.18). Therefore, fracture risk increases as bone becomes 'over-adapted' to the primary loading direction [Kleerekoper, Villanueva et al., 1985; Ciarelli, Fyhrie et al., 2000]. The

degree to which the bone becomes 'over-adapted' to the primary loading direction is therefore an important indication of fracture risk independent of bone quantity which can be captured through orientation dependent measures.

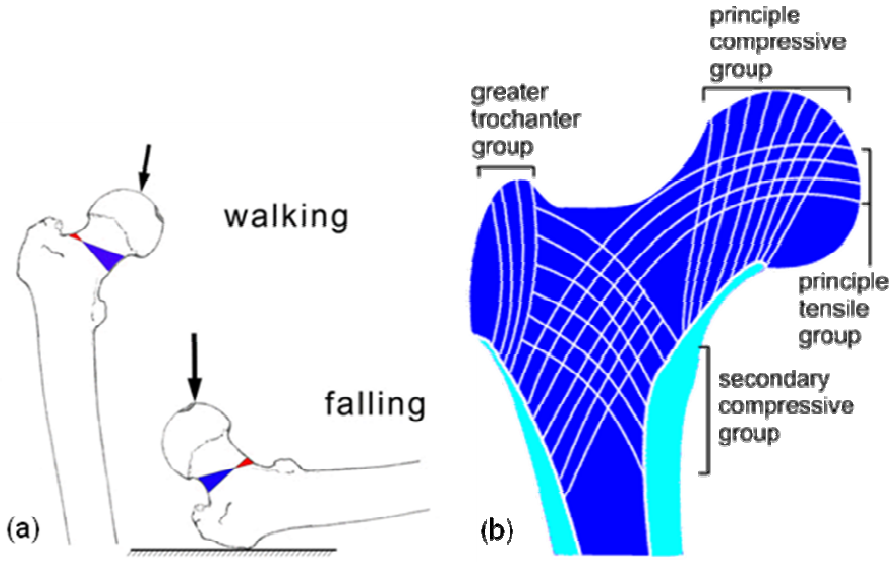

Figure 1.18 a) During walking, mechanical stresses on the femoral neck occur in compression (blue) at the inferior surface with small tension at the superior surface (red). The stresses reverse during a fall. b) The alignment of TB within the femur enhances the susceptibility to failure during loading conditions typical of a fall. From [Turner, 2005].

1.7 Objectives and chapter outline

The need for sufficient image acquisition and analysis techniques for the assessment of the directional dependence of TB has motivated this work. The objective of this thesis is to assess the TB fabric tensor in the limited spatial resolution and SNR regime of *in vivo* μMRI. Knowledge of the TB fabric may improve the estimation of fracture risk by providing directional information indicative of bone strength under different loading conditions. Further, it will allow physicians to track changes in structural anisotropy due to aging, disease, treatment, and mechanical usage/disuse. The work is

divided into three components: 1) processing of TB images to extract the fabric tensor, 2) acquiring *in vivo* images suitable for the characterization of the fabric tensor; and 3) relating the TB fabric tensor to mechanical competence evaluated by micro finite-element modeling.

The following chapters describe the techniques and methods developed for achieving these goals. The second chapter serves as a review of the basics of MRI as it pertains to trabecular bone imaging in the distal extremities. The third chapter introduces a novel method to assess the fabric tensor from high-resolution images of trabecular bone and compares it to the standard technique in images characteristic of *in vivo* µMRI. The fourth chapter advances TB imaging to 3T where the improved SNR is traded for resolution isotropy using partially parallel imaging. The isotropic acquisition is evaluated relative to the standard acquisition in terms of reproducibility and reliability. Chapter five validates the *in vivo* measurement of fabric tensor by way of its relationship to bone's elastic behavior, determined using µFE simulations. The sixth and final chapter summarizes the main findings of this thesis and suggests a direction for future research.

2 Chapter 2 μMRI of trabecular bone micro-architecture

2.1 Motivation

Its excellent soft-tissue contrast and noninvasiveness make magnetic resonance imaging well-suited for the assessment of TB micro-architecture. However, limitations in high-resolution μMRI exist and are important drivers for efforts to improve the current system of image acquisition and analysis. The purpose of this chapter is to introduce some of the challenges faced by μMRI of TB, including resolution, SNR, and involuntary motion. In order to better address the technical limitations, a few basic concepts of magnetic resonance imaging are first introduced. In the second section, the primary imaging and analysis techniques comprising the virtual bone biopsy (VBB) are presented. It is assumed that the reader has some general understanding of the fundamentals of nuclear magnetic resonance (NMR).

2.2 Concepts in magnetic resonance imaging

2.2.1 Spatial encoding

The basic distinction between NMR and MRI is, in MRI, linearly-varying gradient fields are applied to spatially encode the excited signal. The spatial encoding process is described for an arbitrarily-shaped object in a static magnetic field $B_0\hat{\mathbf{z}}$. Let a volume element $dxdydz$ located at position $\vec{\mathbf{r}} = x\hat{\mathbf{x}} + y\hat{\mathbf{y}} + z\hat{\mathbf{z}}$ have a spin density $m(\mathrm{x},\mathrm{y},\mathrm{z})$ and angular precession frequency $\omega_0 = 2\pi\gamma B_0$ where γ is the gyromagnetic ratio (42.57 MHz/T for hydrogen nuclei). In the presence of a linear time-varying gradient field $\vec{\mathbf{G}} = G_x(t)\hat{\mathbf{x}} + G_y(t)\hat{\mathbf{y}} + G_z(t)\hat{\mathbf{z}}$, the angular frequency becomes a function of position:

$\omega(\vec{\mathbf{r}}) = 2\pi\gamma(\mathrm{B}_0 + \vec{\mathbf{G}} \bullet \vec{\mathbf{r}})$. A linear gradient applied relative to $\hat{\mathbf{y}}$ direction, $\vec{\mathbf{G}} = G_0\hat{\mathbf{y}}$, is shown in Figure 2.1. In the rotating reference frame (with characteristic angular frequency $\omega_0 = 2\pi\gamma\mathrm{B}_0$), the angular frequency due to the applied gradient simplifies to $\omega(\vec{\mathbf{r}}) = 2\pi\gamma(\vec{\mathbf{G}} \bullet \vec{\mathbf{r}})$. The detectable signal $d\mathbf{S}$ from this volume element is given by Eq. 2-1.

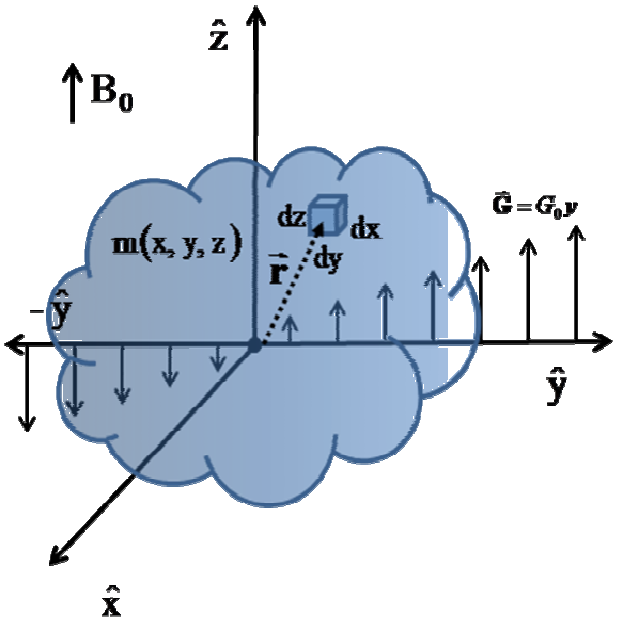

Figure 2.1 Object with spin density $\mathrm{m}(\mathrm{x},\mathrm{y},\mathrm{z})$ in magnetic field B_0 contains a voxel element of volume $dxdydz$ located at position $\vec{\mathbf{r}} = x\hat{\mathbf{x}} + y\hat{\mathbf{y}} + z\hat{\mathbf{z}}$. An applied gradient $\vec{\mathbf{G}} = G_0 y$ causes linear frequency variation along $\hat{\mathbf{y}}$ axis.

Eq. 2-1 $$d\mathbf{S} = \mathrm{m}(\mathrm{x},\mathrm{y},\mathrm{z})\exp(-j2\pi\vec{\mathbf{r}} \bullet \vec{\mathbf{k}})dxdydz$$

The phase of $d\mathbf{S}$ is dependent on position $\vec{\mathbf{r}} = x\hat{\mathbf{x}} + y\hat{\mathbf{y}} + z\hat{\mathbf{z}}$ and spatial frequency vector $\vec{\mathbf{k}}$ (in units of inverse distance) which encompasses the amplitude and duration of the gradient waveform, i.e.

Eq. 2-2 $$\vec{\mathbf{k}} = k_x\hat{\mathbf{x}} + k_y\hat{\mathbf{y}} + k_z\hat{\mathbf{z}} = \gamma\int G_x(t)\hat{\mathbf{x}} + G_y(t)\hat{\mathbf{y}} + G_z(t)\hat{\mathbf{z}}\,dt\,.$$

Integration over all voxels provides the signal produced from the entire object, i.e.:

Eq. 2-3

$$\mathbf{S}(k_x, k_y, k_z) = \iiint d\mathbf{S} = \iiint m(x,y,z)\exp(-j2\pi\vec{\mathbf{r}} \bullet \vec{\mathbf{k}})dxdydz$$
$$= \iiint \mathrm{m}(\mathrm{x},\mathrm{y},\mathrm{z})\exp\left(-j2\pi\left(k_x x + k_y y + k_z z\right)\right)dxdydz$$

Although the detected signal is a function of the applied gradient field, expressing the signal as a function of spatial frequency is convenient as $m(x,y,z)$ and $\mathbf{S}(k_x, k_y, k_z)$ is conjugate variables. Thus, the original spin density can be recovered by inverse Fourier transform of the detected signal:

Eq. 2-4 $$m(x, y, z) = \iiint \mathbf{S}(k_x, k_y, k_z)\exp\left(j2\pi\left(k_x x + k_y y + k_z z\right)\right)dk_x dk_y dk_z$$

In order to selectively excite a specific region of an object, a rotating RF field or B_1-field is applied in the presence of an encoding gradient. Assuming a small flip-angle RF pulse, a boxcar slab of the object is excited using a *sinc*-shaped pulse. The bandwidth-BW_{RF} of the excitation pulse and the gradient amplitude G_z define the slice thickness (ψ):

Eq. 2-5 $$\psi = \frac{BW_{RF}}{\gamma G_z}.$$

2.2.2 Field-of-view and resolution

In spectroscopy, the temporal sampling rate determines the maximum resolvable frequency (i.e. the bandwidth). An analogous relationship holds between the sampling rate in spatial frequency, denoted by sample spacing Δk_y, and field of-view (FOV_y) of the image (Eq. 2-6a). Conversely, the range of k-space points, denoted by $2k_{y,max}$, determines the voxel size Δy (Eq. 2-6b).

Eq. 2-6a $$\Delta k_y = \left(\frac{1}{FOV_y} \right)$$

Eq. 2-6b $$2k_{y,max} = \left(\frac{1}{\Delta y} \right)$$

Figure 2.2 illustrates these concepts in two dimensional space relative to the y spatial coordinate, although the relationships are readily extended to x and z directions in three dimensional space.

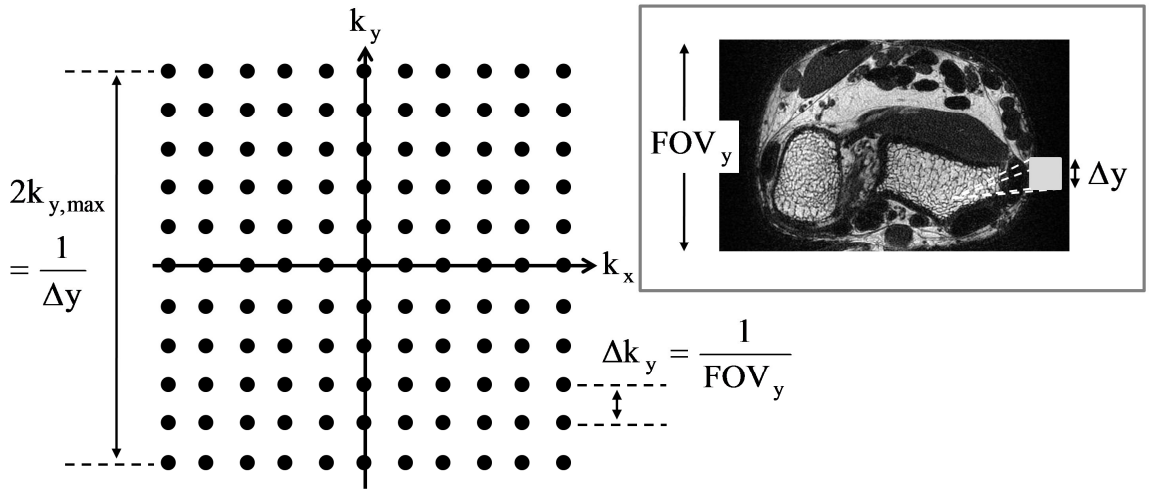

Figure 2.2 Sampling rate Δk_y and sampling range $2k_{y,max}$ in k-space govern image field-of-view (FOV_y) and voxel size Δy. Parameters along the x- and z-directions are analogously determined.

Following Eq. 2-2 and Eq. 2-6b, increasing the gradient amplitude or duration would cause $2k_{y,max}$ to increase, resulting in a smaller voxel width. The minimum resolution needed for an accurate depiction of the TB structure is not clear, but it is in the neighborhood of the trabecular thickness, which ranges between 80-150 μm. However, it should be noted that true resolution, i.e. the smallest detectable detail within an image,

is also dependent on relaxation, data filtering, and diffusion. Each of these processes can affect either the magnitude or phase of the acquired k-space data points. The modulation transfer function (MTF), which in the absence of these processes is unity, is a useful construct in demonstrating how these processes impact the k-space measurements. Its Fourier transform, the point-spead function (PSF), relates the impact of these processes on image resolution. As the MTF is applied to the k-space signal via multiplication, the acquired image $\tilde{m}(x,y,z)$ is the convolution ($\otimes$) of the unmodulated image $m(x,y,z)$ and the PSF: $\tilde{m}(x,y,z) = m(x,y,z) \otimes PSF(x,y,z)$. In spin warp imaging, the truncation of k-space by a rectangular sampling window results in a PSF of $\sin(\pi\Delta x/\Delta x)$ which has a full-width at half-maximum of 1.21*Δx where Δx is the pixel size [Wehrli, Hwang et al., 1998]. Thus, when setting the voxel size, in addition to the scale of the object to be imaged, relaxation effects, data filtering, and the diffusivity of the measured spins should be also considered. Additionally, it is necessary to consider the impact of voxel size on scan time and SNR.

2.2.3 Signal to noise ratio

The achievable SNR is a function of field strength, image voxel size, and sample size. Put simply, SNR is the voltage induced in a loop of wire (S) resulting from a precessing magnetization divided by the voltage induced by random fluctuations (noise) resulting from the electronics and the imaging object (N). Both S and N depend on the resonance frequency ω_0. For a small homogeneous sample of volume V_s placed in a homogenous field B_0, the signal voltage can be expressed as:

Eq. 2-7 $$|S| = \omega_0 M_0 B_\perp V_s ,$$

where M_0 is the equilibrium magnetization and $B_\perp$ is the reception field of the receiver [Haacke, Brown et al., 1999]. This relationship ignores relaxation. Ultimately, signal is proportional to the field strength squared, i.e. $S \propto \omega_0^2 = \gamma^2 B_0^2$. One of the angular frequency terms results from the spin polarization $M_0 \propto \omega_0$ and the second originates from the time derivative of the magnetization (Faraday's Law). The root-mean-squared noise voltage N consists of Johnson noise (thermal motion of charges in the electronics) and sample-noise (thermal motion of ions in the tissue). Both noise sources are modeled as series resistances:

Eq. 2-8 $$N = \sqrt{4kT\Delta f(R_c + R_s)},$$

where k is Boltzman's constant, T the absolute temperature, and Δf the receiver band-width. The noise resistance of the coil is simply the net resistance of the wire and connectors used in the RF coil. At high frequencies, current flowing through a conductor is confined to a thin surface layer or skin depth [Harpen, 1988]. For a circular loop of wire with radius r_l made of a cylindrical conductor with radius r_c and conductivity σ_c, the coil resistance is:

Eq. 2-9 $$R_c \propto \frac{r_l}{r_c}\sqrt{\frac{\omega_0 \mu}{2\sigma_c}},$$

where μ is the magnetic permeability of the conductor. The noise resistance R_s from the sample results from the conductivity of the tissue. For a non-zero reception field $B_\perp$ over a spherical region of radius ρ within an object of conductivity σ_t, Hoult et al. calculated the sample resistance as [Hoult and Lauterbur, 1979]:

Eq. 2-10 $$R_s \propto \sigma_t \omega_0^2 B_\perp^2 \rho^5.$$

By combining Eq. 2-8 through Eq. 2-10, SNR can be expressed as the ratio of Eq. 2-7 and Eq. 2-8 in terms of ω_0, the reception field $B_\perp$, and the radii of the coil loop and object:

Eq. 2-11 $$\mathrm{SNR} = \frac{S}{N} \propto \frac{\omega_0^2 B_\perp}{\sqrt{\alpha r_l \omega_0^{1/2} + \beta \omega_0^2 B_\perp^2 \rho^5}}.$$

The terms α and β include the remaining variables in Eq. 2-9 and Eq. 2-10. As $\omega_0 = \gamma B_0$, S scales as B_0^2 and N scales as $B_0^{1/4}$ or B_0^1 depending on field strength and sample size. In the limit of small samples (and coils) and moderate magnetic field strength (0.5-1.5T), the coil resistance dominates and thus SNR is proportional to $B_0^{7/4}$. For large samples and high field strengths, the sample resistance dominates and thus, SNR scales linearly with resonance frequency ω_0. The latter regime is more typical of *in vivo* imaging.

Eq. 2-11 shows a strong dependence of SNR on coil size. In general, a coil should achieve maximum coupling with the precessing magnetization by being suitably sized to closely surround the object [Edelstein, Glover et al., 1986]. Second, the coil should be designed for minimal coil losses and provide a high coil quality factor Q when loaded. Third, the coil should provide high RF homogeneity, which is particularly important if the same coil is used for transmission and reception. The two conventional types of receivers in MRI are volume coils and surface coils (see Figure 2.3). Volume coils produce homogeneous B1-fields, and through reciprocity, have uniform $B_\perp$ sensitivity across the object. Their size relative to the object causes them to pick up sample noise from a large portion of the object, therefore the noise in volume coils is

generally considered “body-dominated”. Conversely, surface coils have locally defined sensitivities (i.e. $B_{\perp}$ is non-uniform over the object). Thus less of the sample contributes to the sample noise and for lower fields, the noise is “coil dominated”.

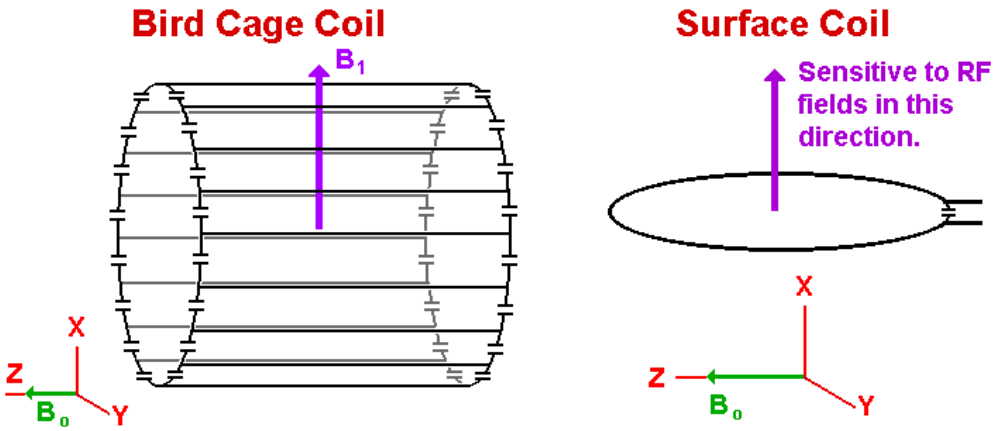

Figure 2.3 Volume (bird-cage) and surface coils illustrated relative to scanner coordinate system. From [Hornak, 2000].

Referring to Eq. 2-7, the signal dependence on V_s is a crucial restriction on high-resolution applications. SNR increases linearly with the number of spins per unit volume (voxel volume), and thus as the third power of linear resolution. Given a particular experimental setup, the only means of increasing resolution without penalizing SNR is by signal averaging via $SNR \propto \Delta x \Delta y \Delta z \bullet \sqrt{t_{acq}}$ where t_{acq} is acquisition time. Signal averaging can be accomplished by acquiring additional repetitions or by extending the length of the readout window through the reduction of the receiver bandwidth. The latter approach does not increase the scan time assuming the repetition time (TR) is long enough. However a longer data acquisition window does impact image quality in a number of ways, e.g. T2- blurring from the PSF along the readout axis and susceptibility distortions [Callaghan, 1991]. Alternatively, if a second scan is acquired, the combined

signal of the two scans scales linearly with scan time while the noise increases as the square-root of scan time, thus resulting in SNR's square-root dependence on scan time.

To achieve a given SNR, scan time scales as the reciprocal sixth power of linear resolution. The relationship between scan time and linear resolution is demonstrated for a fixed SNR of 10 in two applications at 1.5T in Figure 2.4: 1) clinical brain imaging and 2) micro-imaging of the radius [Wehrli, Hwang et al., 1998]. Scan times exceeding ten minutes increase the potential for involuntary motion due to the subject becoming restless or uncomfortable, thus making longer scan times impractical. It is clear that signal averaging is not an effective means of SNR enhancement.

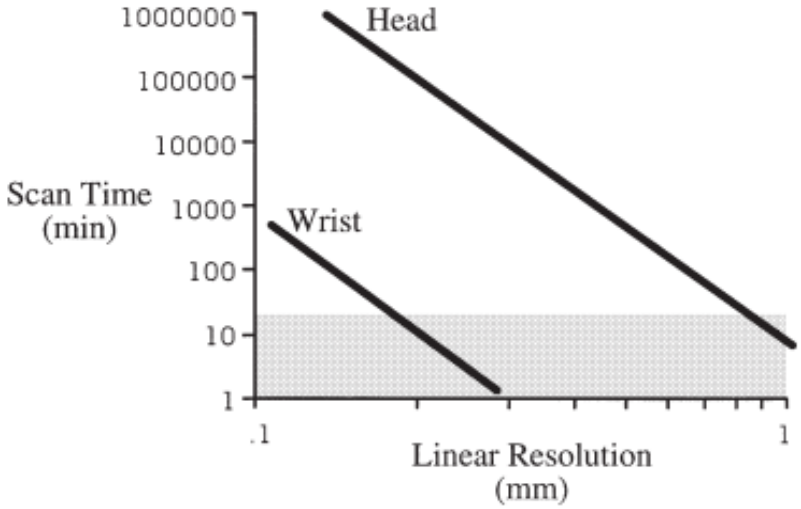

Figure 2.4 Scan time versus linear resolution at 1.5T using a head-sized RF coil and a small wrist coil for TB imaging. The shaded area indicates the range of scan times tolerable for patient imaging. From [Wehrli, Hwang et al., 1998].

2.2.4 Motion

In vivo high-resolution TB images are often degraded by artifacts due to involuntary subject motion [Gomberg, Wehrli et al., 2004]. Unlike breathing which

results in a periodic deformation of the diaphragm and chest, movement of a distal extremity is typically erratic and of the rigid-body nature. In MR microscopy, even slight displacements can result in significant blurring of the fine structures. A translational motion-corrupted image is shown in Figure 2.5a.

Immobilization devices are typically used in MRI to limit the degree of motion-corruption. These devices vary relative to the anatomy being imaged and are often combined with the coil construct. While immobilization devices reduce the degree of motion possible, they cannot prevent motion from occurring. Therefore, methods to detect motion so as to allow correction of the images are desirable.

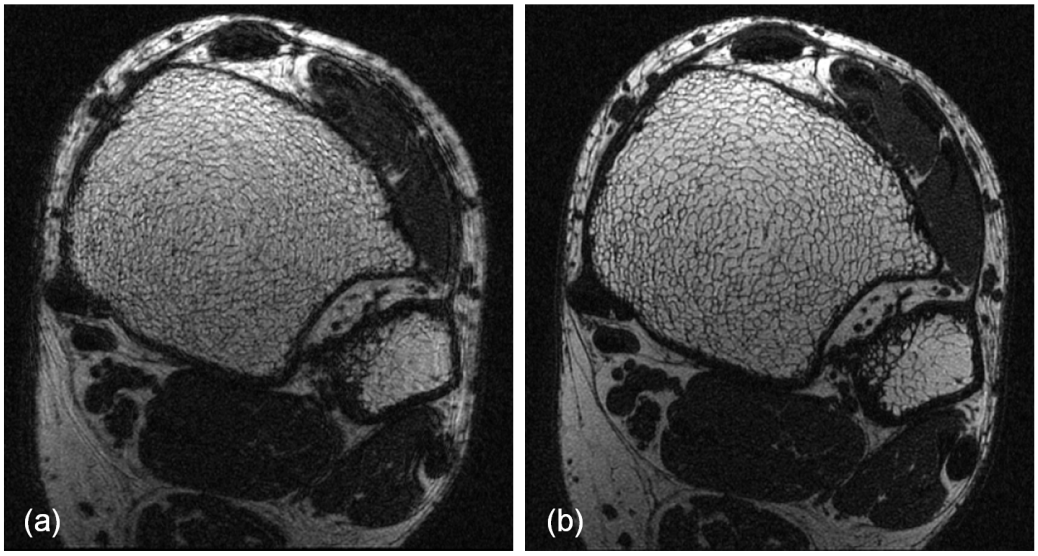

Figure 2.5 (a) High-resolution MR image of distal tibia acquired at 1.5T corrupted by in-plane translational motion of 4 pixels along x and 6 pixels along y. (b) Image from (a) after navigator-based correction.

Current techniques to correct for motion in TB imaging address in-plane translation and rotations. Through-plane motion is more challenging to correct as the excited slab, and thus the generated signal, is not constant throughout the acquisition.

One method for the detection and correction of in-plane motion involves acquiring additional data for each pulse sequence repetition. Traditionally, the acquired navigator echo is not phase encoded and therefore represents a projection of the object relative to the readout direction which can be alternated between x- and y-axes. A translation of the object will cause a similar displacement in the projection which can be measured as Δx and Δy over the course of the scan. Assuming the motion occurs between readouts, the detected translations are applied as phase shifts to the appropriate lines of k-space via:

Eq. 2-12 $$\mathbf{S}(k_x, k_y, k_z) = \mathbf{S}_0(k_x, k_y, k_z)\exp(-j2\pi(k_x\Delta x + k_y\Delta y)),$$

where $\mathbf{S}_0$ and $\mathbf{S}$ are the acquired and navigator-corrected signals. The usefulness of this technique in TB imaging was demonstrated by Song and Wehrli [Song and Wehrli, 1999], and is evident in the navigator-corrected image of Figure 2.5b.

An alternative method, called autofocusing, estimates the motion trajectory on the basis of the acquired image data [Atkinson, Hill et al., 1999]. Trial translations and rotations are iteratively applied to blocks of k-space data to maximize an image quality metric, such as the image sharpness, for example normalized gradient squared or NGS. The set of translational and rotational shifts that optimize the NGS value for a block of lines are then applied as phase shifts to the k-space data. The iterative nature of this technique makes it time-consuming, however its usefulness in correcting blurring due to translational and rotational motion in TB images has been demonstrated [Lin, Ladinsky et al., 2007].

2.3 Virtual bone biopsy

MRI is capable of inferring TB structural information indirectly though measuring relaxation mechanisms [Yablonskiy and Haacke, 1994] and signal amplitude reduction [Fernandez-Seara, Song et al., 2001] dependent on the amount of bone per unit volume. Another indirect method involving the detection of the long-range dipolar interactions in bone marrow may permit the non-invasive measurement of material anisotropy [Bouchard, Wehrli et al., 2005]. While these techniques are promising, this thesis focuses on the direct detection of the TB micro-architecture via MR microscopy. The current system of instruments and programs used to assess the structural aspects of TB non-invasively within the Laboratory of Structural NMR Imaging (LSNI) is collectively termed the virtual bone biopsy or VBB. The following section describes some of the most important aspects of the VBB. The specialized RF coils used to image the distal extremities are not discussed in detail; however their design and SNR performance are paramount in producing high quality images as described in Section 2.2.3. The key elements in the VBB that are discussed relate to the pulse sequence and image processing techniques used to quantify select structural parameters. For a more comprehensive discussion, the reader is directed to a recent review [Wehrli, Song et al., 2006].

2.3.1 The FLASE pulse sequence

A significant advancement in TB imaging was the introduction of the 3D FLASE (fast large-angle spin echo) pulse sequence, a modified spin-echo sequence optimized for short repetition time (TR) applications [Ma, Wehrli et al., 1996]. The sequence is shown in Figure 2.6. The magnetization is partially inverted and nutated into the transverse plane by a large angle (α) slab selective RF pulse. The longitudinal

magnetization is then restored while the transverse magnetization is rephased by a non-selective phase-reversal pulse. Since short-TR SE sequences produce many coherence pathways, some of which result in stimulated echo artifacts, RF-spoiling (random phase offset to α-pulse) is employed to make them phase-incoherent [Ma, Wehrli et al., 1996]. In addition, alternating navigator projections acquired in a slab shifted relative to the imaging slab are used for translational motion correction. The combination of the large angle α pulse and the refocusing pulse allow shorter repetition and scan times as only part of the longitudinal magnetization is used in each TR and the spin-lattice relaxation (T_1) is accelerated. In the case of fatty marrow, T1≈300ms and α=140° for a TR=80ms.

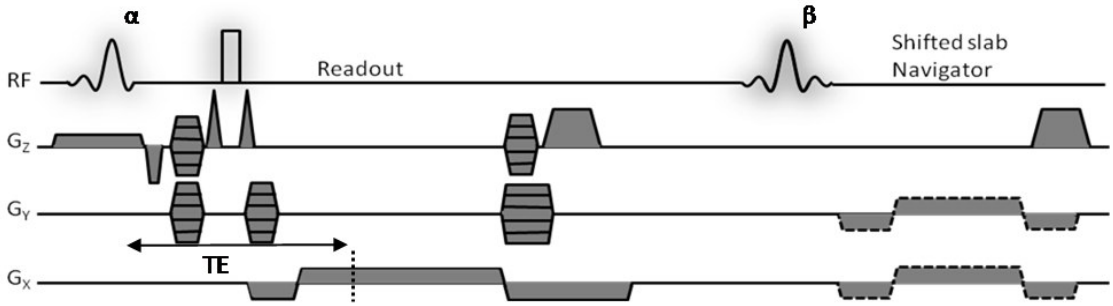

Figure 2.6 The preferred embodiment of the 3D FLASE pulse sequence. Both α and β RF pulses are large (>90°) flip angle RF pulses designed using the Shinnar Le Roux (SLR) algorithm [Pauly, Le Roux et al., 1991]. Dashed lines indicate navigator gradient echoes alter between the read and phase encoding axes. Typical pulse sequence parameters are: α~140º, β~140º, TR/TE=80/10.5 ms. From [Magland, Wald et al., 2009].

The spin echo (SE) acquisition of FLASE is advantageous over a gradient-echo acquisition (GRE) as phase-dispersion due to the susceptibility-induced field gradients at the bone and bone marrow interface are refocused at echo time, providing a more accurate depiction of trabeculae. This benefit comes at the cost of longer echo and repetition times, i.e. more T_2 decay prior to the imaging echo and longer scan times. Still, SNR efficiency of FLASE is higher than the alternative gradient echo (GRE) based sequences for transverse and longitudinal relaxation times of ~60ms and ~300ms,

respectively [Techawiboonwong, Song et al., 2005]. The primary disadvantage of the FLASE sequence relative to GRE alternatives is specific-absorption rate (SAR) as there are two large-flip-angle pulses per repetition. SAR is a considerable concern and restriction at higher field strengths (>3T).

The 3D FLASE pulse sequence has been implemented to acquire transverse images of the distal tibia (Figure 2.7) with a 137x137x410 μm^3 voxel size over a 13 mm slab in approximately 16 minutes [Wehrli, Ladinsky et al., 2008]. Application to the distal radius using the same sequence parameters but smaller in-plane FOV equates to a 10 minute scan. The anisotropic voxel size is chosen as a means of improving SNR (see Eq. 2-7) under the notion that a reduced slice resolution least affects the perceived TB micro-architecture as TB is typically oriented preferentially in the through-slice direction (i.e. bone's longitudinal direction).

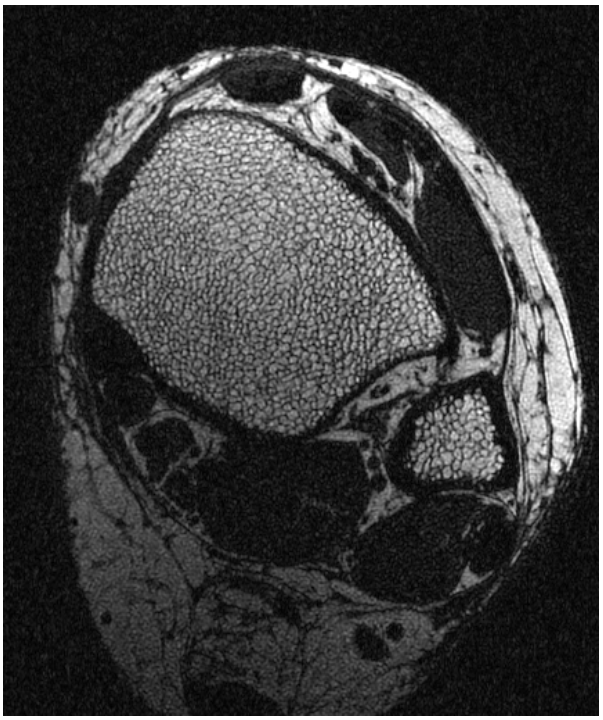

Figure 2.7 Representative *in vivo* FLASE acquisition (137x137x410 μm^3 voxel size) acquired on 1.5T Siemens Sonata using two-channel phased–array RF coil. The image is from a middle-aged, female kidney-transplant patient. The FLASE sequence is optimized for 3D imaging of bone marrow, which appears bright relative to bone. The TB architecture is therefore imaged indirectly.

2.3.2 Image processing and analysis

2.3.2.1 Masking and registration

Prior to quantifying structural parameters, a number of processing steps are performed in order to identify the analysis region. First, the region containing TB is identified either manually or through an auto-masking procedure [Vasilic and Wehrli, 2005]. In longitudinal studies, masked regions must be compared across all time-points in order to define the common analysis region. This step is important as the TB structure is highly heterogeneous and different analysis regions could cloak or artificially enhance changes associated with treatment or disease progression. Analysis of the same anatomical region is ensured by image registration of the scan volumes between two time points. The technique developed by Magland et al. fits six parameters of rigid displacement using a collection of small 2D image-tiles within the TB region [Magland, Jones et al., 2009]. Assuming small through-plane rotation, each image-tile is matched to its location in the follow-up image using correlation. The average values of the three displacements and three rotation angles for a collection of 2D image-tiles are then used to resample the follow-up volume into alignment with the baseline dataset. This technique improved the correlation between structural parameters from two time points in twenty-eight subjects [Magland, Jones et al., 2009].

2.3.2.2 Bone volume fraction mapping

Due to the limited resolution of *in vivo* MRI, structures on the order of 100-200 μm cannot be visualized free of partial-volume blurring. As the signal originates from the marrow compartment, it is useful to invert the image into a bone volume fraction map (BVF-map) prior to quantifying features of the TB network. A BVF-map is a three-dimensional image whose intensities represent the percentage of bone within each

voxel. The presence of Rician noise and RF coil shading make the computation of a BVF-map more difficult than simple contrast inversion.

Two techniques had previously been developed to calculate a BVF-map: histogram deconvolution [Hwang and Wehrli, 1999] and local thresholding [Vasilic and Wehrli, 2005]. Both techniques are applied to the original image where marrow is bright and bone is dark to initially create marrow volume fraction (MVF) maps. Histogram deconvolution is an iterative process in which Rician noise and coil shading are modeled in the image histogram. At each step of the iteration, the histogram of an ideal image is compared with that of the original image. Information from the difference histogram is used to modify denoising and deshading parameters until the incremental change in error between iterations reaches a cutoff value. The BVF map is then determined by inverting the denoised and deshaded image.

The local thresholding approach makes use of the fact that trabecular bone is surrounded by more marrow voxels than bone voxels at the image resolutions achievable *in vivo*. This condition is generally true as the total bone per unit volume is typically less than 20% and the voxel size is on the order of the trabecular thickness. Each voxel, denoted by index j, in the TB region is mapped to its MVF by scaling it relative to its local marrow intensity I_m. I_m is computed in an NxN neighborhood around voxel j following Figure 2.8. I_m is the intensity at which a fitted line (fit between the intensities of each k observation point in the NxN region and the intensities of k's four nearest-neighbors) intersects the line of identity (y=x). The line of identity is used as this represents the pure marrow signal. For *in vivo* images with an in-plane pixel size of

137x137 μm^2, N is typically chosen as 10 pixels. A BVF map is then computed by setting voxels with MVFs larger than 100 to 100 and inverting the contrast.

The local thresholding approach has been shown to be faster and more sensitive to thin trabeculae in images with low SNR than histogram deconvolution [Vasilic and Wehrli, 2005]. Consequently, local thresholding is currently utilized to normalize *in vivo* MR images of TB.

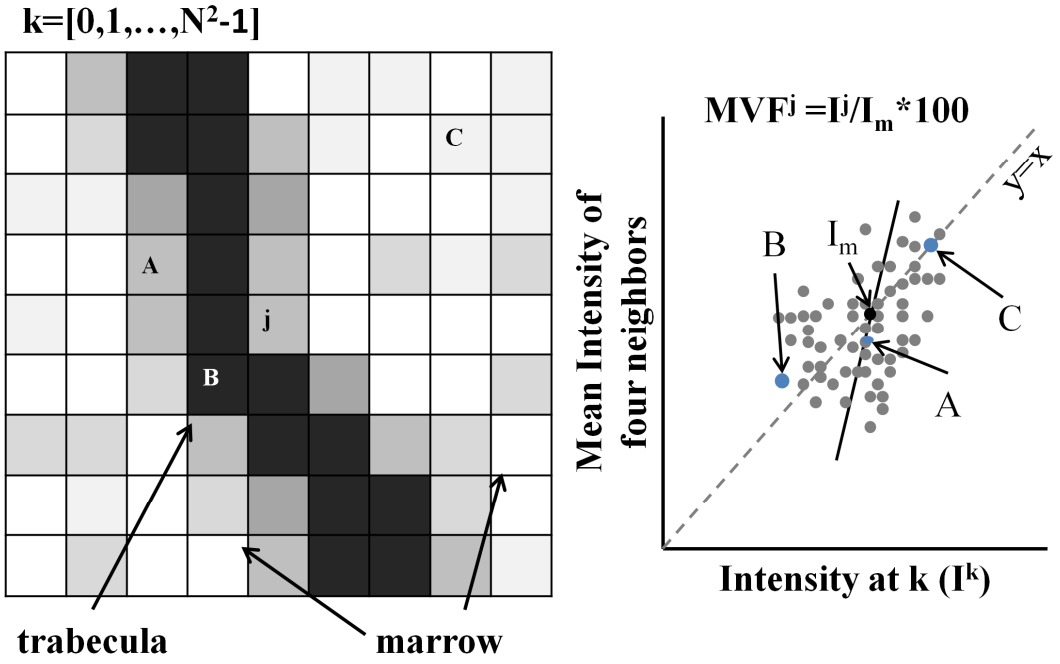

Figure 2.8 Local thresholding approach to MVF-mapping in a synthetic image containing a single trabecula surrounded by marrow. The neighborhood size N is chosen according to the voxel size such that marrow is the predominant signal around any point j in the TB region. The marrow level is calculated as the intensity at which the fitted line crosses y=x. In the plot, the intensities of voxels A, B, and C relative to the intensities of their four nearest neighbors are indicated to illustrate how different voxels in the NxN region are positioned in the plot. A BVF map is then computed by setting MVFs>100 to 100 and inverting the contrast.

2.3.2.3 Digital topological analysis

In osteoporotic bone loss, trabecular plates become fenestrated into rod-like elements which, due to further thinning, eventually become disconnected. To characterize the transition from plate-like to rod-like structures, a method, termed digital topological analysis (DTA), has been developed [Gomberg, Saha et al., 2000]. In DTA, the TB structure determined by *in vivo* μMR imaging is classified relative to its local topology. The theory and algorithms were initially conceived by Saha and Chaudhuri to characterize the topological classes of digitized structures [Saha and Chaudhuri, 1996]. The DTA classification proceeds as follows: input images are *sinc*-interpolated, BVF-mapped, binarized using a threshold BVF of 15%, thinned into a skeleton representation (trabecular elements are either one or two dimensional objects), and finally classified as belonging to a curve, surface, or junction by considering the local 3x3 neighborhood of each bone voxel. Figure 2.9 illustrates a hypothetical trabecular skeleton containing only surfaces, curves, and junctions. As shown in Figure 2.9, further classification using an extended neighborhood can also be performed. Surface-voxel density (SD) and curve-voxel density (CD) are calculated as (surface or curve voxels)/TV, respectively. Composite parameters (e.g. the ratio of surface voxels to curve voxels or surface-to-curve ratio) are typically considered instead of the number of voxels in each classification. The surface-to-curve ratio (S/C = SD/CD) expresses the ratio of plate-like to rod-like trabeculae and the erosion index (EI) yields the ratio of voxel densities that decrease to those that increase with osteoclastic bone resorption [Gomberg, Saha et al., 2000].

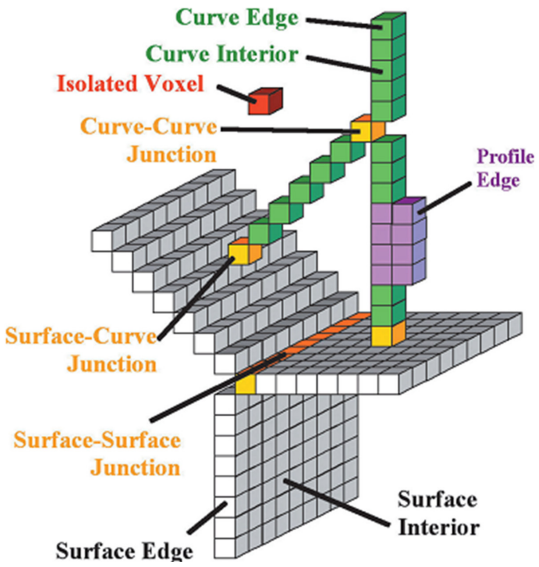

Figure 2.9 Idealized digital representation of trabecular skeleton indicating topological classification of individual bone voxels. Typical classifications of surface, curve, and junction are skeleton analogs to trabecular plate, rod, and junction. From [Ladinsky, Vasilic et al., 2008].

2.3.2.4 Trabecular Thickness

In osteoporosis, bone atrophy leads to either homogeneous or heterogeneous thinning of the trabecular elements. Reductions in the trabecular thickness are also associated with bone loss due to long-term corticosteroids usage [Aaron, Francis et al., 1989] and rheumatoid arthritis [Mellish, O'Sullivan et al., 1987]. The thickness of the trabeculae is therefore an important determinant of TB mechanical competence. In high-resolution μCT images of TB, trabecular thickness (Tb.Th) can be estimated by the diameter of the largest inscribed sphere within the structure [Hildebrand and Ruegsegger, 1997]. In the presence of partial volume blurring, an alternative method is necessary. Saha and Wehrli developed a method for estimating Tb.Th on the basis of images with partial volume blurring. The fuzzy distance transform (FDT) involves finding the shortest non-Euclidean, BVF-weighted distance between a voxel within a trabeculae to a neighboring voxel of pure marrow [Saha and Wehrli, 2004]. Eq. 2-13 expresses the FDT for a point at index k in bone, denoted p_k, where the non-Euclidean path π_k

connects p_k to p_{N-1} - the closest voxel of pure marrow. $\|p_i - p_{i+1}\|$ denotes the distance between consecutive points along path π_k. The fuzzy distance is computed for all voxels with a non-zero BVF, and the average thickness for the TB region is calculated by sampling the fuzzy distance values along the digitized skeleton (skeleton description is in Section 2.3.2.3).

Eq. 2-13 $$FDT(p_k) = \sum \frac{1}{2}\left(BVF(p_i) + BVF(p_{i+1})\right)\|p_i - p_{i+1}\|,\ i \in [k, N-1] = \pi_k$$

2.3.2.5 Image Processing Software

The techniques described in this chapter have been implemented in a programming environment developed within the Laboratory for Structural NMR Imaging at the University of Pennslyvania called *Chainlink* (*http://chainlink.sourceforge.net/*). *Chainlink* was designed by Dr. Jeremy Magland to combine MATLAB style scripts with C source code. Through this combination, rigorous analysis techniques in the C programming language are readily run in series with routines for reading, displaying, and manipulating images.

3 Chapter 3 Assessment of trabecular bone fabric tensor

3.1 Overview

Recent research suggests that structure contributes to bone strength in a manner complementary to BMD. Trabecular bone's structural anisotropy plays an important role in bone's mechanical integrity as trabeculae are preferentially oriented along the directions of local stress. However, the study of trabecular bone (TB) orientation has been primarily confined to *ex vivo* imaging methods, in particular serial reconstructions of anatomic sections and μCT images. *In vivo* evidence of changes in TB structural anisotropy associated with disease and therapy is sparse due to limitations on *in vivo* image quality. For example, resolution demands and restrictions on acquisition duration restrict the achievable SNR of high-resolution magnetic resonance images of TB. The intensity histogram of *in vivo* MR images of TB is typically monomodal, making image binarization difficult. The most common method for measuring structural anisotropy of TB, the mean-intercept-length (MIL) method [Whitehouse, 1974], involves image binarization to distinguish bone from bone marrow.

In this chapter a novel technique is presented, based on the 3D spatial autocorrelation function (ACF), for mapping the fabric tensor of TB. In *ex vivo* TB images acquired from specimens using micro computed tomography (μCT) and high-resolution magnetic resonance imaging (μMRI), the ACF-derived fabric tensor shows good agreement with MIL. Performance tests of the two techniques relative to common technical limitations of *in vivo* μMRI indicate the ACF method as more robust to

variations in resolution and SNR. ACF is also at least an order of magnitude faster than MIL in quantifying the orientation dependence of TB images. However, MIL and ACF are susceptible to errors associated with voxel anisotropy along the slice direction and RF coil inhomogeneity, suggesting that images with isotropic resolution are best suited for the detection of TB orientation and that image shading due to RF coil sensitivity should be corrected prior to structural anisotropy analysis.

3.2 Introduction

Trabecular bone is characterized by a complex architecture which precludes predicting strength from density alone. The arrangement of trabeculae in the spine, femur, wrist, and tibia, which are thicker and more plate-like along the longitudinal than the transverse direction, is an adaptive response to functional loading. Transversely oriented trabeculae stabilize the network by preventing the longitudinal struts from buckling and therefore play an important role in distributing loads uniformly [Borah, Dufresne et al., 2002]. This adaptive behavior continues even as the trabecular bone becomes more porous [Keaveny, Morgan et al., 2001]. During aging, trabeculae, particularly those found transverse to the bone axis, become thinner and sparser. This phenomenon is exacerbated in osteoporosis. The thinning and eventual loss of transverse struts, which has been termed ‘overadaptation’ to the primary loading axis, is associated with increased mechanical anisotropy [Homminga, McCreadie et al., 2002] and an increased likelihood of fracture [Kleerekoper, Villanueva et al., 1985].

Overadaptation is marked by an increase in structural anisotropy (SA) [Ciarelli, Fyhrie et al., 2000], which has been shown to be the second largest contributor, next to BMD, to mechanical competence [Oden, Selvitelli et al., 1998; Homminga, McCreadie et

al., 2002]. Women with hip fractures were distinguished from bone-volume- fraction-matched peers without hip fractures on the basis of SA within the proximal femur [Ciarelli, Fyhrie et al., 2000] (Figure 3.1). Although significant evidence exists in studies performed *ex vivo*, changes in TB SA *in vivo* have not been widely observed. The primary reasons for this are the inferior quality of *in vivo* images and the lack of suitable techniques to quantify the orientation dependence of TB on the basis of *in vivo* images.

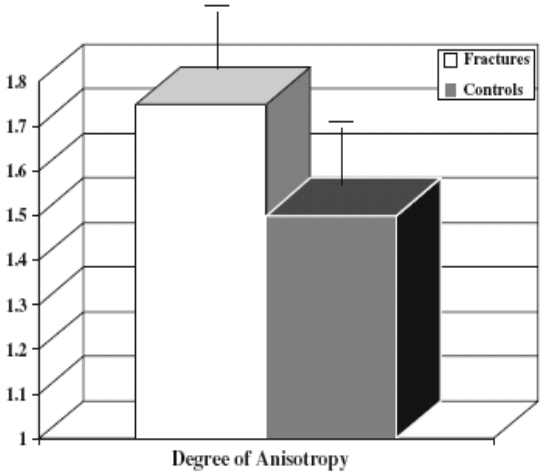

Figure 3.1 Structural anisotropy is higher in TB from the proximal femur of women who have sustained a hip fracture (N=19) relative to women without a fracture but with similar bone volume fraction (N=11). Measurements of structural anisotropy were made on the basis of µCT images of 8mm cubes of trabecular bone from cadaveric femur specimens. Adapted from [Ciarelli, Fyhrie et al., 2000].

In recent years, µMRI has demonstrated its potential for noninvasive imaging of TB microstructure [Majumdar, 2002; Wehrli, Saha et al., 2003]. Morphological indices of TB have been shown to reflect the mechanical integrity [Kleerekoper, Villanueva et al., 1985; Wehrli, Gomberg et al., 2001; Wehrli, Leonard et al., 2004] of the skeleton and to assist in monitoring disease progression [Beuf, Ghosh et al., 2002] and the response to intervention [Borah, Dufresne et al., 2002]. However, these measurements lack the orientation information inherent to bone resulting from stress-induced bone turnover [Wolff, 1892; Frost, 1987].

Techniques used to analyze TB micro-architecture, particularly SA, on the basis of *ex vivo* images generally employ binarization of the bone and marrow phases, often through the application of a threshold. A threshold can be chosen on the basis of the image's intensity histogram as shown in Figure 3.2a-b. In a µCT image with a 16 µm isotropic resolution, the threshold is easily selected from the histogram as the intensity corresponding to the minimum count between the bone and bone marrow modes. Unlike the bimodal distribution of *ex vivo* µCT, the intensity histogram of a µMR image of TB is monomodal (Figure 3.2c-d) due to lower signal-to-noise ratio and resolution. The choice for a threshold dramatically impacts the appearance of the segmented bone. In Figure 3.3, thresholding at the mid-point between bone and marrow signals causes a disconnected TB network. In the few cases where SA has been analyzed *in vivo*, it is noted that measurement accuracy diminishes under conditions of low signal-to-noise (SNR) and partial volume blurring [Newitt, Majumdar et al., 2002; Gomberg, Saha et al., 2003]. Therefore, techniques obviating the need for binarization are desirable for quantifying architectural parameters of TB on the basis of *in vivo* images.

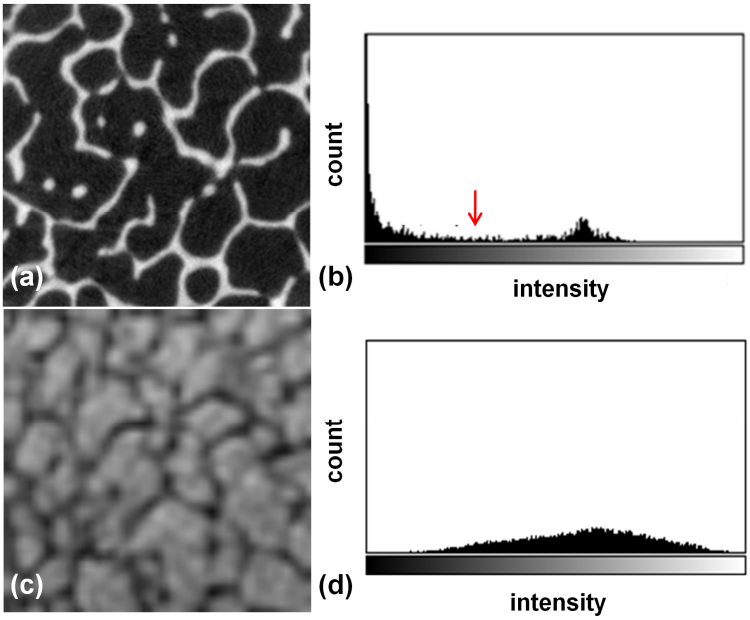

Figure 3.2 Illustration of differences between *ex vivo* µCT image (a) and an *in vivo* µMR image (c) of TB. At a 16µm isotropic resolution, the histogram (b) shows a bimodal distribution where the bone intensities are substantially higher than the marrow intensities. The threshold is selected as the intensity of the count minimum between the bone and bone marrow modes. Besides the contrast being inverted in (c), the histogram (d) of the *in vivo* MR image (137x137x410 µm^3 resolution) is monomodal due to partial volume blurring and lower SNR.

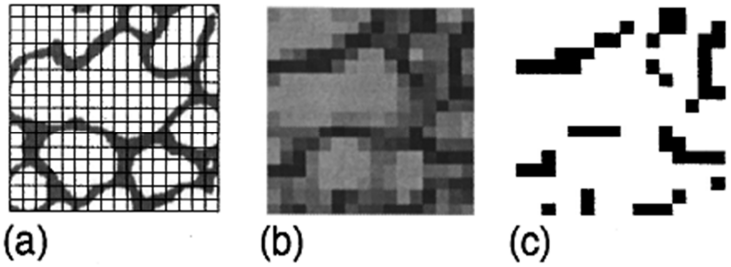

Figure 3.3 Thresholding at an intensity of 0.5 in a low resolution image of TB (b) (created from down-sampling (a)) with intensities ranging from 0 (bone) to 1 (marrow) causes errors in identifying trabeculae (c). From [Hwang, Wehrli et al., 1997].

In this chapter, the ability of the spatial autocorrelation function (ACF) as a three-dimensional method for quantifying structural anisotropy of TB networks is examined. Based on the ACF method not requiring thresholding, it is hypothesized that the ACF method is better suited for the quantification of TB orientation on the basis of *in vivo* MR images. To test this hypothesis, the ACF and MIL techniques were compared in terms

of SA and orientation on the basis of μCT and μMR images. Experiments were designed to test their relative sensitivities to differences in SA and changes in orientation, their performance in the presence of partial volume blurring due to resolution degradation, changes in signal-to-noise ratio (SNR), resolution anisotropy, and RF coil inhomogeneity. Finally, the ACF and MIL methods were applied to an *in vivo* μMR image of the wrist to examine the role of BVF-mapping via the local thresholding approach (see Chapter 2 for an introduction of BVF-mapping) as a preprocessing step.

3.2.1 Structural anisotropy and fabric tensor

A material's structural anisotropy can be generally described by main directions and numbers describing the concentration of the material relative to the main directions. Fabric tensors provide compact descriptions of orthotropic architectural anisotropy in the form of a 3x3 matrix, where the eigenvectors $\hat{\mathbf{v}}_1, \hat{\mathbf{v}}_2, \hat{\mathbf{v}}_3$ give the main directions, and the eigenvalues $\lambda_1, \lambda_2, \lambda_3$ give the degree of concentration around the main directions. For example, λ_3 denotes the degree of concentration around the principal fabric direction $\hat{\mathbf{v}}_3$. The eigenvectors provide directions perpendicular to symmetry planes in the structure. If $\lambda_1 = \lambda_2 = \lambda_3$, the material is considered isotropic as there is no preferred direction. Isotropic materials have no unique planes of material symmetry. If $\lambda_3 > \lambda_2 = \lambda_1$, the material is considered transversely isotropic with one unique plane of mirror symmetry perpendicular to $\hat{\mathbf{v}}_3$. If $\lambda_3 > \lambda_2 > \lambda_1$, the material is called orthotropic and has at least two orthogonal planes of symmetry. Orthotropic materials can be transverse isotropic or isotropic. Structural anisotropy (*SA)* is defined by the ratio λ_3 / λ_1

where λ_1 is the magnitude of the smallest eigenvalue (*SA*=1 for isotropic materials). TB is generally considered to possess orthotropic symmetry.

The advantage of representing TB by a fabric tensor is demonstrated in Figure 3.4. The measure of bone volume fraction is direction-less and thereby associated with a sphere (Figure 3.4b). Alternatively, a fabric tensor describes the directional dependence of a specific TB property in terms of both scale (eigenvalues) and orientation (eigenvectors). Assuming TB to possess orthotropic symmetry, a fabric tensor can be represented by an ellipsoid (Figure 3.4c).

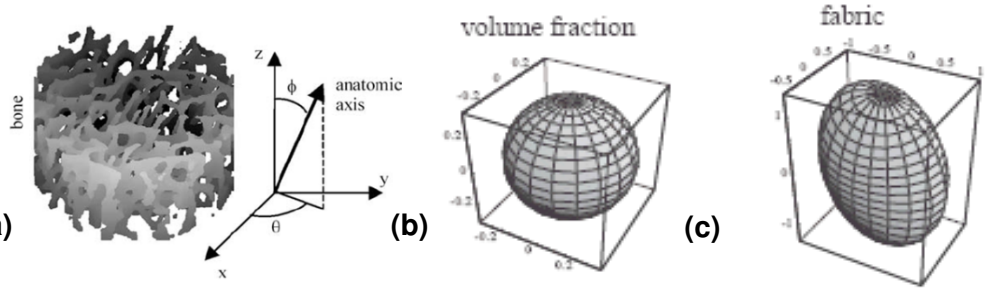

Figure 3.4 Cylindrical core of TB in (a) can be represented by the scalar measure of bone volume fraction (b) or by a fabric tensor (c) that provides information on TB orientational dependence. Adapted from [Zysset, 2003].

3.2.2 Quantification of fabric tensor

The traditional technique used to quantify a TB fabric tensor, the mean intercept length or MIL, was introduced in TB morphometry by Whitehouse [Whitehouse, 1974]. The *mean intercept length* is the mean distance between material intersections (bone–marrow interfaces) along linear traverses over a range of orientations (see Figure 3.5). The MIL method consists of placing a set of parallel lines of length L oriented in a given direction θ onto the structure and counting the intersections of the lines on the

bone/bone-marrow interface $N_I(\theta)$. MIL at a given orientation, $MIL(\theta)$, is therefore defined as:

Eq. 3-1 $$MIL(\theta) = \frac{L}{N_I(\theta)}.$$

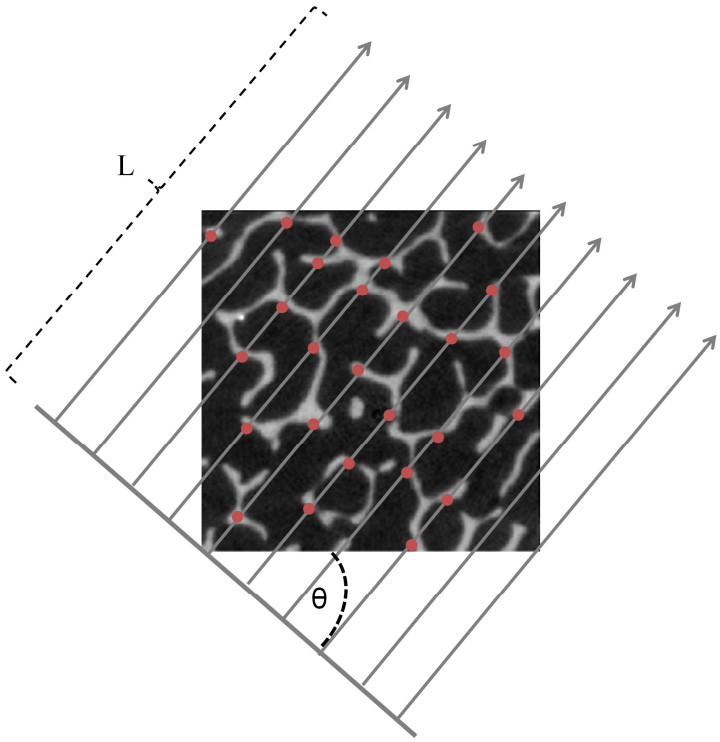

Figure 3.5 MIL technique in 2D where lines of length L aligned with direction θ are overlaid onto the image and the intersections with bone (red points) are detected, allowing computation of MIL(θ) via Eq. 3-1.

MIL detects the interface anisotropy of the TB structure (i.e. the TB surface). When plotting MIL relative to θ, Whitehouse noted that the distribution could be approximated by an ellipse. By extending the MIL technique into 3D using polar angles φ and θ, the Rose plot $MIL(\varphi,\theta)$ can be represented by an ellipsoid that Harrigan and Mann [Harrigan and Mann, 1984] expressed as the quadratic form of a second-rank tensor $\mathbf{M}$, i.e. the MIL anisotropy tensor. From the measurements $MIL(\varphi_i,\theta_i)$ and the associated directional cosines x_i, y_i, z_i where $i = 1,...,n$ represent the number of orientations sampled, the MIL anisotropy tensor $\mathbf{M}$ can be calculated by multiple

regression analysis or singular value decomposition of the canonical expression of an ellipsoid. This equates to finding the values of A, B, C, D, E, and F, which correspond to the directional cosines of the inverse radii-squared of the best fit ellipsoid following Eq. 3-2.

Eq. 3-2

$$\begin{bmatrix} MIL(\varphi_1,\theta_1) \\ \vdots \\ MIL(\varphi_i,\theta_i) \\ \vdots \\ MIL(\varphi_n,\theta_n) \end{bmatrix} = \begin{bmatrix} x_1^2 & y_1^2 & z_1^2 & 2x_1y_1 & 2x_1z_1 & 2y_1z_1 \\ & & & \vdots & & \\ x_i^2 & y_i^2 & z_i^2 & 2x_iy_i & 2x_iz_i & 2y_iz_i \\ & & & \vdots & & \\ x_n^2 & y_n^2 & z_n^2 & 2x_ny_n & 2x_nz_n & 2y_nz_n \end{bmatrix} \begin{bmatrix} A \\ B \\ C \\ D \\ E \\ F \end{bmatrix}; \qquad \mathbf{M} = \begin{bmatrix} A & D & E \\ D & B & F \\ E & F & C \end{bmatrix}$$

For convenience, Cowin defined a fabric tensor $\mathbf{H}$ as the inverse square root of $\mathbf{M}$ so that the eigenvector corresponding to the largest eigenvalue of $\mathbf{H}$ aligned with the direction of largest stiffness [Cowin, 1986]. Therefore, $\mathbf{H}$ is defined by Eq. 3-3 as the inverse square-root of $\mathbf{M}$.

Eq. 3-3

$$\mathbf{H} = \mathbf{M}^{-1/2} = \begin{bmatrix} A & D & E \\ D & B & F \\ E & F & C \end{bmatrix}^{-1/2}.$$

Because of this simple inverse-square-root relationship, the directional dependence of the structure is fully depicted by either $\mathbf{M}$ or $\mathbf{H}$. Further, either 3x3 matrix, $\mathbf{M}$ or $\mathbf{H}$, can be decomposed into its eigenvectors $\hat{\mathbf{v}}_1, \hat{\mathbf{v}}_2, \hat{\mathbf{v}}_3$ that provide the main directions and eigenvalues $\lambda_1, \lambda_2, \lambda_3$ giving the degree of concentration around the main directions where $\lambda_1 \le \lambda_2 \le \lambda_3$. For simplicity and clarity for the remainder of this chapter, when referring to the eigenvalues and eigenvectors of the fabric tensor, $\mathbf{H}$ is implied. In addition, because $\mathbf{H}$ is computed using two different approaches, $\mathbf{H}_{MIL}$ will represent the fabric tensor determined by MIL.

Although MIL is the original method for quantifying a fabric tensor in TB, it is not considered the only method. When assessing a fabric tensor using any method, the material property of interest must be specified. Since the sample lines used in the MIL method traverse both bone and marrow, the result is a combined measure of both phases. Variations of the MIL technique as well as other methods to capture various properties of TB have been developed. One variant of the MIL technique (referred to here as average-bone-length or ABL) considers only the length within the bone phase relative to direction, thereby reflecting the relative amount of bone as opposed to the number of bone crossings. This approach is not considered to have added significant information, as both empirical and theoretical arguments suggest structural anisotropy to be independent of pore size [Gibson, 1985; Turner and Cowin, 1987; Gibson and Ashby, 1988]. The line frequency deviation (LFD) technique, which was originally used in radiographs of TB, determines the standard deviation of the relative lengths within the bone phase (Figure 3.6a) for each direction [Geraets, van Ruijven et al., 2006]. LFD creates slender and irregularly-shaped polar plots (i.e. higher SA than MIL) and is therefore deemed more sensitive to orientation. Another technique, established by Odgaard, and designed to detect the longest intercepts in bone, is volume orientation (VO) [Odgaard, Jensen et al., 1990]. Rather than sampling along a set of lines as done in MIL, the longest intercept length inside bone is determined at each point within a point-grid (Figure 3.6b). A similar sampling procedure is used in calculating the star volume distribution (SVD) [Cruz-Orive, Karlsson et al., 2005] (Figure 3.6c), which represents the distribution of non-obscured infinitesimal cones emanating in various directions from a point within bone (marrow) until they encounter a boundary. While the calculations of ABL, LFC, VO, and SVD along a given direction θ are different from MIL,

their Rose-plots can be similarly input into the left-hand side of Eq. 3-2 to compute associated fabric tensors via Eq. 3-3. Like the MIL technique, these methods are amenable with binarized images.

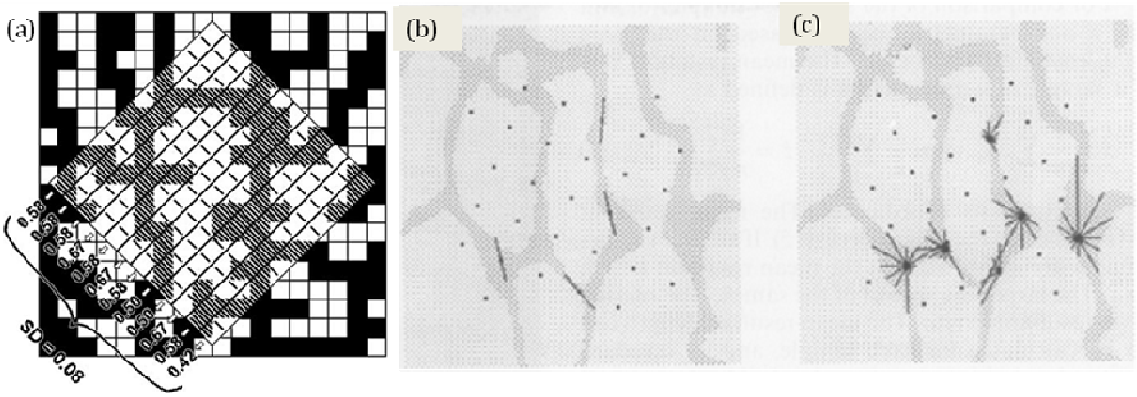

Figure 3.6 Alternative methods for quantifying a fabric tensor in TB images. Line-frequency deviation (a) entails measuring the standard deviation of the sampled lengths in bone according to an oriented line grid. Volume orientation (b) captures the longest segments within bone for randomly placed points within the bone phase. Similar to volume orientation, star volume distribution (c) involves sampling the lengths of all lines emanating from points randomly placed within bone.

While the four techniques (ABL, LFD, VO, and SVD) are capable of capturing the structural anisotropy of TB, they are most appropriate for high-resolution images where the pixel size is smaller than the trabecular width, i.e. *ex vivo* µCT. Since the techniques focus on the bone phase, errors associated with resolution are important to the accuracy of the measurements. The relative errors in detecting MIL are smaller as MIL depends only on the presence of intercepts, not their actual width. Therefore, MIL is better suited for images with lower resolutions. Authors of the other noted techniques have suggested MIL to be a poor representation of structural anisotropy for various artificially generated structures, yet these artificial structures have little resemblance to TB [Odgaard, 1997]. Further, studies of VO and SVD have not demonstrated any definite advantage over MIL when predicting mechanical properties of bone [Odgaard, Kabel et

al., 1997] and LFD has shown only marginal improvement relative to MIL in predicting Young's modulus [Geraets, van Ruijven et al., 2008].

3.2.3 Spatial autocorrelation function

Spatial autocorrelation function or ACF has also been used to describe the SA of TB. Its use in characterizing porous materials was first described by Berryman from an image processing perspective [Berryman, 1985] and then later related to NMR diffraction theory by Barrall et al. [Barrall, Frydman et al., 1992]. Hwang et al. [Hwang, Wehrli et al., 1997] used ACF to describe the tubularity of TB samples from human distal radii imaged by μMRI (78x78x78 μm^3 voxel size). Rotter et al. used ACF to describe TB anisotropy in 2D *in vivo* MR images of the calcaneus and noted its potential for distinguishing osteoporotic and healthy individuals [Rotter, Berg et al., 2001]. Unlike MIL and the previously mentioned techniques that require image segmentation via thresholding, the ACF method does not involve binarization. Alternatively, it relates the statistical probability of bone being located at specified distances away from a given bone voxel. This feature of the ACF makes it particularly useful when assessing TB structure on the basis of *in vivo* MR images.

For simplicity, the autocorrelation function will be denoted in one dimension as $\Phi(\Delta r)$ relative to a shifting variable Δr. Given a 1D intensity profile $S(r)$ obtained by sampling a real-valued image along a line, $\Phi(\Delta r)$ provides the probability, when starting in a trabecular element at $\Delta r = 0$, of finding bone at each Δr along the shifting direction. Mathematically, $\Phi(\Delta r)$ is the convolution of $S(r)$ with its complex conjugate $S^*(r)$. From the convolution theorem, $\Phi(\Delta r)$ can be expressed as the inverse Fourier

transform of the signal's power spectral density, $|S(k)|^2$ where k is the spatial frequency (Eq. 3-4). By considering a TB image composed of only bone and bone marrow as a quasi-periodic signal, the bone width and trabecular separation are estimated from $\Phi(\Delta r)$ as the full-width-at-half-maximum (FWHM) of the parent peak and the distance between the parent and secondary maxima ($\Delta r = d_1$), as shown in Figure 3.7. Since the presence of a secondary maximum depends on the degree of periodicity along a given orientation, d_1 may not be accurately quantified in all TB images and thus, is not a focus of this work as its ability to quantify orientation dependence is limited. However, d_1 is generally well-defined in the transverse plane of TB images, and thus can be measured reliably in concert with the FWHM.

Eq. 3-4 $$\Phi(\Delta r) = \int_{-\infty}^{\infty} S(r)S^*(r+\Delta r)dr = \int_{-\infty}^{\infty} |S(k)|^2 \exp(ik\Delta r)dk$$

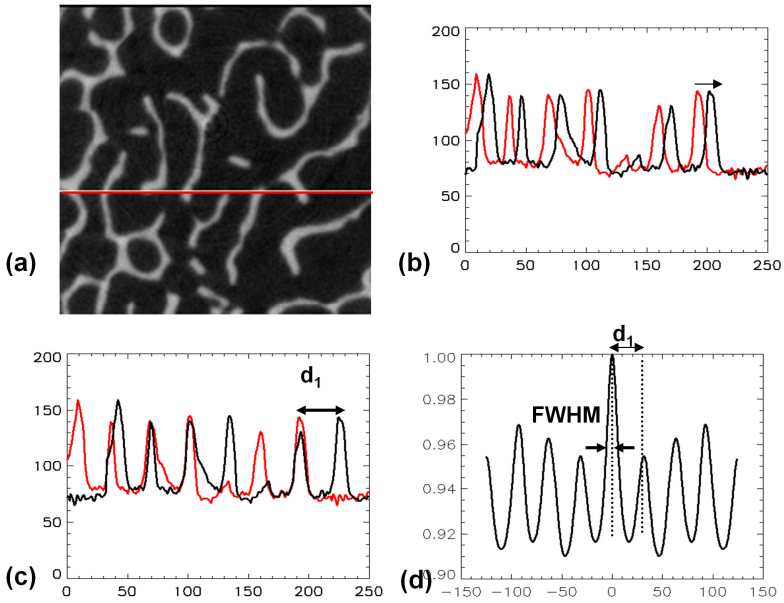

Figure 3.7 Auto-correlation function of an intensity profile $S(r)$ from a TB image: a) a µCT image with a (16µm)3 voxel size; b) intensity profile $S(r)$ (red) with its shifted counterpart $S(r+\Delta r)$ (black); c) maximum overlap occurs at $\Delta r = d_1$ resulting in a local maximum in (d); FWHM and d_1 of $\Phi(\Delta r)$ correspond to bone length and trabecular separation within $S(r)$.

In 3D, $\Phi(\Delta r)$ is defined relative to polar angles, i.e. $\Phi(\Delta r, \varphi, \theta)$, which is readily calculated by extending the integral of Eq. 3-4 to three dimensional space. The Rose plot of the FWHM measurement in 3D, denoted as $\mathrm{FWHM}(\varphi, \theta)$, is radially sampled from $\Phi(\Delta r = 0, \varphi, \theta)$ with respect to polar and azimuthal angles φ and θ. Using Eq. 3-2, the ACF-derived anisotropy tensor $\mathbf{A}$ (3x3 matrix reflecting FWHM measurements) can be computed, from which a fabric tensor $\mathbf{H}_{FWHM}$ is determined via Eq. 3-3. Similarly, eigenvalues $\lambda_1, \lambda_2, \lambda_3$ of $\mathbf{H}_{FWHM}$ reflect the concentration of FWHM relative to the three material directions denoted by eigenvectors $\hat{\mathbf{v}}_1, \hat{\mathbf{v}}_2, \hat{\mathbf{v}}_3$.

3.2.4 Important notation

In this work, a fabric tensor, denoted by $\mathbf{H}$, is estimated using MIL and ACF in rectilinear parallelepiped volumes containing only TB. The MIL and ACF associated fabric tensors are denoted as $\mathbf{H}_{MIL}$ and $\mathbf{H}_{FWHM}$. The usage of 'FWHM' instead of 'ACF' as the subscript was chosen to avoid confusion with the measurement of d_1 (also determined from $\Phi(\Delta r)$). Eigenvalues and eigenvectors of each fabric tensor are simplified into three parameters: structural anisotropy or SA and two metrics defining the direction of the principal fabric direction $\hat{\mathbf{v}}_3$. Structural anisotropy, denoted by SA_{MIL} and SA_{FWHM}, relates the ratio of largest to smallest eigenvalues (i.e. λ_3 / λ_1) for each method. The principal fabric direction $\hat{\mathbf{v}}_3$ is captured by $\Delta\theta_z$ and $[\delta x, \delta y]$ (see Figure 3.8). Angle $\Delta\theta_z$ is the angle between the image axis $\hat{\mathbf{z}}$ and $\hat{\mathbf{v}}_3$: $\Delta\theta_z = \cos^{-1}(\hat{\mathbf{v}}_3 \bullet \hat{\mathbf{z}})$. The position $[\delta x, \delta y]$ reflects the projection of $\hat{\mathbf{v}}_3$ into the transverse plane of the image ($\hat{\mathbf{x}}$-$\hat{\mathbf{y}}$ plane). Since $\hat{\mathbf{v}}_3$ is a unit vector, locations δx and δy lie within the unit circle on the $\hat{\mathbf{x}}$-$\hat{\mathbf{y}}$ plane. These two measures of orientation are designated relative to MIL and ACF as $\Delta\theta_{z,MIL}$, $\Delta\theta_{z,FWHM}$, $[\delta x, \delta y]_{MIL}$, and $[\delta x, \delta y]_{FWHM}$, respectively.

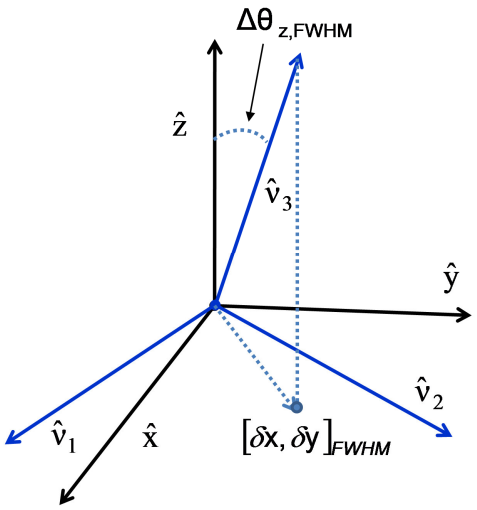

Figure 3.8 Metrics $\Delta\theta_{z,FWHM}$ and $[\delta x, \delta y]_{FWHM}$ are used to describe the principal material axis $\hat{\mathbf{v}}_3$ determined from $\mathbf{H}_{FWHM}$ relative to $\hat{\mathbf{x}}$, $\hat{\mathbf{y}}$, and $\hat{\mathbf{z}}$ image axes (i.e. the measurement coordinate system). Similar measures $\Delta\theta_{z,MIL}$ and $[\delta x, \delta y]_{MIL}$ are found relative to $\hat{\mathbf{v}}_3$ of $\mathbf{H}_{MIL}$.

3.3 Materials and methods

Experiments were designed in μCT and μMR images to quantitatively compare and investigate the performance of ACF and MIL in the presence of common limitations to *in vivo* μMRI of TB, namely, SNR, resolution, and RF coil inhomogeneity. Both methods were then applied to an *in vivo* MR image of the distal radius in order to examine the implications of normalizing the image via BVF-mapping. A discussion of the programming aspects of these two techniques concludes the section. The primary parameters of interest are structural anisotropy - SA_{FWHM} and SA_{MIL} - and principal material orientation (defined by $\Delta\theta_{z,FWHM}$ and $[\delta x, \delta y]_{FWHM}$ for ACF and $\Delta\theta_{z,MIL}$ and $[\delta x, \delta y]_{MIL}$ for MIL).

3.3.1 Comparison of ACF and MIL

As MIL serves as the standard approach for quantifying TB orientation, SA_{FWHM} was compared to SA_{MIL} in rectilinear parallelepiped subvolumes of TB from μCT and

μMR images. Thirty cadaveric distal tibia specimens of 25 mm in length in the axial direction were obtained from 15 donors (55-84 years of age, 4 females and 11 males) [Rajapakse, Magland et al., 2010]. At a collaborating research lab, each 25 mm cross-section was demarrowed using a water jet and the central 10mm section was imaged at a 25μm isotropic voxel on a Scanco μCT 80 [Liu, Zhang et al., 2010]. Specimens were then fixed in 1 mM aqueous Gd-DTPA/10% formalin solution (T_1 =300 ms) and centrifuged at 2000 rpms for 5 minutes to remove air bubbles and residual bone marrow. Each specimen was positioned within a two-channel phased-array ankle coil and imaged with the 3D fast large-angle spin echo (FLASE) pulse sequence [Magland, Wald et al., 2009] on a Siemens 1.5T Sonata scanner (see Chapter 2 for more details on FLASE sequence). A central 20 mm section from each specimen was acquired at a voxel size of 160x160x160 μm^3 using the following pulse sequence parameters: TE/TR/BW=11ms/80ms/32kHz, scan time=40 minutes.

Micro-CT images were manually thresholded so as to maintain bone as bright relative to marrow (Figure 3.9a-b). Micro-MR datasets were processed [Vasilic and Wehrli, 2005] to yield gray-scale bone volume fraction (BVF) images with pure bone and pure marrow corresponding to intensities of 100 and 0 (see Figure 3.9c-d), respectively (see Chapter 2 for details on BVF-mapping). Micro-MR images were registered to μCT images using the following steps: 1) image down-sampling of the μCT images to a voxel size of 150x150x150 μm^3, 2) *sinc* up-sampling of the BVF-mapped μMR images to a voxel size of 150x150x150 μm^3, and 3) full 3D registration using a collection of fits from 2D tiles of TB [Magland, Jones et al., 2009]. Trabecular bone subvolumes of 7.5x7.5x7.5mm^3 were extracted from the original binarized μCT (25 μm voxel dimension) and the registered BVF-mapped μMR images (150 μm voxel dimension). Each

7.5x7.5x7.5mm^3 subvolume was processed using ACF and MIL algorithms. SA_{FWHM} and SA_{MIL} were then compared in the μCT and μMR images and independently between the two modalities.

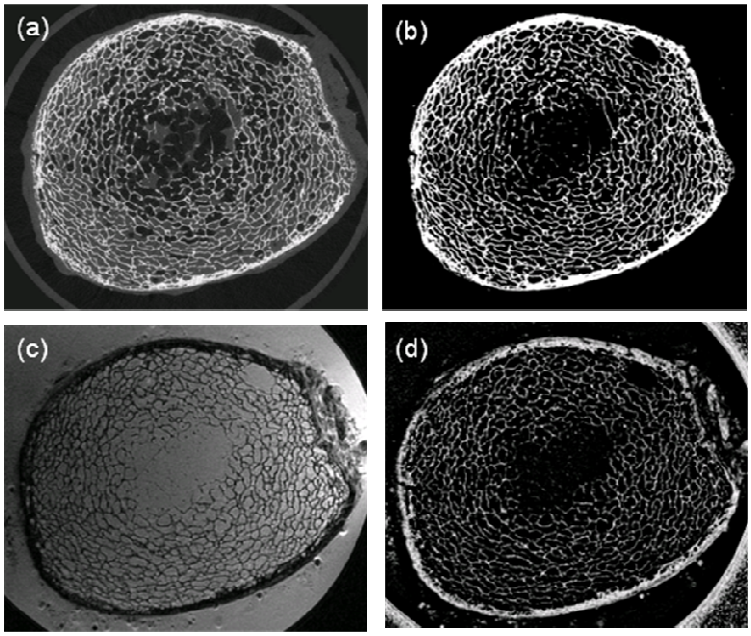

Figure 3.9 a) Original μCT image of a tibia specimen (25μm resolution); b) image in (a) after thresholding; c) original μMR image of a tibia specimen (150μm isotropic voxel size) in formalin mixture; and d) image in (c) after BVF-mapping.

An image rotation experiment was devised to test the techniques' relative ability to capture changes in TB orientation. Because TB of the distal tibia is known to be preferentially oriented along the skeletal axis, the rotation was chosen relative to a transverse axis (image x-axis). To prevent errors from image corners, a 7.5x7.5x7.5mm^3 volume of TB from a μCT dataset was converted to a spherical volume with a radius of 3.5mm. The spherical volume was then rotated by 15 degree increments in the counter clockwise (CCW) direction (Figure 3.10a-b) from 0 to 90 degrees around the x-axis of the image, resulting in seven datasets. Rotations were accomplished by inverse Fourier transform to k-space, applying the rotation to the k-space points using a *sinc*-regridding kernel, followed by Fourier transform back to image domain. ACF and MIL were applied

to each rotated dataset. $\Delta\theta_{z,FWHM}$ and $\Delta\theta_{z,MIL}$ were used to track changes in preferential direction. For MIL, the same threshold was employed for all rotated images.

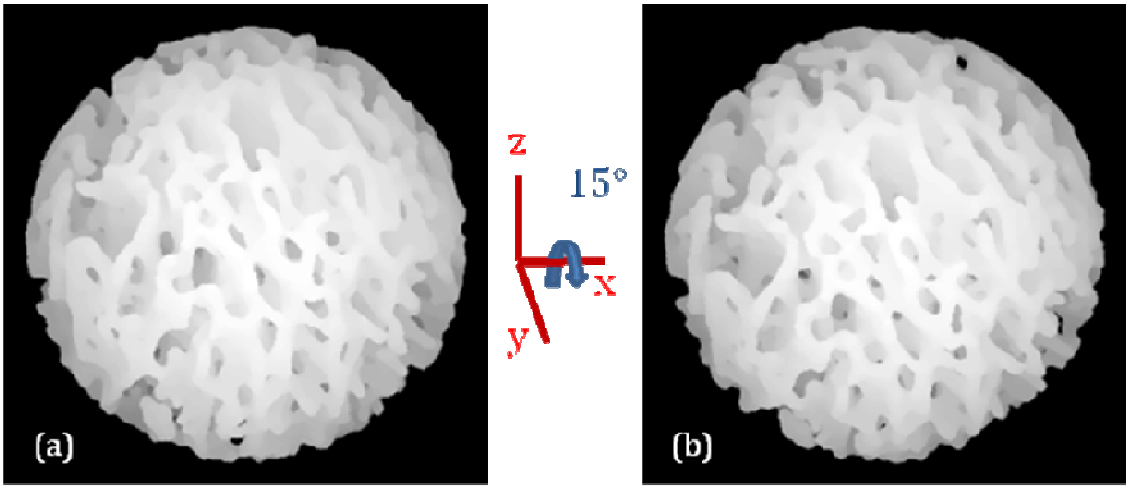

Figure 3.10 a) Spherical volume of TB (radius =3.5mm) from a µCT image of a tibia specimen (25µm resolution) used in the rotation experiment; b) volume after CCW rotation by 15° around x-axis (left-to -right direction). Subsequent 15° rotations created a set of 7 images rotated by 0° to 90°.

3.3.2 Performance evaluation

3.3.2.1 Computational speed

As image processing techniques designed to quantify TB fabric on the basis of high-resolution images, the relative speediness of MIL and ACF is important to consider. In this experiment, three byte-precision µCT images of TB with matrix sizes of 128^3 were analyzed with MIL and ACF using a $3°$ angular sampling step in both polar and azimuthal angles. The algorithms were run single-threaded on a 2.6 GHz AMD Opteron CPU. Details on the specific algorithms are provided in Section 3.3.4.

3.3.2.2 Resolution and SNR

To test the sensitivity of ACF and MIL to resolution and SNR, a 6.4x6.4x5mm^3 volume of TB was extracted from one of the μCT images to serve as a high-resolution (25 μm isotropic) and SNR (infinite) reference image. The binarized image was then inverted to MRI-type contrast (bone=0, marrow=150), resulting in the top-left image of Figure 3.11.

To investigate the implications of limited resolution (partial volume blurring) on structural anisotropy values and tensor orientations, the reference μCT image was down-sampled by varying degrees following MRI principles. The reference image was initially inverse Fourier transformed to the spatial frequency domain. A rectilinear window function centered at k-space center was then used to null the higher spatial frequencies (i.e. function had value of 1 inside and 0 outside). Upon Fourier transformation back to the image domain, a lower resolution image was created while maintaining a 25 μm voxel size and the original image grid. As the resolution in MRI is inversely proportional to the maximum sampled spatial frequency (i.e. $\Delta x = 1/k_{x,\max}$), by reducing the dimension of the rectilinear window by half (i.e. $k_{x,\max} \rightarrow k_{x,\max}/2$) and then Fourier transforming back to the image domain, the resulting image resolution would be doubled ($\Delta x \rightarrow 2\Delta x$). Accordingly, image resolutions ranging from the original resolution of 25 μm to 250 μm by increments of 25 μm (10 images in total) were created by varying the width of the window function. This process simulates acquiring an MR image at a given resolution and *sinc*-interpolating (zeropadding in k-space) the image to a 25 μm voxel size, a process regularly practiced during image processing to improve measurement precision. Ringing artifacts near trabecular edges stemming from the *sinc* point-spread function are evident in Figure 3.11.

Each of the 10 images (one original and nine down-sampled) was then subjected to the same SNR degradation process. MR noise was modeled through the addition of varying amplitudes of complex Gaussian distributed noise to k-space. When the real and imaginary components of k-space noise are normally distributed with equal variance, the resulting magnitude image demonstrates noise with a Rician probability density function (pdf) [Gudbjartsson and Patz, 1995]. The Rician pdf is given in Eq. 3-5 where A_0 is the magnitude of the real and complex amplitudes, σ is the variance of the complex noise, and $J_0(\ )$ is the zero-order Bessel function of the first kind.

Eq. 3-5 $$P(t) = \frac{t}{\sigma^2}\exp(-(t^2 + A_0{}^2)/2\sigma^2)J_0(\frac{A_0 t}{\sigma^2}), \quad t > 0.$$

As the amplitude of the complex noise increases, the Rician pdf approaches a Gaussian distribution. Similarly, as the variance increases, the noise in the magnitude image approximates a Rayleigh distribution.

By increasing the amplitude of the Gaussian noise in k-space, a collection of 10 magnitude images with increasing amounts of Rician noise was created. This procedure was applied to each of the 10 images of varying resolution, resulting in 10x10=100 test images (Figure 3.11). SNR was determined from the images as the mean marrow signal divided by the mean signal within a relatively thick trabecular element. Measurements of signal and noise were made at identical locations within each image. As both lowering the resolution and adding noise caused the measured SNR to reduce relative to the reference image, SNRs were different for each of the 100 images. The discrete values of the noise amplitudes were determined retrospectively such that the SNRs for the images at an isotropic voxel size of 150μm ranged from 3 to 20 - a SNR range achievable using *in vivo* MRI.

Each of the 100 images indicated in Figure 3.11 were subjected to BVF-mapping prior to calculating $\mathbf{H}_{MIL}$ and $\mathbf{H}_{FWHM}$. SA_{MIL} and SA_{FWHM} and orientation, defined by $[\delta x, \delta y]_{MIL}$ and $[\delta x, \delta y]_{FWHM}$, were computed for all 100 images. As BVF-mapping normalizes the image, a threshold value of 15% was used in the MIL calculation for all images.

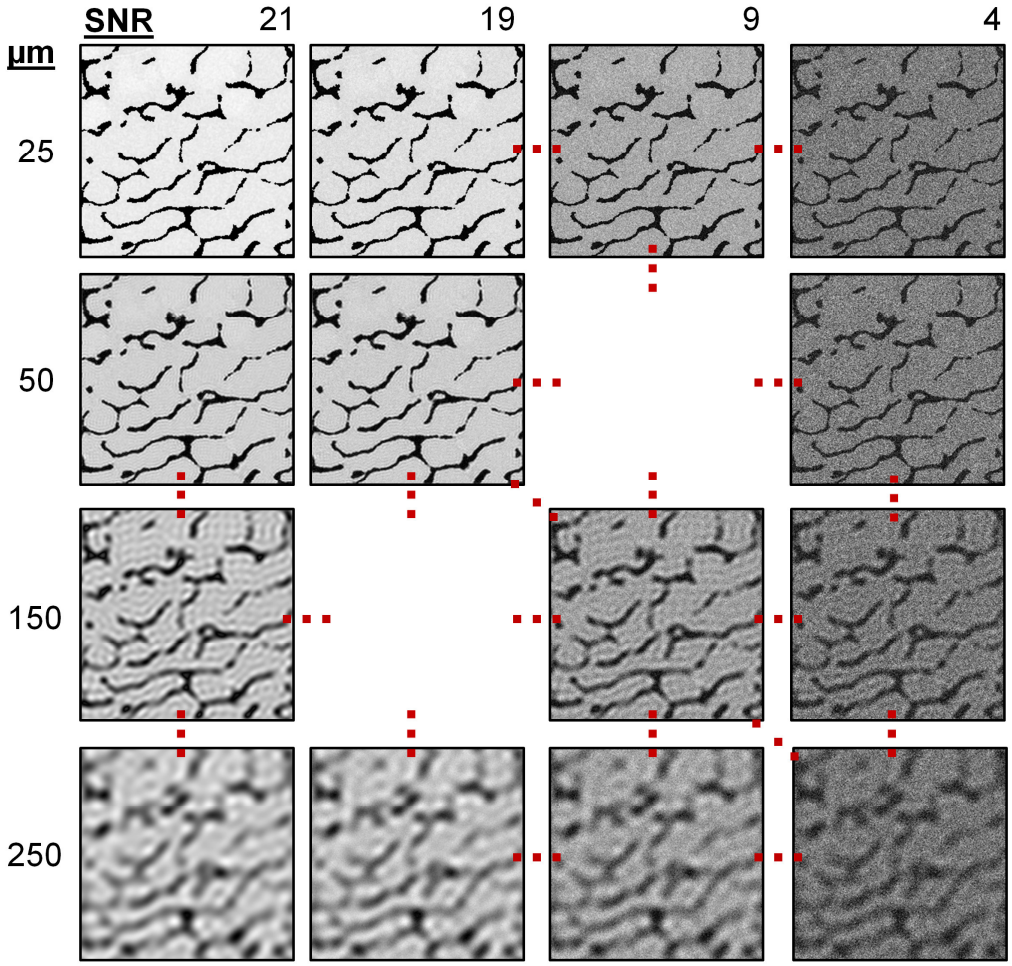

Figure 3.11 Test bed of images used for evaluating performance of ACF and MIL techniques relative to resolution (vertical direction) and SNR (horizontal direction). A 3D µCT image (top-left) was Fourier down-sampled to resolutions ranging from 25µm to 250µm by increments of 25µm (from top to bottom). Rician noise was added to each down-sampled image to create a series of images with lowering SNR (right-to-left direction). SNR measurements along the top row reflect mean marrow signal divided by mean bone signal for the set of images at 150µm resolution.

3.3.2.3 Anisotropic resolution

Since SNR scales with voxel volume, to obtain sufficient SNR, the slice resolution of *in vivo* TB images is often relaxed relative to the in-plane resolution. As TB generally aligns with the bone's longitudinal axis, the primary imaging plane is typically chosen perpendicular to this direction to limit the loss of structural information. Voxels typical of *in vivo* imaging have longitudinal dimensions three-times (or more) the in-plane dimension (e.g. 137x137x410 μm^3) [Wehrli, Saha et al., 2002]. The lower resolution along the $\hat{\mathbf{z}}$ axis limits the detection sensitivity of structural detail oriented perpendicular to this direction (e.g. transverse trabecular rods and longitudinal plate perforations). The effect of the augmented slice resolution on ACF and MIL measures was explored using the previously described µMR datasets of human distal tibia specimens.

Each of the 30 specimen images (voxel size of $(160\ \mu m)^3$) was down-sampled along the longitudinal direction (k-space down-sampled as described in 3.3.2) to produce 30 datasets with an effective resolution of 160x160x480 μm^3. After BVF-mapping all images, 8x8x8 mm^3 subvolumes of TB centrally located in each tibia cross section were cropped from isotropic and down-sampled datasets at identical locations. The cubic volumes of TB were then processed using ACF and MIL to assess the differences in SA and orientation associated with the augmented slice resolution.

3.3.2.4 RF Coil Inhomogeneity

Surface receiver coils give rise to inhomogeneous reception profiles resulting in "image shading" effects. In longitudinal studies, inconsistencies in the receiver coil performance and/or in the operator's placement of the coil relative to the anatomy of interest can cause different reception profiles across multiple time points. The severity

of the coil-induced image shading increases as the size of the receiver elements decrease [Wang, Reykowski et al., 1995]. Intensity variations due to RF coil inhomogeneity can be seen from the top-right to bottom-left of the MR image in Figure 3.12a. As SNR is a function of position, image shading can cause variations in derived TB structural measures. In this experiment, the impact of coil shading on the measured fabric tensors $\mathbf{H}_{MIL}$ and $\mathbf{H}_{FWHM}$ was explored.

The effect of coil inhomogeneity on derived fabric tensors $\mathbf{H}_{MIL}$ and $\mathbf{H}_{FWHM}$ was assessed using *in vivo* μMR images of TB. The analysis was performed in images of the distal tibia from three healthy female subjects, aged 24-30 years. The data was previously acquired on a 1.5T MR scanner (General Electric Signa) as part of a reproducibility study [Gomberg, Wehrli et al., 2004] using the FLASE sequence (TE/TR/BW=10.5ms/80ms/66 kHz) at a voxel size of 137x137x410 μm^3 covering a 13mm slab in 15 minutes [Ma, Wehrli et al., 1996]. Information on the pulse sequence can be found in Chapter 2.

As marrow is bright in FLASE images, the marrow signal intensity carries the RF coil shading. To capture the spatial variation of the signal without being sensitive to regions of dense TB (regions of low signal due to thick or numerous trabecular elements), the upper 20^{th} percentile intensity over a spherical region was chosen to reflect the marrow component. Prior to this computation, the TB region within each image was manually masked to exclude surrounding soft tissue and cortical bone (Figure 3.12b). Then, the RF coil inhomogeneity for each voxel within the masked region was computed as the 20th percentile intensity from the distribution of signal intensities within a spherical neighborhood (radius=10 pixels) (Figure 3.12c).

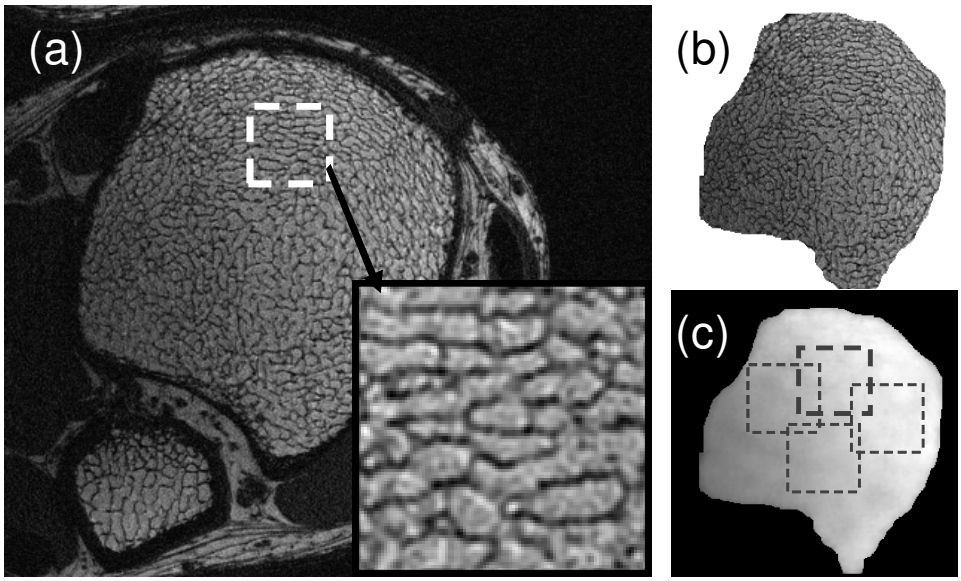

Figure 3.12 a) Axial FLASE image of distal tibia (137x137x410 μm^3 voxel size) used in coil inhomogeneity analysis. Left to right corresponds to antero-posterior direction. Zoom-in indicates region of VOI_C. b) Manually masked region of TB within the cortical shell used to calculate the coil inhomogeneity map; c) computed inhomogeneity map (see text) where the dark box indicates the location of VOI_C and the fainter boxes mark locations of the three regions of signal inhomogeneity applied to VOI_C.

Coil inhomogeneity maps were computed for the three subjects, one of which is shown in Figure 3.12c. Within each masked region a rectilinear parallelepiped subvolume was manually selected. In this experiment, subvolumes of TB will be denoted by volume-of-interest or VOI. VOIs were 50x50xN voxels^3 where N indicates the variable number of slices (up to 32) with sufficient SNR within a given scan/subject. Pixel intensities in this VOI were divided by the corresponding values from the RF coil inhomogeneity map, resulting in an intensity-corrected VOI, denoted VOI_C. RF coil inhomogeneity maps from three different regions (dotted boxes in Figure 3.12c) were then applied to VOI_C. Thus, five VOIs for each subject were examined with both ACF and MIL; the original VOI_0, the corrected dataset VOI_C, and VOI_1, VOI_2, and VOI_3 (i.e. VOI_c with three separate coil inhomogeneity estimates applied). The variations in

SA_{FWHM}, SA_{MIL}, $\Delta\theta_{z,FWHM}$, and $\Delta\theta_{z,MIL}$ due to different regions of the coil inhomogeneity map were estimated for each subject as the mean percentage difference relative to values from the intensity-corrected region VOI_C.

3.3.3 Preprocessing

Prior to applying certain quantification techniques to *in vivo* images, it is common to first preprocess the images into a standardized form. As demonstrated by the histograms in Figure 3.2a-b, µCT images of TB can be segmented using a threshold, while µMR images require a more sophisticated approach. In the tibia specimen and *in vivo* MR images used in the coil inhomogeneity experiment, it was necessary to invert the images into a BVF-map (bone-bright, marrow-dark) prior to ACF and MIL analyses. Yet, by performing this preprocessing step, the results of the ACF and MIL techniques also reflect errors in the BVF-mapping procedure. A possible source of error in BVF-mapping is the partial-thresholding of the marrow signal [Vasilic and Wehrli, 2005]. Alternatively, the images can be gray-scale inverted (GSI) by simply subtracting the image intensities of each from the maximum image intensity. To determine how these two preprocessing steps affect the results of ACF and MIL, an *in vivo* image of the human distal radius was analyzed using ACF and MIL with and without BVF-mapping.

The µMR image used to consider the impact of BVF-mapping is shown in Figure 3.13a. The image was acquired as part of an on-going reproducibility study. Using a transmit/receive birdcage wrist coil with the FLASE pulse sequence on a Siemens Sonata 1.5T MR scanner, the image was acquired in 10 minutes using a 137x137x410 μm^3 voxel size over a 13mm slab. Motion correction was performed using the auto-focusing procedure discussed in Chapter 2 [Lin, Ladinsky et al., 2007].

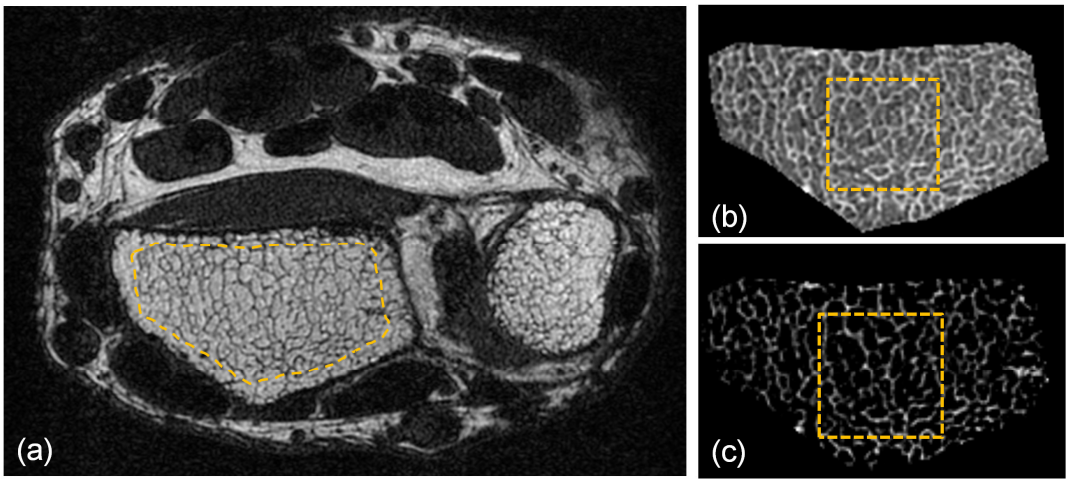

Figure 3.13 a) Axial FLASE image of a wrist (137x137x410 μm^3 voxel size) acquired at 1.5T used to consider effects of BVF-mapping. Highlighted region of TB within the radius was cropped prior to being gray-scale inverted (b) or BVF-mapped (c). Rectilinear parallelepiped subvolumes indicated in (b) and (c) were analyzed using ACF and MIL.

Prior to application of ACF and MIL, the image in Figure 3.13a was first up-sampled by a factor of 3 (zero-padding in k-space) in the slice direction to create a dataset with a 137 μm isotropic voxel size. The cortical shell and surrounding soft tissue was then removed, leaving only the TB region. The image was gray-scale inverted (GSI) using the maximum signal intensity within the TB region (Figure 3.13b). Alternatively, the same TB region was subjected to BVF-mapping through a local-thresholding technique [Vasilic and Wehrli, 2005] designed for images with resolutions on the order of the TB thickness (~100-200 μm). The resulting BVF-map (Figure 3.13c) has a range of 0 to 100 where 0 represents marrow and 100 represents pure bone. Rectilinear parallelepiped volumes of TB, extracted from the same location within the GSI and BVF-mapped images, were analyzed using ACF and MIL.

3.3.4 ACF and MIL implementations

MIL algorithms are rarely reported in the literature, but it is clear that variations in the MIL algorithm exist. Slight modifications were made to optimize the MIL method described in Section 3.2.2. Since the TB volumes are rectilinear parallelepiped, the estimate of intercept lengths close to image corners is error-prone, especially for angles close to 45° relative to one of the image axes. A strategy to prevent such errors is to use a circular or spherical support [Cheal, Snyder et al., 1987; Goulet, Goldstein et al., 1994], similar to that used for the rotation experiment (Figure 3.10). A problem with this approach is that the analysis volume is restricted to spherical volumes, which are not conducive to mechanical assessment, whether performed on the bench or by computer simulation. To rectify the issue occurring close to the corners of the rectilinear parallelepiped subvolumes, instead of using Eq. 3-1, the mean-intercept-length was calculated as the mean distance between consecutive bone segments along each sample line (see 2D example in Figure 3.14). By detecting the distance from the center of one bone crossing to the next, an integer number of intercept lengths are averaged. This approach removes the sample line length L from the calculation and reduces errors associated with the image boundary.

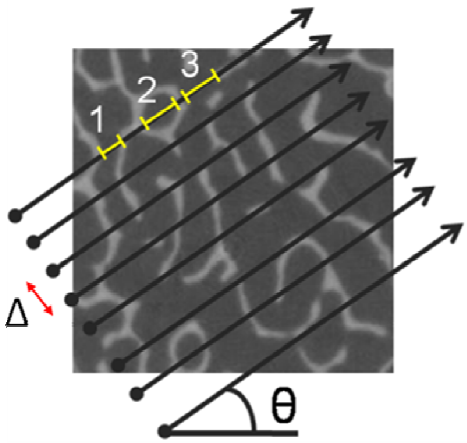

Figure 3.14 MIL implementation only considers the lengths of intercepts (1, 2, and 3) defined by a bone exit point and a bone entry point. This approach prevents errors near image boundaries. The sampling procedure is accelerated by controlling the sample line density by sample line separation Δ.

Besides capturing different features of TB, there were differences between ACF and MIL sampling schemes. In the ACF approach, by computing $\Phi(\Delta\mathbf{r})$ in the first step via the three dimensional extension of Eq. 3-4, only a single linear interpolation, originating from the center of shift space $\Delta\mathbf{r}$, is necessary for each sample direction. In MIL, the sampling lines originate from real-valued points within a plane located outside the image volume, the plane being perpendicular to the sampling direction. The plane contains $3N^2$ points where N is the dimension of the cubic image volume. Since each point in the plane is defined relative to $\Re^3$, every sampling profile must be calculated independently. Thus, the MIL algorithm involves a considerably larger number of operations per sampling direction. To accelerate the MIL calculation, the distance between parallel sampling lines, Δ (see Figure 3.14), was allowed to vary (from one to six pixels) depending on the experiment. For example, if Δ=3 pixels, there would be one sample line for every 3x3 block of points within the originating plane.

Different interpolation techniques were utilized to sample the image intensity in the two methods. A tri-linear interpolation procedure involving the eight nearest-neighboring voxels [Lehmann, Gonner et al., 1999] was used to generate intensity profiles through the center of $\Phi(\Delta\mathbf{r})$. This interpolation procedure samples $\Phi(\Delta\mathbf{r})$ at fixed increments of the smallest voxel/pixel dimension. It is important to note that the tri-linear interpolation scheme used in ACF is applied in the shift space $\Delta\mathbf{r}$ where $\Phi(\Delta\mathbf{r})$ is a real-valued function. This style of sampling was termed 'dense sampling' by Ketcham et al. who identified it as being more accurate than 'graphics' sampling where the sampling increment is at least one pixel length in the fastest changing direction [Ketcham and Ryan, 2004].

As the MIL approach operates on a binary dataset, a more direct sampling scheme, in which intravoxel distances are considered, was used in the MIL algorithm. Instead of performing gray-scale interpolation, the boundaries of each voxel (or pixel in 2D), rather than fixed increments, served as distance markers. To illustrate the difference between the tri-linear interpolation procedure used in ACF and the direct sampling used in MIL, each method is used to calculate the length of a sample line laying within bone in Figure 3.15. The direct sampling approach was used as it permits more accurate measurements of Euclidean lengths within a binary dataset. The accuracy of the direct sampling scheme is most important in low resolution images of TB where interpolation errors are on the order of the structure/pixel size.

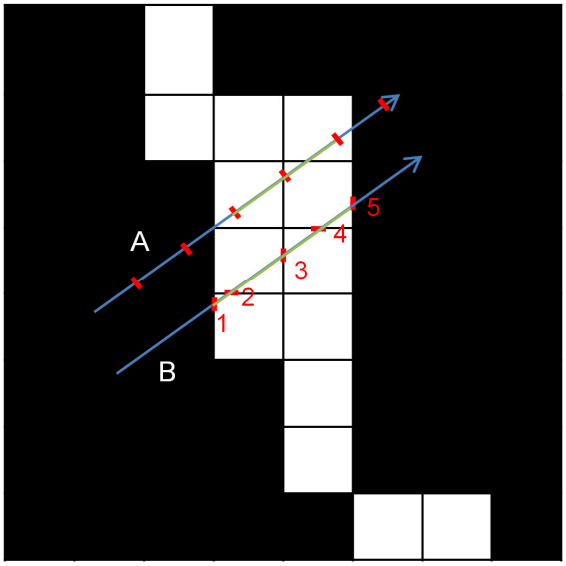

Figure 3.15 Sampling bone length at a 40° angle (relative to the horizontal axis) in a binarized image of a trabecular element with coarse pixel size. In example A, linear interpolation is performed at fixed increments along the sample line resulting in an underestimated length of 2 pixels (green segment of blue sample line). In example B, the pixel boundaries are identified. By summing the distances between pixel boundaries (i.e. 1to2+2to3+3to4+4to5), the true length within bone of 2/cos(40°)=2.6 is found.

Unlike the differences in image intensity sampling, the same procedure was used for ACF and MIL to define the angular samples. To ensure SA was representative of only the structure, uniform angular sampling was employed. Uniform sampling of the sphere was implemented by making the azimuthal angle step $\Delta\theta$ scale as a function of

φ_i: $\Delta\theta = \Delta\varphi / \sin(\varphi_i)$. For example, if the desired angular resolution is $\Delta\varphi = 15°$, a ring of 12 points at $\varphi_i = 30°$ are spaced by $\Delta\theta = 30°$. This approach creates a directional bias when the number of sampling directions is small (<12), but the error is negligible at higher angular resolutions. Other methods for uniform spherical sampling have been demonstrated, such as triangulation of the spherical surface [Ketcham and Ryan, 2004], and the low energy arrangement of point charges (under Coulomb's forces) restrained to the sphere's surface [Erber and Hockney, 1991].

Figure 3.16a-c shows projections on the faces of a cube of a µCT dataset of TB and the corresponding Rose plots, $\mathrm{FWHM}(\varphi,\theta)$ and $\mathrm{MIL}(\varphi,\theta)$, using an input angular spacing of $\Delta\varphi = 15°$. For repeated measures (e.g. resolution, SNR, and rotation experiments), $\Delta\varphi$=10° for both ACF and MIL techniques and Δ=3 pixels. For comparison of *ex vivo* and *in vivo* images, a smaller sampling step of $\Delta\theta$=3º was chosen with a Δ of 1 pixel.

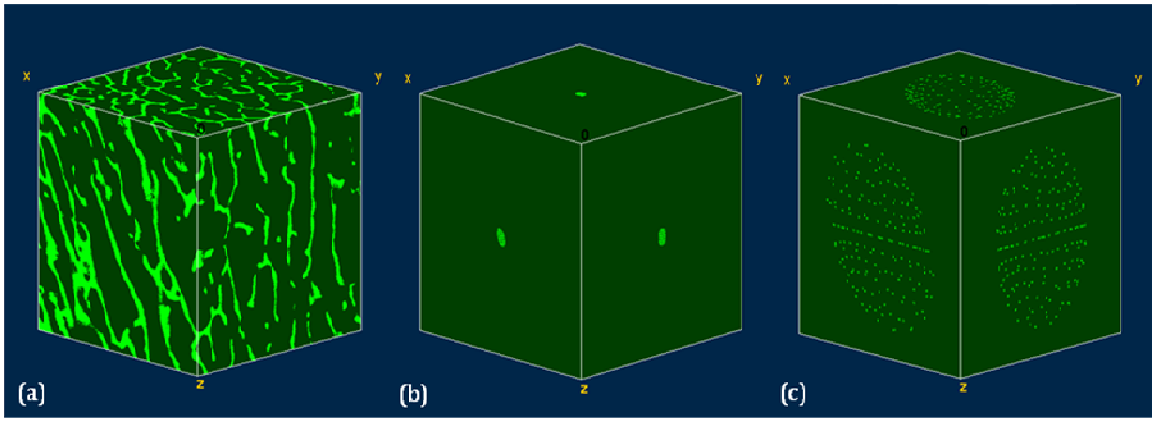

Figure 3.16 a) Three orthogonal faces of a (7.5mm)^3 subvolume of TB from a high-resolution (25 µm) µCT image; Projections of $\mathrm{FWHM}(\theta,\varphi)$ (b) and $\mathrm{MIL}(\theta,\varphi)$ (c) measured in (a) using $\Delta\varphi = 15°$ onto orthogonal faces of box illustrating ellipsoidal distributions.

Fabric tensors $\mathbf{H}_{MIL}$ and $\mathbf{H}_{FWHM}$ were computed following Eq. 3-2 and Eq. 3-3 with respect to the Rose plot data. Eigenvalues $\lambda_1, \lambda_2, \lambda_3$ and eigenvectors $\hat{\mathbf{v}}_1, \hat{\mathbf{v}}_2, \hat{\mathbf{v}}_3$ were computed using singular value decomposition of $\mathbf{H}_{MIL}$ and $\mathbf{H}_{FWHM}$. Ellipsoidal representations of $\mathbf{H}_{MIL}$ and $\mathbf{H}_{FWHM}$ were formulated with radii proportional to normalized eigenvalues (e.g. $\hat{\lambda}_1 = \lambda_1 / (\lambda_1 + \lambda_2 + \lambda_3)$).

The MIL and ACF techniques were implemented in the C programming language. A combination of IDL (Research Systems Inc., Boulder, Colorado) and MATLAB (The Mathworks, Natick, MA) was used for image processing functions such as Fourier transform and random number generation in order to create images with various resolutions and SNRs. Graphical representations and statistical analyses were performed using Microsoft Excel (Microsoft Corp, Seattle, WA), Mathematica (Wolfram Research, Inc., Champaign, IL), and JMP-IN (SAS Institute Inc., Cary, NC).

3.4 Results and discussion

Due to the number of experiments performed in the methods section, the results and discussion of each experiment will be combined to prevent the reader from having to jump back and forth.

3.4.1 Comparing ACF and MIL

Fabric tensors $\mathbf{H}_{MIL}$ and $\mathbf{H}_{FWHM}$ offered complementary information on SA and orientation and were capable of tracking image rotations with high accuracy. Figure 3.17 shows the relationship between $\mathrm{SA}_{\mathrm{FWHM}}$ and $\mathrm{SA}_{\mathrm{MIL}}$ in the μCT and μMR images. With $\mathrm{SA}_{\mathrm{FWHM}}$ as the independent variable, positive correlations with slopes (m) less than

one were found relative to SA_{MIL} in both sets of images. Better agreement between MIL and ACF was found in the μMR datasets: m=0.75, R^2=0.82 versus m=0.59, R^2=0.68 in μCT. SA_{FWHM} was generally higher than, yet well correlated with SA_{MIL} within μCT and μMR datasets (Figure 3.17a-b). Values of $\Delta\theta_{z,FWHM}$ and $\Delta\theta_{z,MIL}$ showed close alignment with the $\hat{\mathbf{z}}$ axis: 6.3±3.1° and 7.8±3.7° in the μMR datasets versus 6.5±3.0° and 6.2±2.9° in the μCT images. Although not shown, $\Delta\theta_{z,FWHM}$ and $\Delta\theta_{z,MIL}$ were significantly correlated in μMRI (R^2=0.5) and μCT (R^2=0.75) datasets.

Independently, SA_{MIL} and SA_{FWHM} showed good agreement across the two imaging modalities: SA_{MIL} (R^2=0.72) and SA_{FWHM} (R^2=0.71) (Figure 3.17c-d). Both techniques considered the TB to be more structurally anisotropic on the basis of the μCT images with mean increases of 0.26 ($p<0.0001$) for SA_{MIL} and 0.44 ($p<0.0001$) for SA_{FWHM}. In addition, significant correlations in principal orientation existed between the two modalities: R^2=0.77 ($\Delta\theta_{z,FWHM}$) and R^2=0.78 ($\Delta\theta_{z,MIL}$). This data suggests the ACF and MIL techniques are capable of estimating μCT-derived values of SA and $\Delta\theta_z$ on the basis of lower resolution μMRI.

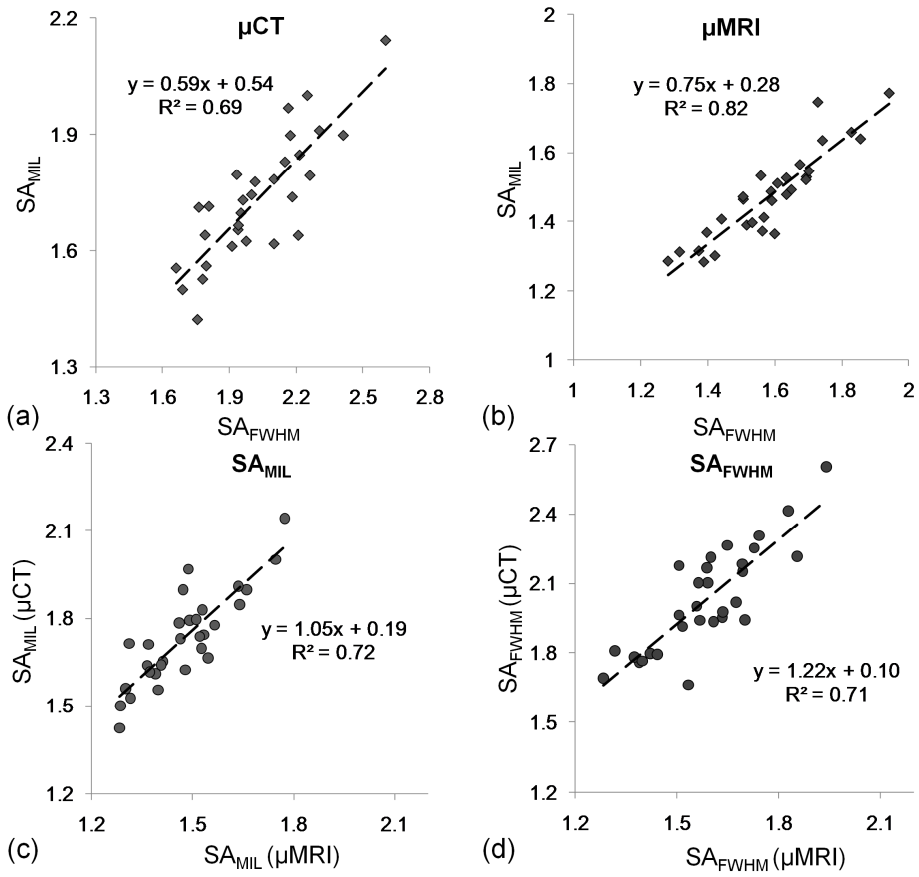

Figure 3.17 Comparisons of SA_{FWHM} and SA_{MIL} within TB subvolumes from thirty µCT images with 25 µm isotropic voxel (a) and thirty µMR images with 150 isotropic voxel (b). Cross modality correlations of SA_{MIL} (c) and SA_{FWHM} (d).

Results from the rotation experiment are summarized in Figure 3.18a-b where $\Delta\theta_{z,FWHM}$ =4.33° and $\Delta\theta_{z,MIL}$ =4.67° in the non-rotated dataset. ACF and MIL detected the applied image rotations with high accuracy (slopes close to unity and R^2s=0.99). On the basis of this experiment, the two methods can be considered equally capable of tracking changes in TB orientation.

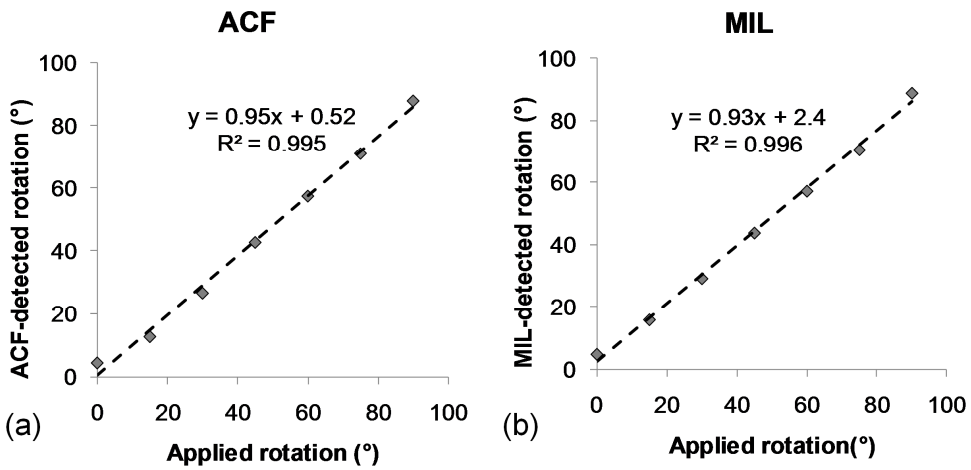

Figure 3.18 Detection of applied rotations (around x-axis) by ACF (a) and MIL (b) techniques in a spherical volume of TB from a 25µm µCT image.

This work represents the first comparison between the ACF and MIL approaches within images of TB. It is not surprising that the parameters reflective of fabric tensors $\mathbf{H}_{MIL}$ and $\mathbf{H}_{FWHM}$ do not agree as the two methods assess different features of the TB network. It should be recognized that no ground truth exists for these metrics. However, it is clear from the experiments that $\mathrm{SA}_{\mathrm{FWHM}}$ varies similarly with, yet overestimates $\mathrm{SA}_{\mathrm{MIL}}$. Lower values of $\mathrm{SA}_{\mathrm{MIL}}$ relative to other techniques, i.e. SVD and LFD, have been reported in the literature [Ketcham and Ryan, 2004; Geraets, van Ruijven et al., 2006].

3.4.2 Performance results

3.4.2.1 Computational speed

In testing MIL's speed relative to ACF in three µCT specimens (matrix size=128^3), for a Δ of 2, MIL took approximately 6000±21 seconds per image. Using a Δ of 3, the average duration of MIL was reduced to 3130±9 seconds. ACF was

considerably faster with a speed of 102±1 seconds per image. This equated to ACF being 60-fold and 30-fold faster, respectively, relative to MIL with a Δ of 2 or 3. The increased speed of the ACF method is a consequence of the implementation using the fast- Fourier transform [Cooley and Tukey, 1965] and that only one interpolation is necessary for each direction. Conversely, MIL involves $(N/\Delta)^2$ interpolations for each direction. Further speed enhancement could be afforded in ACF as the FWHM is measured relative to only a small region close to Δr=0.

3.4.2.2 Resolution and signal-to-noise

The performances of ACF and MIL relative to resolution and SNR are shown in the plots of Figure 3.19a-f. The effect of SNR at high-resolution (25 μm) corresponds with the left wall of each plot while the effect of lowering resolution at high SNR is reflected on the right wall of each plot. The range of $\mathrm{SA}_{\mathrm{FWHM}}$ and $\mathrm{SA}_{\mathrm{MIL}}$ is from 1 to 2.25 such that 1 represents a complete loss of structural sensitivity (i.e. SA=1 for pure Gaussian noise or extreme levels of partial volume blurring). $\mathrm{SA}_{\mathrm{FWHM}}$ was insensitive to SNR above a relative value of 6, with a dramatic drop-off for SNRs below 5. $\mathrm{SA}_{\mathrm{MIL}}$ declined linearly with SNR to an SNR of 5, after which it began to behave non-linearly. $\mathrm{SA}_{\mathrm{FWHM}}$ and $\mathrm{SA}_{\mathrm{MIL}}$ showed marked increases around a resolution of 75 μm, followed by a decrease between resolutions of 100 μm and 250 μm. However, the increase and decrease in $\mathrm{SA}_{\mathrm{FWHM}}$ appears linear while that of $\mathrm{SA}_{\mathrm{MIL}}$ appears non-linear. The effects of resolution and SNR on the MIL- and ACF-defined principal material orientations, denoted by the projection of the principal material direction $\mathbf{v}_3$ into the x-y plane (i.e. $[\delta x, \delta y]_{MIL}$ and $[\delta x, \delta y]_{FWHM}$), are shown in Figure 3.19c-f.

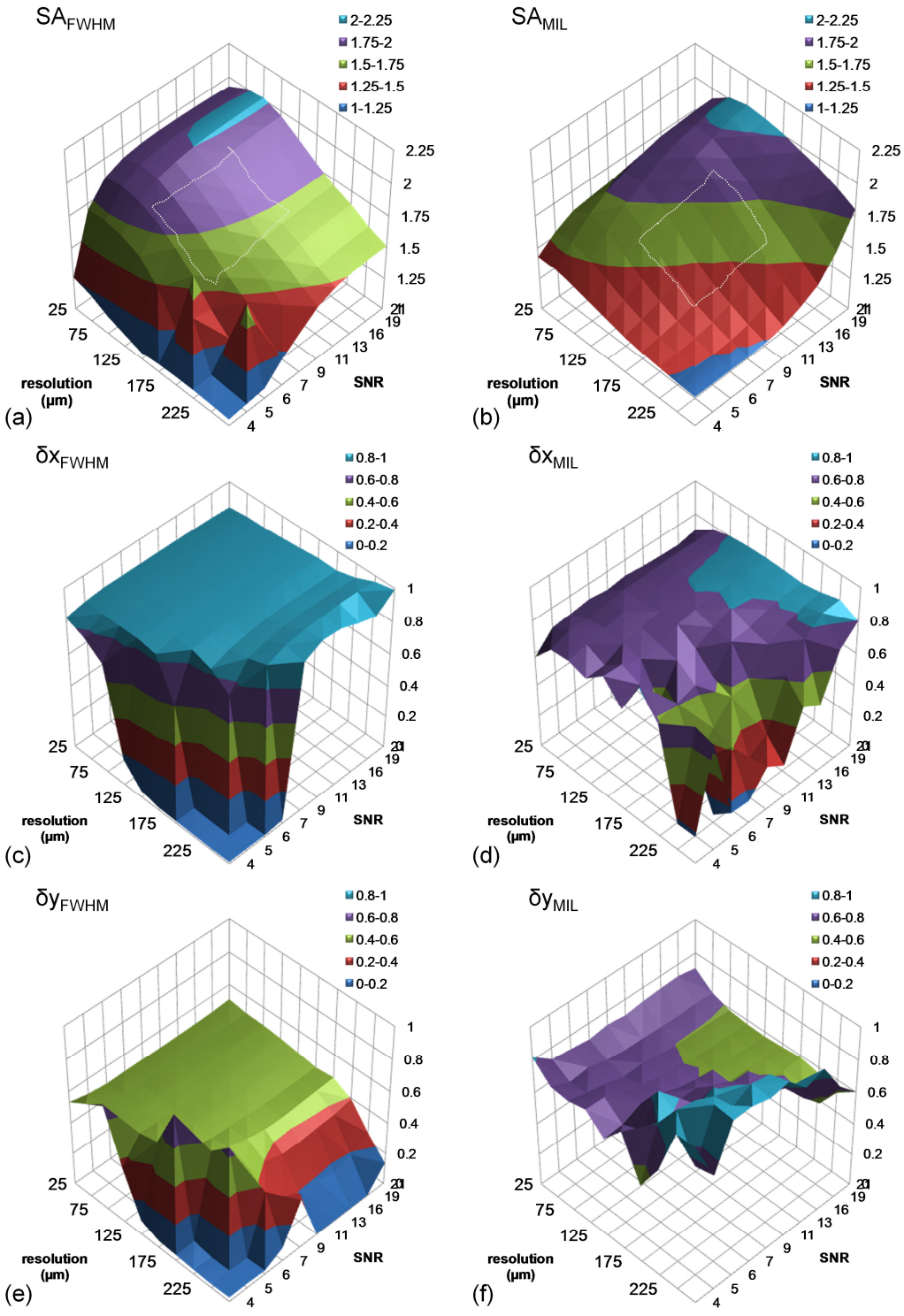
SA_FWHM
2-2.25
1.75-2
1.5-1.75
1.25-1.5
1-1.25
2.25
2
1.75
1.5
1.25
25
75
125
175
225
resolution (μm)
4
5
6
7
9
11
13
16
19
21
SNR
(a)
SA_MIL
(b)
δx_FWHM
0.8-1
0.6-0.8
0.4-0.6
0.2-0.4
0-0.2
1
0.8
0.6
0.4
0.2
(c)
δx_MIL
(d)
δy_FWHM
(e)
δy_MIL
(f)

Figure 3.19 Performance plots for $\mathrm{SA}_{\mathrm{FWHM}}$ (a), $\mathrm{SA}_{\mathrm{MIL}}$ (b), δx_{FWHM} (c), δx_{MIL} (d), δy_{FWHM} (e), and δy_{MIL} (f) relative to resolution (25-250 µm resolution) and SNR (21-4 for image set with a 150 µm isotropic resolution). 4x4 region (white trace) indicated in (a) and (b) represents the regime of resolution and SNR most reflective of *in vivo* µMR imaging.

The sensitivity of ACF and MIL to resolution and SNR on the basis of the performance plots of Figure 3.19a-f was assessed for each measure using partial derivatives relative to resolution $\left(\frac{\partial}{\partial res}\right)$ and SNR $\left(\frac{\partial}{\partial SNR}\right)$. A 4x4 region (see Figure 3.19a-b) was identified as the regime of resolution and SNR most reflective of *in vivo* µMR imaging: isotropic resolutions of 100 µm to 175 µm and SNRs ranging between 13 and 7. The average values of the partial derivatives over the 4x4 "*in vivo*" regime are provided in Table 3.1. $\mathrm{SA}_{\mathrm{MIL}}$ and $\mathrm{SA}_{\mathrm{FWHM}}$ decreased with decreasing SNR and increasing resolution. The variation relative to SNR was greater than that of resolution. All ACF-based measures ($\mathrm{SA}_{\mathrm{FWHM}}$ and $[\delta x, \delta y]_{FWHM}$) were less sensitive to variations in SNR and resolution than MIL-derived measures ($\mathrm{SA}_{\mathrm{MIL}}$ and $[\delta x, \delta y]_{MIL}$). Thus, ACF and MIL were influenced more by SNR than resolution and $\mathbf{H}_{MIL}$ was more sensitive to resolution and SNR than $\mathbf{H}_{FWHM}$.

Table 3.1 Average partial derivatives of MIL and ACF measures relative to SNR and resolution evaluated in 4x4 "*in vivo*" regime.

Table 3.1

(x10^{-3})	$\frac{dSA}{dSNR}$	$\frac{d\delta x}{dSNR}$	$\frac{d\delta y}{dSNR}$	$\frac{dSA}{dres}$	$\frac{d\delta x}{dres}$	$\frac{d\delta y}{dres}$
MIL	47±11	-17±12	-15±14	-3.8±1	1.4±1.3	1.5±1.5
ACF	22±19	-5±7	-3±5	-3.4±0.5	-0.6±0.5	-0.3±0.2

A better understanding of the effects of SNR and resolution on the two measurement techniques is offered through one dimensional examples. The effect of lowering SNR from 8 to 5 for an intensity profile from a μCT image is illustrated in Figure 3.20. At an SNR of 8 the number of bone marrow intercepts is accurately quantified by thresholding (Figure 3.20b), yet when the SNR is 5, erroneous bone crossings are detected (Figure 3.20e), resulting in twice the number of intercepts and a reduced mean-intercept-length. More bone crossings will be detected along other directions, however the number of crossings will have to approximately double in all directions for $\mathrm{SA}_{\mathrm{MIL}}$ to remain constant. The fewest number of intercepts occurs along the preferential direction of TB. Noise-induced bone crossings with sampling lines oriented in this direction will dramatically lower the MIL values while the MIL values measured relative to the transverse plane will be less influenced. Thus, $\mathrm{SA}_{\mathrm{MIL}}$ decreases with decreasing SNR. Alternatively, ACF influenced by SNR since the correlation length of pure white noise is a delta function at zero displacement. The increased noise contribution is manifested as a sharper parent peak ($\Delta\mathbf{r} = 0$), which causes a decrease in the calculated FWHM (Figure 3.20c and f). As the noise is spatially uncorrelated, this sharper parent peak is uniform relative to direction and consequently, $\mathrm{SA}_{\mathrm{FWHM}}$ remains relatively stable with respect to varying SNR.

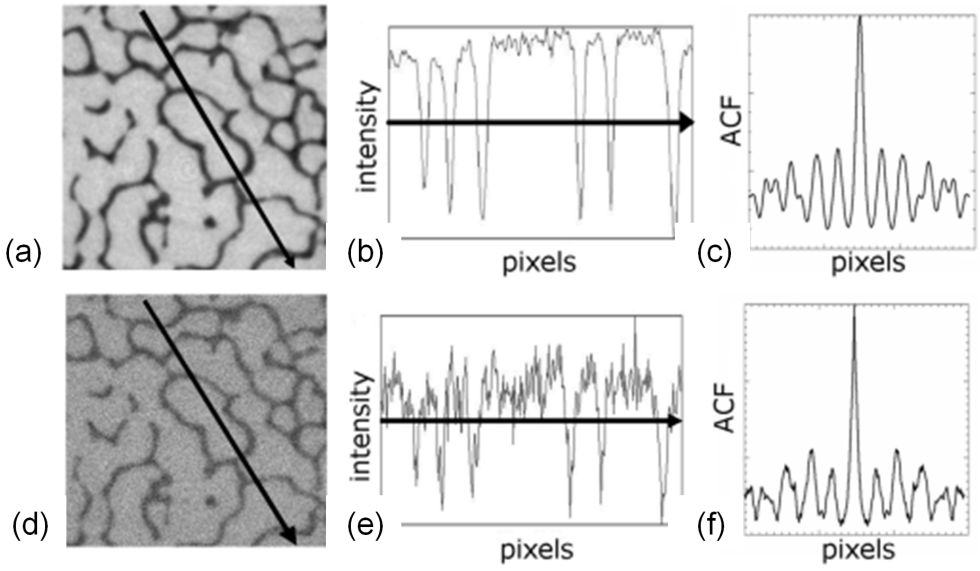

Figure 3.20 Effect of lowering SNR on MIL and ACF in a 1D example. a) inverted µCT image of a TB specimen from human a distal radius (SNR=8); b) intensity profile indicated in (a) with a MIL of 820µm (5 intercepts from 6 bone crossings); c) $\Phi(\Delta r)$ of profile in (b) with a FWHM of 155 µm; d) µCT image with lower SNR of 5; e) profile from (d) with MIL of 405 µm using the same THR (10 intercepts from 11 bone crossings); f) $\Phi(\Delta r)$ of profile (e) with a FWHM of 142 µm.

The effects of partial volume blurring on FWHM and MIL are shown in Figure 3.21. As the effective resolution decreases, the bone/bone marrow interfaces become increasingly indistinct. If significant partial volume blurring occurs, bone intercepts may fall below the user-defined threshold (Figure 3.21e), resulting in fewer intercepts. The FWHM of $\Phi(\Delta r)$ appears to increase between Figure 3.21c and Figure 3.21f. As in the case of SNR, this increase occurs monotonically and uniformly with decreasing resolution for all orientations. Therefore, $\mathrm{SA}_{\mathrm{FWHM}}$ is less influenced by the lowering resolution, although, as Figure 3.19 suggests, some sensitivity exists.

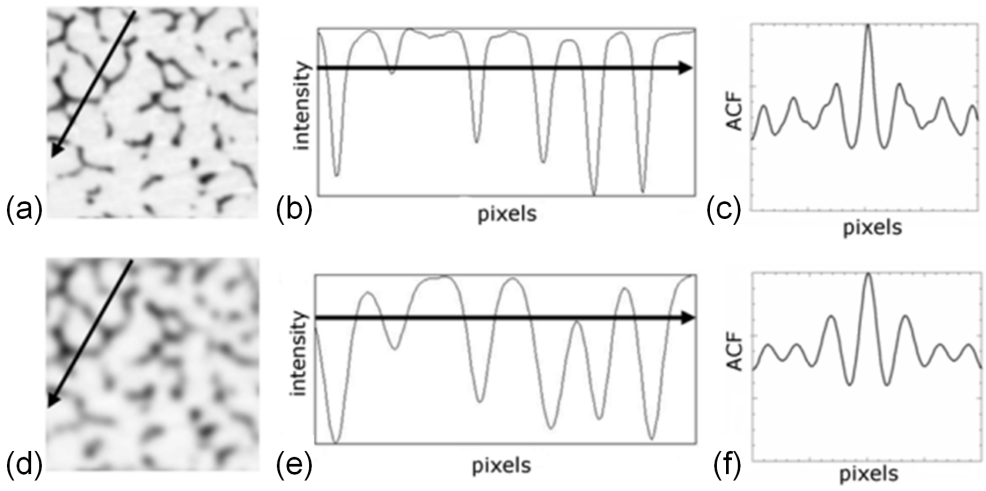

Figure 3.21 Effects of lowering resolution on MIL and ACF in a 1D example: a) inverted μCT image of a TB specimen (50μm resolution); b) intensity profile from (a) using threshold of 80% the signal range indicates 5 intercepts from 6 bone crossings and MIL=640μm; c) $\Phi(\Delta r)$ of profile in (b) with a FWHM of 170 μm; d) μCT image from (a) after down-sampling to 125 μm resolution; e) profile from (d) using the same 80% threshold finds only 3 intercepts from 4 bone crossings resulting in a MIL of 560μm; f) $\Phi(\Delta r)$ of profile (e) with a FWHM of 248 μm.

3.4.2.3 Anisotropic resolution

A reduction in the slice resolution inflates $\mathrm{SA}_{\mathrm{MIL}}$ and $\mathrm{SA}_{\mathrm{FWHM}}$ relative to the isotropic images (mean increase in $\mathrm{SA}_{\mathrm{FWHM}}$ of 0.42, p<0.0001; mean increase in $\mathrm{SA}_{\mathrm{MIL}}$ of 0.24, p<0.0001). The reduced slice resolution also causes variability in the ACF method: 74% of the variation in $\mathrm{SA}_{\mathrm{FWHM}}$ detected at isotropic resolution is captured using a lower slice resolution versus 95% for $\mathrm{SA}_{\mathrm{MIL}}$ (Figure 3.22a-b). The high correlation coefficient for in MIL suggests $\mathrm{SA}_{\mathrm{MIL}}$ can be assessed with a thicker slice resolution. However, the direction of the $\hat{\mathbf{v}}_3$ must also be considered. An augmented slice resolution causes $\hat{\mathbf{v}}_3$ to rotate into closer alignment with the image $\hat{\mathbf{z}}$ axis, as shown by $[\delta x, \delta y]_{FWHM}$ and $[\delta x, \delta y]_{MIL}$ in Figure 3.23a-b. The arrows indicate

changes in orientation caused by down-sampling in the slice direction. The average rotation of $\hat{\mathbf{v}}_3$ attributed to the 3-fold reduction in slice resolution is 4.8°±6.2 (ACF) and 8.8°±9.2 (MIL). Rotations ranged from 0.16° to 23.5° for ACF and from 1.5° to 36.9° for MIL. Thus, despite SA_{MIL} being less affected by the reduced slice resolution than SA_{FWHM}, the principal direction determined by MIL is altered more than that of ACF.

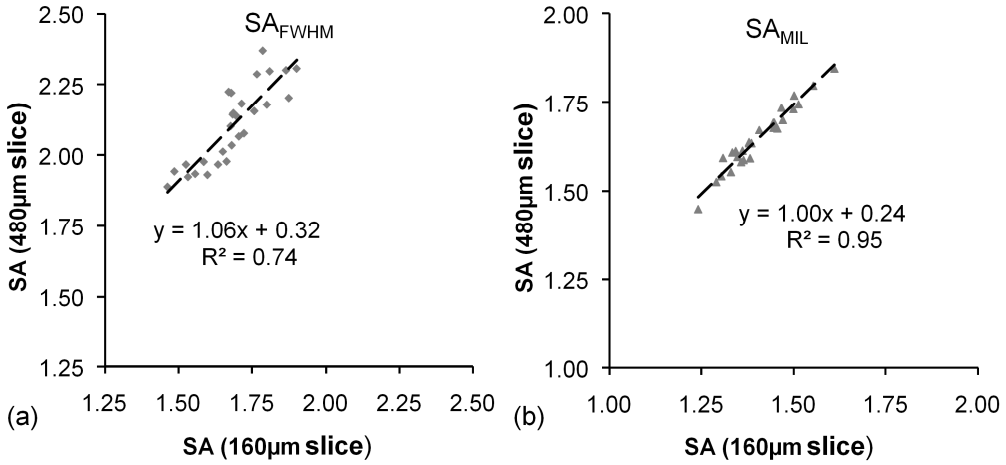

Figure 3.22 Correlations between SA_{FWHM} (a) and SA_{MIL} (b) in TB images with original isotropic resolution of 160µm and down-sampled resolution of 160x160x480µm^3. An augmented slice resolution caused overestimation of SA measures.

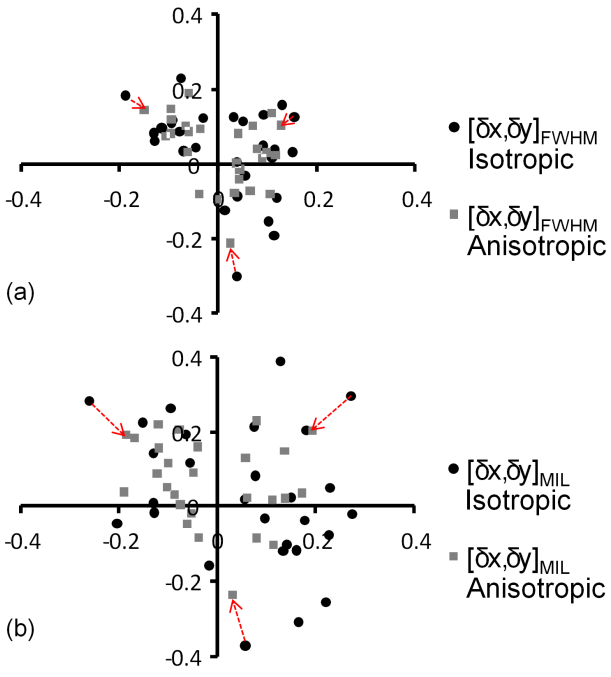

Figure 3.23 $[\delta x, \delta y]$ **calculated using ACF (a) and MIL (b) methods for the 30 specimen images with (160µm)^3 and 160160x480 µm^3 resolutions. Arrows indicate the shifts for several of the datasets caused by augmented slice thickness.**

A closer look at the effect of augmenting the slice thickness is provided in Figure 3.24 for one of the 8x8x8 mm^3 subvolumes of TB. Anecdotally, partial volume blurring along the slice direction leads to the thinning or loss of transverse struts and an overestimation of plate perforations. While the visible changes are only subtle (Figure 3.24a versus b), $\mathrm{SA}_{\mathrm{FWHM}}$ and $\mathrm{SA}_{\mathrm{MIL}}$ increase by 23% and 18%, respectively, as $\hat{\lambda}_3$ increases and $\hat{\lambda}_1$ decreases with larger slice thickness. In addition, rotations of 4.6° for ACF and 7.1° for MIL caused the detected principal material direction $\hat{\mathbf{v}}_3$ to be more closely aligned with $\hat{\mathbf{z}}$.

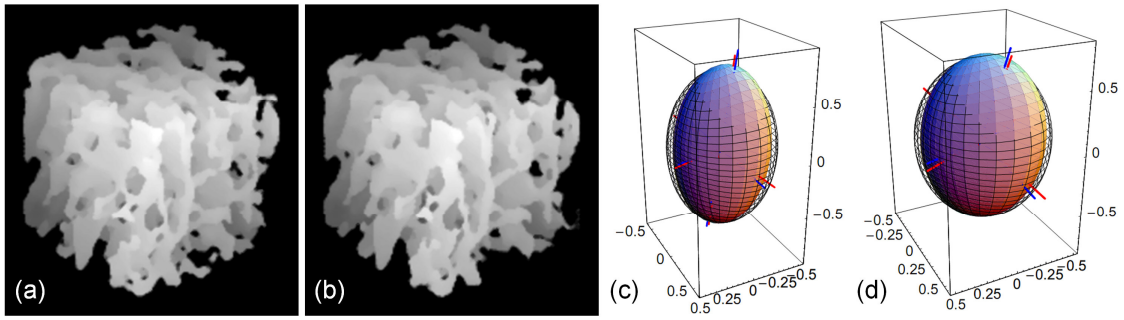

Figure 3.24 Subtle differences in the TB structure can be seen in the 8x8x8 mm^3 volumes of TB with in-plane resolution of 160x160μm^2 and slice thickness of 160μm (a) and 480μm (b). Ellipsoids representing $\mathbf{H}_{FWHM}$ (c) and $\mathbf{H}_{MIL}$ (d) for the two slice resolutions: 160μm- mesh ellipsoid with red eigenvectors, 480μm- solid ellipsoid with blue eigenvectors. In (c), SA_{FWHM} increased from 1.76 to 2.16 (23%) and $\hat{\mathbf{v}}_3$ rotated by 4.6°. In (d), SA_{MIL} increased from 1.5 to 1.77 (18%) and $\hat{\mathbf{v}}_3$ rotated by 7.1°.

Although there is no ground truth, these results indicate anisotropic resolutions impact measures of TB orientation dependence. SA_{MIL} and SA_{FWHM} were larger in the images with lower slice resolution. The strong correlation coefficient demonstrated for SA_{MIL} in Figure 3.22b is contradicted by a larger shift in $\hat{\mathbf{v}}_3$ into closer alignment with $\hat{\mathbf{z}}$ One possible explanation represented in the literature [Odgaard, Jensen et al., 1990; Geraets, van Ruijven et al., 2006] is that the MIL ellipsoid, which is more spherical in shape, has less sensitivity to orientation as it involves higher levels of averaging over the structure. The effect of slice thickness on SA_{MIL} has also been reported on the basis of serial sectioned TB images by Kothari et al. [Kothari, Keaveny et al., 1998]. By varying the slice thickness from 100 μm to 1000 μm, an increase in SA (due to increased $\hat{\lambda}_3$ and decreased $\hat{\lambda}_1$) and alignment with the $\hat{\mathbf{z}}$ axis was observed. While a different down-sampling procedure (i.e. image down-sampling) was utilized in that work, a similar effect on MIL was observed. In agreement with Kothari's work, these results suggest

anisotropic resolutions augment the derived SA of TB and, consequently, support the use of resolution isotropy when assessing TB orientation.

In practice, thinner slices are accompanied by the disadvantage of lower SNR or increased scan time as $SNR \propto \Delta x \Delta y \Delta z \bullet \sqrt{t_{acq}}$ where $\Delta x \Delta y \Delta z$ is the voxel size and t_{acq} is the acquisition time. In μMRI of specimens, the resolution can be increased by increasing the scan time. For example, to achieve the same SNR and field-of-view as in an image with a 137x137x410 μm^3 resolution acquired in 10 minutes but with an isotropic resolution of $(137\ \mu m)^3$, the scan time would have to be increased by a factor of 9 to 90 minutes. This option is not practical for clinical imaging and the trade-off between resolution isotropy and SNR must be considered. Ultimately, enhancements in SNR via more efficient hardware and imaging at higher field strengths present the greatest potential for achieving isotropic resolutions *in vivo*.

3.4.2.4 RF Coil Inhomogeneity

The TB analyzed for the three female subjects in the RF coil inhomogeneity experiment were different relative to SA_{FWHM} and SA_{MIL} (Figure 3.25a). Since the three females subjects were of similar age (24-30 years old), differences in SA were not attributed to age, but more likely due to inherent differences in TB micro-architecture at the distal tibia site. Their ranking relative to SA is the same for both techniques (S1>S3>S2), further supporting the correlations of Figure 3.17b. Conversely, rankings relative to $\Delta\theta_z$ are different, ACF: S1>S3>S2; MIL: S2>S3>S1 (Figure 3.25b).

The effect of applying four separate coil inhomogeneity estimates to each corrected VOI_C is seen in the distribution of SA and $\Delta\theta_z$ in Figure 3.25. The low

frequency signal variations of the RF coil inhomogeneity cause similar variability in ACF- and MIL- derived SA and $\Delta\theta_z$ for the three subjects. The average difference in SA relative to VOI_C was 0.10±0.03 (SA_{FWHM}) and 0.05±0.005 (SA_{MIL}). Average differences for $\Delta\theta_{z,FWHM}$ and $\Delta\theta_{z,MIL}$ were 0.47°±0.006 and 0.41°±0.23°, respectively. Neither method was highly sensitive to image intensity variations associated with inhomogeneity, although it was observed in Figure 3.26 that the presence of RF coil inhomogeneity produced a systematic increase in SA_{FWHM} and $\Delta\theta_{z,FWHM}$ while SA_{MIL} and $\Delta\theta_{z,MIL}$ varied randomly.

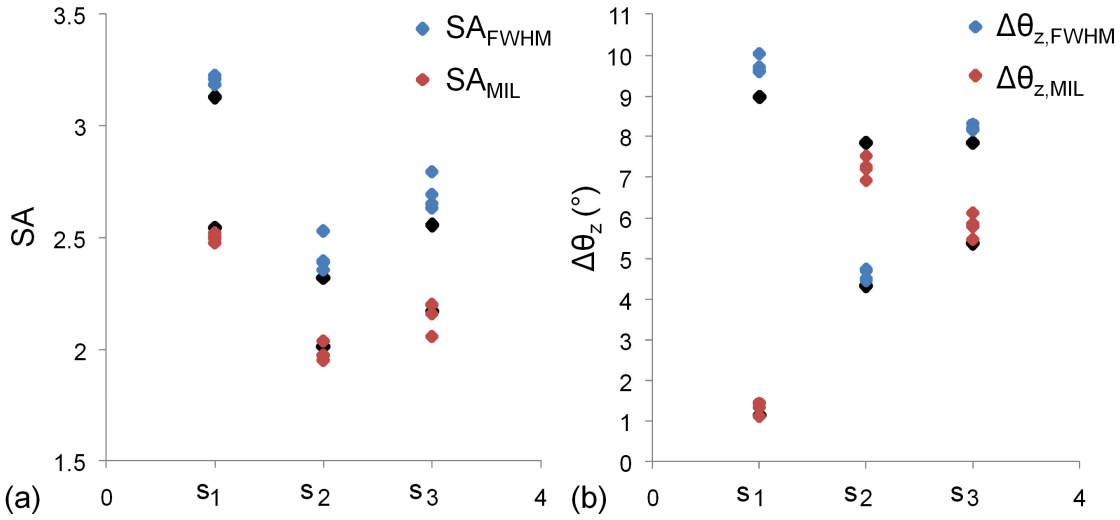

Figure 3.25 Different regions of RF coil inhomogeneity cause variations in SA (a) and $\Delta\theta_z$ (b) for subjects S1, S2, and S3. Values of SA and $\Delta\theta_z$ for VOI_c are indicated by points with a darker outline while those measures influenced by applied coil inhomogeneity are lighter in color.

Low-frequency image intensity variations are further examined in a one dimensional profile from an *in vivo* trabecular bone image (Figure 3.26). A linear variation of ~15% over the image region (Figure 3.26a) has a negligible effect on the

FWHM (<1%). However, since the coil shading varies primarily within the transverse plane, FWHM measures relative to the transverse plane would be influenced whereas longitudinal measures would not, therefore impacting SA by way of only λ_1. MIL appears more sensitive to the presence of intensity gradients when using a global threshold if the intensity variation is severe enough to cause incorrectly identified or missed bone crossings. While this was not the case in the coil inhomogeneity experiments (Figure 3.12c), if larger VOIs were analyzed, MIL, and similarly ACF, are likely to show higher variability. As both ACF and MIL demonstrated similar errors in the three *in vivo* images subjected to different regions of coil shading, removal of the signal variations due to coil shading would improve the reproducibility of the fabric tensors $\mathbf{H}_{FWHM}$ and $\mathbf{H}_{MIL}$. Coil inhomogeneity removal techniques include estimation on the basis of a homogeneous phantom [Mohamed, Vinitski et al., 1999], low-pass filtering of the images [Benito, Vasilic et al., 2005], or local thresholding of the marrow signal [Vasilic and Wehrli, 2005].

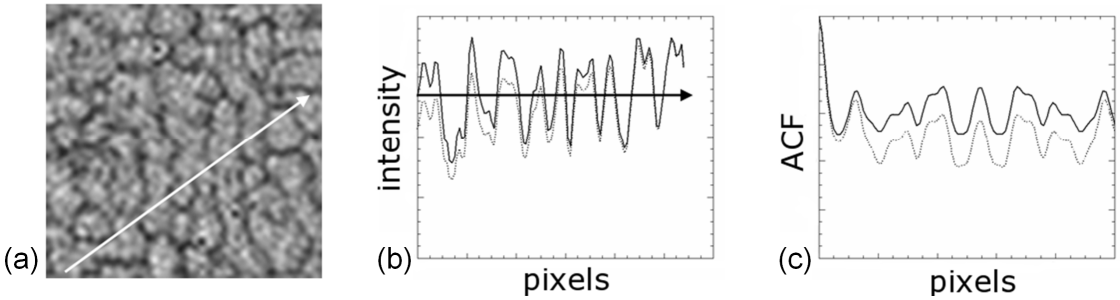

Figure 3.26 Simulated low-frequency signal variation across a 2D *in vivo* μMR image of TB (a); b) Intensity profile (dark) from (a) and profile after superimposing 15% linear variation (gray) where application of a threshold leads to missed intercepts; c) original $\Phi(\Delta r)$ (dark) and $\Phi(\Delta r)$ for adjusted intensity profile (gray) in (b).

3.4.3 Preprocessing

The difference between GSI and BVF-mapping is evident in the zoom-ins and associated histograms of Figure 3.27. The histogram in Figure 3.27c reflects the GSI intensities of the original image of Figure 3.13b while that of Figure 3.27h reflects the BVF-values where the majority of voxels is marrow and thus has a BVF intensity of 0. The resulting ellipsoids for the ACF technique, Figure 3.27b and g show fair agreement in SA_{FWHM} (2.19 versus 2.30) and $\Delta\theta_{z,FWHM}$ (11.8° versus 7.3°, i.e. a net rotation of $\hat{\mathbf{v}}_1$ by 4.4°).

Since the choice of threshold is ambiguous relative to the GSI histogram, two threshold values offering reasonable TB segmentations were selected. The two thresholds produced the ellipsoids in Figure 3.27d and e with SA_{MIL} of 1.42 and 1.75 and $\Delta\theta_{z,MIL}$ of 6.1° and 12.1° (net rotation of $\hat{\mathbf{v}}_1$ by 7.2°), respectively. Since the BVF-mapping procedure involves normalization of the image by a local marrow signal followed by inversion such that the local marrow signal is now set to 0 (see Chapter 2), an obvious choice of threshold on the basis of BVF-maps is 1% (i.e. all non-marrow voxels), which produces the ellipsoid of Figure 3.27i with SA_{MIL}=1.84 and $\Delta\theta_{z,MIL}$=6.7°. Alternatively, a threshold of 15%, which is justified to avoid low-BVF values attributed to low SNR, produces Figure 3.27j where SA_{MIL}=1.94 and $\Delta\theta_{z,MIL}$=8.3° (net rotation of $\hat{\mathbf{v}}_1$ by 1.5°).

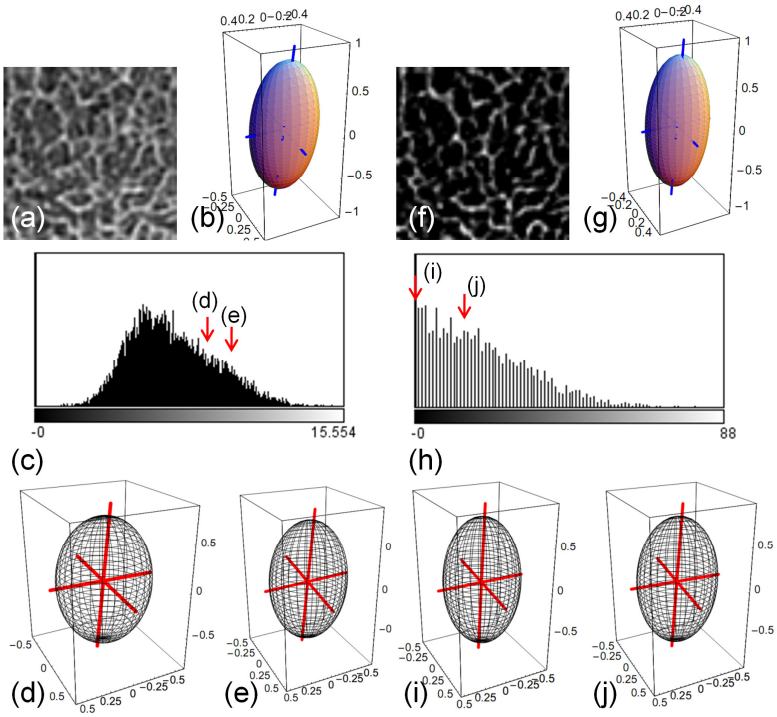

Figure 3.27 Comparison of the effects of different preprocessing steps, GSI - a) through e) - and BVF-mapping - f) through j) - on calculated tensors $\mathbf{H}_{FWHM}$ and $\mathbf{H}_{MIL}$ for *in vivo* MR image of TB: (a) and (f) - zoom-ins of regions identified in Figure 3.13b-c; b) and g) - ellipsoids representing $\mathbf{H}_{FWHM}$; c) and h) - histograms of (a) and (f) with values of THR used to compute ellipsoids representing $\mathbf{H}_{MIL}$ shown in d), e), i), and j).

The choice in preprocessing method influences both ACF and MIL. The ACF technique appears to be fairly robust as SA_{FWHM} only differs by 5% between GSI and BVF-mapping. Further, as no threshold is applied, ACF can be automatically applied to either image. It is evident by the variations in SA_{MIL} and $\Delta\theta_{z,MIL}$ that the selection of threshold has an impact on the computed $\mathbf{H}_{MIL}$, particularly when using GSI. BVF-mapping provides a clearer distribution of intensities than GSI as the marrow compartment is identified via a local threshold and subsequently set to 0. Preprocessing

via BVF-mapping allows the thresholding relative to a meaningful parameter, namely the fractional occupancy of bone or BVF.

An alternative method for setting a threshold has been suggested by Majumdar et al [Majumdar and Genant, 1995]. In the dual-thresholding algorithm [Kothari, Keaveny et al., 1998], the user selects the mean bone I_b and marrow I_m intensities from the image, from which the bone volume fraction (BV/TV) of the image is calculated from $I_r = (BV/TV)I_b + (1 - BV/TV)I_m$ where I_r is the mean intensity of the image. The threshold is then selected in the histogram as the intensity at which the trabecular bone content matches BV/TV. While, the dual-thresholding technique offers a more intuitive determination of a threshold, it is user-dependent and not appropriate for images with coil shading. Additionally, identification of the bone intensity in images with partial volume blurring (i.e. at *in vivo* resolutions) is not straightforward. Although errors are associated with BVF-mapping at SNRs<8 [Vasilic and Wehrli, 2005], this pre-processing step improves the thresholding step used in MIL by using a local threshold to remove the marrow signal. Consequently, BVF-mapping is useful for correcting signal variations due to RF coil inhomogeneity. Thus, BVF-mapping is considered an ideal preprocessing step for MIL and ACF analysis of MR images of TB.

In summary, the intensity histograms of μMR images at the resolution achievable *in vivo* are monomodal (Figure 3.2d) due to partial volume effects, low SNR, and marrow signal intensity variations. Selecting a binarization threshold is therefore a challenge and the ACF technique presents a promising alternative to traditional threshold-based approaches of characterizing TB orientation. In μCT and μMR images of TB, parameters associated with the ACF-fabric tensor $\mathbf{H}_{FWHM}$ showed good agreement with

those of $\mathbf{H}_{MIL}$ in μCT and μMR images. ACF also demonstrated lower sensitivity to SNR and partial volume blurring. Further, the computation of $\mathbf{H}_{FWHM}$ was shown to be faster than that of $\mathbf{H}_{MIL}$ by more than an order of magnitude. When detecting fabric tensor on the basis of *in vivo* μMRI, voxel isotropy is important if sufficient SNR can be achieved (SNR>6). The BVF-mapping procedure should be performed prior to ACF to limit the effect of RF coil inhomogeneity and is an ideal preprocessing step for MIL as it allows a logical threshold selection.

In conclusion, the advantages of ACF make it a promising technique for *in vivo* studies of TB orientation in response to disease, treatment, and usage. Assessment of trabecular bone orientation via ACF may provide important information relevant to predicting fracture risk beyond that determined using material density alone. Of course, issues of reproducibility and validity must be addressed to establish ACF as a useful descriptor of TB orientation. These issues are addressed in subsequent chapters.

4 Chapter 4 In vivo µMRI of trabecular bone at 3T

4.1 Overview

Micro MRI's ability to detect changes in TB micro-architecture associated with disease and treatment is limited by image artifacts, involuntary subject motion, and volume misalignment between successive time-points. Further, resolution demands limit the achievable signal-to-noise ratio (SNR) within a given scan time such that the slice resolution is often compromised. Since trabeculae generally align with the bone's longitudinal axis, the primary imaging plane is typically chosen perpendicular to this direction to limit the loss in structural information. However, the relaxed slice resolution artificially increases the TB structural anisotropy (see Chapter 3), enhances its plate-like appearance [Wald, Magland et al., 2008], and limits the detection of structural detail smaller than the slice thickness [Kothari, Keaveny et al., 1998].

A method for acquisition and processing of high-resolution images of the distal tibia was designed, implemented, and evaluated with the objective of quantifying structural and mechanical parameters that relate to TB architecture. Sources of error including image artifacts due to stimulated echoes, subject motion, and longitudinal volume misalignment were minimized in order to maximize reproducibility, reliability, and sensitivity of structural parameters in seven test subjects. The potential benefit of trading SNR for achieving an isotropic resolution via parallel imaging was considered relative to conventionally acquired images with anisotropic voxels on the basis of image-derived measures of scale, topology, orientation, and elasticity.

Good reproducibility was achieved for both resolution regimes: coefficients of variation of 1-5% (mean: 3.2%±1.2%) for anisotropic images versus 1-9% (mean: 5.4%±2.4%) for isotropic images. The anisotropic voxel size yielded greater measurement reliability (ICC range, mean: 0.75-0.99, 0.92±0.09 in anisotropic versus 0.62-0.99, 0.87±0.10 in isotropic) and better discrimination of the seven subjects (75% versus 50% of the possible comparisons were significantly different ($p<0.05$)) except for measures of structural anisotropy and topology. Isotropic resolution improved detection of measures dependent on orientation, namely structural anisotropy and the ratio of plate-like to rod-like elements, and permitted visualization of small perforations in longitudinal trabecular plates not detected at anisotropic resolution.

4.2 Introduction

Increased image resolution comes at the cost of SNR and scan time: $SNR \propto \Delta x \Delta y \Delta z \bullet \sqrt{t_{acq}}$. In Chapter 2, an obvious means to increase SNR by imaging at higher field strengths is discussed. Theoretical suggestions indicate that in the tissue-noise dominated regime, SNR scales linearly with field strength, and thus a two-fold gain in SNR is expected at 3T relative to 1.5T. The SNR dependence on field strength is discussed in Chapter 2.

An increase in SNR allows flexibility in the image acquisition procedure including the possibility for shortened scan time, higher resolution, or increased volume coverage. As the lower slice resolution typical of µMRI was shown to artifactually increase SA and the alignment of TB with the $\hat{\mathbf{z}}$-axis of the image (see Chapter 3), the theoretical gain in SNR at 3T would permit acquiring isotropic voxels and thus, potentially, more accurate measure of TB orientation. However, a finer slice resolution requires an increase in

scan time. A significant increase in scan time would jeopardize patient-comfort and reduce the likelihood for obtaining motion-free images. To reduce scan time without adversely impacting the resolution or field-of-view (FOV), parallel imaging could be implemented.

Parallel imaging (PI) offers a means of reducing scan time through the use of multiple surface coil elements. In parallel imaging, the image acquisition time is reduced by exploiting spatial information inherent in the geometry of the receiver elements to substitute for phase encoding steps typically produced by switching the magnetic field gradients. The spatial encoding function for a given surface coil array can be estimated in either image space [Pruessmann, Weiger et al., 1999] or k-space [Sodickson and Manning, 1997]. A practically useful technique, called generalized autocalibrating partially parallel acquisitions or GRAPPA, auto-calibrates the encoding function [Griswold, Jakob et al., 2002] without the need to accurately map the coil sensitivity. In the GRAPPA approach, the central portion of k-space is sampled at a rate corresponding to the intended full-FOV whereas the outer phase encoding step is sampled at a reduced FOV. The fully-sampled data points are then used to estimate the encoding function of the RF coil which is subsequently applied in the outer k-space regions to recover the skipped phase-encoding lines.

This chapter focuses on the development of the μMR method for TB imaging in the distal tibia at 3T. The SNR advantage of imaging at 3T is evaluated and, by employing PI, converted into improved resolution without suffering a significant loss in SNR. Reproducibility and reliability of structural and mechanical parameters from the new isotropic acquisition and from the anisotropic FLASE acquisition are evaluated in repeated scans of seven healthy subjects. Image artifacts, motion degradation, and

serial image volume misalignments were controlled to maximize reproducibility of image-derived measures of scale, topology, orientation in terms of structural anisotropy, and finite-element derived Young's and shear moduli. Coefficients of variation (CV%) and intraclass correlation coefficients (ICC) for structural and mechanical parameters were calculated as measures of reproducibility and reliability. The ability of structural and mechanical parameters to discriminate subjects was tested by the analysis of variance (ANOVA).

4.3 Materials and methods

4.3.1 Evaluation of SNR at 3T

Although theory predicts a linear increase in SNR with field strength (see Chapter 2), additional contributory effects on SNR, such as tissue relaxivity and differences in hardware, provide motivation for experimental confirmation. The achievable SNR gain at 3T was evaluated in a tissue equivalent ankle-phantom (TEAP) using a SE pulse sequence and on the basis of *in vivo* images acquired using the FLASE pulse sequence. The TEAP was conceived and designed to mimic the chemical composition of the ankle to aid in RF coil design and pulse sequence testing [Magland, Wald et al., 2009]. The phantom consisted of a cylindrical plastic container (7 cm diameter) filled with agarose gelatin and two smaller plastic containers of corn oil (3 cm and 4 cm diameters). The sizes and positions of the oil-filled containers placed within the larger container were chosen to mimic the relative sizes and locations of the tibia and fibula in the distal ankle. The agarose gelatin was doped with $GdCl_3$ and NaCl according to the published formula [Kato, Kuroda et al., 2005] to match the relaxivity and conductivity of knee muscle.

Plastic tubes of varying sizes with a wall thickness comparable to that of bone trabeculae were inserted into one of the oil containers.

On the 1.5T Siemens Sonata Scanner (Siemens, Erlangen, Germany), a custom-built two-channel, overlapping phased-array coil was used for signal reception. On the 3T Siemens TIM Trio Scanner (Siemens, Erlangen, Germany), images were acquired using a four-channel, overlapping phased-array coil (Insight MRI, Worcester, MA). The RF coils consist of two and four hexagonal, receive-only loops arranged in a linear, overlapping configuration within plastic horseshoe-shaped housings that cover the anterior surface of the ankle. The two coils are shown positioned on the left ankle in Figure 4.1. Images of the TEAP were acquired using identical sequences at both 1.5T and 3T: a 2D spin-echo acquisition with a voxel size of 1x1x3mm^3 and a long repetition time of 2 seconds to prevent signal differences arising from T_1 relaxation of the oil protons (T_1=300ms).

The SNR difference between 1.5T and 3T was also evaluated *in vivo*. The gain in SNR achievable *in vivo* using the 3D FLASE pulse sequence (TR/TE=80/10.5ms, 137x137x410 μm^3) was estimated relative to five randomly selected scans from a pool of baseline control subjects in an ongoing study at 1.5T and five 3T scans obtained in the reproducibility study. Both scan populations were considered healthy.

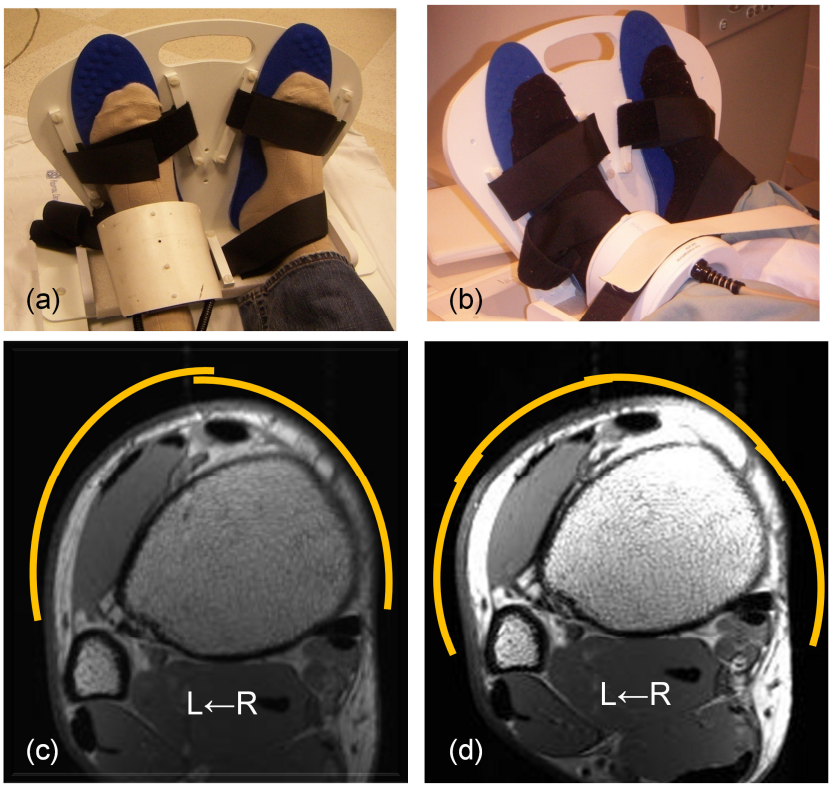

Figure 4.1 Phased array coils with two- (a) and four- (b) channels positioned on left ankle of subjects strapped into custom-designed immobilization platform. Axial SE images acquired at 1.5T with a 2-channel RF coil (c) and 3T with a 4-channel RF coil (d). Images (c),(d) are scaled identically.

Because images at 1.5T and 3T were acquired using differing number of channels, comparing SNR required special considerations. In the SE images, SNR was measured relative to noise-normalized square-root sum-of-squares reconstructions (NN-SRSS). A noise-normalized image was created by dividing a single channel's magnitude reconstruction by the standard deviation of the noise in a signal-free region of its complex image. The NN-SRSS images can be compared between coils having an unequal number of channels. By scanning the phantom in the same position for both scans, the ratio of the resulting NN-SRSS images could be divided to directly calculate the spatial dependence of the SNR difference between images acquired at 1.5T and 3T.

A different procedure was used to determine the SNR gain relative to the FLASE pulse sequence *in vivo*. SNR in 3T images relative to 1.5T was measured using a

traditional two regions-of-interest (ROIs) approach in the SRSS reconstructions. 'Signal' was measured in a ROI inside the bone marrow region where the signal appeared to be maximal. 'Noise' was measured in the signal-free background of the SRSS reconstruction which is known to overestimate the standard deviation of zero-mean uncorrelated Gaussian noise. Since coils with unequal channel numbers are being used, a correction factor, $M(N)= [1*3*5*...*(2N-1)*(pi/2)^{1/2}] / [2*4*6*...*(2N-2)]$ where N is the number of channels (see Appendix for derivation), was applied before comparing SNR measurements. The correction factor arises from combining Rician-distributed noise in magnitude images from multiple coils.

Sum-of-squares reconstructions and the ratio of NN-SRSS images for the TEAP at 1.5T and 3T are shown in Figure 4.2. The average SNR gain at 3T versus 1.5T within the oil region of the phantom, which closely mimics fatty bone marrow, was 110±9%. This represents the achievable gain in fatty marrow at 3T relative to 1.5T based on the two coils, independent of relaxation effects.

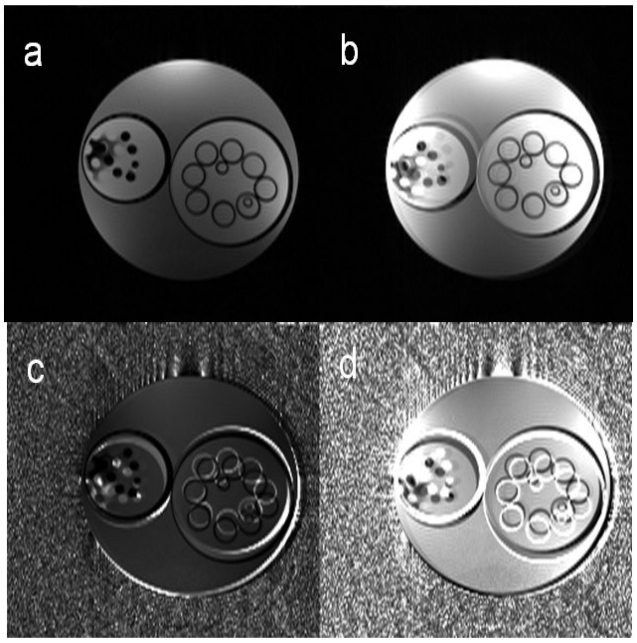

Figure 4.2 Images of TEAP acquired using a SE pulse sequence ($TR>>T_1$) at 1.5T (a) and 3T (b). Inner plastic cylinders are filled with vegetable oil to mimic fatty bone marrow within the tibia and fibula. Ratio images of the NN-SRSS: 1.5T/3T (c) and 3T/1.5T (d). Average SNR gain in oil was 110%. Image pairs (a),(b) and (c),(d) are identically scaled.

SNR measurements in the images acquired using the four channel array (3T) were multiplied by M(4)=2.74 and those from the two-channel at 1.5T were multiplied by M(2)=1.88, resulting in: SNR(3T-4ch)=36.8 +/- 3.95 and SNR(1.5T-2ch)=18.6 +/- 2.39. This reflects a 98.6% gain in SNR at 3T relative to 1.5T. The approximate two-fold gain permits halving of the voxel volume or a 26% gain in linear resolution, resulting in an isotropic voxel size of approximately $160\,\mu\mathrm{m} = (137*137*410/2)^{1/3}$.

4.3.2 Optimal reconstruction

Multi-column multi-line interpolation (MCMLI), an extension of GRAPPA, provides improved reconstruction accuracy [Wang, Wang et al., 2005] by including neighboring points along the readout (k_x) direction during the estimation of the encoding function and the subsequent interpolation. Recovery of the skipped phase encoding points (¬ACQ) through interpolation of the acquired data (ACQ) using MCMLI-GRAPPA (R=2) is illustrated for the 2D k-space acquired by a single coil element in Figure 4.3. The interpolation involves a weighting matrix, w, with dimensions of $nxnxCxL$ where n is the number of receiver channels, C is an odd integer number of columns (k_x points), and L is an even integer number of lines (k_y points). The fully-sampled region or auto-calibration region (ACR) typically corresponds to the low-spatial frequency region of k-space as it has the largest signal intensities. A shortened scan time results from under-sampling the outer phase encodings at intervals of $R\Delta k_y$ (i.e. $2\Delta k_y$ represents $FOV_y/2$). The kernel $w(j,k,c,l)$ is first determined through least squares fitting of Eq. 4-1 in the ACR. Then the signal intensities of the skipped phase encoding points $S_j^{\neg ACQ}(k_x, k_y - m\Delta k_y)$ are estimated from Eq. 4-1 from the acquired points

$S_k^{ACQ}(k_x + c, k_y + lR\Delta k_y)$ such that $1 \le m \le R-1$. Accordingly, the full FOV data is recovered by iterating over the skipped PE_y lines for every coil. The number of lines in the ACR, $NACL$, affects the effective acceleration factor R_{eff} and the number of neighboring lines L considered in the interpolation. As L approaches half the total number of PE_y points, an exact SENSE-like reconstruction is achievable, although this level of accuracy has been deemed unnecessary and impractical [Griswold, Jakob et al., 2002].

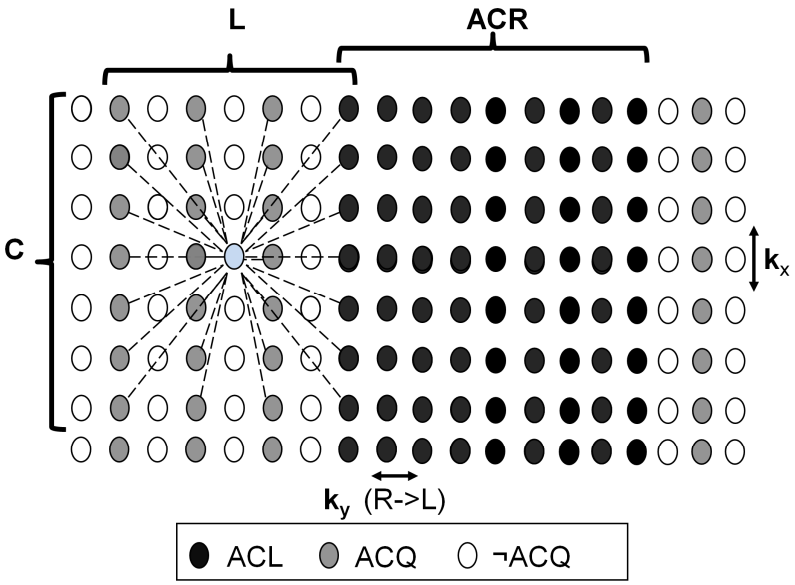

Figure 4.3 Sampling and reconstruction paradigms for GRAPPA-MCMLI in a single channel's k-space. Interpolation kernel w, an nxnxCxL array (n=#coils, C=#columns, and L=#lines), is auto-calibrated in the fully-sampled region (ACR). Then, the skipped k_y lines (¬ACQ, R=2) are recovered through interpolation of the surrounding ACQ lines using w.

Eq. 4-1

$$S_j^{\neg ACQ}(k_x, k_y - m\Delta k_y) = \sum_{k=0}^{n} \sum_{c=-C/2}^{C/2} \sum_{l=-L/2}^{L/2-1} w(j,k,c,l) S_k^{ACQ}(k_x + c, k_y + lR\Delta k_y)$$

As the interpolation process is prone to errors associated with measurement noise and non-ideal coil geometries, reconstruction accuracy is dependent on the pulse

sequence, RF coil, and acceleration factor. Optimal sizes of w and ACR for a FLASE acquisition in the distal tibia using the four-element, horseshoe-shaped RF coil were investigated. A two-fold acceleration was simulated in a fully-sampled *in vivo* 3D FLASE dataset acquired on a Siemens TIM Trio 3T scanner using the four-channel phased array ankle coil. The fully sampled dataset (137x137x410 μm^3 resolution) was reconstructed and used as a reference (I^{ref}). Approximate two-fold accelerated acquisitions were simulated by zeroing alternate k_y-lines. The size of the ACR, denoted by $NACL$, varied from 5-200, representing scan times of 8min10s (R_{eff}=1.88) to 15min (R_{eff}=1.03). For each value of $NACL$, GRAPPA-MCMLI was performed with rectangular weighting kernels of varying sizes, denoted as LxC. The residual-root-mean-square, $RRMS(NACL, LxC)$, was computed from Eq. 4-2 (i=index of N image voxels) to quantify the reconstruction artifact relative to $NACL$ and LxC.

$$RRMS(NACL, LxC) = RRMS(I^{ref}, I^{recon,NACL,LxC}) = \sqrt{\frac{1}{N}\sum_{i=0}^{N-1}\left\| I_i^{ref} \right| - \left| I_i^{recon,NACL,LxC} \right\|^2}$$

Eq. 4-2

Normalized $RRMS(NACL, LxC)$ is plotted with respect to $NACL$ for 11 rectangular kernels in Figure 4.4. As expected, independent of kernel size, the normalized RRMS demonstrates a trend towards 0 as $NACL$ approaches half the total number of PE_y lines (i.e. full-density sampling). Standard GRAPPA, corresponding to a 2x1 kernel, performs better than the linear kernels, 4x1 and 6x1, which use additional phase encoding points in the interpolation. GRAPPA-MCMLI was superior to GRAPPA for most kernel sizes, although, a 2x5 kernel had the largest RRMS of all kernels. Several kernel sizes produced good reconstructions (i.e. low errors). To differentiate them, the first derivative of the RRMS relative to $NACL$ was evaluated. For $NACL$=28, a 4x5 kernel produced

the lowest RRMS value and its derivative was closest to zero. Thus, a combination of $NACL$ =28 and 4x5 kernel provided the optimal reconstruction in the shortest scan time, resulting in a total scan time of 8min54sec (R=1.73). The optimal reconstruction is shown in Figure 4.5 relative to I^{ref} and the conventional reconstruction of the R=1.78 simulated acquisition.

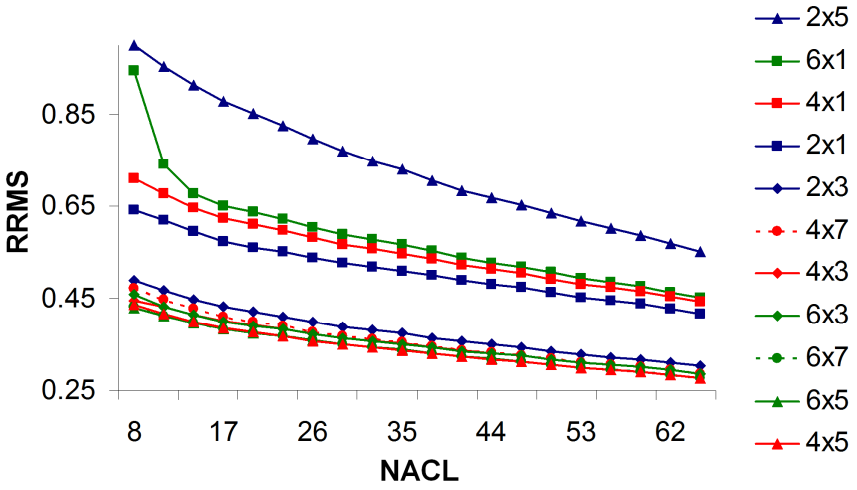

Figure 4.4 Normalized RRMS dependence on $NACL$ and interpolation kernel w, denoted by it size LxC. Kernel sizes in legend match highest to lowest ordering of RRMS in plot.

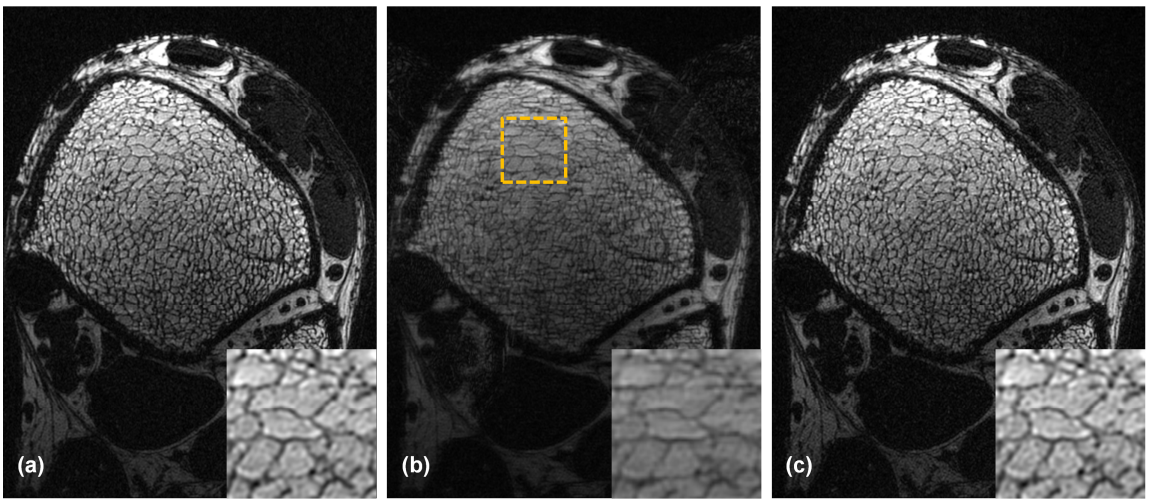

Figure 4.5 (a) Fully sampled FLASE image (137x137x410 μm^3 resolution) used as I^{ref}; (b) conventional reconstruction of simulated R=1.78 (8min54sec) acquisition showing characteristic ghosting artifact in R→L direction; (c) optimal MCMLI-GRAPPA using $NACL$ =28 and 4x5 kernel. Zoom-ins within (a), (b), and (c) from location indicated in (b) depict high correspondence in TB appearance between (a) and (c).

4.3.3 Isotropic resolution

High-resolution imaging of TB micro-architecture is preferably performed with spin-echo-type pulse sequences as the signal loss due to static field gradients near the bone-bone marrow interface are rephased by the refocusing pulse [Techawiboonwong, Song et al., 2005]. However, the combination of a non-selective 180° pulse and a short repetition time make the sequence prone to stimulated echo artifacts [Ma, Wehrli et al., 1996]. To minimize stimulated echo artifacts in the FLASE pulse sequence, RF spoiling and crusher gradients are used to dephase magnetization excited by an imperfect, non-selective refocusing pulse. In the anisotropic scan mode, gradient crusher moments of 0.36 T*sec/m were applied relative to the z-axis to scramble spin phase by 2π across the 410μm slice. For a 160μm slice, 0.92 T*sec/m was necessary which, in conjunction with the increased amplitudes of the slice encoding, caused a slight increase in TE relative to that of the anisotropic sequence (410μm slice). However, even a 0.92 T*sec/m crusher moment was found to be inadequate to fully eliminate stimulated echo formation when slice encoding was the inner phase encoding loop. Figure 4.6 illustrates a repetition of the isotropic FLASE pulse sequence. Due to an imperfect 180º refocusing pulse, transverse magnetization produced by the 140º pulse is stored as phase encoded (and crushed) longitudinal magnetization. This encoded magnetization returns with the excitation pulse in the subsequent repetition, where it experiences additional phase encoding.

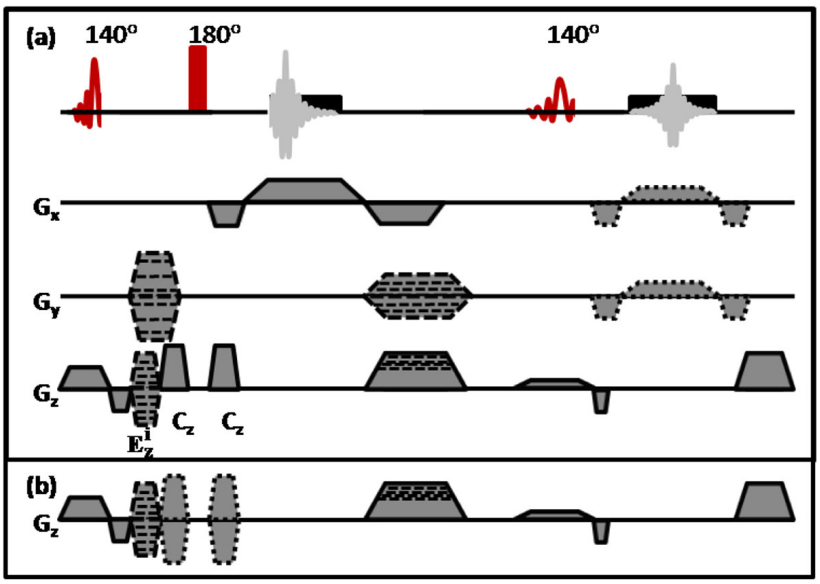

Figure 4.6 Isotropic fast large-angle spin echo (FLASE) sequence used for imaging TB microstructure. The first 140º SLR pulse The second 140º SLR pulse excites a parallel slice to generate a navigator echo that is alternated between x and y-axes. By matching the polarity of the crusher gradients (C_z) to that of the slice-encoding gradients a stimulated echo in the subsequent repetition resulting from imperfections in the 180º refocusing pulse, can be avoided. For details see text.

To simplify, only the z-encoding gradients (slice and crusher moments) are considered. There are two pathways to consider, and the total encoding for these pathways are: P1 = (PE1+ C_z) + PE2 and P2 = -(PE1+C_z)+ PE2, where PE1 and PE2 are phase encoding moments for the two repetitions and C_z is the additional encoding moment due to the crusher. Pathway P2 is never a problem since PE1 ≈ PE2. However, pathway P1 can lead to an echo when the condition PE1+PE2 ≈ - C_z is met. C_z would have to be twice as large as the largest slice encoding moment to prevent stimulated echo formation, i.e. C_z=1.84 T*sec/m, resulting in a significant increase in TE and further signal loss due to T2-decay. In examining P1, an alternative strategy was identified in which C_z always has the same polarity as the slice-encoding moment.

Using this approach, P1 would never become rephrased and C_z could instead be reduced, resulting in less T2 signal decay (thus higher SNR).

The polarized crusher moment approach was validated in the TEAP using the isotropic FLASE sequence (Figure 4.6) at 3T with and without the proposed modification. Figure 4.7 illustrates the effect of alternating the sign of the crusher gradients in the isotropic FLASE sequence. The stimulated echo (Figure 4.7b) and its resulting sinusoidal artifact (Figure 4.7c) were eliminated by alternating the sign of the crusher gradient moment (Figure 4.7d and e).

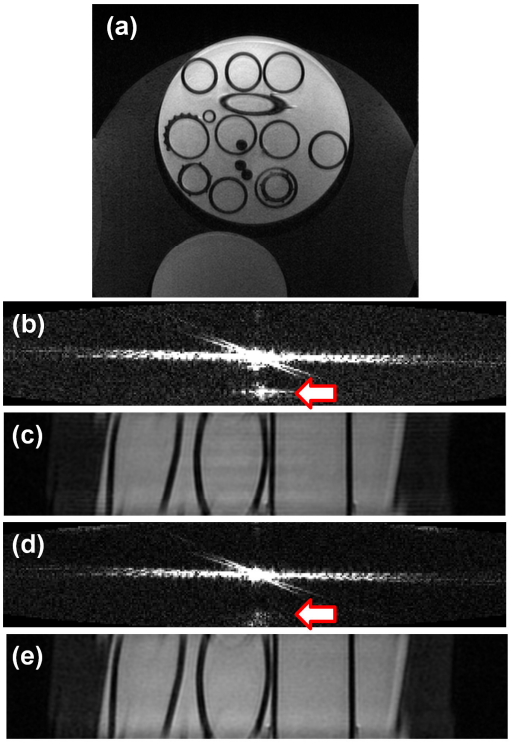

Figure 4.7 a) FLASE image of TEAP with $(160\mu m)^3$ isotropic voxel size acquired using the sequence shown in Figure 4.6. b) $k_x - k_z$ plane (k_y=0) indicating central image echo and stimulated echo (indicated by arrow) appearing where slice-encoding gradients combine to approximately equal the crusher gradient moment, causing a sinusoidal signal variation from the spurious echo (c). By alternating the polarity of the crusher, encoding gradients no longer oppose the crusher moment (d), and the banding artifact is eliminated (e). Please refer to Figure 4.6 for a diagrammatic representation of this implementation.

4.3.4 Reproducibility study

The developments mentioned in the previous sections (4.3.1-4.3.3) were united into an isotropic FLASE acquisition which achieves a 160 µm voxel size in images of the

distal tibia in less than 17 minutes. The isotropic FLASE sequence was evaluated in terms of reproducibility and reliability relative to the traditional anisotropic FLASE acquisition (voxel size of 137x137x410 μm^3) at 3T in a group of volunteers. It was hypothesized that measures of the TB micro-architecture derived from images with isotropic resolution would be more sensitive to architectural differences between-subjects (i.e. higher ICC) than those obtained from anisotropic images.

4.3.4.1 Subjects

Seven healthy subjects (5 males, 2 females, age range 24-42 years) were recruited from the author's institution. None suffered from adverse conditions known to affect bone mineral homeostasis. All underwent three μMRI scans of their left distal tibia, resulting in a total of 21 examinations performed over the course of six months. Each subject's three scans were separated by at least one week and all repeat exams were completed within eight weeks of their baseline scan. The Institutional Review Board approved the study protocol, and all study participants gave their written informed consent.

4.3.4.2 Control for subject movement and hardware

A rigid immobilization platform was constructed to minimize artifacts from involuntary subject motion. Subjects were positioned feet-first, supine with both feet secured to a rigid polyvinyl chloride platform using Velcro© (Velcro USA Inc., Manchester, NH) straps at a 150° incline relative to the scanner table (Figure 4.1b). The entire platform was designed to latch onto the scanner table in order to prevent its displacement during image acquisition. Imaging was performed on a 3T Siemens TIM Trio scanner with the four-channel phased-array coil depicted in Figure 4.1b. The four-

channel RF coil was secured with a Velcro© strap to the anterior surface of the ankle using the medial malleolus as a landmark.

4.3.4.3 Imaging pulse sequences

The imaging protocol consisted of two multi-slice gradient echo (GRE) localizers to ensure correct coil positioning relative to the distal tibial end-plate, two spin-echo sequences (one axial, one sagittal) to aid in the prescription of the high-resolution scan volume, a 3D fast-GRE acquisition for prospective registration [Rajapakse, Magland et al., 2008], and two high-resolution acquisitions based on a modified FLASE pulse sequence [Magland, Wald et al., 2009]. The 3D GRE acquisition is designed for prospective registration of the follow-up exams to their baseline scans to ensure reproducible placement of the high-resolution imaging regions. The registration series covered a 80x80x256mm^3 volume centered 16.5mm proximally from the tibia's distal end-plate with (1mm)^3 voxels in 2min 8 sec (TR/TE=40/15ms; flip angle=40°, 80 slices). The distal end-plate of the tibia was chosen as the anatomical landmark as it is easily identified in the center slice of the sagittal SE localizer. The first FLASE acquisition covered a 70x64x13mm^3 volume with an anisotropic voxel of 137x137x410µm^3 in 15m23s (TR/TE=80/11ms, flip angle=140°, 32 slices). A second FLASE sequence was subsequently performed to image a 80x64x10mm^3 volume with an 160µm isotropic voxel size in a scan time of 17m25s achieved with PI (R=1.8, TR/TE=80/11ms, flip angle=140°, 64 slices). The (160µm)^3 voxel volume is approximately half that of the 137x137x410µm^3 voxel.

4.3.4.4 Prospective registration

The analyzable volume of the TB volume that is common between baseline and follow-up scans diminishes due to misalignments in acquisition volume between time points, a consequence of subtle changes in patient positioning. To minimize such misalignments, a prospective registration utility involving a 3D GRE localizer was implemented using the algorithm described by Rajapakse et al. [Rajapakse, Magland et al., 2008]. Upon follow-up, the 3D localizer scan volume was registered to the baseline localizer image by maximizing their correlation. Through the use of the fast Fourier transform, the necessary transformation parameters can be obtained within minutes, permitting adjustment of the high-resolution volume prior to its acquisition.

4.3.4.5 Image reconstruction

The raw k-space data were motion corrected for in-plane translations based on x- and y- navigator echoes acquired in a slab outside the imaging region [Magland, Wald et al., 2009]. Translational displacements were detected along x- and y- directions for each 2.4 sec period and then applied as phase shifts to the associated PE_y lines [Song and Wehrli, 1999]. Each set of images were visually inspected as the motion detection and correction scheme is susceptible to errors due to non-translational motion and measurement noise. Images suspected of being corrupted due to rotational motion were further subjected to autofocusing correction [Lin, Ladinsky et al., 2007]. The autofocusing technique is briefly described in Chapter 2.

After motion correction of the isotropic datasets, skipped PE_y lines were recovered using GRAPPA-MCMLI [Wang, Wang et al., 2005] with the optimal values of $NACL$ and LxC determined from section 4.3.2. Anisotropic and isotropic k-space datasets were then reconstructed using the following steps: homodyne reconstruction of

partial readout, apodization using a Fermi filter to reduce Gibbs ringing, Fourier transformation to image space, and square-root sum-of-squares (SRSS) combination of images from each of the four channels. Each SRSS reconstruction was then subjected to an auto-masking procedure to define the TB region. Subsequently, the cortical shell was manually segmented for μFE analysis of the full cross-sectional volume.

Signal-to-noise ratio was evaluated on the basis of the SRSS images as the mean marrow signal intensity divided by the mean of the Rician distributed noise. The marrow signal was determined from the signal intensity distribution within the masked TB region. Since this region contains both marrow and trabeculae, the higher 80% of the signal within this region was attributed to the marrow (assuming a copious bone volume fraction of 20%) and the mean signal was calculated relative to this signal component [Fernandez-Seara, Song et al., 2001]. The mean intensity of the noise was computed within a 50x50 $pixel^2$ signal-free and artifact-free region of the image containing only Rician distributed noise.

4.3.4.6 Retrospective registration

To ensure the analyzable volume of TB is consistent across the three time-points, a retrospective registration approach was implemented. Six transformation parameters consisting of three translations and three rotations were determined using a fast, rigid body registration technique [Magland, Jones et al., 2009]. The transformation parameters were then applied to the follow-up images using two methods referred to as: 1) volume-registration and 2) volume- and orientation-registration. Volume-registration was employed to compare structural parameters independent of orientation, such as those describing scale and topology. This involved resampling the binary masks while

maintaining the underlying image to prevent resampling errors associated with rounding errors and resolution anisotropy. To compare parameters with an orientational dependence (e.g. shear moduli and structural anisotropy), volume- and orientation-registration were performed by aligning the follow-up images and associated binary masks with the reconstruction grid of the baseline image, followed by intersection of the three analysis masks [Magland, Jones et al., 2009] to determine the overlapping analysis volume.

4.3.4.7 Image processing

Three analysis volumes were derived from each SRSS image (Figure 4.8a) for processing. First, full cross-sectional volumes were manually segmented to include both the cortical shell and TB for the purpose of computing axial stiffness by μFEA (Figure 4.8b). Full cross-sectional volumes were translated into alignment with baseline prior to compression simulations for the calculation of E_{ZZ}^{cs}, as shown in Figure 4.8c. Second, volume-registered regions, encompassing only TB (Figure 4.8d), were analyzed for parameters of scale and topology (Figure 4.8e-g). Third, 7x7xN mm^3 parallelepiped subvolumes (Figure 4.8h) were extracted from the volume- and orientation-registered regions of TB. The subvolumes were subjected to orientation analysis (Figure 4.8i and 8j) and grayscale μFE analysis (Figure 4.8k). The 7x7xN mm^3 parallelepiped-shaped subvolumes were selected at the centroids of the volume- and orientation-registered masks where N varied with the degree of overlap between the three scans (Figure 4.8h). The faces of the parallelepiped subvolume were aligned with the image axes $\hat{\mathbf{x}}$, $\hat{\mathbf{y}}$, and $\hat{\mathbf{z}}$ which approximately coincide with the anteroposterior (A→P), left-right (L→R), and infero-superior (I→S) directions. Parallelepiped subvolumes were additionally analyzed

for parameters of scale and topology in order to explore associations between parameters assessed within the subvolumes.

A processing scheme similar to that described by Magland and Wehrli was implemented on the masked 3D grayscale images [Magland and Wehrli, 2008]. All datasets were *sinc* interpolated by zero padding k-space in all three dimensions to yield an isotropic voxel size of 69μm^3. Using a local thresholding approach [Vasilic and Wehrli, 2005], marrow-volume fraction maps were obtained and subsequently inverted into bone-volume-fraction maps (BVF-maps) in which intensities ranged from 0 (pure marrow) to 100 (pure bone, Figure 4.8e). Finally, the BVF-maps were reduced to a skeleton representation (Figure 4.8f) using a BVF-threshold of 15% and removal of unconnected components.

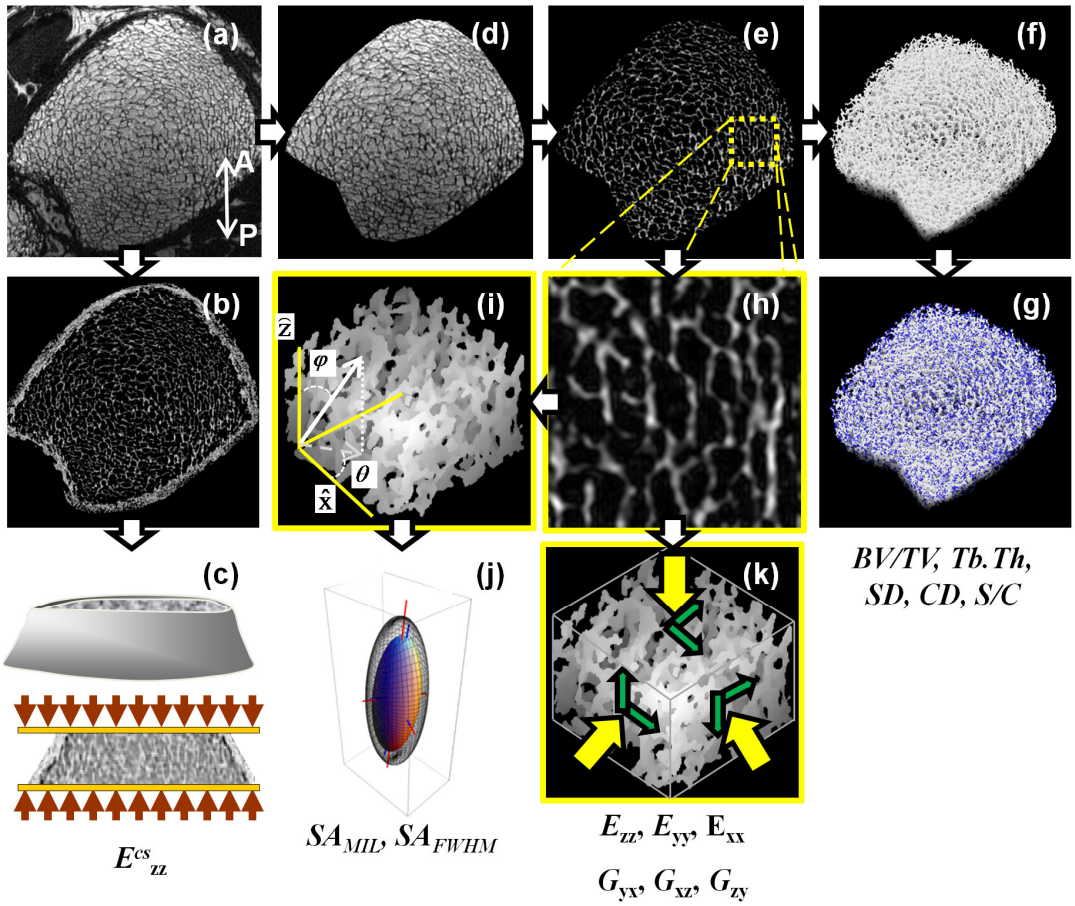

Figure 4.8 Processing chain for evaluation of structural and mechanical parameters: a-c) Pathway for quantification of axial whole-section stiffness: a) acquired image; (b) BVF map covering cortical and trabecular compartment; c) simulated µFE compression test; d- g) pathway for quantification of topology: d) raw image after disconnection of cortex and soft tissue; e) trabecular bone BVF map ; f) 3D skeleton map; (g) same as f) with topological classifications: curve voxels (blue), surface voxels (white); e, h, k) pathway for subvolume µFE analysis: h) subvolume extracted from e); simulated compression and shear FE tests to compute Young's and shear moduli. i, j) orientation analysis by MIL and ACF.

4.3.4.8 Scale and topology

The commonly computed measures of scale, BV/TV and trabecular thickness (Tb.Th), were assessed in this study. BV/TV was computed as the ratio of the summed fractional bone occupancy relative to the total volume of the masked region. Tb.Th was calculated using the fuzzy distance transform (FDT) [Saha and Wehrli, 2004], in which

thickness is estimated as the shortest non-Euclidean BV/TV-weighted distance between a bone voxel and a neighboring marrow voxel.

Topology was quantified using digital topological analysis (DTA) in which each voxel in the skeleton is classified by its local topology as belonging to either a surface (S), curve(C), or their mutual junction [Gomberg, Saha et al., 2000]. In Figure 4.8g, curve voxels are marked in blue and surface voxels in white. The surface-to-curve ratio (S/C) expresses the ratio of plate-like to rod-like trabeculae and the erosion index (EI) yields the ratio of voxel densities that decrease to those that increase with osteoclastic bone resorption [Gomberg, Saha et al., 2000]. Further details on the FDT calculation of Tb.Th and DTA are provided in Chapter 2.

4.3.4.9 Orientation dependence

The mean-intercept-length (MIL) [Whitehouse and Dyson, 1974] and the spatial autocorrelation function (ACF) [Wald, Vasilic et al., 2007] (see Chapter 3 for details), were used to examine the spatial distribution of TB within the rectilinear parallelepiped subvolumes of TB. A threshold of ≥15% BVF was applied to identify bone from marrow in the MIL algorithm and the full-width at half-maximum (FWHM) of the spatial autocorrelation function reflected the trabecular width. Both measures were sampled uniformly over a sphere using 5° increments in polar angles φ and θ.

Singular values $\lambda_1, \lambda_2, \lambda_3$ of the 3x3 fabric tensor depict the relative distribution of bone along eigenvectors $\hat{\mathbf{v}}_1, \hat{\mathbf{v}}_2, \hat{\mathbf{v}}_3$. The non-normalized magnitudes of $\lambda_{3,\mathrm{FWHM}}$ and $\lambda_{3,\mathrm{MIL}}$ were considered as structural parameters in concert with the structural anisotropies: $\mathrm{SA}_{\mathrm{FWHM}}$ and $\mathrm{SA}_{\mathrm{MIL}}$. As defined in Chapter 3, SA is the ratio of the

largest and smallest normalized eigenvalues, $\hat{\lambda}_3 / \hat{\lambda}_1$, where $\hat{\lambda}_i = \lambda_i / (\lambda_1 + \lambda_2 + \lambda_3)$ for i=1,2,3. As TB is known to adapt to its mechanical environment according to Wolff's law, the ability to detect changes in TB orientation is important. To capture the reproducibility of $\hat{\mathbf{v}}_3$, $\Delta\theta_z = \cos^{-1}(\hat{\mathbf{v}}_3 \bullet \hat{\mathbf{z}})$ reflects the angle between the average $\hat{\mathbf{v}}_3$ and $\hat{\mathbf{z}}$ and $\Delta\theta_3$ reflects the average variation angle within each subject relative to the average $\hat{\mathbf{v}}_3$.

4.3.4.10 Finite-element computation of elastic constants

Orthotropic elastic coefficients were determined through simulated axial compression and shear tests on grayscale BVF-maps of the parallelepiped subvolumes and in the segmented full-cross sectional volume. Each voxel with a BVF greater than 15% was modeled as a single hexahedral (eight-node) finite element with a Young's modulus proportional to its BVF - $\mathrm{YM}_{i,j,k} = (\mathrm{BVF})_{i,j,k} * \mathrm{E}_{\mathrm{tissue}}$ where $\mathrm{E}_{\mathrm{tissue}} = 15\,\mathrm{GPa}$ and a Poisson's ratio of 0.3 [Rajapakse, Magland et al., 2010]. Weighting each voxel's Young's modulus by its BVF more accurately enables a consideration of the contributions from partial-volumed voxels. Each compression and shear was applied relative to the faces of the subvolume, as shown in Figure 4.8k, while restricting the other faces. The structure's apparent Young's moduli, E_{xx}, E_{yy}, and E_{zz} and shear moduli, G_{yx}, G_{yz}, and G_{zx} relative to the image coordinate system $\hat{\mathbf{x}}, \hat{\mathbf{y}}, \hat{\mathbf{z}}$ were calculated by minimizing the stress through the conjugate gradient descent. Since E_{xx} (along R→L direction) was generally the smallest of the three elastic moduli and E_{zz} (along I→S direction) the largest, mechanical anisotropy was defined by E_{zz}/E_{xx}. In addition, finite-element linear compression tests performed along the bone's longitudinal axis of the full

cross-section resulted in Young's modulus, E^{CS}_{zz}. A more detailed description of the linear μFE simulations are provided in Chapter 5.

4.3.4.11 Statistical analyses

Parameter reproducibility was assessed by the coefficient of variation (CV). The intra-class correlation coefficient (ICC) of each parameter was computed to evaluate statistical reliability. Analysis of variance (ANOVA) was performed to determine the method's relative sensitivity to discriminate subjects on the basis of the measured metrics. The Fisher Z- transform [Fisher, 1925] was used to compare correlation coefficients between the anisotropic and isotropic data. Statistical analyses were performed in Microsoft Excel (Microsoft Corp., Seattle, WA) and JMP-IN (SAS Institute Inc., Cary, NC).

4.4 Results

4.4.1 Image quality

Image quality (motion-induced artifacts, image artifacts, and SNR) was consistent over the course of the study. Navigator detected in-plane translations did not exceed 4 pixels (~500 μm) for any one scan, implying robust immobilization during acquisition. Two out of the forty-two scans were motion corrected using the autofocusing technique as image blurring was obvious despite navigator correction. This is most likely due to the deleterious effects of rotation motion during the course of the scan which cannot be addressed by employing FLASE-based navigators. Mean SNRs in the anisotropic and isotropic images were 18.7±1.7 and 7.8±1.2, respectively. The analysis volume retained after retrospective registration for the anisotropic

(isotropic) datasets ranged from 45% (41%) to 93% (91%) with mean overlaps of 75% (72%) of the original mask volume. Baseline and follow-up anisotropic resolution images from a 40-year old female volunteer are provided in Figure 4.9 to illustrate the visual reproducibility afforded by combining the prospective and retrospective registration techniques. For this example, 68% of the original baseline volume was retained across the follow-up time points.

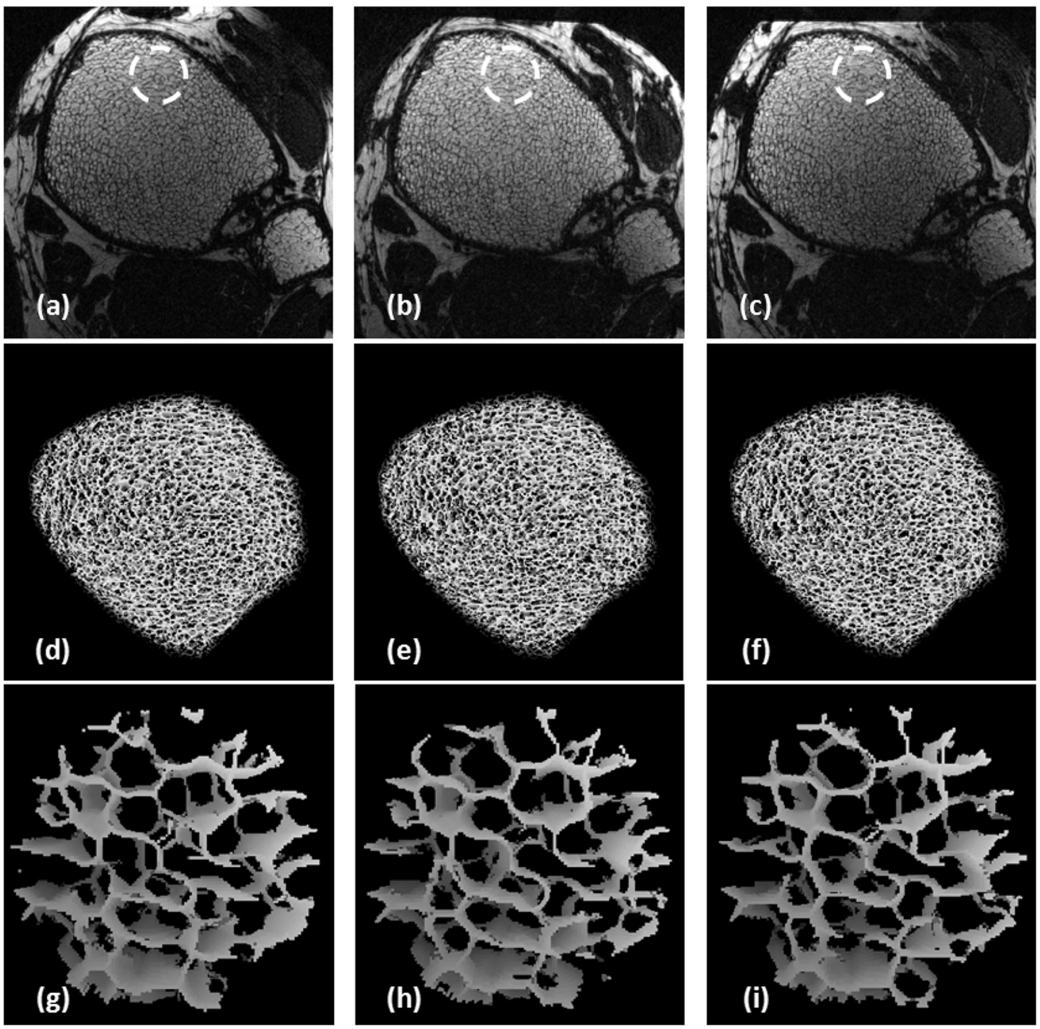

Figure 4.9 Illustration of serial reproducibility in one study subject (F, 40 years): a-c): acquired 3D FLASE images in the anisotropic resolution mode; d-f) 3D rendition of skeletonized images; g-i) virtual cores from locations indicated in a) through c).

4.4.2 Reproducibility and reliability

Ranges, means, CV±σ, and ICCs for parameters of scale, topology, orientation, and elasticity are summarized for all subjects in Table 4.1. Principal material directions were closely aligned with the z-axis of the scanner coordinate system (essentially paralleling the tibial axis). Angles $\Delta\theta_z \pm \Delta\theta_3$ for MIL and ACF were 3.8±3.2° and 3.8±3.1°, respectively, in the anisotropic images. Corresponding values derived from the isotropic images showed greater offsets relative to $\hat{\mathbf{z}}$, 5.8°±6.1 and 5.9°±6.2, respectively. As expected, the predicted Young's modulus along the bone's long axis (E_{zz}) was largest. Mechanical anisotropy was larger than structural anisotropy in all subjects for both resolution modes.

Table 4.1 Reproducibility results for parameters of scale, topology, orientation, and elasticity

Table 4.1

	Anisotropic				Isotropic			
	Range	**Mean**	**CV%**	**ICC**	**Range**	**Mean**	**CV%**	**ICC**
BV/TV (%)	[9,13.1]	10.8	2.4	0.97	[9.0,13.8]	11.8	2.8	0.94
Tb.Th (μm)	[107,123]	115	1.0	0.96	[122,134]	127	0.87	0.94
S/C	[5.4,10.7]	7.6	5.2	0.97	[1.7,7.3]	4.1	8.1	0.99
EI	[0.4,0.8]	0.6	5.2	0.97	[1,4.5]	2.0	7.9	0.98
SA_{FWHM}	[2.0,2.3]	2.2	3.3	0.69	[1.2,1.5]	1.3	3.3	0.86
$\lambda_{3,FWHM}$	[7.1,10.9]	8.7	2.8	0.98*	[3.6,5.6]	4.4	5.3	0.93
SA_{MIL}	[1.9,2.2]	2.1	2.3	0.75	[1.2,1.4]	1.3	3.2	0.79
$\lambda_{3,MIL}$	[55,103]	83.0	4.2	0.98*	[31,65]	47.0	6.0	0.94
E_{xx} (GPa)	[0.3,0.5]	0.39	2.4	0.99*	[0.4,0.6]	0.53	4.6	0.89
E_{yy} (GPa)	[0.3,0.62]	0.44	4.1	0.98*	[0.5,0.8]	0.63	8.9	0.62
E_{zz} (GPa)	[0.9,1.4]	1.11	3.5	0.98*	[0.6,1.3]	0.92	7.5	0.85
G_{xy} (GPa)	[0.1,0.2]	0.18	2.9	0.99*	[0.2,0.3]	0.26	4.9	0.82
G_{xz} (GPa)	[0.2,0.4]	0.28	3.6	0.98*	[0.2,0.4]	0.31	7.4	0.69
G_{zy} (GPa)	[0.2,0.3]	0.26	1.5	0.99*	[0.2,0.3]	0.30	4.5	0.91
E_{zz}/E_{xx}	[2.6,3.4]	2.9	3.3	0.89	[1.25,2.0]	1.7	6.7	0.86
E^{CS}_{zz} (GPa)	[0.9,1.7]	1.2	3.9	0.97	[0.5,1.1]	0.81	5.8	0.96

Fisher Z-transform was used to compare ICCs between the two image resolutions - * indicates significantly different ICC.

Reproducibility was generally higher in the anisotropic data although parameters of scale, BV/TV and Tb.Th, were highly reproducible in both resolution regimes (CV<2.8%). Topological measures (S/C and EI), which are more sensitive to variations in SNR, were less reproducible than measures of scale and structural anisotropy. The apparent values of BV/TV and Tb.Th were greater in the isotropic images, presumably due to the larger in-plane voxel size employed relative to the anisotropic images. Furthermore, in the isotropic images, the TB network appears more rod-like and less structurally anisotropic as indicated by lower S/C, SA_{FWHM}, SA_{MIL}, and E_{zz}/E_{xx}. The

order of apparent moduli was consistent between the two resolution regimes even though absolute values were different (0.92 GPa, 0.63 GPa, and 0.53 GPa for the isotropic acquisition versus 1.11 GPa, 0.44 GPa, and 0.39 GPa for E_{zz}, E_{yy} and E_{xx} in the anisotropic acquisition, respectively) and the mechanical anisotropy derived from the isotropic images was lower. Reliability, as measured in terms of the ICC, was higher for all parameters derived from the anisotropic images, except S/C, EI, and SA_{FWHM}, and SA_{MIL}.

Images obtained at the two distinct resolutions from a 35-year old male volunteer acquired in the same session are displayed in Figure 4.10. Lower SNR is evident in Figure 4.10b (SNR=8.5) relative to 10a (SNR=18.2). Virtual cores in Figure 4.10c and d show good alignment and visual agreement consistent with the patient positioned identically during both acquisitions. Surface perforations visible in the virtual core generated from the isotropic resolution data are not evident for the cores derived using at anisotropic resolution.

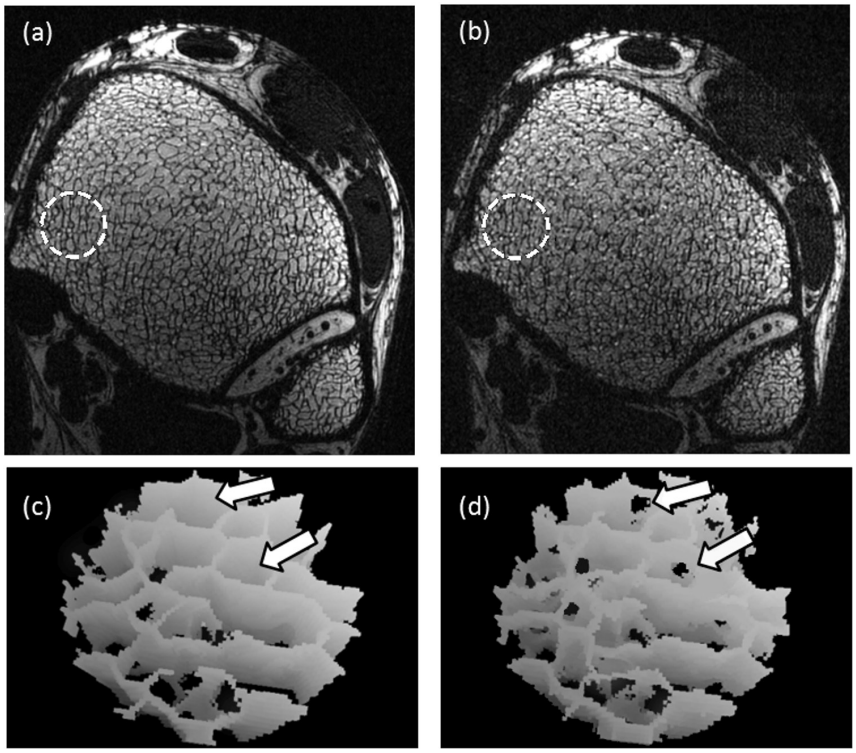

Figure 4.10 Baseline 3D FLASE images of distal tibia in a 35-year old male volunteer acquired with anisotropic (a) and isotropic (b) resolution protocol. Locations of virtual cores (c) and (d) after 90° clock-wise rotation, are indicated by the dashed circles in a) and b). Virtual cores are digital skeletons of TB image (voxel size 69.5 x 69.5 x 69.5 μm^3 after sinc interpolation). Arrows indicate locations of perforations in longitudinal plates visible in (d) but not (c).

Scatter plots for selected structural measurements are given in Figure 4.11a-f to illustrate the methods' ability to discriminate subjects. Table 4.2 details the results of variance analysis indicating the anisotropic protocol to afford greater discrimination with an average of 15.8 of the 21 possible pairs being significantly different, versus 10.6 pairs in the isotropic imaging protocol (75% versus 50%).

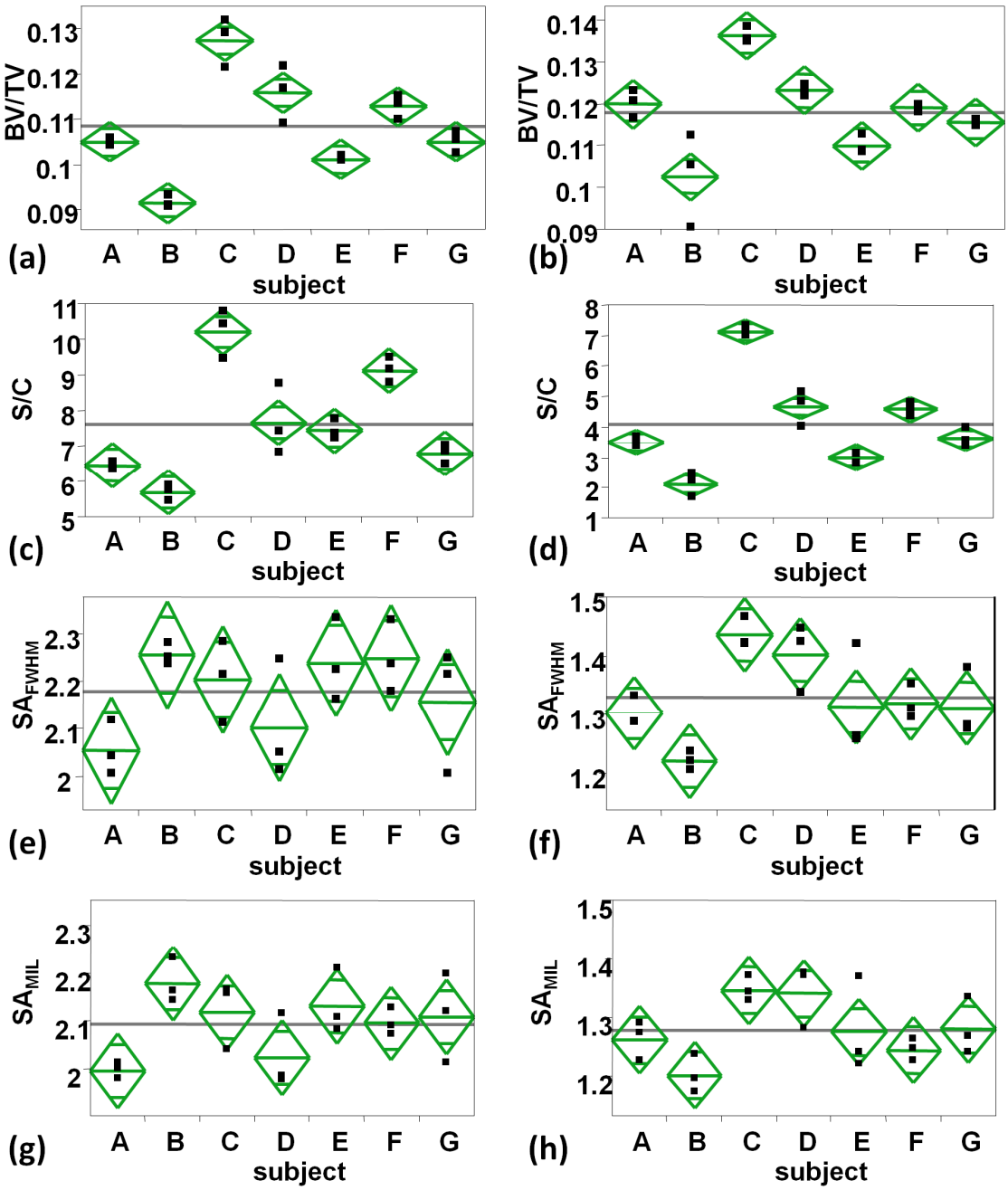

Figure 4.11 Scatter plots of select structural parameters in seven subjects for both resolution regimes showing degree of inter-subject discrimination and extent of serial reproducibility: a), c), e), and g) anisotropic; b), d), f), and h) isotropic. BV/TV and S/C were assessed in the large masked regions where as SA measures were determined in rectilinear parallelepiped subvolumes (see Figure 4.8). Diamonds represents 95% confidence interval around parameter means.

Table 4.2 Number of significantly different pairs of parameter means derived from anisotropic and isotropic exams for all 7 subjects (out of total of 21) showing discriminating ability of the method.

Table 4.2

Parameter	Anisotropic	Isotropic
BV/TV (%)	17	13
Tb.Th (μm)	19	13
S/C	16	17
EI	19	17
SA_{FWHM}	3	12
$\lambda_{3,FWHM}$	17	12
SA_{MIL}	5	5
$\lambda_{3,MIL}$	15	13
E_{xx} (GPa)	18	1
E_{yy} (GPa)	18	11
E_{zz} (GPa)	18	9
G_{xy} (GPa)	18	6
G_{xz} (GPa)	20	12
G_{zy} (GPa)	17	13
E_{zz}/E_{xx}	15	5
E^{CS}_{zz} (GPa)	18	10
Average	**15.8**	**10.6**

Table 4.3 Correlations of single structural and mechanical parameters derived from images obtained in the two resolution regimes (anisotropic versus isotropic). Fitting parameters reflect comparison of means from three repeat scans in seven subjects.

Table 4.3

Parameter	Slope	Intercept	R^2	p-value
BV/TV (%)	0.893	0.021	0.94	****
Tb.Th (μm)	0.57	61.2	0.96	**
S/C	0.93	-2.97	0.83	**
EI	5.5	-1.4	0.72	**
$\lambda_{3,FWHM}$	0.53	0.17	0.88	**
$\lambda_{3,MIL}$	0.52	0.43	0.90	**
E_{xx} (Gpa)	0.23	0.53	0.17	
E_{yy} (Gpa)	0.45	0.38	0.52	
E_{zz} (Gpa)	0.72	0.12	0.90	***
G_{xy} (Gpa)	0.37	0.19	0.43	
G_{xz} (Gpa)	0.52	0.16	0.84	**
G_{zy} (Gpa)	0.44	0.19	0.72	*
E^{CS}_{zz} (Gpa)	0.61	0.08	0.80	*

**p<0.01, **p<0.005, ***p<0.001, ****p<0.0005*

Slopes, intercepts, R^2 values and p-values for single-parameter correlations between the two resolution regimes are given in Table 4.3. Parameters of scale and topology were positively correlated (R^2>0.72, p<0.005), however the slopes deviated substantially from unity. Longitudinal components of fabric ($\lambda_{3,FWHM}$, $\lambda_{3,MIL}$) and elastic moduli (E_{zz} and E^{CS}_{zz}) were well correlated between the two voxel sizes ($0.8 \leq R^2 \leq 0.9$,

p<0.005). Elastic constants perpendicular to the longitudinal axis, E_{xx}, E_{yy}, and G_{xy}, were not significantly correlated nor were direction-dependent measures like SA and E_{zz}/E_{xx}. The lack of correspondence in these measures is likely a result of the limited overlap in parallelepiped subvolumes from the two acquisitions.

For both voxel sizes, strong inter-parameter correlations were observed (Figure 4.12a-b) for instance, between BV/TV and E_{zz} (R^2=0.93, p<0.0005 and R^2=0.95, p<0.0005), and between S/C and E_{zz} (R^2=0.72, p<0.01 and R^2=0.79, p<0.01). Mechanical anisotropy paralleled SA_{FWHM} and SA_{MIL}, as shown in Figure 4.12c for the isotropic voxel size (R^2=0.82, p<0.005 and R^2=0.89, p<0.005 for MIL and ACF, respectively). On the other hand, structural and mechanical anisotropy were not well correlated in the anisotropic data, emphasizing the importance of resolution isotropy when detecting directionally

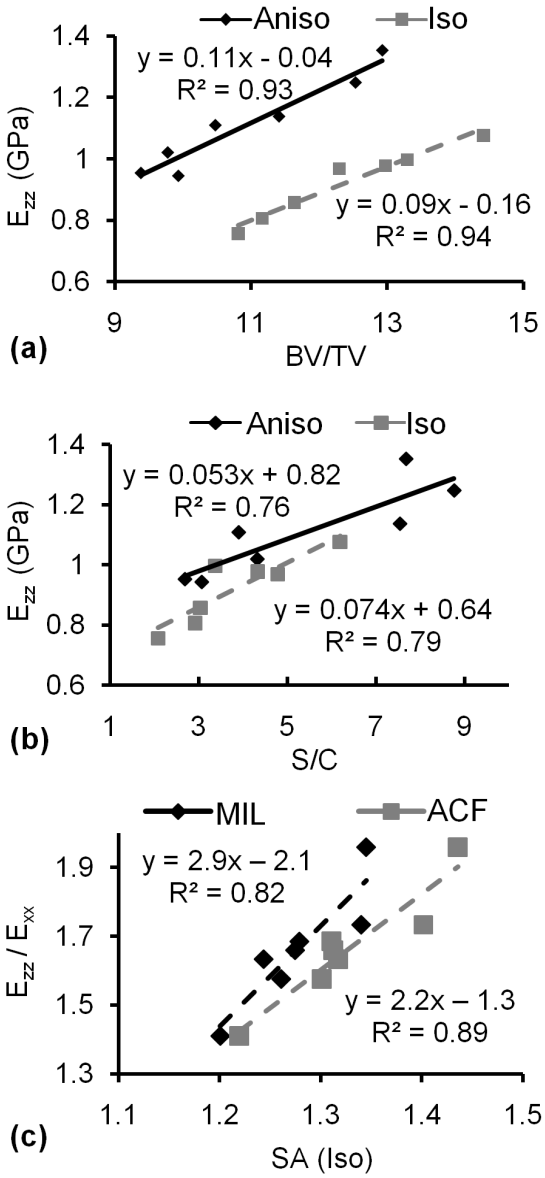

Figure 4.12 In (a) and (b), correlations between selected structural and mechanical parameters in both resolution regimes showing extent of correlation at both resolution regimes. (c) Mechanical anisotropy versus both SA_{MIL} and SA_{FWHM} in the isotropic images. In (a-c), each data point corresponds to the mean parameter value of a single subject.

dependent metrics. In addition, SA_{FWHM} and SA_{MIL} were better aligned in the isotropic images (Figure 4.13) although SA_{FWHM} was larger in magnitude than SA_{MIL}.

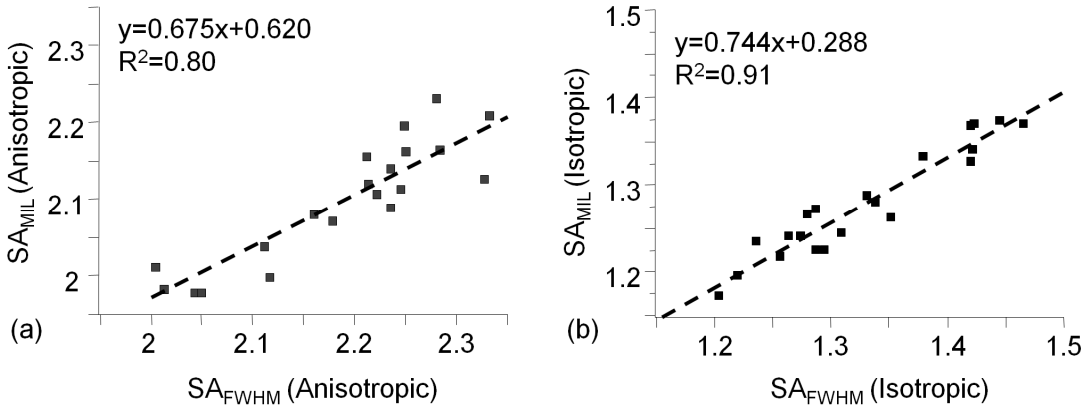

Figure 4.13 Correlations between SA_{MIL} and SA_{FWHM} in parallelepiped subvolumes from twenty-one anisotropic (a) and isotropic (b) images.

4.5 Discussion

The incorporation of PI techniques has not been widely practiced in μMR imaging of TB due to SNR limitations. However, the SNR offered at higher field strength allows some flexibility. The feasibility of PI in μMRI of TB has been demonstrated with fast gradient echo and balanced steady-state free precession (bSSFP) sequences in the calcaneus, knee, and hip using an auto-calibrated approach similar to the one used here [Banerjee, Choudhury et al., 2006]. In that work, PI was used to reduce the scan time and increase SNR efficiency of a multiple-acquisition bSSFP sequence using R=2, 3, and 4 at 3T. The authors observed an increase in trabecular number for successive increases in the reduction factor in all three anatomical locations. The largest increase was observed in the femur where the sensitivity encoding function of the receiver coil was inferior to that achieved in the knee and calcaneus. It is expected that the results

found in that work should carry over to the tibia, however differences in receiver hardware, pulse sequence, and anatomy make the results unique to each implementation. In this work, PI as a method of limiting the scan time increase associated with higher resolution was evaluated in terms of the reproducibility and sensitivity of image-derived TB structural and mechanical parameters.

In concert with evaluating the potential for isotropic resolution, common sources of error encountered in high-resolution TB imaging including image artifacts, image degradation from subject motion, and repeat scan volume misalignment were addressed to improve the reproducibility of repeated measures. Through-slice signal fluctuation attributed to a specific stimulated echo was minimized by changing the sign of the crusher moment relative to that of the slice-encoding gradient. As the size and position of a subject's ankle within the RF coil can impact B1 inhomogeneity (the major source of stimulated echo artifacts due to deviations of the phase-reversal pulse from 180º) [Vasilic, Song et al., 2004], elimination of the stimulated echo artifact would improve scan quality and the reproducibility of quantitative measures.

It is well known that even subtle motion during the scan can cause large errors in the derived structural parameters [Gomberg, Wehrli et al., 2004; Lin, Ladinsky et al., 2007]. Here, motion corruption was minimized by introducing a rigid platform that is fixed to the scanner table and provides tight immobilization of the foot. Retrospective motion correction using navigators [Song and Wehrli, 1999] and autofocusing [Lin, Ladinsky et al., 2007] were also employed. In prior studies, cases have occurred in which, despite no visible subject motion-induced degradation, lower quality images (measured using NGS metric) after navigator-based motion correction were observed.

This situation presumably results from errors in the estimated motion trajectories due to the lower SNR of the navigator echoes. By using the optimal excitation flip angle (140°) and pulse timing within the FLASE pulse sequence [Rad, Wald et al., 2009], the SNR of the navigator acquisitions was maximized allowing for greater motion detection sensitivity. However, non-rigid motion within the surrounding soft tissue, such as muscle contractions and skin depressions, and through-plane translations/rotations may also lead to navigator-corrected images with lower NGS values. In such cases, visual inspection of motion-corrected and uncorrected images was necessary to assess the extent of motion-induced blurring and whether correction would yield optimum results or not. However, no such cases occurred in this study.

The combination of utilizing an immobilization platform and prospective registration greatly improved the reproducible positioning of the ankle. However, the overlap of the scan volumes was significantly reduced when the tibia's longitudinal axis was misaligned by 15° or more between baseline and follow-up acquisitions. Misalignments of this magnitude cause errors in the prospective registration method [Rajapakse, Magland et al., 2008], and in one case resulted in the common volume being only 43% of the original scan volume. Another potential pitfall of the prospective registration strategy pertains to the susceptibility gradients arising from the bone to bone-marrow interface, which is dependent on the angle between the main magnetic field and the preferential direction of the TB [Yablonskiy, 1998]. By adjusting the gradient axes instead of physical realignment of the ankle, the appearance of TB in such regions is vulnerable to artifactual thickening due to susceptibility-induced dephasing.

Although this study involved only healthy volunteers between 24 and 42 years of age, the relative range in the parameters, for instance BV/TV (8.8% -13.6%) and S/C (5.0- 16.6), are of similar order of magnitude as those seen in recent patient studies [Benito, Vasilic et al., 2005; Wehrli, Ladinsky et al., 2008]. While these relatively large inter-subject differences may be surprising, they are unlikely artifactual, such as arising from mismatch in the scan location between subjects, since anatomically correspondent locations were selected with an inter-subject variation of no more than 1-2 mm between subjects. Also, the inter-subject variations are similar in magnitude to those in an earlier reproducibility study involving subjects of similar age [Gomberg, Wehrli et al., 2004].

Coefficients of variation for the anisotropic data demonstrated substantially improved reproducibility for parameters of scale and topology of 1-5% relative to those reported previously (3%-9%) in the distal tibia at the same 137x137x410 μm^3 voxel size at 1.5T [Gomberg, Wehrli et al., 2004]. For images acquired with isotropic voxels, CVs were somewhat larger (1-8%), likely resulting from reduced SNR and, on average, a smaller analysis volume. Micro-FE-derived elastic coefficients had mean CVs in the range of 1-4% and 4-9% (anisotropic and isotropic, respectively) compared to the 4-9% variability found for similar parameters derived from images of the distal radius with a 156x156x500μm^3 voxel size in seven subjects at 1.5T [Newitt, van Rietbergen et al., 2002].

The enhanced reproducibility was not achieved at the expense of sensitivity, as shown by the intra-class correlation coefficients, which were generally greater than 0.9, and variance analysis (Table 4.2 and Figure 4.11). ICCs of the isotropic images averaged 0.87 for all parameters investigated versus 0.92 for the anisotropic images. A

pair-wise comparison of mean parameter values among subjects showed that most parameters were significantly different from each other. For the parameters derived from the anisotropic data in Table 4.2, on average, 15.8 (of the possible 21 pair-wise comparisons) were significant, whereas for the isotropic data only 10.6 were significant. However, measurements sensitive to the structural anisotropy of TB, namely S/C, EI, SA_{FWHM}, and SA_{MIL}, were stronger discriminators in the isotropic images as indicated by higher ICCs in Table 4.1. Of these parameters, only SA_{FWHM} approached significance ($p<0.09$) and showed a substantial improvement in differentiating subject pairs: 12 in the isotropic images versus only 3 in the anisotropic images. Although values of $\Delta\theta_3$ for both MIL and ACF indicated better reproducibility of $\hat{\mathbf{v}}_3$ when using anisotropic voxels, this is likely a manifestation of the thicker slices used here resulting in increased alignment with the image $\hat{\mathbf{z}}$ axis (see Chapter 3 for effect of thicker slices on TB orientation).

Qualitatively, despite lower SNR in the isotropic FLASE images, some of the surface-rendered skeleton maps show clear delineation of specific structural features, in particular perforations in longitudinal plates (Figure 4.10). Even though the ground truth is not known, it is plausible that such features are more likely masked by partial volume averaging as the resolution is relaxed along the orientation of the longitudinal trabeculae. Similarly, certain structural features, i.e. rod-like structures and plate perforations, are lost upon down-sampling an image of TB from a distal tibia specimen with voxel size of $(160\mu m)^3$ to $160\text{x}160\text{x}480\mu m^3$ (Figure 4.14). The structure in the virtual core extracted from the anisotropic dataset (Figure 4.14c) appears more plate-like than that obtained from the isotropic data (Figure 4.14d). Magnifications of Figure 4.14e and 14f show

trabecular rods (curves, labeled blue) at the isotropic voxel size, which are either unresolved or are rendered as plates (surfaces, labeled gray) at the lower through-plane resolution. Single parameter correlations between the two regimes (Table 4.3) suggest that the between-subject variability in many parameters (including BV/TV, Tb.Th, S/C, EI, and E_{zz}) can be detected at either voxel size.

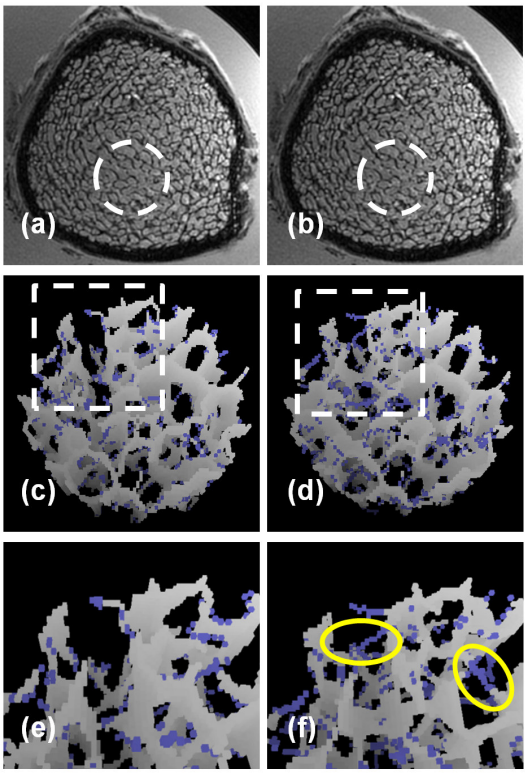

Figure 4.14 3D FLASE images of fixed cadaveric distal tibia specimen: a) image after downsampling along slice direction from 160µm (b) to 480µm. Images in (a) and (b) have in-plane voxel dimension of 160µm. c-f) Virtual cores highlighting loss of transverse trabecular rod (i.e. curve in skeleton representation, left yellow ellipse of panel (f)), and similarly, two nearby curves (right yellow ellipse in panel (f)) that appear as a surface at lower z-resolution in panel (e).

Correlations between the measured structural and mechanical parameters are of interest as Wolff's Law predicts their interdependence [Wolff, 1892; Cowin, 1986]. For example, the degree of directional dependence of TB, characterized by its SA, has been shown to increase with age and disease [Mosekilde, Viidik et al., 1985]. Structural anisotropy increases due to the preferential loss of transverse trabeculae making the bone more prone to failure by buckling. The measured agreement between structural

and mechanical anisotropies is limited as we quantified the elastic constants relative to image coordinate axes (which may be slightly offset from the anatomical axes due to small misalignment in the scanner) and SA relative to calculated material axes. A tensor rotation of the elasticity tensor such that it aligns with the principal material directions is necessary for their direct comparison. Although such a rotation was not performed, the strong correlation between structural and mechanical anisotropy in the isotropic images is gratifying (Figure 4.12c).

MIL and ACF performed similarly in the two resolution regimes. The agreement found in both anisotropic and isotropic images (Figure 4.13) suggests the methods have similar sensitivity to TB directional dependence. Principal material directions were closely aligned with $\hat{\mathbf{z}}$ of the scanner coordinate system (essentially paralleling the tibial axis). Since angles $\Delta\theta_z \pm \Delta\theta_3$ for MIL and ACF were quite similar, neither can be conclusively identified as being more sensitive to changes in orientation. Unfortunately, patient repositioning, differences in superior-inferior coverage (10mm versus 13mm), and inter-scan registration prevented successful registration of the parallelepiped subvolumes between scanning modes (anisotropic and isotropic), thus barring a comparison of MIL and ACF across the two resolution regimes. However, similar to the results of Chapter 3, SA was higher in images with anisotropic resolution and the principal material direction was more closely aligned with $\hat{\mathbf{z}}$.

The reduced SNR of the isotropic data is presumably a significant cause of the differences found in the structural parameters between the two regimes examined, as previously shown by Li et al. [Li, Magland et al., 2008], thereby mitigating the potential benefit of voxel isotropy. The isotropic 3T protocol should yield SNR comparable to a

previous 1.5T protocol given a 100% gain in SNR measured in bone marrow at 3T relative to 1.5T with the same pulse sequence. In the present work, the measured SNR was less than half that achieved with the anisotropic FLASE sequence at 3T. The lower SNR observed in the isotropic data is attributed to noise correlation associated with parallel reception [Pruessmann, Weiger et al., 1999; Blaimer, Breuer et al., 2004].

Even though the distal tibia is not a common osteoporotic fracture site, it is load-bearing site similar to the principal osteoporotic fracture sites, the vertebrae and femur, and should therefore undergo similar structural and mechanical changes with aging and disease progression. Furthermore, the distal tibia has been shown to respond to antiresorptive intervention including estrogen and testosterone supplementation [Benito, Vasilic et al., 2005; Wehrli, Ladinsky et al., 2008]. The methodology described is applicable to other appendicular locations such as the calcaneus, proximal tibia, distal femur, or distal radius, the latter being a fracture site. Lastly, there is some potential for μMRI in the proximal femur [Krug, Banerjee et al., 2005], the site of the most traumatic osteoporotic fractures, albeit at much lower resolution, due to the lower intrinsic SNR achievable at this location.

This study was performed in young, healthy subjects who are expectantly more tolerant to holding still than older subjects. Therefore, the reproducibility achieved in these subjects represents a higher bound to what is achievable in patient studies. Further, the primary limitation of the technology is the relatively long scan time. For scan times greater than five minutes, involuntary subject motion can become significant, therefore demanding immobilization and motion correction techniques. However, as demonstrated here, technical improvements such as parallel imaging and improved

receive coil design can substantially reduce scan time and ultimately the costs associated with the procedure.

In conclusion, enhancements in image acquisition and processing techniques at 3T substantially improve the reproducibility of structural and mechanical parameters derived from high-resolution MRI of distal tibia trabecular bone. The ability to distinguish between seven healthy subjects suggests the method is sensitive to the detection of treatment-induced changes in micro-architecture and mechanical competence. Isotropic voxel size offers improved sensitivity to directionally dependent measures of the TB structure, but lower SNR largely offsets the added detection sensitivity in this application. Further development of the technique and advancements in hardware and pulse sequence design can potentially improve reproducibility and make acquisition of TB images with isotropic resolutions more routine.

Appendix

The effect of multiple receiver channels on measured mean of noise in signal-free region of square-root sum of squares (SRSS) reconstruction

Assumptions:

1) Noise is Gaussian distributed with mean of 0 and standard deviation of 1.

2) Noise sources are independent and uncorrelated.

Complex Gaussian noise in SRSS image for N=1 channel

$$Noise = n_1 + in_2$$

$$Noise = \frac{1}{\sqrt{2\pi}}\exp(-x_1^2/2) + i\frac{1}{\sqrt{2\pi}}\exp(-x_2^2/2)$$

The mean of the magnitude is:

$$M(|Noise|,1) = \left(\frac{1}{\sqrt{2\pi}}\right)\int_{-\infty}^{\infty}\sqrt{\left(x_1^2 + x_2^2\right)}\exp(-(x_1^2 + x_2^2)/2)dx_1dx_2 \qquad (1)$$

Complex Gaussian noise in SRSS image for N channels

$$M(|Noise|,N) = \left(\frac{1}{\sqrt{2\pi}}\right)^N\int_{-\infty}^{\infty}\sqrt{\left(x_1^2 + x_2^2 + ... + x_{2N}^2\right)}\exp(-(x_1^2 + x_2^2 .... + x_{2N}^2)/2)dx_1dx_2...dx_{2N}. \qquad (2)$$

Simplifying by changing variables $r = \sqrt{x_1^2 + x_2^2 + \cdots x_{2N}^2}$ for $r: 0 - \infty$

$$M(|Noise|, N) = \left(\frac{1}{\sqrt{2\pi}}\right)^N \int r \exp(-r^2/2) d^{2N} r = \frac{a_{2N}}{\sqrt{2\pi}^N} \int_0^\infty r^{2N} \exp(-r^2/2) dr = \frac{a_{2N}}{2\pi^{N/2}} A(N)$$

(3)

a_{2N} is the shape factor corresponding to 2N-dimensional hyper-sphere, and

$$A(N) = \int_0^\infty r^{2N} \exp(-r^2/2) dr = (2N-1) \int_0^\infty r^{2N-2} \exp(-r^2/2) dr = (2N-1) A(N-1)$$
$$= (2N-1) * (2N-3) \cdots 5 * 3 * 1 * A(0)$$

$$\text{Since } A(0) = \int_0^\infty \exp(-r^2/2) dr = \sqrt{\pi/2} \quad ,$$

$$A(N) = 1 * 3 * 5 * \cdots * (2N-1) * \sqrt{\pi/2} \qquad (4)$$

Returning to a_{2N} , this 2N Gaussian distribution should integrate to 1 over the entire hyper-sphere, therefore

$$1 = \frac{a_{2N}}{(2\pi)^N} \int_0^\infty r^{2N-1} \exp(-r^2/2) dr = \frac{a_{2N}}{(2\pi)^{N/2}} B(N) \qquad (5)$$

Similar to (4), $B(1) = \int_0^\infty r \exp(-r^2/2) dr = 1$;

$$B(N) = 2 * 4 * 6 * \cdots (2N-2)$$

Combining (1)-(4), we get

$$M(|Noise|, N) = \frac{1 * 3 * 5 * \cdots * (2N-1) * \sqrt{\pi/2}}{2 * 4 * 6 * \cdots (2N-2)} \qquad (6)$$

Conclusions:

For N=2; $M(|Noise|,2)$ =1.88

For N=4; $M(|Noise|,4)$ =2.74

When comparing Signal/noise between two coils with N=2 and N=4, the mean noise measurements should be divided by M(N).

For a measured signal/noise of 10 for N=2, signal/noise=10*1.88=18.8

For a measured signal/noise of 10 for N=4, signal/noise=10*2.74=27.4

5 Chapter 5 Fabric and elasticity tensors in μMR images of trabecular bone

5.1 Overview

The main objective of this study was to evaluate the relationship between the fabric and elastic properties of trabecular bone (TB) on the basis of *in vivo* micro-magnetic resonance images of the distal tibia metaphysis. A second aim was to compare the ability of the fabric tensors determined by the mean-intercept-length (MIL) and the spatial autocorrelation function (ACF) to predict the elastic constants of TB. Fabric and elastic measures were determined from μMRI of TB from the distal tibia in specimens (N=30) and live human subjects (N=16). Images were obtained using the fast large-angle spin echo pulse sequence in isotropic resolution mode. The fabric tensor was assessed by both MIL and ACF in rectilinear parallelepiped subvolumes of TB from the images. Elastic properties of the same TB subvolumes were calculated by micro-finite element analysis (μFEA). By modeling TB as an orthotropic material, a model of bone volume fraction and fabric measures predicted the elastic constants with high precision: mean adjusted correlation coefficients (R^2_{adj}) of 0.92 (MIL) and 0.92 (ACF) in the specimen images and 0.82 (MIL) and 0.86 (ACF) in the *in vivo* images. The measurement of bone volume fraction was significantly less capable of predicting the variations in elastic constants associated with location and test direction: R^2_{adj}=0.57 (specimen) and R^2_{adj}=0.13 (*in vivo*). The results emphasize (1) the importance of fabric as a predictor of bone mechanical properties and (2) that the ACF-based fabric tensor is as predictive of TB mechanical competence as the MIL fabric tensor. In conclusion, the

relationship between fabric and elasticity can be assessed in the limited resolution and signal-to-noise ratio regime of *in vivo* μMRI.

5.2 Introduction

Osteoporosis and bone fragility is principally associated with low bone mass. The material density of bone as measured by bone mineral density has been shown to theoretically [Gibson, 1985] and experimentally [Carter and Hayes, 1977] predict bone strength. Several studies suggest a square relationship between apparent density and elastic modulus [Carter and Hayes, 1977]. However, there is some debate about the appropriate power law relationship and in general, the exponent ranges between 1 and 3 [Rice, Cowin et al., 1988; Rho, Ashman et al., 1993]. Nevertheless, a small increase in material density can produce a large increase in strength, and thus material density is considered the primary determinant of bone strength. However, material density is only one component of bone strength. Further, its ability to predict treatment response [Claes, Wilke et al., 1995; Cummings, Karpf et al., 2002; Sarkar, Mitlak et al., 2002] and assess fracture-risk [Ciarelli, Fyhrie et al., 2000; Schuit, van der Klift et al., 2004] is limited. Additional contributors to bone quality, such as trabecular and cortical micro-architecture, are critical to fully characterize the risk of osteoporotic fractures.

Trabecular bone's (TB) structural and mechanical properties are of interest as fragility fractures typically occur at skeletal sites rich in TB. The importance of structural arrangement on mechanical strength is evident in TB trajectories, which follow the main directions of mechanical stress [Wolff, 1892]. Loading experiments have shown TB's mechanical properties vary significantly within and across anatomic locations according to specific functional demands [Bevill, Farhamand et al., 2009]. Though bone density

also varies with location, a significant fraction of the variance (20-50%) in mechanical properties remains unexplained by bone density [Goulet, Goldstein et al., 1994]. An important characteristic of the TB micro-architecture, namely its structural anisotropy, is known to greatly enhance bone's load-carrying capacity without increasing mass, as shown by Hwang et al. in high-resolution magnetic resonance images of specimens of TB from the wrist [Hwang, Wehrli et al., 1997].

Although TB's structural anisotropy was observed as early as the 19th century, the directional dependence of TB was first quantified by the line intercept method in reconstructions of serial sections in 1974 [Whitehouse, 1974]. In three dimensions, the angularly sampled mean-intercept-length measurements were fit to an ellipsoid, which was later expressed as a second-rank tensor known as the fabric tensor [Harrigan and Mann, 1984]. Fabric tensors, which are introduced in Chapter 3, provide compact descriptions of orthotropic structural anisotropy in the form of a 3x3 matrix, where the eigenvectors $\hat{\mathbf{v}}_1, \hat{\mathbf{v}}_2, \hat{\mathbf{v}}_3$ define the main directions of the ellipsoid's axes and the eigenvalues $\lambda_1, \lambda_2, \lambda_3$ the axis lengths. Regressions between elastic moduli and the eigenvalues of the fabric tensor indicated a significant contribution from fabric information to the variation in modulus and strength of TB [Goldstein, Goulet et al., 1993]. Further studies have shown that structural anisotropy improves the BMD-based prediction of failure stress [Oden, Selvitelli et al., 1998] and differentiates individuals with hip fracture from normal controls on the basis of biopsies from the femoral neck [Ciarelli, Fyhrie et al., 2000].

Advances in high-resolution peripheral quantitative computed tomography (HR-pQCT) [Boutroy, Bouxsein et al., 2005] (see Chapter 1) and micro magnetic resonance

imaging (μMRI) [Magland, Wald et al., 2009; Wald, Magland et al., 2010] permit non-invasive assessment of structural information about bone, beyond simple bone densitometry [Genant and Jiang, 2006]. In tandem with micro-finite element (μFE) analysis, these imaging techniques offer the capability to investigate a structural contribution to bone's elastic properties *in vivo*. In this chapter, the contribution of fabric tensor to the prediction of the elastic constants was tested on the basis of specimen and *in vivo* μMR images of the human distal tibia. An orthotropic model developed by Cowin et al. [Cowin, 1985] was used to relate the image-derived fabric tensors to the elastic constants derived by μFEA. The relative abilities of the fabric tensors derived from mean-intercept-length and spatial autocorrelation to explain the variation in TB mechanical properties were also evaluated. The sensitivity of the derived model of BV/TV and fabric measures is then tested in two populations with distinct age and gender differences.

5.2.1 Biomechanics of orthotropic materials

In most skeletal sites, TB possesses orthotropic symmetry, i.e. it has three mutually orthogonal planes of mirror symmetry [Odgaard, Kabel et al., 1997; Zysset, Goulet et al., 1998]. These planes are represented by surface normal vectors $\hat{\mathbf{u}}_1, \hat{\mathbf{u}}_2, \hat{\mathbf{u}}_3$. Relative to this coordinate system, the material possesses nine distinct orthotropic elastic constants: three Young's moduli, E_{11}, E_{22}, E_{33}, three shear moduli, G_{12}, G_{13}, G_{23}, and three independent Poisson's ratios, $\upsilon_{12}, \upsilon_{13}, \upsilon_{23}$. The Young's modulus, E_{jj} (j=1,2,3), is the ratio of the stress T_{jj}, which is applied on the sample plane with normal to direction *j* in the direction *j*, to the strain ε_{jj}, which is measured relative to the plane

with normal to direction *j* along direction *j*. Analogously, the shear modulus (G_{jk}) is the ratio of the shear stress T_{jk} to the shear strain ε_{jk} where subscripts *j* and *k* (j, k=1, 2, 3) define the plane upon which the force is applied and the direction of the force, respectively. Poisson's ratio (υ_{jk}) is the negative ratio of the strain ε_{kk} occurring in the *k* direction to the strain ε_{jj} occurring in the *j* direction due to an applied stress T_{jj}.

The nine elastic constants are arguments in the expressions of the elastic coefficients of the fourth-rank elasticity tensors $\mathbf{C}$ and $\mathbf{S}$, also known as the compliance and stiffness tensors. The compliance tensor relates the stress tensor $\mathbf{T}$ to the strain tensor $\boldsymbol{\varepsilon}$ following Hooke's Law, shown in indicial notation in Eq. 5-1 [Cowin, 1985]:

Eq. 5-1 $$\boldsymbol{\varepsilon}_{ij} = \mathbf{C}_{ijkm}\mathbf{T}_{km} \quad \ni i,j,k,m = 1,2,3$$

$\mathbf{C}$ has 81 entries and maps the nine entries of $\mathbf{T}$ to the nine entries of $\boldsymbol{\varepsilon}$. The condition of moment equilibrium states that at equilibrium, the forces in one direction are balanced by equal and opposite forces, i.e. $T_{ij} = T_{ji} \forall i \neq j$. Therefore $\mathbf{T}$ and $\boldsymbol{\varepsilon}$ are symmetric and the 3x3 matrices can be represented instead by 6x1 vectors [Cowin, 1989]. Consequently, $\mathbf{C}$ simplifies to a 6x6 matrix. The stiffness tensor $\mathbf{S}$, defined as the inverse of the compliance tensor $\mathbf{C}$, relates the shear tensor $\boldsymbol{\varepsilon}$ to the stress tensor $\mathbf{T}$.

The strength of TB can be considered through mechanical testing of TB samples, although experimental assessment of the mechanical properties of cancellous bone is subject to large errors [Keaveny, Morgan et al., 2001]. Alternatively, mechanical simulations using μFEA of TB images can be used to infer changes in strength. An introduction to μFEA is provided in Chapter 1. Micro-FEA of TB images allows the

determination of the mechanical properties of TB in the form of $\mathbf{C}$ and $\mathbf{S}$. Compression and shear tests are simulated relative to the laboratory or image reference frame, denoted by images axes $\hat{\mathbf{x}}, \hat{\mathbf{y}}, \hat{\mathbf{z}}$. In a simulation experiment on a rectilinear parallelepiped volume of TB, compression stresses $\mathbf{T}_{xx}, \mathbf{T}_{yy}, \mathbf{T}_{zz}$ and shear stresses $\mathbf{T}_{yz}, \mathbf{T}_{xz}, \mathbf{T}_{xy}$ are applied relative to the image axes $\hat{\mathbf{x}}, \hat{\mathbf{y}}, \hat{\mathbf{z}}$ as the normal vectors to the faces of the specimen are aligned with the image axes. If $\hat{\mathbf{x}}, \hat{\mathbf{y}}, \hat{\mathbf{z}}$ align with $\hat{\mathbf{u}}_1, \hat{\mathbf{u}}_2, \hat{\mathbf{u}}_3$ (on-axis configuration), respectively, the orthotropic elastic coefficients of the compliance tensor $\mathbf{C}$ can be computed by solving a set of linear equations derived from Eq. 5-2 [Bartel, Davy et al., 2006] as follows:

Eq. 5-2

$$\begin{bmatrix} \varepsilon_{xx} \\ \varepsilon_{yy} \\ \varepsilon_{zz} \\ \varepsilon_{yz} \\ \varepsilon_{xz} \\ \varepsilon_{xy} \end{bmatrix} = \begin{bmatrix} \frac{1}{E_{xx}} & \frac{-v_{yx}}{E_{yy}} & \frac{-v_{zx}}{E_{zz}} & 0 & 0 & 0 \\ \frac{-v_{xy}}{E_{xx}} & \frac{1}{E_{yy}} & \frac{-v_{zy}}{E_{zz}} & . & . & . \\ \frac{-v_{xz}}{E_{xx}} & \frac{-v_{yz}}{E_{yy}} & \frac{1}{E_{zz}} & . & . & . \\ 0 & . & . & \frac{1}{2G_{yz}} & . & . \\ 0 & . & . & . & \frac{1}{2G_{xz}} & . \\ 0 & . & . & . & . & \frac{1}{2G_{xy}} \end{bmatrix} \begin{bmatrix} T_{xx} \\ T_{yy} \\ T_{zz} \\ T_{yz} \\ T_{xz} \\ T_{xy} \end{bmatrix}$$

For an orthotropic material in which the test axes $\hat{\mathbf{x}}, \hat{\mathbf{y}}, \hat{\mathbf{z}}$ are aligned with $\hat{\mathbf{u}}_1, \hat{\mathbf{u}}_2, \hat{\mathbf{u}}_3$, respectively, $\mathbf{C}$ is represented by the diagonal matrix of Eq. 5-2, which will be denoted as $\mathbf{C}_0$ and referred to as the orthotropic compliance tensor. If the material is orthotropic but $\hat{\mathbf{x}}, \hat{\mathbf{y}}, \hat{\mathbf{z}} \neq \hat{\mathbf{u}}_1, \hat{\mathbf{u}}_2, \hat{\mathbf{u}}_3$ (off-axis configuration), the measured elastic constants (e.g. E_{xx}, E_{yy}, E_{zz}) are functions of the on-axis elastic constants E_{jj}, G_{jk}, v_{jk} (where j, k=1,

2, 3). In this case, $\mathbf{C}$ is no longer in the diagonalized form shown in Eq. 5-2 [Cowin, 1989]. Non-zero off-diagonal elements result from a coupling between normal stresses and shear strains. To recover the on-axis orthotropic compliance tensor $\mathbf{C}_0$, and thus the on-axis coefficients, a 3D coordinate transformation matrix $\mathbf{R}_{\Theta_x,\Theta_y,\Theta_z}$ must be applied to the off-axis compliance tensor: $\mathbf{C}_0 = \mathbf{R}^{\mathsf{T}}_{\Theta_x,\Theta_y,\Theta_z}\ \mathbf{C}\ \mathbf{R}_{\Theta_x,\Theta_y,\Theta_z}$. The column vectors of the 3x3 transformation matrix $\mathbf{R}_{\Theta_x,\Theta_y,\Theta_z}$ are the axes of orthotropic symmetry, i.e. $\hat{\mathbf{u}}_1, \hat{\mathbf{u}}_2, \hat{\mathbf{u}}_3$, and the rotation angles $\Theta_x, \Theta_y, \Theta_z$ are applied about the x-, y-, and z-axes of the image coordinate system. One way of determining the coordinate transformation matrix, $\mathbf{R}_{\Theta_x,\Theta_y,\Theta_z}$, and thus $\Theta_x, \Theta_y, \Theta_z$, is by estimating the fabric tensor of TB as the eigenvectors $\hat{\mathbf{v}}_1, \hat{\mathbf{v}}_2, \hat{\mathbf{v}}_3$ of the fabric tensor approximate the axes of orthotropic symmetry.

For convenience, the image is often assumed to be acquired relative to $\hat{\mathbf{u}}_1, \hat{\mathbf{u}}_2, \hat{\mathbf{u}}_3$, i.e. $\hat{\mathbf{x}}, \hat{\mathbf{y}}, \hat{\mathbf{z}} = \hat{\mathbf{u}}_1, \hat{\mathbf{u}}_2, \hat{\mathbf{u}}_3$. This was the procedure used in Chapter 4 and in the work of Rajapakse et al. [Rajapakse, Magland et al., 2010]. Several studies have confirmed this approximation by showing the orthotropic coefficients, computed through μFEA, were more than two orders of magnitude larger than any remaining term [Odgaard, Kabel et al., 1997; Zysset, Goulet et al., 1998]. However, the off-axis derived elastic coefficients in TB can be up to 40% smaller than the on-axis coefficients [Ohman, Baleani et al., 2007].

5.2.2 Relating elasticity to structure

The relationship between the TB fabric tensor and its mechanical behavior was mathematically defined by Cowin in 1985 [Cowin, 1985]. Cowin's model relates the fabric tensor $\mathbf{H}$ to the elastic coefficients of TB possessing orthotropic symmetry. The model is based on the following two assumptions: 1) the matrix material is linear elastic and isotropic such that the mechanical anisotropy of TB results solely from its micro-architecture; 2) the TB microstructure possesses orthotropic symmetry (i.e. it has at least two planes of mirror symmetry) [Cowin, 1985]. Implicit in the second condition is that an orthotropic material's structural anisotropy can be fully characterized by a second-rank fabric tensor (i.e. the fabric directions $\hat{\mathbf{v}}_1, \hat{\mathbf{v}}_2, \hat{\mathbf{v}}_3$ are aligned with the normal vectors to the planes of orthotropic symmetry $\hat{\mathbf{u}}_1, \hat{\mathbf{u}}_2, \hat{\mathbf{u}}_3$). Cowin's model expresses the nine coefficients of the orthotropic compliance tensor $\mathbf{C}_o$ in terms of fabric eigenvalues $\lambda_1, \lambda_2, \lambda_3$, the second invariant of the fabric tensor $\Pi = \lambda_1\lambda_2 + \lambda_2\lambda_3 + \lambda_1\lambda_3$, and nine functions of the bone volume fraction $k_1 - k_9$ [Turner, Cowin et al., 1990] as follows:

Eq. 5-3a $$\frac{1}{E_{ii}} = \frac{1}{E_{tissue}}\left(k_1 + 2k_6 + (k_2 + 2k_7)\Pi + 2(k_3 + 2k_8)\lambda_i + (2k_4 + k_5 + 4k_9)\lambda_i^2\right)$$

5-3b $$\frac{-\nu_{ij}}{E_{ii}} = \frac{1}{E_{tissue}}\left(k_1 + k_2\Pi + k_3(\lambda_i + \lambda_j) + k_4(\lambda_i^2 + \lambda_j^2) + k_5\lambda_i\lambda_j\right)$$

5-3c $$\frac{1}{G_{ij}} = \frac{1}{E_{tissue}}\left(k_6 + k_7\Pi + k_8(\lambda_i + \lambda_j) + k_9(\lambda_i^2 + \lambda_j^2)\right)$$

5-3d $$k_m = k_{am} + k_{bm}\rho^{-\alpha}$$

such that $i,j = 1,2,3; i \neq j$. Eq. 5-3d reflects the power-law dependence of the elastic modulus on the material volume fraction ρ where k_{am}, k_{bm} are eighteen empirically determined constants such that *m*=1, 2, …, 9. Turner et al. showed that a simplified

version of Cowin's model explained 72% to 94% of the variance in elastic constants [Turner, Cowin et al., 1990] in TB samples from bovine femur and human proximal tibia. Van Rietbergen et al. also demonstrated the inclusion of fabric to improve the bone volume fraction-based prediction of the elastic constants in serial reconstructions of twenty-eight TB specimens from a whale vertebral body [Van Rietbergen, Odgaard et al., 1998].

5.3 Materials and methods

The following section outlines the experimental techniques used to image the TB micro-architecture, obtain a fabric tensor representation of TB subvolumes extracted from the μMR images, determine the orthotropic elastic constants via μFEA and coordinate transformation, and relate the resulting fabric measures to the orthotropic elastic constants via Cowin's model.

5.3.1 Specimen imaging

The specimen images used in this study have been previously described in Chapter 3. Briefly, as part of an earlier study [Rajapakse, Magland et al., 2010], fifteen left and fifteen right human distal tibia specimens of 25mm axial length were obtained from cadavers of fifteen donors (four females and eleven males, age range of 55-84 years, mean=70 years). The thirty specimens were demarrowed and fixed prior to imaging them with a custom-designed 3D fast spin-echo sequence (FLASE) on a 1.5T Siemens Sonata Scanner. Each specimen was positioned with the bore of the magnet in accordance with the anatomical positioning of a human subject, i.e. the anterior portion of the tibia specimen facing upward towards the receiver coil. A 64x64x20mm^3

slab was acquired using a 160 μm isotropic voxel in 40 minutes with the following sequence parameters: TE/TR=11ms/80ms, flip angle=140°. Signal-to-noise ratio (SNR) was estimated for each image as the mean marrow signal within the entire TB region divided by the mean intensity of the signal-free region in the background.

5.3.2 Subjects and *in vivo* imaging

High-resolution MR images of the distal left tibiae of sixteen subjects (seven young and healthy and nine post-menopausal) were analyzed. Images of the younger subjects corresponded to baseline acquisitions from a completed reproducibility study (see description in Chapter 4) in which 2 female and 5 male volunteers (age range 24-40 years, mean=34 years) were imaged at three time points over an eight week period [Wald, Magland et al., 2010]. The data associated to the seven young subjects will be referred to as the volunteer (V) data. Baseline MR images of distal tibiae from nine female subjects (60-84 years old, mean=68 years) were selected from an ongoing study evaluating antiresorptive medications on post-menopausal bone loss. Images of the post-menopausal group (PM) were selected based on the absence of motion-induced blurring. All imaging procedures were approved by the IRB and all subjects enrolled in the study had provided informed consent.

The same imaging protocol was implemented for all sixteen (V+PM) subjects. A 64x64x10mm^3 volume at the distal tibia metaphysis was acquired with a four channel phased-array ankle coil on a 3T Siemens Tim Trio using the isotropic FLASE pulse sequence [Wald, Magland et al., 2010] with an approximate two-fold acceleration. Sequence parameters (e.g. TE, TR, flip angle) were identical to those used in specimen imaging. The two-fold acceleration, achieved by variable-density sampling in the right-

left phase encoding direction, reduced the scan time to under 17 minutes. Translational motion tracking and correction was performed using out-of-slab navigator echoes [Magland, Wald et al., 2009] optimized with respect to SNR [Rad, Wald et al., 2009]. Images were reconstructed using the generalized autocalibrating partially parallel acquisitions or GRAPPA technique [Griswold, Jakob et al., 2002; Wang, Wang et al., 2005]. Details on the imaging protocol are provided in Chapter 4 [Wald, Magland et al., 2010].

5.3.3 Processing and structural analysis

Each specimen image (Figure 5.1a) was bone volume fraction processed (i.e. BVF-mapped: marrow-volume fraction mapped [Vasilic and Wehrli, 2005] followed by contrast inversion) to yield images with pure bone and pure marrow corresponding to intensities of 100 and 0 (Figure 5.1b), respectively. BVF is used to describe the partial bone occupancy of a single voxel, while BV/TV (i.e. bone volume/total volume) represents the average BVF of all the voxels within an image volume. As the in-plane trabecular orientation in the distal tibia is known to follow the endosteal cortical boundary, three 8x8x8mm^3 subvolumes of TB were selected at the posterior (P), lateral (L), and anterior-medial (AM) portions (Figure 5.1c-e) of each tibia specimen.

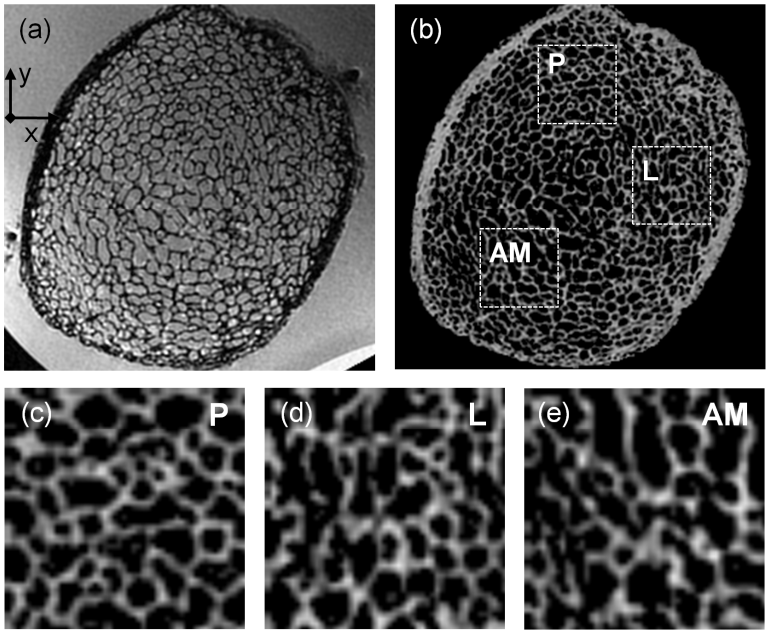

Figure 5.1 (a) Image of distal tibia specimen (52 year old male subject) acquired with isotropic FLASE pulse sequence (positive y-axis corresponds to antero-posterior direction); (b) BVF-map of (a) with three 8x8x8mm^3 subvolumes from posterior-P, lateral-L, and anterior-medial-AM portions of the tibia; (c, d, e) Zoom-ins of three subvolumes indicated in (b).

Prior to processing the *in vivo* images, a high SNR region of TB was manually traced in the anterior portion of the distal tibia image (Figure 5.2a). The average SNR was calculated as the mean marrow signal within this region divided by the mean intensity from a signal-free region. The high SNR region was then BVF-mapped [Vasilic and Wehrli, 2005] and a single rectilinear parallelepiped subvolume of TB was selected (Figure 5.2b).

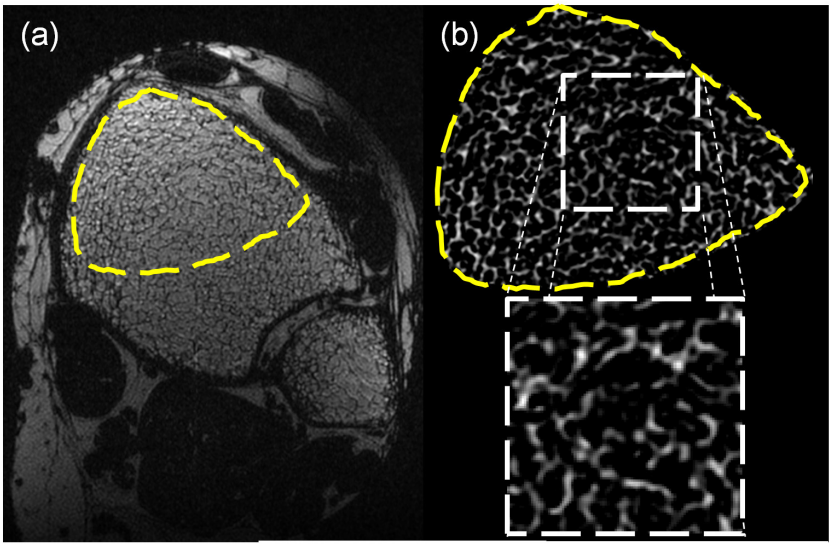

Figure 5.2 (a) *In vivo* isotropic FLASE image of distal tibia from 68 year old female (post-menopausal group) with high-SNR region indicated. (b) BVF-map of high-SNR region with 8x8x8mm^3 subvolume used in structural and mechanical analyses.

Bone volume fraction (BV/TV) and fabric tensor were calculated for all 8x8x8mm^3 BVF-mapped subvolumes (Figure 5.3a). Structural anisotropy of the bone-bone marrow interface was considered using mean-intercept-length (MIL) [Whitehouse, 1974]. Structural anisotropy of the bone phase was assessed by the full-width-at- half-maximum (FWHM) of the spatial autocorrelation function (ACF) [Wald, Vasilic et al., 2007]. Both MIL and the FWHM were sampled in three dimensions at 5° angular increments of polar angles φ and θ (Figure 5.3b), resulting in 905 samples of both MIL and FWHM evenly distributed relative to the unit sphere. A threshold value of BVF ≥15% was used to identify the bone phase during intercept sampling. The MIL and ACF structural tensors, denoted **M** and **A**, were computed following the description in Chapter 3.

According to the inverse square-root relationship defined by Cowin et al. [Cowin, 1986], the associated fabric tensors, denoted $\mathbf{H}_{\mathrm{MIL}}$ and $\mathbf{H}_{\mathrm{FWHM}}$, were computed. Using singular value decomposition of $\mathbf{H}_{\mathrm{MIL}}$ and $\mathbf{H}_{\mathrm{FWHM}}$, normalized eigenvalues of

$\lambda_1, \lambda_2, \lambda_3$ and their eigenvectors $\hat{\mathbf{v}}_1, \hat{\mathbf{v}}_2, \hat{\mathbf{v}}_3$ were determined and organized such that $\lambda_3 > \lambda_2 > \lambda_1$ for each method. Structural anisotropies SA_{MIL} and SA_{FWHM} were calculated as ratio of their respective eigenvalues (λ_3 / λ_1).

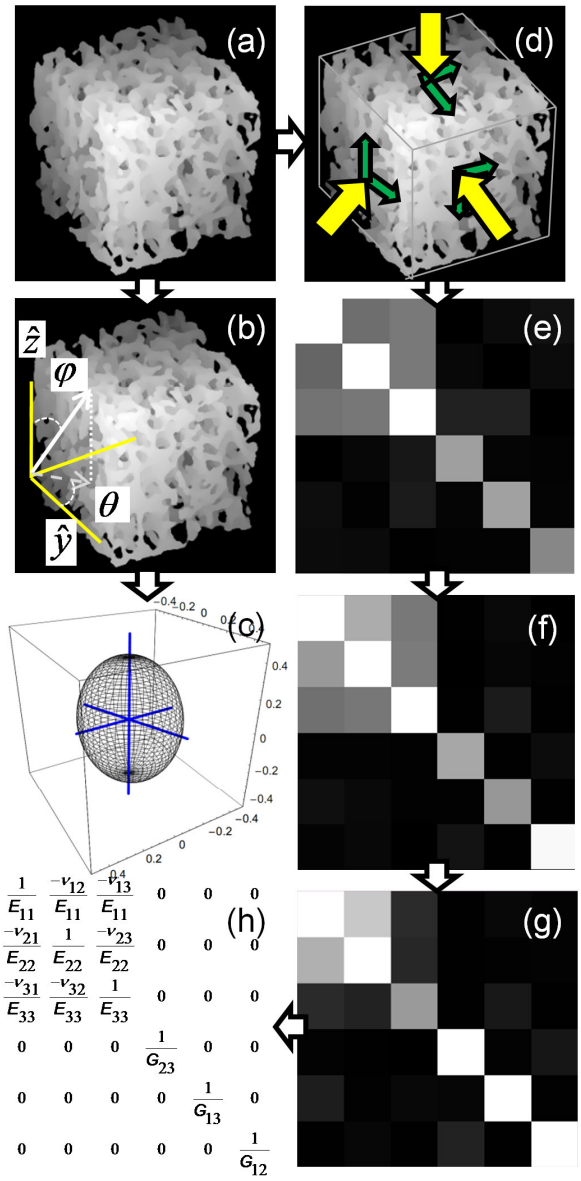

Figure 5.3 Analysis steps for rectilinear parallelepiped subvolume of TB. (a) Surface-rendering of 8x8x8mm^3 subvolume of TB from Figure 5.2b rotated CCW by 30°. (b-c) Calculation of fabric tensor by two methods-MIL and ACF: (b) uniform spherical sampling of mean-intercept-length and FWHM of ACF in image coordinate system; (c) resulting fabric ellipsoid with eigenvectors indicating TB's principal material directions. Steps in estimation of orthotropic elastic constants - E_{11}, E_{22}, E_{33}, G_{12}, G_{13}, G_{23}, ν_{12}, ν_{13}, ν_{23}: (d) six simulated stress and strain experiments to compute stiffness tensor $\mathbf{S}$ shown as image in (e); (f) $\mathbf{S}_o$ is found by the diagonalization (see text) of $\mathbf{S}$; (g) compliance matrix $\mathbf{C}$ was calculated as inverse of $\mathbf{S}_o$; and (h) orthotropic compliance matrix $\mathbf{C}_0$ (off diagonals set to zero) used in determining elastic constants.

5.3.4 Micro-finite element analysis

The 6x6 stiffness matrix was computed using six stress/strain simulations via μFE analysis [Rajapakse, Magland et al., 2010] (Figure 5.3d) of each BVF-mapped rectilinear parallelepiped subvolume. Image voxels were modeled as hexahedron elements with a Poisson's ratio of 0.3 and tissue moduli (E_{tissue}) proportional to BVF such that for pure bone voxels (BVF=100%), E_{tissue}=15GPa. All voxels with a BVF greater than or equal to 15% were retained while those under the 15% cut-off were nulled to prevent errors associated with low SNR. Each finite element vertex (node) was assumed to have three degrees of freedom corresponding to displacements along x, y, and z axes in the image coordinate system [Rajapakse, Magland et al., 2010]. The nodes surrounded by eight elements with zero BVF values (after thresholding) were excluded from the model to save memory and computation time. Simulations were performed relative to the image coordinate system using open-cell boundary conditions, i.e. only the opposite plane was restricted.

The resulting stiffness tensor $\mathbf{S}$ from the μFEA has the following form:

Eq. 5-4

$$\mathbf{S} = \begin{bmatrix} S_{11} & S_{12} & S_{13} & \delta_{14} & \delta_{15} & \delta_{16} \\ S_{12} & S_{22} & S_{23} & \delta_{24} & \delta_{25} & \delta_{26} \\ S_{13} & S_{23} & S_{33} & \delta_{34} & \delta_{35} & \delta_{36} \\ \delta_{14} & \delta_{24} & \delta_{34} & S_{44} & \delta_{45} & \delta_{46} \\ \delta_{15} & \delta_{25} & \delta_{35} & \delta_{45} & S_{55} & \delta_{56} \\ \delta_{16} & \delta_{26} & \delta_{36} & \delta_{46} & \delta_{56} & S_{66} \end{bmatrix}.$$

An image depiction of $\mathbf{S}$ for a typical TB subvolume is shown in Figure 5.3e in which the off-diagonal values δ_{ij} are non-zero but small relative to those of S_{ij} (i, j=1, …,6). Through the tensor rotation of $\mathbf{S}$ from the measurement coordinate system (i.e. $\hat{\mathbf{x}},\hat{\mathbf{y}},\hat{\mathbf{z}}$) to the coordinate system of approximate orthotropic symmetry (i.e. $\hat{\mathbf{u}}_1,\hat{\mathbf{u}}_2,\hat{\mathbf{u}}_3$) -

$\mathbf{S}_o = \mathrm{R}^{\mathrm{T}}_{\Theta_x,\Theta_y,\Theta_z}\ \mathbf{S}\ \mathrm{R}_{\Theta_x,\Theta_y,\Theta_z}$ - the values δ_{ij} of $\mathbf{S}_o$ are minimized (i.e. zero if material is purely orthotropic). Thus, an orthotropic stiffness matrix $\mathbf{S}_o$ (Figure 5.3) was estimated by tensor rotating $\mathbf{S}$ such that the residual function [Van Rietbergen, Odgaard et al., 1996],

Eq. 5-5 $$res = \frac{\sum_{i,j} \delta_{i,j}^2}{\sum_{i,j} S_{i,j}^2} \quad \ni i,j = 1,...,6,$$

was minimized. The minimization was performed brute-force such that $\Theta_x, \Theta_y, \Theta_z$ (rotation angles about the x-, y-, and z-axes of the image coordinate system) were varied from -45° to 45° by 1° increments. The resulting 3x3 coordinate transformation matrix $\mathrm{R}_{\Theta_x,\Theta_y,\Theta_z}$ defines the axes of approximate orthotropic symmetry (i.e. $\hat{\mathbf{u}}_1, \hat{\mathbf{u}}_2, \hat{\mathbf{u}}_3$).

The compliance tensor associated with $\mathbf{S}_o$ was then calculated as $\mathbf{C} = \mathbf{S}_o^{-1}$ (Figure 5.3g). The nine orthotropic elastic constants (three Young's moduli – E_{ii} (i=1, 2, 3), three shear moduli – G_{ij} (i, j=1, 2, 3,i≠j), and three Poisson's ratios – v_{ij} (i, j=1, 2, 3,i≠j)) were determined from the expressions in Figure 5.3h for the orthotropic compliance matrix $\mathbf{C}_o$ (i.e. $\mathbf{C}$ with all δ_{ij} replaced by zeros). Mechanical anisotropy was calculated as $E_{33} / \min(E_{11}, E_{22})$. The error in the stress-strain relationship [Van Rietbergen, Odgaard et al., 1996] caused by forcing orthotropic symmetry was calculated as $\xi = \left\| \mathbf{I} - \mathbf{C}_0^{-1}\mathbf{C} \right\|$ where $\mathbf{I}$ is the 6x6 identity matrix and $\| \ \|$ is the matrix norm operator. The orthotropic error ξ is sensitive to the degree to which the material possesses orthotropic symmetry and the accuracy of the tensor rotation procedure using Eq. 5-5.

5.3.5 Sensitivity to changes in orientation

The performance of the stiffness tensor diagonalization procedure was evaluated by applying known rotations to a rectilinear parallelepiped subvolume of TB. The subvolume (6x6x6mm^3) was extracted from a μCT image (25 μm isotropic voxel size) of a distal tibia specimen (see Chapter 3 for details on μCT images of distal tibia specimens). Clockwise rotations about $\hat{\mathbf{y}}$ and $\hat{\mathbf{z}}$ image axes, which are denoted by angles α_y and α_z, were used to create seven datasets of different orientation, i.e. the original non-rotated subvolume and six rotated subvolumes. The angle α_y was incremented by 10° from 10° to 60°. The six y-rotated datasets (α_y=10°,20°,30°,40°, 50°,60°) were subsequently rotated by α_z, which ranged from 0° to 25° by 5° increments, such that the sixth rotated subvolume had undergone two rotations, first around the y-axis by α_y=60° followed by rotation around the z-axis by α_z=25°. After the binarization of the original subvolume (bone=100, marrow=0) and determination of its BV/TV, the six rotated subvolumes were binarized using thresholds selected such that their BV/TV was within ±5% of the BV/TV of the original non-rotated dataset. Rectilinear parallelepiped subvolumes of 4mm sides were extracted from the center of the seven datasets for μFEA. The original TB subvolume and the subvolume after rotation of α_y=20° followed by α_z=5° are shown in Figure 5.4.

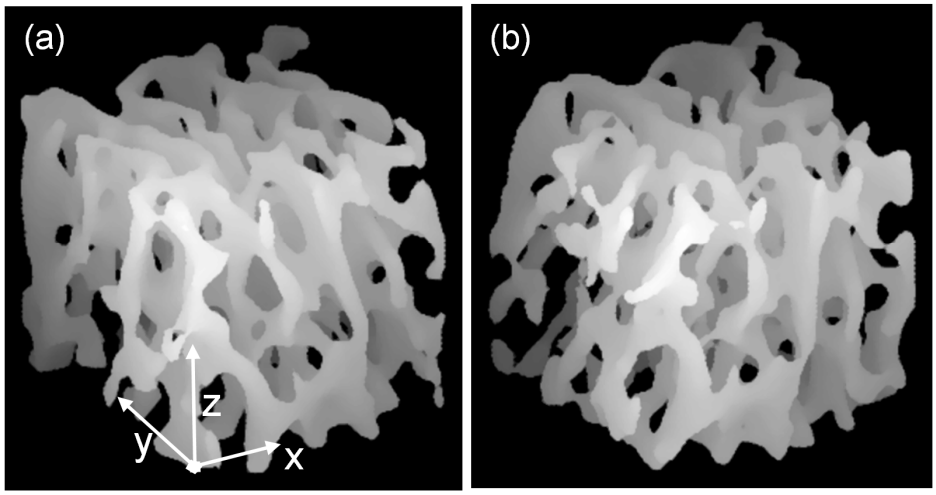

Figure 5.4 (a) Surface-rendering of original μCT subvolume of TB (25μm voxel size) used in orientation experiment. (b) TB subvolume from (a) after rotations around the image y-axis and z-axis by 20° and 5°, respectively. Both subvolumes were 4x4x4mm^3.

The 4mm subvolumes of TB were subjected to six stress/strain simulations using the previously described μFE model [Rajapakse, Magland et al., 2010]. The resulting stiffness tensor $\mathbf{S}$ was diagonalized according to the minimization procedure described above and, from the transformation matrix $R_{\Theta_x,\Theta_y,\Theta_z}$, the rotations angles about the y- and z-axes of the image, Θ_y and Θ_z, were computed. Θ_y and Θ_z were then correlated to the applied rotations α_y and α_z to determine the sensitivity of the diagonalization procedure. In addition, MIL and ACF fabric tensors, $\mathbf{H}_{MIL}$ and $\mathbf{H}_{FWHM}$, were computed for the seven 4mm subvolumes of TB. Angles of rotation defined by MIL and ACF served as independent estimates of the applied rotation angles.

5.3.6 Testing Cowin's model

The degree of alignment between the fabric axes $\hat{\mathbf{v}}_1, \hat{\mathbf{v}}_2, \hat{\mathbf{v}}_3$ and the orthotropic mechanical axes $\hat{\mathbf{u}}_1, \hat{\mathbf{u}}_2, \hat{\mathbf{u}}_3$ (as determined from minimization of Eq. 5-5) was evaluated using an average misalignment angle. The average misalignment angle between the MIL-derived fabric axes $\hat{\mathbf{v}}_1, \hat{\mathbf{v}}_2, \hat{\mathbf{v}}_3$ and $\hat{\mathbf{u}}_1, \hat{\mathbf{u}}_2, \hat{\mathbf{u}}_3$ was calculated as $\Omega^{MIL} = \frac{\sum_{i=1}^{3} \Omega_i^{MIL}}{3}$ where $\Omega_i^{MIL} = \cos^{-1}(\hat{\mathbf{v}}_i \bullet \hat{\mathbf{u}}_i)$. A similar average misalignment angle, denoted by Ω^{FWHM}, was defined for the ACF-derived fabric axes $\hat{\mathbf{v}}_1, \hat{\mathbf{v}}_2, \hat{\mathbf{v}}_3$.

Following Cowin's second assumption, it was assumed that Ω^{MIL} and Ω^{FWHM} were both small. The fabric eigenvalues determined from MIL and ACF, BV/TV, and the nine calculated compliance entries were input into the matrix formulation of Eq. 5-3:

Eq. 5-6
$$\begin{bmatrix} \mathbf{A} & \mathbf{A} * \mathrm{BV/TV}^{-\alpha} \end{bmatrix} \begin{bmatrix} k_{am}^{\alpha} \\ \\ k_{bm}^{\alpha} \end{bmatrix} = \begin{bmatrix} 1/E_{ii} \\ .. \\ -\nu_{ij}/E_{ii} \\ .. \\ 1/G_{ij} \end{bmatrix}.$$

Here, $\mathbf{A}$ is a 9x9 matrix containing the fabric tensor information. Since the right-hand side of Eq. 5-6 is expressed in terms of reciprocal modulus, the fabric information used in $\mathbf{A}$, i.e. the eigenvalues derived from MIL and ACF, is reflective of the inverse of $\mathbf{H}_{\mathrm{MIL}}$ and $\mathbf{H}_{\mathrm{FWHM}}$. If, instead, coefficients of the stiffness tensor were fit, $\mathbf{A}$ would be composed of the eigenvalues of either $\mathbf{H}_{\mathrm{MIL}}$ and $\mathbf{H}_{\mathrm{FWHM}}$.

The eighteen unknown constants $k_{am}^{\alpha}, k_{bm}^{\alpha}$ of Eq. 5-6 were found using a least-squares approximation for each power α which was varied between 1 and 3 by

increments of 0.1. Goodness of fit parameters, R^2, were calculated for each correlation and then adjusted, when necessary, to account for the degrees of freedom in multiple parameter-fits according to $R^2_{adj} = 1-(1-R^2)(N-1)/(N-K-1)$, where N is the number of measurements and K is the number of unknowns [Turner, Cowin et al., 1990]. The joint fit of Eq. 5-6 relative to the pooled specimen (*in vivo*) data, involves N=90x9=810 (16x9=144) and K=18+1=19. The eighteen unknown constants $k^{\alpha}_{am}, k^{\alpha}_{bm}$ and exponent α were calculated using the joint fit. When considering regressions of specific elastic constants, e.g. the three Young's moduli – E_{11}, E_{22}, E_{33}, N is 90x3=270 (16x3=48) for the specimen (*in vivo*) subset while K remains 19. The nine μFE-derived elastic constants were also correlated to linear and power-law models of BV/TV, from which the best fit relative to BV/TV was compared to the best fit determined using the model of Eq. 5-6.

5.3.7 Evaluating sensitivity to differences in elastic constants

As the age and gender make-up were different in the PM (mean: 68 years, nine females) and V (mean: 34 years, five male and 2 females) sub-groups, differences in TB elastic constants were expected between the two groups. Unpaired T-tests were used to determine if the mean values for each of the nine elastic constants were the same between the PM and V subgroups. For the elastic constants that showed significant differences ($p<0.05$) between PM and V subgroups, significance levels of the same elastic constants predicted by the best-fit model of BV/TV and fabric were compared.

5.4 Results

Image quality was generally better in the specimen images (Figure 5.1a versus Figure 5.2a) as motion correction was not necessary and SNR was higher. The

apparent mean SNRs were 13.1±1.4 (specimen) versus 10.2±1.7 (*in vivo*) with ranges from 11.12 to 15.3 (specimen) and from 7.95 to 13.46 (*in vivo*).

Structural and mechanical measures of the TB subvolumes were in the expected ranges. Values of BV/TV in the subvolumes from the *in vivo* FLASE acquisitions were lower (mean: 10.7±0.94%, range 9.0-12.0%) that those observed in the TB subvolumes from the specimen images (mean: 21.1±6.9%, range: 7.9-34.5%). MIL and ACF fabric tensors confirmed the directional dependence visually evident in the datasets, as shown in Figure 5.5 for the three specimen subvolumes and one *in vivo* subvolume of TB. Average structural anisotropies (λ_3/λ_1) in the specimen and *in vivo* datasets were MIL: 1.60±0.25 (ACF: 1.59±0.14) and MIL: 1.28±0.053 (ACF: 1.34±0.064), respectively

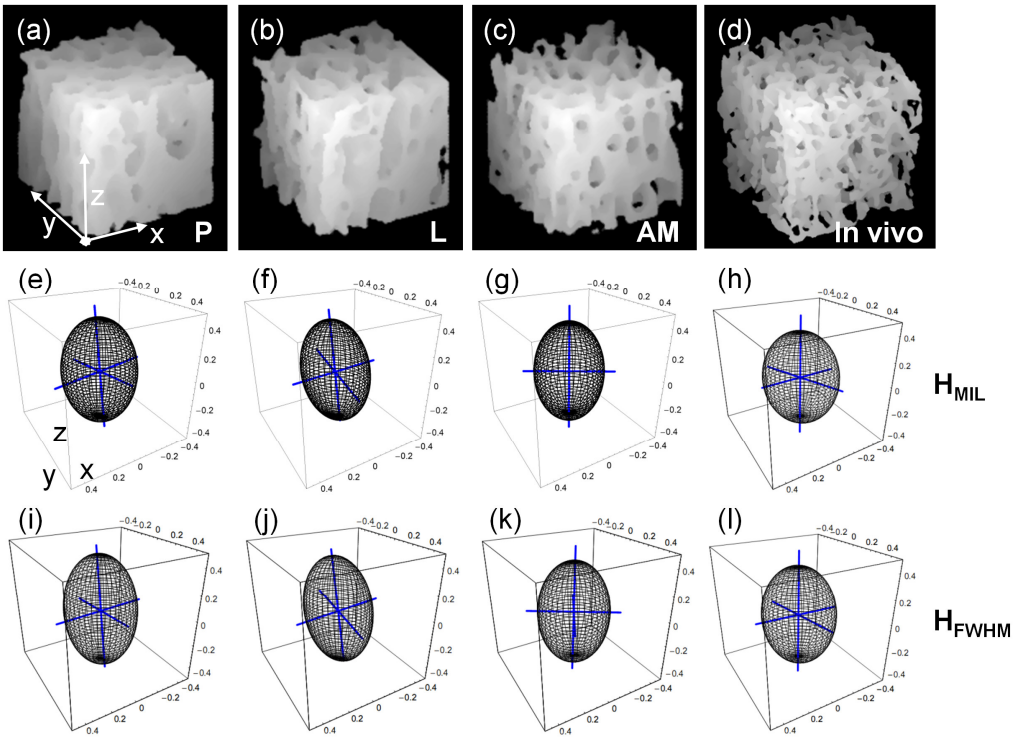

Figure 5.5 In-plane TB directional dependence was captured by ACF and MIL. (a-d) Surface-renderings of the TB subvolumes rotated CCW by 30° relative to image z-axis. Illustrations of rectilinear parallelepiped (8mm)^3 subvolumes of TB from three locations within specimen shown in Figure 5.1: (a) posterior-P, (b) lateral-L, and (c) anterior-medial -AM. Surface rendering in (d) is from location within *in vivo* image of Figure 5.2. Ellipsoids and fabric eigenvectors in (e-h) and (i-l) correspond to MIL fabric tensor $\mathbf{H}_{MIL}$ and ACF fabric tensor $\mathbf{H}_{FWHM}$, respectively, for subvolumes in (a-d). The in-plane directional dependence seen in (a-d) is captured by the eigenvectors and ellipsoids of MIL and ACF.

Results of the rotation experiment testing the effectiveness of the stiffness diagonalization procedure are provided in Table 5.1. Based on the slopes (m), intercepts (b), and regression coefficients (R^2), MIL predicted the applied rotations angles, α_y and α_z, the best, followed by ACF, and lastly the matrix $R_{\Theta_x,\Theta_y,\Theta_z}$ that diagonalized the stiffness matrix. R^2-values of 0.93 and 0.74 indicated the diagonalization procedure was capable of reproducibly identifying the approximate axes of orthotropic symmetry in TB subvolumes.

Table 5.1 Prediction of applied image rotations by ACF, MIL, and coordinate transformation of stiffness tensor

	α_y- 0:10:60°			α_z - 0:5:20°		
	m	b	R^2	m	b	R^2
ACF	1.16	-12.44	0.97	0.85	-1.57	0.95
MIL	1.11	-6.68	0.99	0.96	1.15	0.99
Stiffness	1.15	-14.53	0.93	0.71	1.57	0.74

Table 5.1 Prediction of applied image rotations by ACF, MIL, and coordinate transformation of stiffness tensor

Orthotropic elastic constants for the specimen subvolumes covered a wide range of values: E_{ii} ranged from 0.178 to 4.2 GPa, G_{ij} from 0.095 to 1.78 GPa, and v_{ij} from 0.095 to 0.406. Elastic constants within the sixteen *in vivo* subvolumes ranged from 0.349 to 1.032 GPa, from 0.181 to 0.348 GPa, and 0.132 to 0.288. As expected, E_{33} was the largest of the three Young's moduli in the specimen and *in vivo* subvolumes. Mean mechanical anisotropies were 2.02±0.45 (specimen) and 1.83±0.19 (*in vivo*).

Orthotropy errors ξ based on $\mathbf{S}$ were 30±17% and 24±11% for the specimen and *in vivo* subvolumes, respectively. Values of ε were 18±9% (specimen) and 16±7% (*in vivo*) for $\mathbf{S}_o$, corresponding to reductions of 40% and 33% relative to $\mathbf{S}$. Thus, diagonalization significantly impacted the μFE-derived elastic constants. Using $\mathbf{R}_{\Theta_x,\Theta_y,\Theta_z}$ to define $\hat{\mathbf{u}}_1,\hat{\mathbf{u}}_2,\hat{\mathbf{u}}_3$, average misalignment angles Ω^{MIL} indicated the fabric axes $\hat{\mathbf{v}}_1,\hat{\mathbf{v}}_2,\hat{\mathbf{v}}_3$ were 9.9±10.2° (specimen) and 8.7±6.7° (*in vivo*) offset from the axes of approximate orthotropic symmetry ($\hat{\mathbf{u}}_1,\hat{\mathbf{u}}_2,\hat{\mathbf{u}}_3$). Average misalignment angles relative to the ACF-based fabric tensor (i.e. Ω^{FWHM}) were 11.1±10.9° (specimen) and 7.7±5.9° (*in*

vivo). The agreement between MIL and ACF principal directions was better: mean misalignment angle of 5.6±6.9° with a range from 0.30° to 15.1°. Therefore, MIL and ACF principal directions were in closer alignment than either were to axes $\hat{\mathbf{u}}_1, \hat{\mathbf{u}}_2, \hat{\mathbf{u}}_3$, i.e. the axes of orthotropic symmetry determined from diagonalization of the stiffness tensor.

Variations in mechanical anisotropy were evident across the three subvolumes relative to Young's moduli. Young's moduli from the three subvolume locations required individual power-law fits relative to BV/TV (R^2s=0.92-0.98, Figure 5.6a-c) with exponents ranging from 1.3 to 1.8 depending on subvolume location and test direction. E_{33} was largest in all locations within the tibiae, but the ordering of E_{11} and E_{22} differed for each location. Table 5.2 summarizes the dependence of the nine elastic constants (individual and pooled) on BV/TV in specimen and *in* vivo images. After pooling the elastic constants from the three subvolumes, separate power-law functions of BV/TV with exponents of 1.4-1.7 were necessary to predict the individual elastic constants (leftmost column of Table 5.2). Pooled constants E_{ii}, G_{ij}, and v_{ij} were fit to general models of BV/TV which predicted 74% (Figure 5.7a), 92%, and 3.4% of the variations in E_{ii}, G_{ij}, and v_{ij} respectively.

Linear models of BV/TV provided the best predictions of E_{ii} and G_{ij} in the *in vivo* subvolumes. Similar to the specimen data, different linear models of BV/TV were necessary to predict individual elastic constants, although these fits did not demonstrate strong correlations (leftmost column of *in vivo* data in Table 5.2). Pooled E_{ii} were not significantly predicted by BV/TV although a positive correlation was demonstrated (Figure 5.7b). Pooled G_{ij} was significantly predicted by BV/TV while v_{ij} was uncorrelated to BV/TV (see Table 5.2).

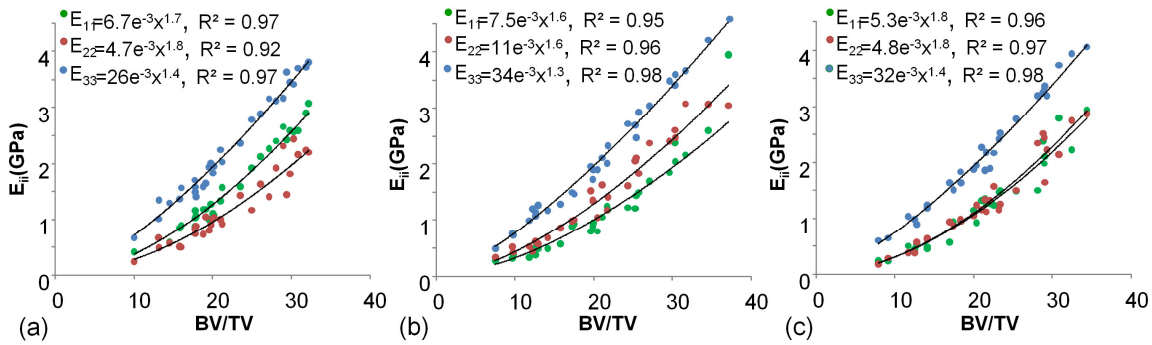

Figure 5.6 Individual Young's moduli (E_{11}, E_{22}, E_{33}) relative to BV/TV for thirty posterior-P (a), thirty lateral-L (b), and thirty anterior-medial-AM (c) subvolumes from the tibia specimen images.

Table 5.2: Dependence of μFE-derived elastic constants on BV/TV(%)

	Ex vivo				In vivo			
	BV/TV		BV/TV Pooled		BV/TV		BV/TV Pooled	
	Model	R^2	Model	R^2	Model	R^2	Model	R^2
E_{11}	$0.0061x^{1.7}$	*0.938**			0.022x+0.21	*0.075*		
E_{22}	$0.0075x^{1.6}$	*0.914**	$0.0115x^{1.6}$	*0.744**	0.074x-0.22	*0.544**	0.054x +0.037	*0.083*
E_{33}	$0.0322x^{1.4}$	*0.980**			0.065x+0.12	*0.613**		
G_{12}	$0.0051x^{1.5}$	*0.960**			0.021x-0.0033	*0.783**		
G_{13}	$0.0076x^{1.4}$	*0.954**	$0.0061x^{1.5}$	*0.920**	0.020x+0.035	*0.357**	0.026x -0.024	*0.321**
G_{23}	$0.0077x^{1.5}$	*0.949**			0.036x-0.10	*0.708**		
v_{12}	-0.0003x+0.28	*0.002*			-0.012x +0.35	*0.110*		
v_{13}	0.0029x+0.10	*0.421**	0.0018x+ 0.16	*0.034**	0.00046x +0.15	*0.003*	0.0006x+ 0.19	*0.000*
v_{23}	0.0027x+0.10	*0.349**			0.0096x+ 0.072	*0.142*		

* indicates significance ($p<0.05$)

Table 5.2 Dependence of μFE-derived elastic constants on BV/TV(%)

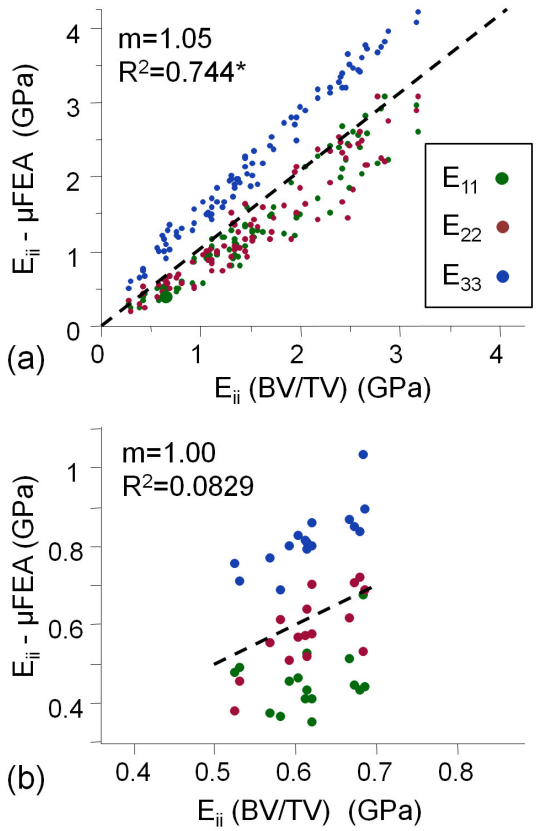

Figure 5.7 Pooled fits of µFE-derived and BV/TV-predicted E_{ii} from specimen (a) and *in vivo* (b) data. In (a), the independent variable was a power-law dependence of BV/TV: $E_{ii}=0.0115*BV/TV^{1.59}$, whereas a linear model was used in (b): $E_{ii}=0.054*BV/TV+0.037$. Slopes (m) and R^2-values reflect dashed-line fit between µFE-derived and model-predicted E_{ii}s and * indicates significance ($p<0.05$).

The effect of varying the exponent α on the orthotropic model's prediction (R^2_{adj}) of E_{ii}, G_{ij}, and v_{ij} is shown for MIL and ACF in Figure 5.8. The best fit of pooled elastic constants occurred for α=1.5, while the best fits of E_{ii}, G_{ij}, and v_{ij} corresponded to α's of 1.3, 1.4, and 2.2, respectively. There was not a noticeable difference in R^2_{adj} when using either $\mathbf{H}_{MIL}$ or $\mathbf{H}_{FWHM}$ as inputs into the model of Eq. 5-3. The effect of α on R^2_{adj} in the *in vivo* data was not significant as the elastic constants from the *in vivo* images were best predicted by a linear model of BV/TV.

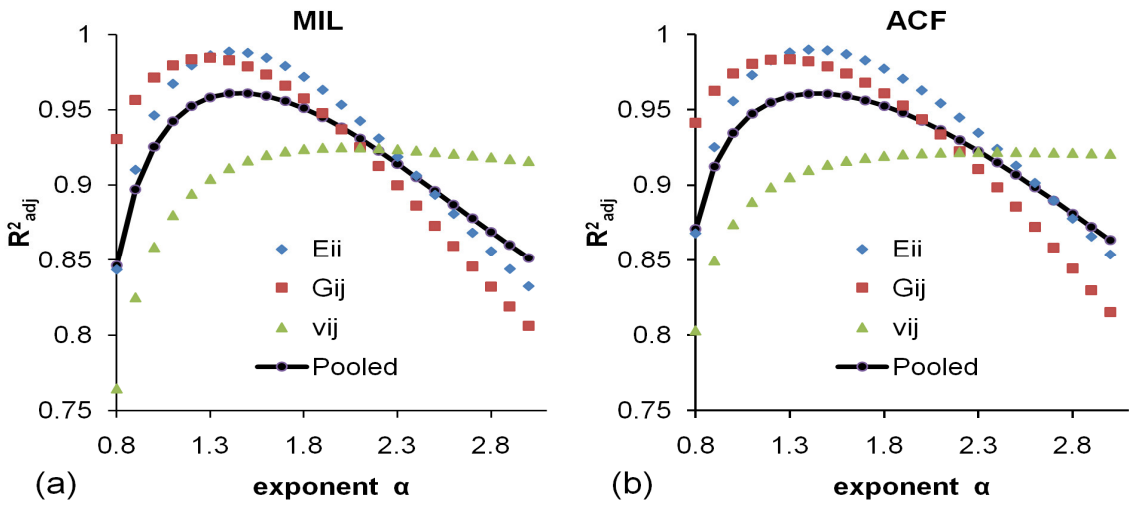

Figure 5.8 Dependence of goodness-of-fit parameter (R^2_{adj}) on power α in Eq. 5-6 for E_{ii}, G_{ij}, v_{ij}, and all 9 elastic constants pooled using fabric information from MIL(a) and ACF (b). Best average R^2_{adj} for the nine elastic constants occurred for α=1.5 for both MIL and ACF.

Table 5.3 summarizes the dependences of the pooled μFE-computed elastic constants on BV/TV and fabric (both $\mathbf{H}_{MIL}$ and $\mathbf{H}_{FWHM}$) according to Eq. 5-3 for α=1.5. Inclusion of fabric information derived from both MIL and ACF significantly improved (determined by Fisher's Z-transform using $p<0.05$) the prediction of E_{ii}, G_{ij}, and v_{ij} in both specimen and *in vivo* images. This result supports the notion that the directional dependence of TB is highly influential on its elastic behavior. In Figure 5.9, BV/TV and fabric tensor were highly predictive of the computed E_{ii} in the ninety subvolumes (MIL: R^2_{adj}=0.973 - Figure 5.9a, ACF: R^2_{adj}=0.976 - Figure 5.9b) and in the sixteen *in vivo* datasets (MIL: R^2_{adj}=0.928 - Figure 5.9c, ACF: R^2_{adj}=0.943 - Figure 5.9d).

Table 5.3: Dependence of μFE-derived elastic constants on model of on BV/TV(%) and fabric tensor **H** for α=1.5

	Ex vivo				**In vivo**			
	BV/TV, $\mathbf{H}_{MIL}$ Pooled		BV/TV, $\mathbf{H}_{ACF}$ Pooled		BV/TV, $\mathbf{H}_{MIL}$ Pooled		BV/TV, $\mathbf{H}_{ACF}$ Pooled	
	Model	R^2_{adj}	Model	R^2_{adj}	Model	R^2_{adj}	Model	R^2_{adj}
E_{ii}	y=0.91x+ 0.12	*0.973*†*	y=0.93x+ 0.088	*0.976*†*	y=0.95x+ 0.0319	*0.928*†*	y=0.96x+ 0.029	*0.943*†*
G_{ij}	y=0.86x+ 0.053	*0.954*†*	y=0.88x+ 0.033	*0.955*†*	y=0.92x+ 0.0150	*0.810*†*	y=0.96x+ 0.0049	*0.827*†*
v_{ij}	y=0.69x- 0.054	*0.836*†*	y=0.81x+ 0.028	*0.830*†*	y=0.65x- 0.061	*0.735*†*	y=0.69x- 0.053	*0.824*†*

• indicates significance ($p<0.05$),
† indicates R^2 is significantly different from R^2 of BV/TV-only model in Table 1

Table 5.3 Prediction of μFE-derived elastic constants using Cowin's model using α=1.5

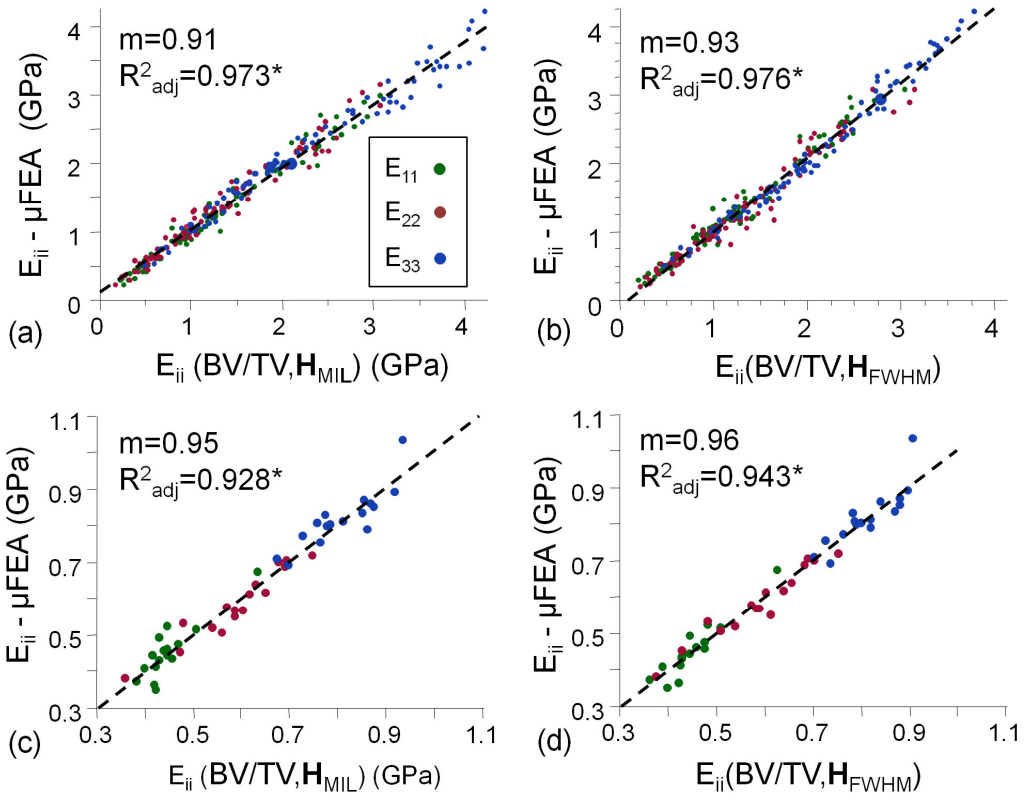

Figure 5.9 Specimen (a & b) and *in vivo* (c & d) results for pooled fits of μFE-derived E_{ii} and model predicted E_{ii} using exponent α=1.5 and $\mathbf{H}_{MIL}$ (a & c) and $\mathbf{H}_{FMHM}$ (b & d). Slopes (m) and R^2_{adj} correspond to dashed-line fits between μFE-derived and model-predicted E_{ii}s. Symbol * indicates significance (p<0.05).

Table 5.4 summaries the ANOVA results for the elastic constants in the seven young/ healthy volunteers (V) and the nine post-menopausal women (PM). BV/TV was significantly different between the sub-groups (p<0.05): 11.3±0.73 (V) versus 10.3±0.90 (PM). Five of the elastic constants determined using μFEA were able to differentiate (p<0.05) the groups. Strong discrimination (p<0.01) was found relative to E_{22}, v_{12}, and v_{23} and the most pronounced difference between the two sub-groups was seen relative to Shear modulus G_{23} (p<0.0005). The significant differences in μFE-derived elastic constants between the V and PM groups were paralleled by differences in elastic constants predicted from Cowin's model of BV/TV (α=1.5) and fabric measures from

both $\mathbf{H}_{MIL}$ and $\mathbf{H}_{FWHM}$. However, the significance levels (i.e. p-values) were slightly lower in the model-derived elastic constants (see Table 5.4).

Table 5.4: Comparison of Group Means (ANOVA)

	μFE		BV/TV, $\mathbf{H}_{MIL}$		BV/TV, $\mathbf{H}_{FWHM}$	
	V	PM	V	PM	V	PM
E_{11}	0.42±0.055	0.48±0.086	0.44±0.034	0.46±0.07	0.43±0.039	0.47±0.07
E_{22}	0.66±0.057**	0.52±0.074	0.67±0.058**	0.53±0.085	0.67±0.062**	0.53±0.091
E_{33}	0.83±0.068	0.81±0.091	0.84±0.073	0.79±0.076	0.85±0.057	0.79±0.059
G_{12}	0.24±0.021*	0.21±0.019	0.22±0.014*	0.20±0.018	0.22±0.015*	0.20±0.018
G_{13}	0.25±0.036	0.25±0.033	0.26±0.020	0.25±0.031	0.26±0.021	0.25±0.031
G_{23}	0.33±0.020****	0.26±0.029	0.31±0.022***	0.27±0.022	0.31±0.021**	0.27±0.031
v_{12}	0.20±0.015**	0.24±0.035	0.19±0.013*	0.22±0.033	0.19±0.013*	0.22±0.032
v_{13}	0.15±0.006	0.15±0.008	0.16±0.011	0.16±0.008	0.15±0.01	0.16±0.009
v_{23}	0.20±0.018***	0.16±0.016	0.19±0.011*	0.17±0.016	0.19±0.012*	0.17±0.016

*p<0.05, **p<0.01,***p<0.005,****p<0.0005

Table 5.4 Comparison of Group mean elastic constants

5.5 Discussion

Trabecular bone subvolumes from μMR images of the distal tibia were used as the basis for gray-scale structural analysis and μFE simulations. As the voxel dimension is on the order of the trabecular thickness, the effect of partial voluming was considered using BVF-mapping [Vasilic and Wehrli, 2005]. The BVF-maps were able to retain the grayscale structural information without the need for traditional thresholding. Lower values of BV/TV were observed in the *in vivo* data (mean: 11±1%) relative to specimens (mean: 21±7%). MIL and ACF confirmed the principal direction of trabeculae closely

parallels the longitudinal direction of the tibia (the image $\hat{\mathbf{z}}$ axis). There orientations depicted by MIL and ACF fabric tensors were similar and in good visual agreement with the TB images (see Figure 5.5). The ranges in SA_{MIL} and SA_{FWHM} for both specimen and *in vivo* datasets were consistent with those reported by others [Turner, Cowin et al., 1990; Odgaard, Kabel et al., 1997].

The rotation angles determined by the coordinate transformation of the stiffness tensor were in agreement with the applied rotations, however the correlation was not as high as that of the principal material axes of MIL and ACF fabric tensors (see Table 5.1). As the image rotation procedure could not restrict the image volume to the exact same subvolume of TB, deviations in the predicted angle from each method are expected, particularly for the larger rotations angles (>10°). However, the MIL fabric tensor is less influenced by the differences near the edges of the rotated subvolumes as the MIL sampling procedure was designed to limit the effect of image boundaries (see Chapter 3). Therefore, the higher R^2-values for MIL may be attributed, at least partially, to the sampling procedure.

The orthotropic elastic constants derived from μMR images were in good agreement with values reported by others, including those obtained from serially sectioned optical images [Kabel, van Rietbergen et al., 1999] and direct mechanical testing [Van Rietbergen, Odgaard et al., 1996]. However, in this work, the absolute values of the elastic constants are less important than their variability. Young's moduli obeyed the well-established power-law dependence relative to BV/TV [Carter and Hayes, 1977; Yang, Kabel et al., 1998; Kabel, Odgaard et al., 1999] within the specimen data (see Figure 5.6). Likely due to the narrow range in BV/TV in the *in vivo* images, a linear

relationship with BV/TV best described the elastic constants. Regression parameters for both linear and power-law relationships varied with test direction and location (i.e. P, L, and AM locations) within the distal tibia. BV/TV was capable of predicting the elastic constants within a specific tibial location; however different models of BV/TV were required for different locations and test directions. Hence, a general model of BV/TV was not capable of predicting the elastic constants with good agreement. Most notably, BV/TV was not a significant predictor of the *in vivo* Young's moduli (Figure 5.7b). These results parallel Ulrich et al.'s findings in subvolumes of TB from four anatomical sites in 70 donors (mean age of 69 years) [Ulrich, van Rietbergen et al., 1999]. They demonstrated that while more than 86% of the variation in the elastic properties of TB samples could be explained by BV/TV, differences in moduli between samples with the same BV/TV could be as large as 53% [Ulrich, van Rietbergen et al., 1999].

This study aimed to evaluate Cowin's model on the basis of three dimensional μMR images of distal tibiae. By correlating the results of a gray-scale μFE analysis with those of the MIL and ACF fabric measures, the eighteen constants in the volume fraction dependence of Cowin's model were determined for specimen and *in vivo* images. All nine orthotropic elastic constants could be predicted (mean R^2_{adj}s: 0.92 - specimen, 0.82 - *in vivo*) from measurements of BV/TV and fabric tensor independent of sub-region and test direction with the best fit occurring for an exponent α of 1.5.

Young's moduli, Shear moduli, and Poisson's ratios were better determined by the model including BV/TV and either MIL or ACF-derived fabric measures than a model of BV/TV alone (Table 5.3). This result supports the notion that the directional dependence of TB is highly influential on its elastic behavior. The importance of TB fabric on the

mechanical properties is further illustrated in Figure 5.10. Based on BV/TV alone, all nine elastic constants can be predicted within ±29% for the specimen and ±27% for the *in vivo* data relative to their μFE-derived values (95% confidence). When including MIL fabric measures, the nine elastic constants are predicted within ±13.1% and ±8.6% of their μFE-derived values with equal confidence. ACF fabric measures were similarly capable of predicting the nine elastic constants: ±13.1% for specimens and ±6.4% for live subjects with 95% confidence. While ACF and MIL appeared to predict the elastic constants similarly in the specimen data, ACF fabric measures performed better *in vivo* (within ±2.1% of μFE-derived E_{ii} and G_{ij}) than MIL fabric measures (within ±5.8% of μFE-derived E_{ii} and G_{ij}). However, this improvement was not statistically significant. The improvement achieved using ACF could be explained by its operation on gray-scale images of TB and/or its improved performance relative to resolution and SNR (see Chapter 3).

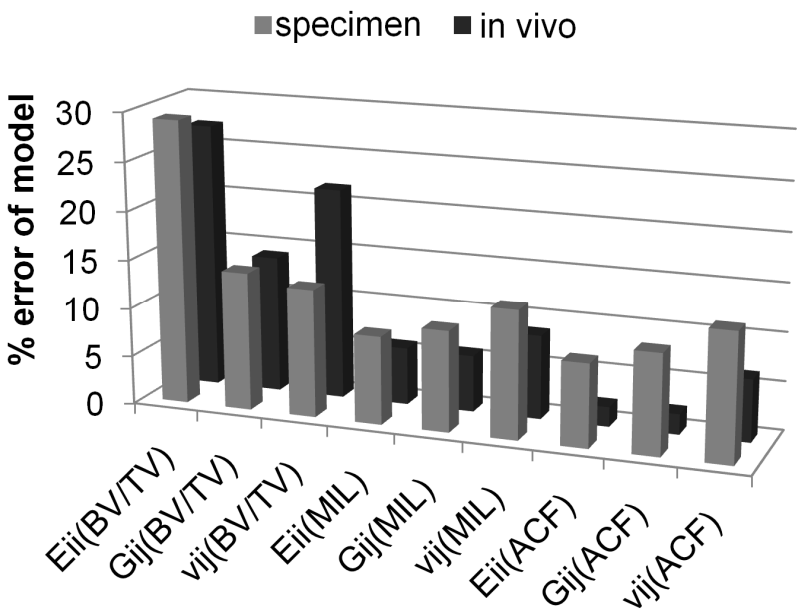

Figure 5.10 Percentage error of each model (BV/TV alone, BV/TV and H_{MIL}, and BV/TV and H_{FWHM}) relative to the µFE-calculated E_{ii}, G_{ij}, and v_{ij} for specimen and *in vivo* datasets. Percent error is calculated as the standard error of the regression divided by the mean value of the associated µFE-calculated elastic constant. A 95% confidence interval was used.

The improved prediction of elastic constants using fabric tensor as an input was also associated with better sensitivity to differences in TB mechanical properties. Four elastic constants assessed by µFEA and derived from the model of Eq. 5-3 demonstrated better discrimination of the PM and V sub-groups ($p<0.01$) than BV/TV alone ($p<0.05$). The differences in BV/TV and elastic constants between PM and V sub-groups are assumed to result from the loss of bone quality with age and/or gender differences. While the true differences between the sub-groups are not known, this experiment highlights the potential improvement in discriminating subjects on the basis of TB microarchitecture when considering TB orientation.

Correspondence between the present study and the assumptions of Cowin's model should be highlighted. First, an isotropic tissue modulus was assumed as only the TB structure was assessed in the MRI experiments. An isotropic tissue modulus has been supported by studies comparing compression tests to finite-element results [Hou, Lang et al., 1998; Kabel, van Rietbergen et al., 1999]. More recent work has demonstrated heterogeneity in the tissue modulus [Hengsberger, Kulik et al., 2001; Hengsberger, Enstroem et al., 2003] as a result of differing lamellar orientations [Hofmann, Heyroth et al., 2006]. Renders et al. found Young's and shear moduli to be overestimated by an average 21% when assuming homogeneous mineralization in μFE models of TB from the human mandibular condyle relative to a model incorporating heterogeneous mineralization determined by μCT [Renders, Mulder et al., 2008]. Therefore, inclusion of vBMD via peripheral quantitative computed tomography may offer more accurate estimates of the elastic constants.

Cowin's second condition is that the TB possesses orthotropic symmetry and thus its structural anisotropy can be represented by a second-rank tensor. The orthotropy error ξ estimated the degree to which each subvolume possessed orthotropic symmetry. Assuming orthotropy resulted in a ~17% error (ξ) in the calculated elastic constants. This error is considerably larger than the 6% error found in μCT images of $(4mm)^3$ TB specimens from seven distinct human metaphyseal locations [Zysset, Goulet et al., 1998]. A possible reason for the large mean error in this work is the proximity of the three subvolumes relative to the cortical boundary of the tibia. Close to the cortical shell, the mechanical environment is expectedly less homogeneous. The TB subvolumes from the latter study were likely extracted from more centrally located regions of the skeleton where the mechanical environment is more homogeneous.

The deviation from orthotropic symmetry also impacts the alignment between fabric directions and axes of approximate orthotropic symmetry. In cases of either material isotropy or pure anisotropy, the axes of approximate orthotropic symmetry cannot be accurately defined, resulting in larger variability in misalignment angles: Ω^{MIL} and Ω^{FWHM}. In this study, most subvolumes demonstrated structural anisotropy greater than 1.2 which was considered adequate to dismiss the errors associated with structural isotropy. The average misalignment angles Ω^{MIL} and Ω^{FWHM} were similar and indicative of the fabric axes $\hat{\mathbf{v}}_1, \hat{\mathbf{v}}_2, \hat{\mathbf{v}}_3$ being approximately 10±10° (specimen) and 8±7° (*in vivo*) offset from the axes of approximate orthotropic symmetry. Similar misalignment angles were found in human TB by others [Zysset, Goulet et al., 1998] using MIL. Larger values of Ω^{MIL} were associated with increasing *res*, as shown for the specimen and *in vivo* data in Figure 5.11. Hence, the MIL-based fabric tensor was less capable of characterizing the directional dependence of TB subvolumes that did not adhere to strict orthotropic symmetry. A similar trend occurred for Ω^{FWHM}.

The misalignments between fabric axes and axes of closest orthotropic symmetry are a source of error in the model. Turner minimized this error source by excluding TB subvolumes that did not adhere to approximate orthotropic symmetry defined by an error of less than 4% [Turner, Cowin et al., 1990]. As mean errors in the measured Young's (Shear) moduli of 9.5% (1.1%) were found for a 10° misalignment angle [Turner and Cowin, 1988], a substantial number of datasets would have been discarded using the same cut-off error. Instead, all datasets were retained at the sacrifice of accuracy in the model prediction.

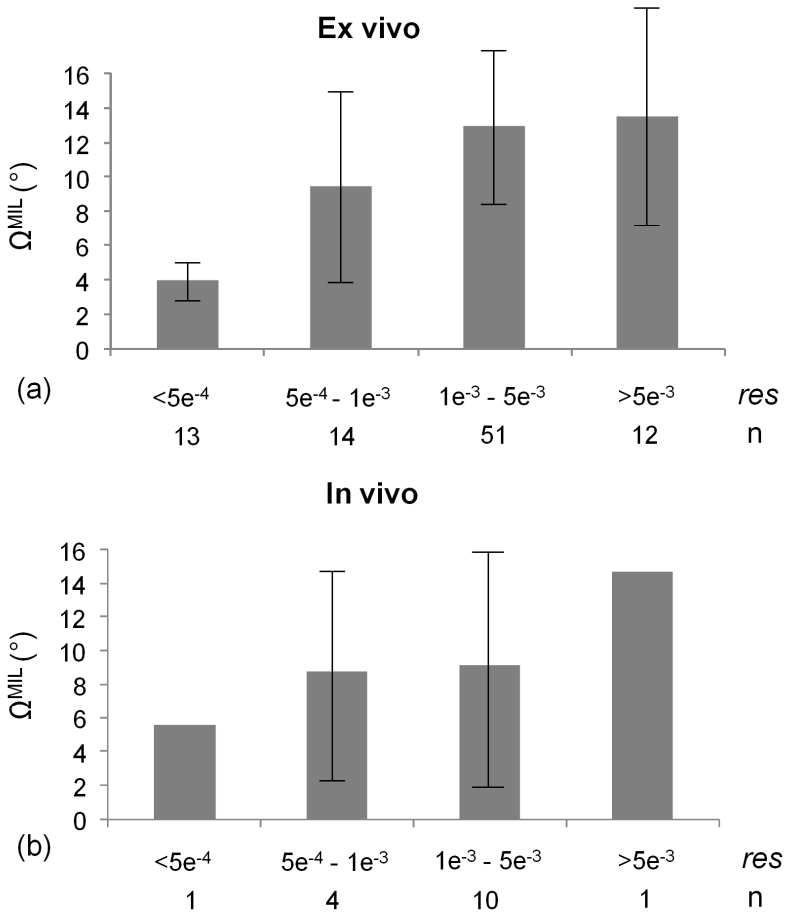

Figure 5.11 Mean misalignment angle Ω^{MIL} relative to *res* (Eq. 5-5) for specimen (a) and *in vivo* (b) datasets. n indicates the number of datasets that fall into the associated range of *res*. Plots for Ω^{FWHM} versus *res* were highly similar.

The limitations of this study can be considered relative to the feasibility of the imaging procedure and the ability of the derived elastic constants to reflect the actual mechanical properties of the intact bone. With respect to the imaging procedure, the primary limitation relates to the long scan times required to achieve sufficient resolution and SNR *in vivo.* The current scan time for imaging with a 160µm voxel is under 17 minutes. This duration may be too long for elderly subjects to remain still and comfortable. As certain image-processing algorithms are known to lose sensitivity at

SNRs below 7-8 [Vasilic and Wehrli, 2005], the analysis was restricted to 8mm rectilinear parallelepiped subvolumes of TB from the anterior portion of the tibia where the SNR was sufficiently high. In doing so, the results are not representative of whole-bone mechanical properties. Although the distal tibia is not a common site of osteoporosis-related fractures, the described protocol is translatable to the wrist and calcaneus. Improvements in SNR via hardware advancement or imaging at higher field strengths are likely necessary to achieve suitable image quality in the femur and vertebrae.

This study is the first application, to the authors' knowledge, of Cowin's model to *in vivo* µMR images of TB. The fabric tensor has been assessed in *ex vivo* µMR images of TB in order to improve the prediction of Young's moduli relative to aBMD from quantitative computed tomography [Majumdar, Kothari et al., 1998]. Majumdar et al. predicted 38% of the mechanically measured Young's moduli using aBMD and fabric measures relative to ~18% by aBMD alone. The relatively low R^2-values relative to the present study can be explained by low measurement reproducibility in Young's modulus and by the TB specimens originating from skeletal sites (vertebra, calcaneus, and distal and proximal femur) differing in structural and mechanical heterogeneity.

In summary, the inclusion of trabecular bone fabric measures via Cowin's model improved the BV/TV-based prediction of the elastic constants derived from linear µFE analysis of µMR images. MIL and ACF based measures of the fabric tensor were equally capable to predict the elastic constants. Through the combination of structural and µFE analyses, potential physiologic optimization strategies can be investigated in light of treatment paradigms or disease progression. The data emphasize (1) the

importance of fabric as a predictor of bone mechanical properties, and (2) that these relationships can be assessed in the limited resolution and SNR regime of μMRI. Developing similar models in other anatomical locations, specifically fracture sites, would allow the differentiation between changes in TB elastic properties due to bone loss and changes related to the adaptation of the TB micro-architecture. Such information is expected to be useful when evaluating how medications and physical activity impact skeletal remodeling and may improve the assessment of fracture risk when considering common fracture mechanisms.

6 Chapter 6 Summary and conclusions

6.1 Summary of research

Osteoporosis is a skeletal disease characterized by loss of bone mass, architectural changes, and increased susceptibility to fracture [Bonnick, 2007]. The incidence of osteoporotic fractures is expected to increase over the coming decades due to a growing population of elderly people in industrialized countries [Konnopka, Jerusel et al., 2009]. More than 50% of osteoporotic fractures occur in patients with a DEXA T-score greater than the diagnostic threshold of -2:5 SD [Siris, Chen et al., 2004] and bone mineral density measures do not sufficiently explain reductions in fracture risk associated with treatment [Sarkar, Mitlak et al., 2002] [Schuit, van der Klift et al., 2004]. With such a high fracture rate, a more precise method is necessary to identify patients at risk and determine treatment response as early as possible.

The directional dependence of TB has been identified as an important determinant of TB mechanical competence [Goldstein, Goulet et al., 1993] [Oden, Selvitelli et al., 1998]. Methods for estimating a fabric tensor, for example the mean intercept length (MIL), are rooted in *ex vivo* studies where high-resolution imaging techniques offer images suitable for binarization by thresholding [Whitehouse, 1974] [Odgaard, 1997]. As the skeleton is a dynamic system that remodels according to external stimuli (e.g. mechanical loading) and internal stimuli (e.g. hormonal changes), non-invasive techniques capable of tracking changes in the structural arrangement of bone are desirable. Micro-magnetic resonance imaging (μMRI) offers a non-invasive and non-ionizing tool for the assessment of TB micro-architecture [Wehrli, Song et al., 2006] well-suited for the repeated measurements necessary for monitoring changes in

bone integrity. However, images obtained using *in vivo* μMRI suffer from partial-volume blurring, lower signal-to-noise ratio, RF coil shading, and anisotropic voxel sizes. These image characteristics obviate simple thresholding as a means of binarization, thereby limiting the accuracy and reproducibility of the estimated fabric tensor.

The objective of this dissertation was to accurately and reproducibly determine the structural arrangement of TB *in vivo* by assessing a fabric tensor on the basis of *in vivo* μMRI. Three contributions towards achieving this objective are presented in the thesis: 1) the introduction and evaluation of a novel method to map the TB fabric tensor based on the spatial autocorrelation function; 2) the further development of *in vivo* μMR imaging and analysis; and 3) validation of the image-derived TB fabric tensor through its relationship with TB mechanical competence calculated using micro-finite element analysis (μFEA).

In Chapter 3, a novel method for assessing the TB fabric tensor was introduced and evaluated relative to MIL as a means of quantifying the TB fabric tensor *in vivo*. The approach makes use of the full-width-at-half maximum of the spatial autocorrelation function (ACF) to quantify the probabilistic distribution of bone relative to orientation within rectilinear parallelepiped volumes of TB. In μMR images with a 160μm voxel size and micro-CT images with a 25μm voxel size, ACF-derived structural anisotropy overestimated, yet showed good agreement, with MIL-derived structural anisotropy. In sensitivity tests, ACF was less sensitive to changes in resolution and variations in SNR than MIL while both techniques showed mild sensitivity to RF coil inhomogeneity which could be reduced through bone-volume fraction mapping [Vasilic and Wehrli, 2005]. Finally, ACF and MIL derived structural anisotropies were overestimated in images with

slice thickness larger than the in-plane voxel dimension, suggesting the importance of isotropic resolutions when assessing directionally dependent measures in images of TB.

In Chapter 4, a two-fold gain in SNR at 3T was traded for an isotropic voxel size through partial parallel imaging. The optimized isotropic FLASE acquisition was compared in terms of reproducibility and reliability of structural and mechanical parameters to the standard anisotropic FLASE acquisition in repeated measures of seven subjects. Enhancements in the acquisition procedures (i.e. prospective registration [Rajapakse, Magland et al., 2008], immobilization, and motion correction [Song and Wehrli, 1999; Lin, Ladinsky et al., 2007]) and in the image analysis techniques (i.e. retrospective registration [Magland, Jones et al., 2009] and analysis volume matching) resulted in high reproducibility and good differentiation between seven healthy subjects for both acquisition modes. Structural and mechanical parameters were more reproducible in images obtained using FLASE in the anisotropic mode (3.2%±1.2%) versus the isotropic mode (5.4%±2.4%). Although 75% of the possible inter-subject comparisons were distinguishable using the anisotropic images versus 50% for the isotropic images, measures dependent on orientation, namely structural anisotropy and the ratio of plate-like to rod-like elements, were more distinguishing of the subjects in images with the isotropic voxel size. These results suggest resolution isotropy offers better sensitivity to differences in structural anisotropy despite the lower SNR relative to the standard anisotropic voxel size of 137x137x410μm^3.

In Chapter 5, MIL- and ACF-derived TB fabric tensors were demonstrated as important determinants of the orthotropic elastic constants derived from μFEA of TB subvolumes extracted from specimen and *in vivo* μMR images of human distal tibiae.

Using Cowin's model [Cowin, 1985], bone volume fraction and fabric tensor were significantly better predictors of elastic measures than bone volume fraction alone. The former achieved mean R^2s of 0.92 (specimen) and 0.84 (*in vivo*) and the latter produced mean R^2s of 0.57 (specimen) and 0.13 (*in vivo*). Relative to MIL, the ACF-based fabric tensor was at least equally capable of predicting the orthotropic elastic constants. Within the *in vivo* images, the ACF-derived fabric tensor achieved slightly improved agreement with the elastic constants in comparison to MIL; however the improvement was not statistically significant.

6.2 Future work

The ability of the TB fabric tensor to provide directional information indicative of bone strength highlights its potential in improving fracture risk assessment. However, the assessment of TB fabric tensor via μMRI is still at an early stage. The techniques developed here permit the routine assessment of trabecular bone structural anisotropy in images previously acquired and forthcoming studies. Yet, the relationship between fabric and elastic tensors has only been assessed in images with isotropic resolution. Therefore, a short-term project would entail the examination of the fabric and elastic tensors in images with anisotropic voxel size acquired at the distal radius and tibia at 1.5T and 3T. Longer-term efforts can be divided into two directions: 1) further technical development of the method and 2) application of the method to evaluate the contribution of TB structural arrangement on the improvement or decline of bone strength due to treatment efficacy or disease progression. These two areas of development are discussed in the following section.

6.2.1 Technical development

Further technical development would involve improving the measurement accuracy of the method and extending the model into the non-linear mechanical regime. Improvements in measurement accuracy through improvements in SNR and/or higher resolutions are desirable. Potential means to improve SNR include advancements in hardware design and imaging at higher field strengths. Optimal coil designs for each anatomical location are necessary when the highest achievable resolutions are desired. In imaging the ankle at 3T, a four-element phased array receiver only coil was used. While this coil was custom-designed for imaging the tibia, a multi-element phased array surrounding the entire ankle may offer improved SNR and improved spatial encoding for parallel imaging. However the gain in SNR expected for an optimally designed coil array is not as significant as the linear increase in SNR with field strength. By moving from 1.5T to 3T, a two-fold gain in SNR was attained in FLASE images of the distal tibia (see Chapter 4). Improved SNR at higher fields, e.g. 7T, are possible and have been suggested in the literature [Banerjee, Krug et al., 2008]. One potential obstacle at higher field is the specific absorption rate (SAR). SAR increases with the square of field strength. Consequently, SAR limitations hinder the use of sequences employing multiple large angle RF pulses from being performed at higher field strengths. Alternative sequences like turbo spin echo based sequences have been demonstrated at 7T [Magland, Rajapakse et al., 2010]. Improvements in SNR and resolution will increase the sensitivity (i.e. accuracy and reproducibility) of the method to changes associated with disease and treatment.

Another direction for this research involves the implementation of non-linear μFEA to study bone failure mechanisms in TB images. The model implemented in Chapter 5 involved only the estimation of the elastic constants of TB subvolumes by

BV/TV and fabric measures. Strong relationships have also been demonstrated in human TB samples between volume fraction, fabric and yield properties [Rincon-Kohli and Zysset, 2009]. In addition, compressive fatigue due to cyclical loading of vertebral TB samples has been associated with properties of the fabric tensor [Rapillard, Charlebois et al., 2006]. Demonstrating a relationship between failure loads and the TB fabric tensor *in vivo* will provide further insight into the role of structural orientation on fracture resistance.

6.2.2 Clinical applications

6.2.2.1 Physiological effects of a therapeutic intervention

The contribution of the structural arrangement of TB on mechanical competence can be tested relative to various experimental paradigms (e.g. the introduction of anabolic agents such as growth hormone or changes in physical activity). One possible application of the current analysis procedure in the distal tibia would be to estimate the effect of low-magnitude mechanical stimulation on the mechanical competence of TB and determine if the changes in directional elastic modulus are explained by alterations in the fabric tensor. As the use of low-magnitude mechanical stimulation has been associated with increased bone formation in children [Ward, Alsop et al., 2004] and young women [Gilsanz, Wren et al., 2006], this study would focus on younger individuals without age-related osteoblastic deficits [Srinivasan, Agans et al., 2003]. The study design could be comprised of two groups of twenty young men and women in which one group receives low-magnitude mechanical stimulation for two minutes per day over the course of a year while the other groups serves as age- and gender-matched controls. µMR imaging of the distal tibia would be performed at baseline, six months, and twelve

months from which elastic, fabric, and BV/TV measures would be obtained. Compliance with the prescribed usage of the device would be the most significant limitation to such a study.

6.2.2.2 Translation to the wrist

Alternatively, as the tibia is not a site associated with osteoporotic fracture and site-specific measurements have shown the highest significance for site-specific fracture predictions [Kanis, McCloskey et al., 2008], development of the technology in fracture-relevant sites is desirable. Wrist fractures in osteopenic patients tend to occur prior to fractures of the hip and vertebral column [Cuddihy, Gabriel et al., 1999]. The distal radius is therefore a favorable site for diagnosis of osteoporosis [Eastell, 1996]. Being a peripheral site with a relative small amount of surrounding soft tissue, the architecture of the distal radius can be easily and accurately assessed by *in vivo* μMRI. To translate the method described in this thesis to the wrist, hardware suitable for parallel imaging of the wrist would need to be designed to allow for the acquisition of images with isotropic resolution in a reasonable scan time. Current wrist images are obtained using an elliptical birdcage coil, which is not suitable for the spatial encoding necessary for parallel imaging. A wrist coil capable of parallel imaging might consist of four or six rectangular receive-only surface elements of 4x3 cm^2 dimensions encircling the wrist confined within an elliptical birdcage wrist coil for transmission. Based on the current acquisition at 1.5T using a 137x137x410 μm^3 voxel size and assuming a two-fold gain in SNR at 3T, such a coil would permit the acquisition of images of the distal radius with a 160 μm voxel size in approximately 10 minutes using the isotropic FLASE sequence at 3T. The following two applications involving the assessment of TB fabric tensor are

based on the assumption that such a coil could be fabricated and isotropic images of the radius could be achieved in a suitable scan time.

6.2.2.3 Evaluating TB remodeling in the wrist in response to activity

A potential study using the relationship between TB fabric and elastic tensors could involve the effect of introducing a new physical activity on the bone structure and mechanical competence within the distal radius. Activities involving short bouts of mechanical loading are expected to result in improved bone structure and strength [Robling, Hinant et al., 2002]. One such exercise involving mechanical loading of the wrist is boxing a punching bag. Such a study would entail acquiring isotropic μMR images of the distal radius over the course of 1-2 years. Subjects would be divided into two groups: one group receiving a punching bag with instructions to hit the bag for a 10-minute period twice-a-week over the course of the study and the other group serving as age-matched controls. Besides improving the muscle tone of the forearms, the impact incurred during punching could serve as an anabolic stimulus resulting in bone formation (or reduced bone resorption) and a change in TB structural anisotropy within the distal radius, ultimately causing increased mechanical properties as detected by μFEA. By assessing both the BV/TV and fabric tensor and relating them to the elastic constants, improvements in the elastic constants can be attributed to changes in either BV/TV or fabric tensor.

6.2.2.4 The relationship between local TB structure and whole bone mechanics

Another potential application for the *in vivo* assessment of TB fabric tensor in the wrist is through the study of whole bone fracture mechanisms and how they relate to TB orientation. The most common fracture of the wrist is Colles' fracture, which occurs

within the distal 10–12% region of the radius. Colles' fractures result from axial compression and bending, mainly when falling onto an out-stretched hand [Varga, Baumbach et al., 2009]. Using cadaveric human radii, the cortical and trabecular bone geometries in the wrist can be imaged using μMRI. These images would then be input into a large-scale μFEA in which the loading mechanisms experienced during a fall could be simulated in either the linear elastic (or non-linear plastic) regime. Using collected evidence from actual fractures and the simulation results, regions of high stress localization (or failure) within the TB could be identified [Varga, Baumbach et al., 2009]. The TB fabric tensor could be assessed in these locations and compared to similar locations identified in TB images obtained using *in vivo* μMRI of the distal radius. By identifying similarities between TB structure in terms of BV/TV and fabric, at fracture relevant sites, a more precise assessment of site-specific fracture risk could be obtained.

This thesis demonstrates the relevance of TB orientation to mechanical competence within *in vivo* images. With further work improving the sensitivity of μMRI and efforts demonstrating the ability of TB fabric tensor to explain changes in mechanical competence associated with disease and/or treatment efficacy, the directional dependence of TB could progress into a clinically relevant measure of bone integrity.

References

Aaron, J. E., R. M. Francis, et al. (1989). "Contrasting microanatomy of idiopathic and corticosteroid-induced osteoporosis." Clin Orthop Relat Res(243): 294-305.

Assessment, O. o. T. (1994). Hip fracture outcomes in people age 50 and over. Washington, DC, U.S. Congress, Office of Technology Assessment: 95p.

Atkinson, D., D. L. Hill, et al. (1999). "Automatic compensation of motion artifacts in MRI." Magn Reson Med 41(1): 163-70.

Bagi, C. M., D. Wilkie, et al. (1997). "Morphological and structural characteristics of the proximal femur in human and rat." Bone 21(3): 261-7.

Banerjee, S., S. Choudhury, et al. (2006). "Autocalibrating parallel imaging of in vivo trabecular bone microarchitecture at 3 Tesla." Magn Reson Med 56(5): 1075-84.

Banerjee, S., R. Krug, et al. (2008). "Rapid in vivo musculoskeletal MR with parallel imaging at 7T." Magnetic resonance in medicine : official journal of the Society of Magnetic Resonance in Medicine / Society of Magnetic Resonance in Medicine 59(3): 655-60.

Baron, R. (1999). Anatomy and ultrastructure of bone. Primer of the metabolic bone diseases and disorders of mineral metabolism. M. J. Favus. Philadelphia, PA, Lippincott Williams and Wilkinsz: 3-10.

Barrall, G. A., L. Frydman, et al. (1992). "NMR diffraction and spatial statistics of stationary systems." Science 255(5045): 714-7.

Bartel, D. L., D. T. Davy, et al. (2006). Orthopaedaedic Biomechanics: Mechanics and Design in Musculoskeletal Systems. Upper Saddle River, NJ, Pearson Education, Inc.

Benito, M., B. Vasilic, et al. (2005). "Effect of testosterone replacement on trabecular architecture in hypogonadal men." J Bone Miner Res 20(10): 1785-91.

Bennell, K. L., K. M. Khan, et al. (2002). "Age does not influence the bone response to treadmill exercise in female rats." Med Sci Sports Exerc 34(12): 1958-65.

Berryman, J. G. (1985). "Measurement of spatial correlation functions using image processing techniques." Journal of Applied Physics 57: 2374-2384.

Beuf, O., S. Ghosh, et al. (2002). "Magnetic resonance imaging of normal and osteoarthritic trabecular bone structure in the human knee." Arthritis Rheum 46(2): 385-93.

Beuf, O., D. C. Newitt, et al. (2001). "Trabecular structure assessment in lumbar vertebrae specimens using quantitative magnetic resonance imaging and relationship with mechanical competence." J Bone Miner Res 16(8): 1511-9.

Bevill, G., F. Farhamand, et al. (2009). "Heterogeneity of yield strain in low-density versus high-density human trabecular bone." J Biomech 42(13): 2165-70.

Blaimer, M., F. Breuer, et al. (2004). "SMASH, SENSE, PILS, GRAPPA: how to choose the optimal method." Top Magn Reson Imaging 15(4): 223-36.

Bonaiuti, D., B. Shea, et al. (2002). "Exercise for preventing and treating osteoporosis in postmenopausal women." Cochrane Database Syst Rev(3): CD000333.

Bone Bioengineering Laboratory, C. U. (2010). "Image Analysis." Retrieved August 20, 2010, from http://boneserver1.bme.columbia.edu/research/Image%20Analysis.htm.

Bonnick, S. L. (2007). "Noninvasive assessments of bone strength." Curr Opin Endocrinol Diabetes Obes 14(6): 451-7.

Borah, B., T. E. Dufresne, et al. (2002). "Risedronate preserves trabecular architecture and increases bone strength in vertebra of ovariectomized minipigs as measured by three-dimensional microcomputed tomography." J Bone Miner Res 17(7): 1139-47.

Bouchard, L. S., F. W. Wehrli, et al. (2005). "Structural anisotropy and internal magnetic fields in trabecular bone: coupling solution and solid dipolar interactions." J Magn Reson 176(1): 27-36.

Boutroy, S., M. L. Bouxsein, et al. (2005). "In vivo assessment of trabecular bone microarchitecture by high-resolution peripheral quantitative computed tomography." J Clin Endocrinol Metab 90(12): 6508-15.

Brunader, R. and D. K. Shelton (2002). "Radiologic bone assessment in the evaluation of osteoporosis." Am Fam Physician 65(7): 1357-64.

Burge, R., B. Dawson-Hughes, et al. (2007). "Incidence and economic burden of osteoporosis-related fractures in the United States, 2005-2025." J Bone Miner Res 22(3): 465-75.

Burger, E. H. and J. Klein-Nulend (1999). "Mechanotransduction in bone--role of the lacuno-canalicular network." Faseb J 13 Suppl: S101-12.

Caligiuri, P., M. L. Giger, et al. (1994). "Multifractal radiographic analysis of osteoporosis." Med Phys 21(4): 503-8.

Callaghan, P. T. (1991). Principles of nuclear magnetic resonance microscopy. New York, Oxford University Press.

Campbell, G. M., H. R. Buie, et al. (2008). "Signs of irreversible architectural changes occur early in the development of experimental osteoporosis as assessed by in vivo micro-CT." Osteoporos Int 19(10): 1409-19.

Carter, D. R. and W. C. Hayes (1977). "The compressive behavior of bone as a two-phase porous structure." J Bone Joint Surg Am 59(7): 954-62.

Carter, D. R., G. H. Schwab, et al. (1980). "Tensile fracture of cancellous bone." Acta Orthop Scand Suppl 51(5): 733-41.

Cavanagh, P. R., A. A. Licata, et al. (2005). "Exercise and pharmacological countermeasures for bone loss during long-duration space flight." Gravit Space Biol Bull 18(2): 39-58.

Chapurlat, R. D., P. Garnero, et al. (2000). "Serum estradiol and sex hormone-binding globulin and the risk of hip fracture in elderly women: the EPIDOS study." J Bone Miner Res 15(9): 1835-41.

Cheal, E. J., B. D. Snyder, et al. (1987). "Trabecular bone remodeling around smooth and porous implants in an equine patellar model." J Biomech 20(11-12): 1121-34.

Chesnut, C. H., 3rd, M. Azria, et al. (2008). "Salmon calcitonin: a review of current and future therapeutic indications." Osteoporos Int 19(4): 479-91.

Choi, K. and S. A. Goldstein (1992). "A comparison of the fatigue behavior of human trabecular and cortical bone tissue." J Biomech 25(12): 1371-81.

Choi, K., J. L. Kuhn, et al., Eds. (1990). The elastic moduli of human subchondral, trabecular, and cortical bone tissue and the size-dependency of cortical bone modulus. J Biomech. United States.

Ciarelli, T. E., D. P. Fyhrie, et al. (2000). "Variations in three-dimensional cancellous bone architecture of the proximal femur in female hip fractures and in controls." J Bone Miner Res 15(1): 32-40.

Claes, L. E., H. J. Wilke, et al. (1995). "Osteonal structure better predicts tensile strength of healing bone than volume fraction." J Biomech 28(11): 1377-90.

Cooley, J. W. and O. W. Tukey (1965). "An algorithm for the machine calculation of complex Fourier series." Math. Comput. 19: 297-301.

Cork, U. C. (2010). "http://www.ucc.ie/bluehist/CorePages/Bone/Bone.htm." Retrieved May, 2010.

Cowin, S. C. (1985). "The relationship between the elasticity tensor and the fabric tensor." Journal of Mech. Mater. 4: 137-47.

Cowin, S. C. (1986). "Wolff's law of trabecular architecture at remodeling equilibrium." J Biomech Eng 108(1): 83-8.

Cowin, S. C. (1989). Bone Mechanics. New York, NY, CRC Press, Inc.

Cowin, S. C. (2001). Bone Mechanics Handbook, CRC Press.

Cruz-Orive, L. M., L. M. Karlsson, et al. (2005). "Characterizing anisotropy: a new concept." Micron and Microscopica Acta. 23(75).

Cuddihy, M. T., S. E. Gabriel, et al. (1999). "Forearm fractures as predictors of subsequent osteoporotic fractures." Osteoporosis international : a journal established as result of cooperation between the European Foundation for Osteoporosis and the National Osteoporosis Foundation of the USA 9(6): 469-75.

Cummings, S. R., D. B. Karpf, et al. (2002). "Improvement in spine bone density and reduction in risk of vertebral fractures during treatment with antiresorptive drugs." Am J Med 112(4): 281-9.

Currey, J. D. (2003). "The many adaptations of bone." J Biomech 36(10): 1487-95.

Deans, S. R. (1983). The radon Transform and Some of Its Applications. New York, John Wiley & Sons.

Dempster, D. W. (2003). "Bone microarchitecture and strength." Osteoporos Int 14 Suppl 5: S54-6.

Diederichs, G., T. M. Link, et al. (2009). "Assessment of trabecular bone structure of the calcaneus using multi-detector CT: correlation with microCT and biomechanical testing." Bone 44(5): 976-83.

Eastell, R. (1996). "Forearm fracture." Bone 18(3 Suppl): 203S-207S.

Edelstein, W. A., G. H. Glover, et al. (1986). "The intrinsic signal-to-noise ratio in NMR imaging." Magn Reson Med 3(4): 604-18.

Encyclopedia, A. D. A. M. M. (2008). "Hip fracture." from http://www.shands.org/health/HIE%20Multimedia/2/18026.htm.

Ensrud, K. E., D. E. Thompson, et al. (2000). "Prevalent vertebral deformities predict mortality and hospitalization in older women with low bone mass. Fracture Intervention Trial Research Group." J Am Geriatr Soc 48(3): 241-9.

Erber, T. and G. M. Hockney (1991). "Equilibrium configurations of N equal charges on a sphere." J. Phys. A: Math. Gen. 24: 1369-1377.

Ettinger, B., D. M. Black, et al. (1999). "Reduction of vertebral fracture risk in postmenopausal women with osteoporosis treated with raloxifene: results from a 3-year randomized clinical trial. Multiple Outcomes of Raloxifene Evaluation (MORE) Investigators." Jama 282(7): 637-45.

Falgarone, G., R. Porcher, et al. (2004). "Discrimination of osteoporotic patients with quantitative ultrasound using imaging or non-imaging device." Joint Bone Spine 71(5): 419-23.

Faulkner, K. G. and N. Pocock (2001). "Future methods in the assessment of bone mass and structure." Best Pract Res Clin Rheumatol 15(3): 359-83.

Favus, M. J. (1999). Primer on the metabolic bone diseases and disorders of mineral metabolism. Philadelphia, Lippincott Williams & Wilkins.

Fernandez-Seara, M. A., H. K. Song, et al. (2001). "Trabecular bone volume fraction mapping by low-resolution MRI." Magn Reson Med 46(1): 103-13.

Fisher, R. A. (1925). Ch 6: Transformed Correlations. Statistical Methods for Research Workers. London, Oliver & Boyd: 162-175.

Foundation, I. O. (2009). "Basic Bone Biology." from http://www.iofbonehealth.org/health-professionals/about-osteoporosis/basic-bone-biology.html.

Frost, H. M. (1987). "Bone "mass" and the "mechanostat": a proposal." Anat Rec 219(1): 1-9.

Fuchs, R. K., J. J. Bauer, et al. (2001). "Jumping improves hip and lumbar spine bone mass in prepubescent children: a randomized controlled trial." J Bone Miner Res 16(1): 148-56.

Garnero, P., W. J. Shih, et al. (1994). "Comparison of new biochemical markers of bone turnover in late postmenopausal osteoporotic women in response to alendronate treatment." J Clin Endocrinol Metab 79(6): 1693-700.

Genant, H. K. and Y. Jiang, Eds. (2006). Advanced imaging assessment of bone quality. Ann N Y Acad Sci. United States.

Geraets, W. G., P. F. Van der Stelt, et al. (1998). "The radiographic trabecular pattern of hips in patients with hip fractures and in elderly control subjects." Bone 22(2): 165-73.

Geraets, W. G., L. J. van Ruijven, et al. (2008). "Spatial orientation in bone samples and Young's modulus." J Biomech 41(10): 2206-10.

Geraets, W. G., L. J. van Ruijven, et al. (2006). "A sensitive method for measuring spatial orientation in bone structures." Dentomaxillofac Radiol 35(5): 319-25.

Gibson, L. J. (1985). "The mechanical behaviour of cancellous bone." J Biomech 18(5): 317-28.

Gibson, L. J. and M. F. Ashby (1988). Cellular solids. Structure and properties. Oxford, Pergamon.

Giles, J. (2009). "Vertebroplasty not Superior to Placebo for the Treatment of Painful Osteoporotic Fractures." Arthitis News.

Gilsanz, V., T. A. Wren, et al. (2006). "Low-level, high-frequency mechanical signals enhance musculoskeletal development of young women with low BMD." Journal of bone and mineral research : the official journal of the American Society for Bone and Mineral Research 21(9): 1464-74.

Goldstein, S. A., R. Goulet, et al. (1993). "Measurement and significance of three-dimensional architecture to the mechanical integrity of trabecular bone." Calcif Tissue Int 53 Suppl 1: S127-32; discussion S132-3.
Gomberg, B. R., P. K. Saha, et al. (2000). "Topological analysis of trabecular bone MR images." IEEE Trans Med Imaging 19(3): 166-74.
Gomberg, B. R., P. K. Saha, et al. (2003). "Topology-based orientation analysis of trabecular bone networks." Med Phys 30(2): 158-68.
Gomberg, B. R., F. W. Wehrli, et al. (2004). "Reproducibility and error sources of micro-MRI-based trabecular bone structural parameters of the distal radius and tibia." Bone 35(1): 266-76.
Goulet, R. W., S. A. Goldstein, et al. (1994). "The relationship between the structural and orthogonal compressive properties of trabecular bone." J Biomech 27(4): 375-89.
Griswold, M. A., P. M. Jakob, et al. (2002). "Generalized autocalibrating partially parallel acquisitions (GRAPPA)." Magn Reson Med 47(6): 1202-10.
Gudbjartsson, H. and S. Patz (1995). "The Rician distribution of noisy MRI data." Magn Reson Med 34(6): 910-4.
Guldberg, R. E., N. J. Caldwell, et al. (1997). "Mechanical stimulation of tissue repair in the hydraulic bone chamber." J Bone Miner Res 12(8): 1295-302.
Haacke, E. M., R. W. Brown, et al. (1999). "Magnetic Resonance Imaging," Physical Priniciples and Sequence Design. New York, John Wiley & Sons.
Haderslev, K. V., P. B. Jeppesen, et al. (2002). "Short-term administration of glucagon-like peptide-2. Effects on bone mineral density and markers of bone turnover in short-bowel patients with no colon." Scand J Gastroenterol 37(4): 392-8.
Haiat, G., F. Padilla, et al. (2006). "Numerical simulation of the dependence of quantitative ultrasonic parameters on trabecular bone microarchitecture and elastic constants." Ultrasonics 44 Suppl 1: e289-94.
Hans, D., T. Fuerst, et al. (1996). "Bone density and quality measurement using ultrasound." Curr Opin Rheumatol 8(4): 370-5.
Hans, D., C. Wu, et al. (1999). "Ultrasound velocity of trabecular cubes reflects mainly bone density and elasticity." Calcif Tissue Int 64(1): 18-23.
Harpen, M. D. (1988). "Influence of skin depth on NMR coil impedance. Part II." Phys Med Biol 33(5): 597-605.
Harrigan, T. P., M. Jasty, et al. (1988). "Limitations of the continuum assumption in cancellous bone." J Biomech 21(4): 269-75.
Harrigan, T. P. and R. W. Mann (1984). "Characterization of microstructural anisotropy in orthotropic materials using a second-rank tensor." J. Material Science 19: 761-67.
Heaney, R. P. (1990). "Bone mass and osteoporotic fractures." Calcif Tissue Int 47(2): 63-5.
Hengsberger, S., J. Enstroem, et al. (2003). "How is the indentation modulus of bone tissue related to its macroscopic elastic response? A validation study." J Biomech 36(10): 1503-9.
Hengsberger, S., A. Kulik, et al. (2001). "A combined atomic force microscopy and nanoindentation technique to investigate the elastic properties of bone structural units." Eur Cell Mater 1: 12-7.

Hildebrand, T. and P. Ruegsegger (1997). "A new method for the model independent assessment of thickness in three-dimensional images." Journal of Microscopy 185: 67-75.

Hodgskinson, R. and J. D. Currey (1990). "The effect of variation in structure on the Young's modulus of cancellous bone: a comparison of human and non-human material." Proc Inst Mech Eng H 204(2): 115-21.

Hofmann, T., F. Heyroth, et al. (2006). "Assessment of composition and anisotropic elastic properties of secondary osteon lamellae." J Biomech 39(12): 2282-94.

Hollister, S. J., J. M. Brennan, et al. (1994). "A homogenization sampling procedure for calculating trabecular bone effective stiffness and tissue level stress." J Biomech 27(4): 433-44.

Hollister, S. J., D. P. Fyhrie, et al. (1991). "Application of homogenization theory to the study of trabecular bone mechanics." J Biomech 24(9): 825-39.

Homminga, J., B. R. McCreadie, et al. (2002). "Cancellous bone mechanical properties from normals and patients with hip fractures differ on the structure level, not on the bone hard tissue level." Bone 30(5): 759-64.

Homminga, J., B. Van-Rietbergen, et al. (2004). "The osteoporotic vertebral structure is well adapted to the loads of daily life, but not to infrequent "error" loads." Bone 34(3): 510-6.

Hornak, J. P. (2000). "Magnetic Resonance Imaging: Imaging Hardware." Retrieved September 7th, 2010, from http://www.cis.rit.edu/class/schp730/lect/lect-17.htm.

Hou, F. J., S. M. Lang, et al. (1998). "Human vertebral body apparent and hard tissue stiffness." J Biomech 31(11): 1009-15.

Hoult, D. I. and P. C. Lauterbur (1979). "The sensitivity of the zeugmatogrphaic experiment involving human samples." Journal of Magnetic Resonance 34: 425-433.

Huiskes, R., R. Ruimerman, et al. (2000). "Effects of mechanical forces on maintenance and adaptation of form in trabecular bone." Nature 405(6787): 704-6.

Hulme, P. A., S. K. Boyd, et al. (2007). "Regional variation in vertebral bone morphology and its contribution to vertebral fracture strength." Bone 41(6): 946-57.

Hwang, S. N. and F. W. Wehrli (1999). "Estimating voxel volume fractions of trabecular bone on the basis of magnetic resonance images acquired in vivo " Inter J. Imaging Sys. Technology 10: 186-198.

Hwang, S. N., F. W. Wehrli, et al. (1997). "Probability-based structural parameters from three-dimensional nuclear magnetic resonance images as predictors of trabecular bone strength." Med Phys 24(8): 1255-61.

Issever, A. S., T. M. Link, et al. (2010). "Assessment of trabecular bone structure using MDCT: comparison of 64- and 320-slice CT using HR-pQCT as the reference standard." Eur Radiol 20(2): 458-68.

Ito, M., K. Ikeda, et al. (2005). "Multi-detector row CT imaging of vertebral microstructure for evaluation of fracture risk." Journal of bone and mineral research : the official journal of the American Society for Bone and Mineral Research 20(10): 1828-36.

Ito, M., M. Ohki, et al. (1995). "Trabecular texture analysis of CT images in the relationship with spinal fracture." Radiology 194(1): 55-9.
Jackson, R. D., A. Z. LaCroix, et al. (2006). "Calcium plus vitamin D supplementation and the risk of fractures." N Engl J Med 354(7): 669-83.
Jee, W. S. S. (1983). The skeletal tissues.
Jepsen, K. J. (2009). "Systems Analysis of Bone." Wiley Interdiscip Rev Syst Biol Med 1(1): 73-88.
Kabel, J., A. Odgaard, et al. (1999). "Connectivity and the elastic properties of cancellous bone." Bone 24(2): 115-20.
Kabel, J., B. van Rietbergen, et al. (1999). "The role of an effective isotropic tissue modulus in the elastic properties of cancellous bone." J Biomech 32(7): 673-80.
Kabel, J., B. van Rietbergen, et al. (1999). "Constitutive relationships of fabric, density, and elastic properties in cancellous bone architecture." Bone 25(4): 481-6.
Kanis, J. A., E. V. McCloskey, et al., Eds. (2008). A reference standard for the description of osteoporosis. Bone. United States.
Kanis, J. A., A. Oden, et al. (2009). "FRAX and its applications to clinical practice." Bone 44(5): 734-43.
Kato, H., M. Kuroda, et al. (2005). "Composition of MRI phantom equivalent to human tissues." Med Phys 32(10): 3199-208.
Kazakia, G. J., B. Hyun, et al. (2008). "In vivo determination of bone structure in postmenopausal women: a comparison of HR-pQCT and high-field MR imaging." J Bone Miner Res 23(4): 463-74.
Keaveny, T. M., R. E. Borchers, et al. (1993). "Theoretical analysis of the experimental artifact in trabecular bone compressive modulus." J Biomech 26(4-5): 599-607.
Keaveny, T. M., X. E. Guo, et al. (1994). "Trabecular bone exhibits fully linear elastic behavior and yields at low strains." Journal of biomechanics 27(9): 1127-36.
Keaveny, T. M. and W. C. Hayes (1993). "A 20-year perspective on the mechanical properties of trabecular bone." Journal of biomechanical engineering 115(4B): 534-42.
Keaveny, T. M., E. F. Morgan, et al. (2001). "Biomechanics of trabecular bone." Annu Rev Biomed Eng 3: 307-33.
Kentucky, R. A. o. N. (2009). "DEXA Scanning." Retrieved October 21, 2010, from http://www.radassociatesnky.com/diag_DEXAScanning.html.
Ketcham, R. A. and T. M. Ryan (2004). "Quantification and visualization of anisotropy in trabecular bone." J Microsc 213(Pt 2): 158-71.
Kleerekoper, M., A. R. Villanueva, et al. (1985). "The role of three-dimensional trabecular microstructure in the pathogenesis of vertebral compression fractures." Calcif Tissue Int 37(6): 594-7.
Konnopka, A., N. Jerusel, et al. (2009). "The health and economic consequences of osteopenia- and osteoporosis-attributable hip fractures in Germany: estimation for 2002 and projection until 2050." Osteoporos Int 20(7): 1117-29.
Kothari, M., T. M. Keaveny, et al. (1998). "Impact of spatial resolution on the prediction of trabecular architecture parameters." Bone 22(5): 437-43.

Kreider, J. M. and S. A. Goldstein (2009). "Trabecular bone mechanical properties in patients with fragility fractures." Clin Orthop Relat Res 467(8): 1955-63.

Krug, R., S. Banerjee, et al. (2005). "Feasibility of in vivo structural analysis of high-resolution magnetic resonance images of the proximal femur." Osteoporos Int 16(11): 1307-14.

Kuhn, J. L., S. A. Goldstein, et al. (1989). "Comparison of the trabecular and cortical tissue moduli from human iliac crests." Journal of orthopaedic research : official publication of the Orthopaedic Research Society 7(6): 876-84.

Ladinsky, G. A., B. Vasilic, et al. (2008). "Trabecular structure quantified with the MRI-based virtual bone biopsy in postmenopausal women contributes to vertebral deformity burden independent of areal vertebral BMD." J Bone Miner Res 23(1): 64-74.

Laib, A. and P. Ruegsegger (1999). "Comparison of structure extraction methods for in vivo trabecular bone measurements." Comput Med Imaging Graph 23(2): 69-74.

Laugier, P., P. Droin, et al. (1997). "In vitro assessment of the relationship between acoustic properties and bone mass density of the calcaneus by comparison of ultrasound parametric imaging and quantitative computed tomography." Bone 20(2): 157-65.

Lehmann, T. M., C. Gonner, et al. (1999). "Survey: interpolation methods in medical image processing." IEEE Trans Med Imaging 18(11): 1049-75.

Lenchik, L., L. F. Rogers, et al. (2004). "Diagnosis of osteoporotic vertebral fractures: importance of recognition and description by radiologists." American Journal of Roentgenology 183: 949-958.

Li, C. Q., J. F. Magland, et al. (2008). "Implications of resolution and noise for in vivo micro-MRI of trabecular bone." Med Phys 35(12): 5584-94.

Lian, J., J. Gorski, et al. (2004, Updated 1/16/04). "Bone Structure and Function." from http://depts.washington.edu/bonebio/ASBMRed/structure.html.

Lin, W., G. A. Ladinsky, et al. (2007). "Image metric-based correction (autofocusing) of motion artifacts in high-resolution trabecular bone imaging." J Magn Reson Imaging 26(1): 191-7.

Liu, X. S., X. H. Zhang, et al. (2010). "Accuracy of high-resolution in vivo micro magnetic resonance imaging for measurements of microstructural and mechanical properties of human distal tibial bone." J Bone Miner Res.

Lotz, J. C., E. J. Cheal, et al. (1995). "Stress distributions within the proximal femur during gait and falls: implications for osteoporotic fracture." Osteoporos Int 5(4): 252-61.

Lotz, J. C. and W. C. Hayes (1990). "The use of quantitative computed tomography to estimate risk of fracture of the hip from falls." J Bone Joint Surg Am 72(5): 689-700.

Ma, J., F. W. Wehrli, et al. (1996). "Fast 3D large-angle spin-echo imaging (3D FLASE)." Magn Reson Med 35(6): 903-10.

Magland, J. F., C. E. Jones, et al. (2009). "Retrospective 3D registration of trabecular bone MR images for longitudinal studies." J Magn Reson Imaging 29(1): 118-26.

Magland, J. F., C. S. Rajapakse, et al. (2010). "3D fast spin echo with out-of-slab cancellation: a technique for high-resolution structural imaging of trabecular bone at 7 Tesla." Magn Reson Med 63(3): 719-27.

Magland, J. F., M. J. Wald, et al. (2009). "Spin-echo micro-MRI of trabecular bone using improved 3D fast large-angle spin-echo (FLASE)." Magn Reson Med 61(5): 1114-21.

Magland, J. F. and F. W. Wehrli (2008). "Trabecular bone structure analysis in the limited spatial resolution regime of in vivo MRI." Acad Radiol 15(12): 1482-93.

Majumdar, S. (2002). "Magnetic resonance imaging of trabecular bone structure." Top Magn Reson Imaging 13(5): 323-34.

Majumdar, S. and H. K. Genant (1995). "A review of the recent advances in magnetic resonance imaging in the assessment of osteoporosis." Osteoporos Int 5(2): 79-92.

Majumdar, S., M. Kothari, et al. (1998). "High-resolution magnetic resonance imaging: three-dimensional trabecular bone architecture and biomechanical properties." Bone 22(5): 445-54.

Majumdar, S., D. Newitt, et al. (1996). "Magnetic resonance imaging of trabecular bone structure in the distal radius: relationship with X-ray tomographic microscopy and biomechanics." Osteoporos Int 6(5): 376-85.

McKee, M. D., J. B. Jupiter, et al. (1996). "Coronal shear fractures of the distal end of the humerus." J Bone Joint Surg Am 78(1): 49-54.

Mellish, R. W., M. M. O'Sullivan, et al. (1987). "Iliac crest trabecular bone mass and structure in patients with non-steroid treated rheumatoid arthritis." Ann Rheum Dis 46(11): 830-6.

Michigan, U. o. (2010). "BME456 class website." from http://www.engin.umich.edu/class/bme456/bonestructure/bonestructure.htm.

Mohamed, F. B., S. Vinitski, et al. (1999). "A simple method to improve image nonuniformity of brain MR images at the edges of a head coil." J Comput Assist Tomogr 23(6): 1008-12.

Mosekilde, L. (1989). "Sex differences in age-related loss of vertebral trabecular bone mass and structure--biomechanical consequences." Bone 10(6): 425-32.

Mosekilde, L., S. M. Bentzen, et al. (1989). "The predictive value of quantitative computed tomography for vertebral body compressive strength and ash density." Bone 10(6): 465-70.

Mosekilde, L., A. Viidik, et al. (1985). "Correlation between the compressive strength of iliac and vertebral trabecular bone in normal individuals." Bone 6(5): 291-5.

Moyad, M. A. (2003). "Osteoporosis: a rapid review of risk factors and screening methods." Urol Oncol 21(5): 375-9.

Mueller, T. L., M. Stauber, et al. (2009). "Non-invasive bone competence analysis by high-resolution pQCT: an in vitro reproducibility study on structural and mechanical properties at the human radius." Bone 44(2): 364-71.

Newitt, D. C., S. Majumdar, et al. (2002). "In vivo assessment of architecture and micro-finite element analysis derived indices of mechanical properties of trabecular bone in the radius." Osteoporos Int 13(1): 6-17.

Newitt, D. C., B. van Rietbergen, et al. (2002). "Processing and analysis of in vivo high-resolution MR images of trabecular bone for longitudinal studies: reproducibility of structural measures and micro-finite element analysis derived mechanical properties." Osteoporos Int 13(4): 278-87.

Oden, Z. M., D. M. Selvitelli, et al. (1998). "The effect of trabecular structure on DXA-based predictions of bovine bone failure." Calcif Tissue Int 63(1): 67-73.

Odgaard, A. (1997). "Three-dimensional methods for quantification of cancellous bone architecture." Bone 20(4): 315-28.

Odgaard, A., E. B. Jensen, et al. (1990). "Estimation of structural anisotropy based on volume orientation. A new concept." J Microsc 157 (Pt 2): 149-62.

Odgaard, A., J. Kabel, et al. (1997). "Fabric and elastic principal directions of cancellous bone are closely related." J Biomech 30(5): 487-95.

Ohman, C., M. Baleani, et al. (2007). "Mechanical testing of cancellous bone from the femoral head: experimental errors due to off-axis measurements." J Biomech 40(11): 2426-33.

Osteoporosis and related bone diseases national resource center, N. (2009). "Osteoporosis: The Diagnosis." Retrieved May, 1, 2010, from http://www.niams.nih.gov/health_info/bone/osteoporosis/diagnosis.asp.

Pauly, J., P. Le Roux, et al. (1991). "Parameter relations for the Shinnar-Le Roux selective excitation pulse design algorithm [NMR imaging]." IEEE Trans Med Imaging 10(1): 53-65.

Pereda, C. A., R. A. Hannon, et al. (2002). "The impact of subcutaneous oestradiol implants on biochemical markers of bone turnover and bone mineral density in postmenopausal women." Bjog 109(7): 812-20.

Pirnay, F., M. Bodeux, et al. (1987). "Bone mineral content and physical activity." Int J Sports Med 8(5): 331-5.

Pistoia, W., B. van Rietbergen, et al. (2004). "Image-based micro-finite-element modeling for improved distal radius strength diagnosis: moving from bench to bedside." J Clin Densitom 7(2): 153-60.

Pruessmann, K. P., M. Weiger, et al. (1999). "SENSE: sensitivity encoding for fast MRI." Magn Reson Med 42(5): 952-62.

Rad, H. S., M. J. Wald, et al. (2009). High Precision Translational Motion Correction for Micro-MRI of Trabecular Bone Using Cartesian Navigators. Proceedings of the 17th Annual Scientific Meeting of ISMRM, Oahu,HI.

Radin, E. L., R. B. Orr, et al. (1982). "Effect of prolonged walking on concrete on the knees of sheep." J Biomech 15(7): 487-92.

Rajapakse, C. S., J. F. Magland, et al. (2010). "Computational biomechanics of the distal tibia from high-resolution MR and micro-CT images." Bone 47: 556-63.

Rajapakse, C. S., J. F. Magland, et al. (2008). "Fast prospective registration of in vivo MR images of trabecular bone microstructure in longitudinal studies." Magn Reson Med 59(5): 1120-6.

Rapillard, L., M. Charlebois, et al., Eds. (2006). Compressive fatigue behavior of human vertebral trabecular bone. J Biomech. United States.

Ray, N. F., J. K. Chan, et al. (1997). "Medical expenditures for the treatment of osteoporotic fractures in the United States in 1995: report from the National Osteoporosis Foundation." J Bone Miner Res 12(1): 24-35.

Recker, R. R. (1989). "Low bone mass may not be the only cause of skeletal fragility in osteoporosis." Proc Soc Exp Biol Med 191(3): 272-4.
Renders, G. A., L. Mulder, et al. (2008). "Biomechanical effect of mineral heterogeneity in trabecular bone." J Biomech 41(13): 2793-8.
Rho, J. Y., R. B. Ashman, et al., Eds. (1993). Young's modulus of trabecular and cortical bone material: ultrasonic and microtensile measurements. J Biomech. United States.
Rice, J. C., S. C. Cowin, et al. (1988). "On the dependence of the elasticity and strength of cancellous bone on apparent density." J Biomech 21(2): 155-68.
Riggs, B. L., S. Khosla, et al. (1998). "A unitary model for involutional osteoporosis: estrogen deficiency causes both type I and type II osteoporosis in postmenopausal women and contributes to bone loss in aging men." J Bone Miner Res 13(5): 763-73.
Rincon-Kohli, L. and P. K. Zysset (2009). "Multi-axial mechanical properties of human trabecular bone." Biomechanics and modeling in mechanobiology 8(3): 195-208.
Robling, A. G., F. M. Hinant, et al. (2002). "Improved bone structure and strength after long-term mechanical loading is greatest if loading is separated into short bouts." J Bone Miner Res 17(8): 1545-54.
Ross, P. D., J. W. Davis, et al. (1990). "A critical review of bone mass and the risk of fractures in osteoporosis." Calcif Tissue Int 46(3): 149-61.
Rotter, M., A. Berg, et al. (2001). "Autocorrelation analysis of bone structure." J Magn Reson Imaging 14(1): 87-93.
Roux, W. (1881). Der Kampf der Theile im Organismus. Leipzig.
Saha, P. K. and B. B. Chaudhuri (1996). "3D digital topology under binary transformation with applications." Comput. Vision Image Understanding 63: 418-429.
Saha, P. K. and F. W. Wehrli (2004). "Measurement of trabecular bone thickness in the limited resolution regime of in vivo MRI by fuzzy distance transform." IEEE Trans Med Imaging 23(1): 53-62.
Sarkar, S., B. H. Mitlak, et al. (2002). "Relationships between bone mineral density and incident vertebral fracture risk with raloxifene therapy." J Bone Miner Res 17(1): 1-10.
Schuit, S. C., M. van der Klift, et al. (2004). "Fracture incidence and association with bone mineral density in elderly men and women: the Rotterdam Study." Bone 34(1): 195-202.
Siris, E. S., Y. T. Chen, et al. (2004). "Bone mineral density thresholds for pharmacological intervention to prevent fractures." Arch Intern Med 164(10): 1108-12.
Snow, C. M., D. P. Williams, et al. (2001). "Bone gains and losses follow seasonal training and detraining in gymnasts." Calcif Tissue Int 69(1): 7-12.
Sodickson, D. K. and W. J. Manning (1997). "Simultaneous acquisition of spatial harmonics (SMASH): fast imaging with radiofrequency coil arrays." Magn Reson Med 38(4): 591-603.
Song, H. K. and F. W. Wehrli (1999). "In vivo micro-imaging using alternating navigator echoes with applications to cancellous bone structural analysis." Magn Reson Med 41(5): 947-53.

Srinivasan, S., S. C. Agans, et al., Eds. (2003). Enabling bone formation in the aged skeleton via rest-inserted mechanical loading. Bone. United States.
Stauber, M. and R. Muller (2006). "Age-related changes in trabecular bone microstructures: global and local morphometry." Osteoporos Int 17(4): 616-26.
Steiniche, T. (1995). "Bone histomorphometry in the pathophysiological evaluation of primary and secondary osteoporosis and various treatment modalities." APMIS Suppl 51: 1-44.
Techawiboonwong, A., H. K. Song, et al. (2005). "Implications of pulse sequence in structural imaging of trabecular bone." J Magn Reson Imaging 22(5): 647-55.
Trone, D. W., D. Kritz-Silverstein, et al. (2007). "Is radiographic vertebral fracture a risk factor for mortality?" Am J Epidemiol 166(10): 1191-7.
Turner, C. H. (2005). "The biomechanics of hip fracture." Lancet 366: 98-100.
Turner, C. H. (2010). "Turner Biomechanics Laboratory." Our Mission: To better understand the biomechanics of the skeleton in health and disease., from http://www.engr.iupui.edu/~turnerch/biomech.htm.
Turner, C. H. and S. C. Cowin (1987). "Dependence of elastic constants of an anisotropic porous material upon porosity and fabric." Journal of Material Science 22: 3178-3184.
Turner, C. H. and S. C. Cowin (1988). "Errors induced by off-axis measurement of the elastic properties of bone." J Biomech Eng 110(3): 213-5.
Turner, C. H., S. C. Cowin, et al. (1990). "The fabric dependence of the orthotropic elastic constants of cancellous bone." J Biomech 23(6): 549-61.
Ulrich, D., B. van Rietbergen, et al. (1999). "The ability of three-dimensional structural indices to reflect mechanical aspects of trabecular bone." Bone 25(1): 55-60.
van Rietbergen, B., R. Huiskes, et al. (1995). The role of trabeculae architecture in the anisotropic mehcanical properties of bone. Bone Structure and Remodeling. A. Odgaard and H. Weinans. Singapore, World Scientific
van Rietbergen, B., S. Majumdar, et al. (2002). "High-resolution MRI and micro-FE for the evaluation of changes in bone mechanical properties during longitudinal clinical trials: application to calcaneal bone in postmenopausal women after one year of idoxifene treatment." Clin Biomech (Bristol, Avon) 17(2): 81-8.
Van Rietbergen, B., A. Odgaard, et al. (1996). "Direct mechanics assessment of elastic symmetries and properties of trabecular bone architecture." Journal of Biomechanics 29(12): 1653-1657.
Van Rietbergen, B., A. Odgaard, et al. (1998). "Relationships between bone morphology and bone elastic properties can be accurately quantified using high-resolution computer reconstructions." J Orthop Res 16(1): 23-8.
Varga, P., S. Baumbach, et al. (2009). "Validation of an anatomy specific finite element model of Colles' fracture." J Biomech 42(11): 1726-31.
Vasilic, B., H. K. Song, et al. (2004). "Coherence-induced artifacts in large-flip-angle steady-state spin-echo imaging." Magn Reson Med 52(2): 346-53.
Vasilic, B. and F. Wehrli (2005). Semi-automated algorithm for segmentation of the trabecular-bone region in micro-MR images of the distal radius and tibia.

Proceedings 13th Scientific Meeting, International Society for Magnetic Resonance in Medicine, Miami.

Vasilic, B. and F. W. Wehrli (2005). "A novel local thresholding algorithm for trabecular bone volume fraction mapping in the limited spatial resolution regime of in vivo MRI." IEEE Trans Med Imaging 24(12): 1574-85.

Waarsing, J. H., J. S. Day, et al. (2006). "Bone loss dynamics result in trabecular alignment in aging and ovariectomized rats." J Orthop Res 24(5): 926-35.

Wald, M. J., J. Magland, et al. (2008). Implications of Resolution Isotropy on Apparent Topology of Trabecular Bone Architecture in MR Images. Proceedings of the 30th Annual Meeting of ASBMR, Montreal, CA.

Wald, M. J., J. F. Magland, et al. (2010). "Structural and mechanical parameters of trabecular bone estimated from in vivo high-resolution magnetic resonance images at 3 tesla field strength." J Magn Reson Imaging 31(5): 1157-68.

Wald, M. J., B. Vasilic, et al. (2007). "Spatial autocorrelation and mean intercept length analysis of trabecular bone anisotropy applied to in vivo magnetic resonance imaging." Med Phys 34(3): 1110-20.

Waldt, S., N. Meier, et al. (1999). "[The texture-analysis of high-resolution computed tomograms as an additional procedure in osteoporosis diagnosis: in-vitro studies on vertebral segments]." Rofo 171(2): 136-42.

Wang, J., A. Reykowski, et al. (1995). "Calculation of the signal-to-noise ratio for simple surface coils and arrays of coils." IEEE Trans Biomed Eng 42(9): 908-17.

Wang, Z., J. Wang, et al. (2005). "Improved data reconstruction method for GRAPPA." Magn Reson Med 54(3): 738-42.

Ward, K., C. Alsop, et al. (2004). "Low magnitude mechanical loading is osteogenic in children with disabling conditions." Journal of bone and mineral research : the official journal of the American Society for Bone and Mineral Research 19(3): 360-9.

Watts, N. B. (2000). "Focus on primary care postmenopausal osteoporosis: an update." Obstet Gynecol Surv 55(12 Suppl 3): S49-55.

Wehrli, F. W., B. R. Gomberg, et al. (2001). "Digital topological analysis of in vivo magnetic resonance microimages of trabecular bone reveals structural implications of osteoporosis." J Bone Miner Res 16(8): 1520-31.

Wehrli, F. W., S. N. Hwang, et al. (1998). "New architectural parameters derived from micro-MRI for the prediction of trabecular bone strength." Technol Health Care 6(5-6): 307-20.

Wehrli, F. W., G. A. Ladinsky, et al. (2008). "In vivo magnetic resonance detects rapid remodeling changes in the topology of the trabecular bone network after menopause and the protective effect of estradiol." J Bone Miner Res 23(5): 730-40.

Wehrli, F. W., M. B. Leonard, et al. (2004). "Quantitative high-resolution magnetic resonance imaging reveals structural implications of renal osteodystrophy on trabecular and cortical bone." J Magn Reson Imaging 20(1): 83-9.

Wehrli, F. W., P. K. Saha, et al. (2003). "Noninvasize assessment of bone architecture by magnetic resonance micro-imaging-based virtual bone biopsy." Proceedings of the IEEE 91(10): 1520-42.

Wehrli, F. W., P. K. Saha, et al. (2002). "Role of magnetic resonance for assessing structure and function of trabecular bone." Top Magn Reson Imaging 13(5): 335-55.

Wehrli, F. W., H. K. Song, et al. (2006). "Quantitative MRI for the assessment of bone structure and function." NMR Biomed 19(7): 731-64.

Werner, C., B. F. Iversen, et al. (1988). "Contribution of the trabecular component to mechanical strength and bone mineral content of the femoral neck. An experimental study on cadaver bones." Scand J Clin Lab Invest 48(5): 457-60.

Whitehouse, W. J. (1974). "The quantitative morphology of anisotropic trabecular bone." J Microsc 101 Pt 2: 153-68.

Whitehouse, W. J. and E. D. Dyson (1974). "Scanning electron microscope studies of trabecular bone in the proximal end of the human femur." J Anat 118(Pt 3): 417-44.

Wolff, J. (1892). Das Gesetz der Transformation der Knochen (The Law of Bone Remodeling). Berlin Heidelberg New York, Springer 1986 (translated from the German 1892 edition).

World Health Organization, W. (1994). Assessment of fracture risk and its application to screening for postmenopausal osteoporosis: Report of a WHO Study Group, World Health Organization: 843.

Yablonskiy, D. A. (1998). "Quantitation of intrinsic magnetic susceptibility-related effects in a tissue matrix. Phantom study." Magn Reson Med 39(3): 417-28.

Yablonskiy, D. A. and E. M. Haacke (1994). "Theory of NMR signal behavior in magnetically inhomogeneous tissues: the static dephasing regime." Magn Reson Med 32(6): 749-63.

Yamada, M., M. Ito, et al. (1994). "Dual energy X-ray absorptiometry of the calcaneus: comparison with other techniques to assess bone density and value in predicting risk of spine fracture." AJR Am J Roentgenol 163(6): 1435-40.

Yang, G., J. Kabel, et al. (1998). "The anisotropic Hooke's law for cancellous bone and wood." J Elast 53(2): 125-46.

Zysset, P. K. (2003). "A review of morphology-elasticity relationships in human trabecular bone: theories and experiments." J Biomech 36(10): 1469-85.

Zysset, P. K., R. W. Goulet, et al. (1998). "A global relationship between trabecular bone morphology and homogenized elastic properties." J Biomech Eng 120(5): 640-6.